



# Magnetic and physical properties of sediment cores collected along the Lesser Antilles accretionary wedge: natural hazards and influence of lithological changes on the paleomagnetic signal

Arthur Bieber

## ► To cite this version:

Arthur Bieber. Magnetic and physical properties of sediment cores collected along the Lesser Antilles accretionary wedge: natural hazards and influence of lithological changes on the paleomagnetic signal. Earth Sciences. Université Paris Cité; Université du Québec à Rimouski, 2022. English. NNT : 2022UNIP7059 . tel-04210775

HAL Id: tel-04210775

<https://theses.hal.science/tel-04210775>

Submitted on 19 Sep 2023

**HAL** is a multi-disciplinary open access archive for the deposit and dissemination of scientific research documents, whether they are published or not. The documents may come from teaching and research institutions in France or abroad, or from public or private research centers.

L'archive ouverte pluridisciplinaire **HAL**, est destinée au dépôt et à la diffusion de documents scientifiques de niveau recherche, publiés ou non, émanant des établissements d'enseignement et de recherche français ou étrangers, des laboratoires publics ou privés.



Université  
Paris Cité

IPGP  
Sciences pour la planète

UQAR  
ISMER

Université du Québec à Rimouski  
Institut des sciences de la mer de Rimouski

## Université Paris Cité Institut Physique du Globe de Paris

**En cotutelle avec Université du Québec à Rimouski**  
Institut des Sciences de la Mer de Rimouski

Ecole doctorale STEP'UP - ED N°560  
IPGP – *Equipe Géosciences marines*

# Propriétés magnétiques et physiques de carottes sédimentaires prélevées le long du prisme d'accrétion des Petites Antilles : Risques naturels et influence de la lithologie sur le signal paléomagnétique

Par Arthur Bieber

Thèse de doctorat de Science de la Terre et de l'Environnement

Dirigée par Nathalie Feuillet  
Et par Guillaume St-Onge

Présentée et soutenue publiquement le 30 mars 2022

Devant un jury composé de :

**Pascal Bernatchez**, Professeur, Université du Québec à Rimouski, président du jury  
**Guillaume St-Onge**, Professeur, Université du Québec à Rimouski, Institut des sciences de la mer de Rimouski, directeur de recherche  
**Nathalie Feuillet**, Physicienne, Institut de Physique du Globe de Paris, directrice de recherche  
**Christian Beck**, Professeur émérite, Université Savoie Mont-Blanc, rapporteur  
**Torsten Haberzettl**, Professeur, Universität Greifswald, rapporteur



## REMERCIEMENTS

En commençant ce doctorat en septembre 2016, je ne m'attendais certainement pas à mener des recherches sur 5 ans et demi. Au-delà des aléas de la vie, je n'aurais probablement pas pu mener à terme ce projet sans les nombreuses personnes qui y ont contribué de près comme de loin.

Tout commence avec l'offre de projet par Guillaume St-Onge, mon directeur à l'ISMER qui m'a donné cette opportunité. J'ai ainsi eu la chance de participer à la mission océanographique CASEIS, rejoindre le laboratoire de paléomagnétisme et sédimentologie marine, découvrir et développer des connaissances et un métier. Guillaume par tes connaissances et ton inéluctable positivisme et bonne humeur, tu m'as permis d'aller toujours plus loin avec ce jeu de données, malgré toutes les difficultés rencontrées. Ton soutien pendant la pandémie de la COVID-19 a été sans faille tant financièrement qu'humainement. Merci pour les relectures rapides et efficaces alors que je fournissais mes différents chapitres de plus en plus vite pour des *échéances* toujours plus courtes.

C'est bien entendu sans compter sur le développement de la mission CASEIS par ma directrice à l'IPGP, Nathalie Feuillet. Cette mission a été une opportunité incroyable pour moi, de rencontrer de nombreuses personnes, mais aussi de découvrir la paléosismologie marine dans la région des Petites Antilles. Merci pour ta disponibilité à l'IPGP lors de mes venues, mais aussi par mail tout le long. Tu as su être présente malgré les 6h de décalage, notamment à la fin de la rédaction.

A tous les deux un grand merci pour la confiance et le soutien que vous m'avez accordé du début jusqu'à la fin de ce doctorat !

Merci à tous les membres du jury qui ont lu et commenté cette thèse. Merci Pascal Bernatchez, Christian Beck et Torsten Haberzettl pour les questions et discussions durant la soutenance qui ont montré votre intérêt pour mes recherches.

Je tiens aussi à remercier Eva Moreno et Julie Carlut qui m'ont accueilli à l'IPGP et au MNHN pour les analyses réalisées à Paris. Merci pour le soutien tant dans l'échantillonnage que l'utilisation des instruments et l'interprétation des données. Merci d'avoir été disponible lors de mes deux séjours en France. Un grand merci aussi pour votre active participation à la rédaction et l'amélioration des différents papiers qui composent cette thèse, sans parler des différentes (très) courtes *échéances* que j'ai pu imposer lors de la rédaction d'*abstract* et de *poster* en dernière minutes.

Enfin, ces travaux seraient impossibles à réaliser sans le soutien et la disponibilité du personnel administratif tant de l'ISMER que de l'IPGP, et du soutien technique des différents laboratoires. Je remercie chaleureusement Quentin Beauvais, pour ta disponibilité, tes formations sur les instruments et ton aide pour chaque problème rencontré au laboratoire. Merci Maxence St-Onge pour ta disponibilité sur le magnétomètre et l'interprétation des données paléomagnétique. Je me souviens aussi de très bon moment avec toi et Sarah à l'IRM *Summer School* (2018). Merci aussi à Lola Johannes du MNHN de m'avoir accueilli et aidé dans le sous échantillonnage des carottes CASEIS pour les analyses à Paris.

Ce doctorat s'est déroulé quasiment en simultané avec ceux de Chloé Seibert et Pierre Morena. Merci à vous deux pour toutes les discussions qu'on a pu avoir au sujet des Petites Antilles et des paléo-séismes. Il reste encore des questions à répondre et je suis sûr qu'on pourra continuer à parler de ce projet encore longtemps. Le temps passé avec vous, que ce soit sur le navire, à Paris ou à Rimouski et que ce soit pour le travail ou pour nous même, a toujours été agréable.

Basé principalement à l'ISMER, je ne peux pas manquer de remercier tous les membres du laboratoire de géologie que je n'ai pas encore cité, Jean-Carlos et André, mais aussi tous les étudiants que j'ai pu côtoyer au bureau, en laboratoire, au Baro, et plein d'autres endroits : Julie, PAD, Myriam, Simon, Omi, Yan, Naïs, Sarah, Fatma, Illiana, Quentin, Marie, Charles-Edouard, Edouard, Simon, Jade, Adriana, Maria-Emilia, Zélia, Kelsey, Méril, Camille, Florian, Elodie, Juliette, Christian, Pauline. Je pense aussi aux survivants de l'exam' doc : Léo, Laoul, Simon et Atif ! Il y a bien entendu d'autres étudiants de l'ISMER-UQAR, avec qui j'ai pu passer du temps à oublier le doctorat et vivre la vie de Rimouski : Camille, Martin, Tony, Val, Guillaume, Inès, Eloisa, Juli, Xime, Andy, Mélanie, Antoine, Efflam, Bruno, Sarah, Jean, Julie-Camille, Jessie.

Mention spéciale pour les personnes avec qui j'ai été à SPM et à l'IRMSS, ceux avec qui j'ai pu aller à l'EGU, l'AGU ou encore l'ISC ! Et puis il y a ceux qui ont rythmé un peu plus cette vie, les colocs du 27 St Joseph Est, Myriam, Jean et Maité qui m'ont accueilli à bras ouverts en 2016, puis avec les divers changements, Adriana, Gonzalo et Amé ! N'oublions pas le passage de Paprika que je me suis retrouvé à chasser dans Rimouski matin et soir, puis qui me suivait jusqu'à l'ISMER pendant que je travaillais de nuit au 2G, et qui m'attendait au petit matin pour rentrer à la coloc avec moi ! Je n'oublie pas non plus les nuits de discussion au Baro avec Adriana, malgré les barrières linguistiques on a refait le monde à de nombreuses reprises ! Et puis Quentin et Léo, avec qui j'ai eu de nombreuses discussions sur nos projets respectifs et sur nos vies, merci à vous deux !

Je dois bien le concéder, un doctorat ça demande d'évacuer régulièrement ses problèmes, et grâce à Myriam j'ai découvert un super sport ! Je remercie l'équipe de Roller Derby Rimouski (RDR) de m'avoir accueilli en tant que joueur, puis de m'avoir subi dans l'équipe de coach pendant 2 ans. Merci à Sarah, Myriam, André, Alice, Vaness, Steve, Francis, Frank, Joanie, Alex, Matthieu, Gab, Chantal, Fanny, Mina, Mél, Marianne, Carole-Anne, Laurence, Léa, Baptiste, Sherley-Anne, Cat, Michel.

Et puis il y a la famille ! Je vous remercie du fond du cœur de m'avoir soutenu depuis toujours, quels que soient mes choix de vies. Et malgré la pandémie, malgré la distance, vous avez toujours été présents et prêts à m'apporter le réconfort nécessaire.

Forcément, je tiens une place particulière pour celle qui m'a rejoint à Rimouski et qui me supporte depuis, malgré les heures de travaux acharnées à des horaires improbables, et un rythme pas tellement sain... Léa, merci pour ton aide du début à la fin, les relectures de dernières minutes pour le dépôt, pour ton soutien et surtout pour ton amour !

Avant de mettre un point final à ces remerciements, je tiens à nommer quelques personnes particulières qui ont cru en moi à certain moment clé et qui m'ont permis avec ma famille, d'en arriver là : Florance Delavaud (V. Louis), Thierry Mulder, Philipe Martinez, Laurent Londeix, Bruno Malaizé, Nadia Sénéchal, Linda Rossignol, Hervé Gillet, Marion Corbé (laboratoire EPOC) les étudiants du master d'océanographie de bordeaux (promotion 2012-2014), Fatima Mokadem, Séolène Saulnier-Copard, Cyril Castanet et l'ensemble du laboratoire de géographie physique de paris (LGP). Et puis il y a tout ceux que je ne nommerai pas qui ont fait de ma vie étudiante à Bordeaux un souvenir particulier, je pense à ces nombreuses heures passées à la Soucoupe, le Carpe, le Blarney, le Titi-Twister, la Cale Sèche et le Dick Turpin's. Et puis ceux qui ont su garder le contact, alors du fond du cœur, merci Andréa, Maxime et Alexiane.

Enfin, je remercie les institutions qui ont contribué au financement de ce doctorat : ANR, CRSNG, GEOTOP, UQAR, IPGP et la chaire de recherche en géologie marine.

A mes parents, mon frère, mes sœurs et ma nièce !



## AVANT-PROPOS

Ce projet de doctorat est né de la collaboration entre le professeur Guillaume St-Onge de l’Institut des sciences de la mer de Rimouski (ISMER) et de la physicienne Nathalie Feuillet de l’Institut de physique du globe de Paris (IPGP), qui est l’instigatrice et la responsable à la fois de la campagne océanographique CASEIS (CAraïbes – SEISmes) et du projet de l’Agence nationale de la recherche (ANR) CARQUAKES (CAraïbes – EarthQUAKES). La mission s’est déroulée à bord du N/R Le Pourquoi Pas ? de la flotte océanographique française (IFREMER) entre le 29 mai et le 5 juillet 2016. Elle a permis de récolter 34 longues carottes à piston de type CALYPSO et 9 carottes à boite, soit près de 512 mètres de sédiments marins, ainsi que près de 6000 km de profils sismiques et bathymétriques (Chirp et imagerie multifaisceaux). Toutes les données sismiques et sédimentaires récoltées permettent d’étudier les grands séismes qui se sont produits et qui ont modifié la structure géologique de la zone des Petites Antilles au cours du Quaternaire récent. Grâce à la présence de failles sismiques visibles sur les profils Chirps et de dépôts gravitaires associés à ces événements extrêmes, il est envisageable de réaliser une corrélation géographique de l’extension des paléo-séismes, mais aussi une chronologie permettant de mettre en évidence une récurrence de ces événements.

Cette étude a été réalisée en collaboration avec deux autres projets de doctorat de Chloé Seibert et Pierre Morena, terminés en 2019 et 2020, qui portaient respectivement sur les données sismiques et sédimentaires de la zone sud (Guadeloupe et Martinique) et nord (Antigua) des Petites Antilles.

In fine, les résultats issus de l’étude de ces données permettront de mieux comprendre les risques liés aux aléas sismiques qui menacent les îles de l’arc antillais composé de près de 4 millions d’habitants en 2006. De plus, il sera possible d’améliorer notre compréhension du fonctionnement de la zone de subduction des Antilles et de la sismicité associée.



## RÉSUMÉ

L’arc volcanique des Petites Antilles est la résultante d’une zone de subduction avec le plongement des plaques océaniques Atlantique nord et sud sous la plaque des Caraïbes à une vitesse actuelle estimée à 2 cm/an. En plus de la présence d’un volcanisme depuis l’Éocène récent jusqu’à aujourd’hui avec une déviation de l’axe volcanique à la suite de la subduction des rides asismiques de Tiburon et Barracuda, la région est sismiquement active. Les failles en échelons accommodent la composante oblique de la convergence et l’accumulation des tensions mécaniques à l’interface des plaques en question, générant des séismes récurrents, comme en 2004 au large des Saintes ( $M=6.3$ ) et en 2007 au large de la Martinique ( $M=7.4$ ). D’autres séismes plutôt associés à l’interface de subduction, peuvent aussi être dévastateurs comme ceux reportés en 1839 et 1843 au large des îles de la Martinique et de la Guadeloupe qui ont détruit des villes et fait plusieurs centaines de morts. Il est donc important de mieux comprendre le fonctionnement de cette zone de subduction et ses cycles sismiques.

C’est dans ce contexte que la mission océanographique CASEIS a eu lieu durant l’été 2016 pour récolter des carottes sédimentaires et obtenir de nombreux profils sismiques afin de mieux contraindre les aléas sismiques sur des échelles de temps long couvrant une partie du Quaternaire. En effet, des études ont montré qu’il était possible d’utiliser des couches déposées rapidement (RDL) et notamment les turbidites comme marqueur stratigraphique de séismes. Si ces dépôts ont lieu de façon simultanée dans des bassins profonds de l’avant-arc des Petites Antilles, alors il est fort probable qu’ils aient été déclenchés par un séisme. De plus, des complexes homogénites-turbidites ont déjà été identifiés dans la région et sont susceptibles d’être la signature de mégaséismes ou des tsunamis associés. À l’aide des paramètres physiques, magnétiques et lithologiques de cinq carottes sédimentaires, cette thèse de doctorat montre également l’intérêt du paléomagnétisme pour les études de paléosismologie marine.

Dans un premier chapitre, il est question d’établir une magnétostratigraphie régionale à l’aide des variations de paléointensité relative (RPI), des isotopes de l’oxygène et des inversions géomagnétiques passées. En effet, la carotte CAS16-24PC récoltée sur un point haut du prisme d’accretion est datée à plus de 1,15 Ma et présente la dernière inversion Matuyama-Brunhes et le sub-chron Jaramillo. En comparant les données magnétiques et isotopiques à des compilations de mesures datées précisément, de nombreux *tie-points* permettent de cadrer temporellement l’ensemble de cette carotte.

Le second chapitre utilise les dates radiométriques (carbone 14) d’études antérieures, la magnétostratigraphie régionale établie précédemment et la compilation de paléointensités de l’Atlantique Nord (NAPIS-75) pour dater quatre carottes et estimer l’âge des RDL de trois

d'entre-elles. Ces dernières ont été prélevées dans des bassins de l'avant-arc des Petites Antilles et du prisme, isolés les uns des autres et des apports directs des îles et des plateformes carbonatées. Toutes présentent des turbidites et des complexes homogénites-turbidites qui, étant donné la localisation et la profondeur de prélèvement, seraient reliées à des événements sismiques. L'âge des événements est mieux défini à l'aide de la RPI des carottes, et permet d'estimer un super-cycle sismique de 24 ka incluant une période de quiescence de 6 ka.

Le troisième chapitre étudie les variations de l'enregistrement paléomagnétique en fonction de la lithologie. La quantité de RDL identifiée dans les carottes permet d'étudier l'enregistrement du signal paléomagnétique par ces dépôts et d'établir un nouveau modèle de dépôt des complexes homogénites-trubidites (HmTu). Ces résultats s'appuient notamment sur les variations d'enregistrement de l'inclinaison magnétique. En effet, la base des complexes HmTu présente un enregistrement paléomagnétique peu fiable lié à un hydrodynamisme important lors du dépôt, alors que la partie homogène supérieure enregistre une oscillation de l'inclinaison qui serait le fruit d'un effet de seiche induit par un séisme. Enfin, en combinant l'ensemble des turbidites (sans prendre en compte la partie homogène des complexes), une relation linéaire a été mise en évidence entre l'épaisseur de ces couches et les variations d'inclinaison. En revanche, la taille des grains magnétiques présente une relation quasi-logarithmique avec l'épaisseur de ces événements. Ces corrélations montrent que la taille des grains comme la compaction ne permettent pas d'expliquer à eux seuls les variations de l'enregistrement du signal paléomagnétique par les turbidites.

En répondant aux objectifs spécifiques de ce projet, cette thèse répond à la problématique générale. En effet, l'ensemble des trois chapitres permet d'établir une cyclicité des événements sismiques (de l'activité tectonique) au cours des derniers 70 ka dans les Petites Antilles tout en apportant une magnétostratigraphie qui s'étend sur plus d'un million d'année et de nouvelles données sur les processus d'acquisition d'une aimantation rémanente par le sédiment.

Mots-clés : Quaternaire ; Petites Antilles ; Paléosismologie ; Paléomagnétisme ; Turbidites ; complexes homogénites-turbidites

## ABSTRACT

The Lesser Antilles volcanic arc result from the north and south Atlantic plates subducting beneath the Caribbean plate at a velocity of  $2 \text{ cm.yr}^{-1}$ . In addition to Eocene-old volcanism and recent arc migration induced by the subduction of the two aseismic ridges Tiburon and Barracuda, this area continues to remain seismically active. *En echelon* fault system accommodates oblique convergence component that generate several earthquakes such as offshore Les Saintes ( $M=6,3$ ) in 2004 and offshore Martinique ( $M=7,4$ ) in 2007. Subduction interface megathrusts can be devastating, as reported in 1839 and 1843 offshore Martinique and Guadeloupe islands. These two megathrusts have destroyed cities and caused hundreds of deaths. It is essential therefore to better understand how this subduction zone and its seismic cycles work.

In this context, the CASEIS expedition took place during the summer 2016. Several sediment piston-cores and a number of seismic profiles were collected to better constrain the seismic hazard over the recent Quaternary. Several studies reveal rapidly deposited layers (RDL) especially turbidite as good stratigraphic marker for seismic event. If such deposits are found simultaneously in several fore-arc basins of the Lesser Antilles, then these deposits were most probably triggered by seismic events. In addition, homogenite-turbidite complexes were already identified in this region and are probably the fingerprint of megathrusts or associated tsunamis. Using physical, magnetic, and lithologic parameters of five sediment cores, this thesis shows how paleomagnetism can be useful for marine paleoseismologic studies.

In the first chapter, a regional magnetostratigraphy is established using relative paleointensity variations (RPI), oxygen isotopes and geomagnetic reversals. Core CAS16-24PC, which was collected on a topographic high of the accretionary wedge, is dated at over 1,15 Ma and reveal the last Matuyama-Brunhes reversal and the Jaramillo sub-chron. By comparing paleomagnetic and isotopic data to well dated stacks, many tie-points allowed to better constrain the chronostratigraphy of the entire core.

The second chapter uses previously published radiometric dating (carbon 14), the regional magnetostratigraphy, and the North Atlantic paleointensity stack (NAPIS-75) to date four cores and to estimate RDL ages for three of these cores. These cores were retrieved in disconnected fore-arc and accretionary prism basins. These basins are also disconnected from direct carbonate platforms and islands inputs. All cores are interbedded by turbidites and homogenite-turbidite complexes. Considering location and depth, these deposits are probably triggered by seismic events. Events ages are better defined with the combination of

RPI and radiocarbon dating and allow to estimate a seismic super-cycle of 24 ka including a quiescence period of 6 ka.

The third chapter studies variations of paleomagnetic record as function of the lithology. Quantity of RDL identified in all studied cores provided new insight of turbidites and homogenite-turbidite complexes (HmTu) paleomagnetic records and established a new depositional model for the latter. These results rely on paleomagnetic inclination variations. While HmTu basal deposits show unreliable paleomagnetic data linked to a strong hydrodynamic influence, homogenous upper parts record an inclination oscillation. This oscillation results of a seiche effect induced by a seismic event. By combining all turbidites including basal part of HmTu, a linear relationship is found between layer thicknesses and inclination variations. In contrast, magnetic grain size shows a quasi-logarithmic relationship with layer thicknesses. These relationships reveal that grain size and compaction cannot explain themselves the turbidites paleomagnetic signal variations.

This project has better answered the main problem of the seismic cycles of the Lesser Antilles subduction zone. Through the three chapters, we were able to establish a cyclicity of tectonic activity for the last 70 ka in the Lesser Antilles, whilst a regional magnetostratigraphy back to over 1.15 Ma, and new data and knowledge on the acquisition of remanent magnetisation by the sediment.

*Keywords:* *Quaternary; Lesser Antilles; Paleoseismology; Paleomagnetism; Turbidites; Homogenites-turbidites complexes*

## TABLE DES MATIÈRES

REMERCIEMENTS.....	iii
AVANT-PROPOS .....	vii
RÉSUMÉ .....	ix
ABSTRACT.....	xii
TABLE DES MATIÈRES .....	xiii
LISTE DES TABLEAUX .....	xv
LISTE DES FIGURES .....	xvii
INTRODUCTION GÉNÉRALE .....	27
1. LA GEOLOGIE DES CARAÏBES, DU PACIFIQUE A L'ATLANTIQUE .....	29
2. L'ARC ANTILLAIS, DE LA TECTONIQUE AUX SEISMES .....	32
3. LA SEDIMENTATION, DES PROCESSUS A LA COMPOSITION SEDIMENTAIRE .....	35
4. LE PALEOMAGNETISME, DU PRINCIPE A L'OUTIL .....	39
5. LA PALEOSISMATOLOGIE EN MER, UN OUTIL QUI SE DEVELOPPE .....	41
6. PROBLEMATIQUE DU PROJET .....	42
7. OBJECTIFS DE RECHERCHE .....	44
8. ÉCHANTILLONNAGE ET ANALYSES : DES FONDS MARINS JUSQU'A LABORATOIRE .....	46
9. ORGANISATION DE LA THESE .....	50
CHAPITRE 1 CHRONOSTRATIGRAPHIE RÉGIONALE DU PRISME D'ACCRÉTION ET DE L'AVANT-ARC À L'EST DES PETITES ANTILLES : PALÉOINTENSITÉ RELATIVE, stratigraphie isotopique ET INVERSIONS .....	55
1.1 RESUME EN FRANÇAIS DU PREMIER ARTICLE.....	55
1.2 REGIONAL CHRONOSTRATIGRAPHY IN THE EASTERN LESSER ANTILLES QUATERNARY FOREARC AND ACCRETIONARY WEDGE SEDIMENTS: RELATIVE PALEOINTENSITY, OXYGEN ISOTOPES AND REVERSALS.....	57
1.2.1 Introduction .....	57

1.2.2 Regional setting .....	59
1.2.3 Material and methods.....	60
1.2.4 Results.....	65
1.2.5 Discussion.....	77
1.2.6 Conclusion .....	85
<b>CHAPITRE 2 ANALYSE PALEOMAGNETIQUE DES COUCHES DEPOSEES RAPIDEMENT AU COURS DES DERNIERS 90 KA DANS LA ZONE DE SUBDUCTION DES PETITES ANTILLES : EXPRESSION D'UN SUPER-CYCLE SISMIQUE .....</b>	<b>99</b>
<b>2.1 RESUME EN FRANÇAIS DU DEUXIEME ARTICLE .....</b>	<b>99</b>
<b>2.2 PALEOMAGNETIC ANALYSIS OF RAPIDLY DEPOSITED LAYERS OVER THE LAST 90 KA AT THE LESSER ANTILLES SUBDUCTION ZONE: EXPRESSION OF EARTHQUAKE SUPER-CYCLE .....</b>	<b>101</b>
2.2.1 Introduction.....	102
2.2.2 Regional setting .....	104
2.2.3 Material and methods.....	106
2.2.4 Results.....	108
2.2.5 Discussion .....	122
2.2.6 Conclusions.....	128
<b>CHAPITRE 3 Influence des changements lithologiques sur l'enregistrement du signal paléomagnétique basée sur des couches Quaternaires déposées rapidement dans les Petites Antilles : un nouveau modèle de dépôt pour les complexes homogénite- turbidites.....</b>	<b>141</b>
<b>3.1 RESUME EN FRANÇAIS DU TROISIEME ARTICLE .....</b>	<b>141</b>
<b>3.2 INFLUENCE OF LITHOLOGICAL CHANGES ON THE PALEOMAGNETIC RECORD BASED ON QUATERNARY RAPIDLY DEPOSITED LAYERS FROM THE LESSER ANTILLES: A NEW MODEL FOR THE DEPOSITION OF HOMOGENITE-TURBIDITE COMPLEXES .....</b>	<b>143</b>
3.2.1 Introduction.....	144
3.2.2 Materials and methods .....	145
3.2.3 Results.....	147
3.2.4 Discussion .....	153
3.2.5 Conclusion .....	159
<b>CONCLUSION GÉNÉRALE .....</b>	<b>167</b>
<b>ANNEXES .....</b>	<b>175</b>
<b>RÉFÉRENCES BIBLIOGRAPHIQUES .....</b>	<b>195</b>

## LISTE DES TABLEAUX

Table 1 - List of $\delta^{18}\text{O}$ tie points with isotopic composition of the sample and the corresponding LR04 point with age, including the error used in the age-depth model.....	78
Table 2 - List of RPI tie points determined against PISO-1500 (I1-18) and against PADM2M (P1-16), including the error used in the age-depth model.....	80
Table 3 - Physical properties of the three main facies hemipelagic (HMPL), turbidite (Tu) including turbidite from homogenite-turbidite complexes (HmTu) and homogenite (HMG) for cores CAS16-04PC, -14PC and 36PC.....	114
Table 4 - List of RPI tie-points determined using $^1\text{NAPIS-75}$ (Laj et al., 2000); reference record $^2\text{CAS16-24PC}$ (Bieber et al., 2021) and CAS16-12PC, with MCD and age, including the error used in the age-depth model .....	121
Table 5 - Meter composite depth (MCD) correspondence with original coring depth in meters .....	177
Table 6 - Major elemental percentages obtained by energy dispersive X-ray spectroscopy (EDS) in samples indicated in Fig. 16.....	179
Table 7 - List of all samples collected and analyzed on AGM with depth in meter and respective magnetic parameters in tesla.....	187
Table 8 - Meter composite depth (MCD) correspondence with original coring depth in meter.....	191



## LISTE DES FIGURES

Figure 1 - Image issue du modèle Slab2 mettant en évidence la localisation des principales zones de subduction avec la géométrie de plongement des plaques subduites (modifiée de Hayes et al., 2018). ....	27
Figure 2 - Exemples de dégâts structurels liés au séisme des Sainte de 2004. ....	28
Figure 3 - Reconstruction des deux modèles géodynamiques envisagés pour la formation de la plaque Caraïbes depuis le Crétacé moyen (d'après Laurencin et al. 2018). AP: Passage d'Anegada; APs: Plaques Americaines ; BR: Ride de Barracuda ; C: Cuba; CAR: Plaque des Caraïbes ; CT: Fosse des Caïmans ; H: Hispaniola; MR: Rift de Mona ; PR: Puerto Rico ; TR: Ride de Tiburon.....	30
Figure 4 - Carte de la région des Caraïbes présentant les positions relatives des plaques et les différentes régions citées dans le texte (modifiée de Giunta et Orioli, 2011). AP=Passage d'Anegada ; BeR=Ride Beata ; CHC=Block Choco ; CHR=Block Chortis ; CHT=Block Chorotega ; GB=Bassin de Grenade ; MAY=Block Maya.....	31
Figure 5 - A : Carte générale de la région autour de la Mer des Caraïbes avec les principaux courants marins (flèches rouges ; Johns et al., 1998; Zhang et al., 2017). B : Carte des Petites Antilles. Gris clair et gris foncé : îles respectivement de l'arc intérieur et de l'arc extérieur (Mts: Montserrat; MG: Marie-Galante; FaB: Falmouth bank, BB: Bertrand bank, FB: Flandre bank, CB: Colombia bank, DBPB: Dien Bien Phu bank, AB: Amerique Banque). Noir : îles non volcaniques. Étoiles jaunes : tremblements de terre historiques, localisation d'après Feuillet et al. (2011a). Triangles rouges : volcans actifs. Lignes brunes : Débris des dépôts d'avalanche et les glissements de terrain sous-marins de Deplus et al. (2001), Le Friant et al. (2004) et Brunet et al. (2016). Ligne noire graticulée : les systèmes de failles de Feuillet et al. (2001, 2004). Ligne noire avec triangles et ligne en pointillé noir : respectivement la poussée frontale du prisme d'accrétion et la limite supposée du prisme interne. Lignes bleues : canaux (pointillés les lignes sont des canaux supposés). Les rides asismiques sont mises en évidence par des lignes rouges et leurs parties subductées par des lignes pointillées rouges. C : profil de la bathymétrie à travers l'arc des Petites Antilles, emplacement sur la figure B. Les lignes pointillées noires correspondent à la bathymétrie Geomap et les lignes noires à la bathymétrie des missions océanographiques (figure et légende issues de Seibert et al., 2020).....	33

Figure 6 - Séismes historiques de magnitude supérieure à 5 depuis 1900 dans les Petites Antilles. Les étoiles orange sont les séismes de mai 1851 et avril 1897 à proximité de la Guadeloupe.....	34
Figure 7 - Modèle des principaux processus sédimentaires existant autour de l'arc des Petites Antilles (figure modifiée d'après Picard et al. (2006), Carey (2000), Sigurdsson et al. 1981). .....	37
Figure 8 – Composante du champ magnétique terrestre représenté par le vecteur magnétique $B$ (figure de Philippe, 2019).....	40
Figure 9 - Corrélation stratigraphique (traits verts) des paramètres physiques et magnétiques de quatre carottes sédimentaires prélevées dans la fosse de Sumatra. Les dates $^{14}\text{C}$ ont été réalisées sous la base des turbidites (figure de Patton et al., 2013). .....	42
Figure 10 - Banc MSCL insallé à bord du N/R Pourquoi Pas ? pendant la mission CASEIS (© Nathalie Feuillet, 2016). ....	47
Figure 11 – A gauche, prélèvement d'un <i>u-channel</i> dans une demie-section de carotte sédimentaire. A droite, photographie d'un magnétomètre cryogénique SRM-755 de 2G Enterprise. ....	49
Figure 12 - Photographie du magnétomètre à gradient alternatif (MicroMag 2900 de Princeton Measurements Corp.) de l'ISMER. ....	50
Figure 13 - Bathymetric map of the middle Lesser Antilles Arc, western Atlantic Ocean using GEBCO and CASEIS data. Red and yellow lines highlight, respectively, continental slope canyons and forearc basin canyons. The local minimum gravity anomaly limit (black dotted line), the N 294°E strike of the Tiburon ridge (dashed black lines) and the deformation front (white dashed line with teeth) are derived from Bouysse and Wastercamp (1990). The location of reference core CAS16-24PC is indicated in purple. ....	59
Figure 14 - A: Full core high-resolution photography with CT-scan images (left: TOP of the core, right: BOTTOM of the core). B: MSCL and XRF data comprising from left to right: P-wave velocity, density, magnetic susceptibility $k$ , $L^*$ , CT-number, and $\ln(\text{Fe/Ca})$ . The shipboard grain size log is also plotted on the right, including red marks that are pure hemipelagic background sediments used to delimit the background signal with $\pm 2\sigma$ (whitened band between red straight lines). RDL are highlighted as grey horizontal intervals.....	67
Figure 15 - A: Brownish hemipelagic background sediments defined with low and stable magnetic susceptibility ( $k$ ), CT-number, density and P-wave velocity, interbedded with a RDL ( $\approx 5$ cm) between 2.70 m and 2.65 m (yellow band).	

B: Light brown hemipelagic background sediments are defined by low and stable k, CT-number, density and P-wave velocity data. A well-defined RDL between 6.24 m and 6.14 m is darker (dark brown to grey color) with an erosive contact, normal grading (high CT-number, P-wave velocity, density) and high k.....	68
Figure 16 - SEM images for representative bulk sample VIII-1137. The left-hand image is a general view of the sample. The right-hand image is focused on small particles (<10 µm) and matrix analysis. Blue bands are 10 µm scales. Red objects are elemental analyses, as referenced in Table 6 (ANNEXE 1) with the same numbers.....	70
Figure 17 - A: Typical hemipelagic sediment raw hysteresis loops (blue). High-field and mass corrected loops are shown in red. B: Magnetic susceptibility vs. high temperatures. Red curves for heating, while blue curves are for cooling.....	71
Figure 18 - A: Day plot (Day et al., 1977). Red labeled dots are data for the samples presented in Fig. 17. B: King plot (King et al., 1982).....	72
Figure 19 - Magnetic properties of the pelagic sediments (event-free composite record) with concentration, and magnetic grain size-dependent parameters on the left (NRM20 mT, ARM20 mT and IRM20 mT). $k_{ARM}/k$ indicates magnetic grain size variations for a magnetic assemblage dominated by magnetite.....	73
Figure 20 - Paleomagnetic data including from left to right: ChRM10-40 mT, ARM, IRM and SIRM demagnetization steps. Inclination (red line is the ±GAD inclination at the site latitude) and declination (blue dots are data for the discrete samples). MAD values > 15° are indicated in dark red and >20° in red.....	75
Figure 21 - Typical demagnetization curves and orthogonal projections of hemipelagic sediments. Filled blue dots represent the range of demagnetization steps used to calculate the characteristic remanent magnetization (ChRM).....	75
Figure 22 - Comparison of the RPI estimated with the average ratios (superposed red and green curves) and slope methods (red and green curves) in the scatter plots on the left, the correlation is reduced for ARM. Demagnetization curves for NRM, ARM and IRM are presented on the right-hand side.....	76
Figure 23 - Planktic foraminiferal $\delta^{18}\text{O}$ record for core CAS16-24PC (red curve) correlated to the LR04 benthic stack in blue (Lisiecki and Raymo, 2005). Black crosses represents the tie points determined using the AnalySeries software (Paillard et al., 1996) .....	77

Figure 24 - Top: virtual axial dipole moment (VADM) derived from the PISO-1500 stack (Channell et al., 2009) in black. Upper middle: RPI record for core 24PC ratio-method normalized by ARM in red. Lower middle: paleomagnetic axial dipole moment (PADM2M) model (Ziegler et al., 2011) in grey. Notable tie points are indicated with green dots (I-1 to I-18) and blue dots (P-1 to P-16). Bottom: compilation of PISO-1500, PADM2M and RPI record (colors are the same as above with the violet curve derived from the developed slope method). ....	79
Figure 25 - Age-depth model developed using the R package Bacon 2.2 (Blaauw and Christen, 2011) with linear interpolation using 3 paleomagnetic reversals (grey dots) and 37 tie points (blue and green dots) from RPI (see Fig. 24) and 37 tie points (red dots) from $\delta^{18}\text{O}$ stratigraphy (see Fig. 23). Age-errors used for each tie point correspond to half the distance samples (see Fig. 46 in ANNEXE 1). Sedimentation rates are derived from the age-depth model, including RDL (grey dotted lines). B = Brunhes Chron, M = Matuyama Chron, J = Jaramillo Subchron. ....	82
Figure 26 - Planktic foraminiferal $\delta^{18}\text{O}$ record for core CAS16-24PC (blue curve) and RPI record (red curve) using the age-depth model developed in this study (Fig. 25) compared with the LR04 benthic (upper black curve), PISO-1500 (lower black curve) and PADM2M (grey curve) stacks. Odd-numbered MIS are highlighted with grey bands. B = Brunhes Chron, M = Matuyama Chron, J = Jaramillo Subchron. ....	83
Figure 27 - Bathymetric map of the Lesser Antilles Arc, western Atlantic Ocean (A), north of Barbuda island (B) and east of Antigua and Guadeloupe islands (C), using GEBCO and CASEIS data. Maps also reveal the core location in orange for CAS16-04, -14 and -36PC, and purple for core CAS16-12PC.....	105
Figure 28 - Physical and magnetic parameter as a function of depth (m) comprising from left to right: high-resolution photography (P.), CT-scan images (CT-S.), CT-number, density, P-wave velocity, magnetic susceptibility, white (100) to black (0) color space ( $L^*$ ) and magnetic susceptibilities ratio ( $k_{\text{ARM}}/k$ ). RDL are highlighted as light red (turbidite), light brown and yellow-sand (HmTu complexes).....	110
Figure 29 - Examples for each facies of each core with the same parameters as Fig. 28. Top: hemipelagic background sediments (HMPL). Middle: Turbidite facies highlighted in light red with fining upward red arrows on CT-scan images. Bottom: Homogenite-turbidite complexes (HmTu) facies highlighted in light brown (Tu) and sandy-yellow (Hm) with fining upward brown arrows and vertical yellow arrows on CT-scan images.....	111

Figure 30 - King plot (King et al., 1982). A: hemipelagic (HMPL) background sediments (green symbols). B: turbidite (TU) sediments (red symbols). C: homogenite (yellow) turbidite (brown symbols) complexes (HmTu) .....	116
Figure 31 - Paleomagnetic data including from left to right: NRM, ARM and IRM demagnetization steps, inclination ( $I^\circ$ ; red line is the GAD inclination at the site latitude), declination and MAD angles for cores CAS16-04PC, -14PC and -36PC.....	118
Figure 32 - A) Comparison of CAS16-12PC RPI (black curves) with reference records CAS16-24PC (brown curve) and NAPIS-75 (red curves), including coefficient of correlation ( $r$ ). B) Age-depth model of core CAS16-12PC developed using R Package Bacon 2.2 (Blaauw and Christen, 2011), with linear interpolation using five NAPIS-75 tie points (red dots) and seven CAS16-24PC tie points (blue dots). Sedimentation rates are derived from the age-depth model. Interglacial marine isotopic stages (MIS) from 3 to 9 are in blue roman number and all MIS delimited by strait lines from linear interpolation curve to axis.....	120
Figure 33 - Same figure as Fig. 32 but for cores CAS16-04PC (blue curves), -14PC (green curves) and -36PC (purple curves). Blue dots are $^{14}C$ dates while red dots are RPI tie points and green dots reflect the Laschamps geomagnetic excursion. RDL are additionally plotted as chart bar (yellow) with HmTu labeled with event size.....	126
Figure 34 - A) Bar chart of 5 ka grouped and stacked RDL with blue bar for CAS16-04PC RDL (deep blue for HmTu), green bar for CAS16-14PC RDL (deep green for HmTu) and violet bar for CAS16-36PC RDL (deep violet for HmTu) compared to global sea level variations (Spratt and Lisiecki, 2015). B) Bar chart of RDL size function of time. HmTu are labeled from 1 to 11 for each core ante-chronologically. Background bar chart stacked RDL as clustered defined by C. C: box plots of each clustered event (CE-1 to CE-4) with associated quiescence time Q1 to Q3. Red arrows reveal time between each average age of CE .....	127
Figure 35 - Location of cores CAS16-04PC, -14PC, and -36PC in the western Atlantic Ocean (Lesser Antilles fore-arc basins). ....	146
Figure 36 - Inclination (including MAD values in orange)) and magnetic grain size parameter ( $k_{ARM}/k$ ) as a function of rescaled depth (cm) from turbidites identified in each core. Dark red arrows follow grains size variations from the bottom to top of each deposit. Grey arrows represent the range in inclination and $k_{ARM}/k$ .....	148

Figure 37 - Two typical orthogonal projections with the associated demagnetization curves for one turbidite example in each core.....	150
Figure 38 - Inclination (including MAD values in orange) and magnetic grain size parameter ( $k_{ARM}/k$ ) as a function of rescaled depth (cm) from homogenite-turbidite complexes identified in each core. Dark red arrows follow grains size variations from bottom to the top of each deposit. Grey arrows represent the range of inclination and $k_{ARM}/k$ . .....	151
Figure 39 - Typical orthogonal projection (Zijderveld, 1967) with the associated demagnetization curve for one homogenite-turbidite complex in each core. Top: homogenite part; bottom: turbidite part. White circles (green circles) represent projections on the vertical plane (horizontal plane).....	153
Figure 40 - A) Normalized coercivity distribution made from the first derivative of IRM acquisition curves. Brown, yellow and green curves represent Tu, Hm, and hemipelagite respectively. B) Same figure as A) but with a 3D rotation. The depth of each turbidite and hemipelagite are in their respective color.....	155
Figure 41 - Top: Homogenite part of HmTu with from left to right high-definition photography, CT-scan images, MAD ( $^{\circ}$ ), inclination ( $^{\circ}$ ), and declination ( $^{\circ}$ ). Bottom: Same parameters for the turbidite part of HmTu deposits.....	155
Figure 42 - Bar chart of HMPL (green), HMG (yellow) and TU (brown) declination, inclination, and MAD standard deviation ( $\sigma$ ) for each core and total mean values. ....	156
Figure 43 - A) HmTu example from core CAS16-04PC with inclination ( $^{\circ}$ , black line), GAD ( $^{\circ}$ , red line), and MAD ( $^{\circ}$ , grey line) as a function of depth. Transparent rectangles represent Tu (brown), Hm (yellow), and HMPL (green). B) The right side of the figure presents the dynamics, while the left side presents the resulting deposits.....	158
Figure 44 – Left plot is a power-law relationship between magnetic grain size range and turbidite thickness. Right plot is a linear relationship between $\Delta I$ and turbidite thickness. Red dots are strictly turbidite, while green dots are turbidite basal parts of HmTu. Their respective fit curves are in red and blue lines (with a 90 % confidence range) while the blue line is the fit curve of the combination of both datasets. ....	158
Figure 45 - Schematic explanation of age-error used for the age-depth model. The half-time gap between a tie-point and its surrounding values is represented in green and purple segments. The longest half-time gap (green segments) is set as this specific tie-point age-error. ....	175

Figure 46 - Inclination, declination and relative paleointensity records for core CAS16-24PC.....	176
Figure 47 - Physical and magnetic parameter as a function of depth (m) comprising from left to right: high-resolution photography (P.), CT-scan images (CT-S.), CT-number, density, P-wave velocity, magnetic susceptibility, white (100) to black (0) color space ( $L^*$ ) and magnetic susceptibilities ratio ( $k_{ARM}/k$ ). RDL are highlighted as light red (turbidite), light brown and yellow-sand (HmTu complexes). .....	180
Figure 48 - Typical demagnetization curves and orthogonal projections of hemipelagic background sediment (HMPL), turbidite (TU) and homogenite (HMG) for cores CAS16-04PC, -14PC and -36PC.....	182
Figure 49 - Typical raw hysteresis loops (blue) and high-field corrected loops (red) of hemipelagic sediment (solid line) and turbidite (dotted line) for core CAS16-12PC (A, B and C) and cores CAS16-04PC (D), CAS16-14PC (E) and CAS16-36PC (F). G and H are King plot (King et al., 1982) of respectively all the sample listed on Table 7 (ANNEXE 2) and the six hemipelagite hysteresis loops (A to F).....	182
Figure 50 - Comparison of the CAS16-12PC RPI variations estimated with the average ratios (Red + orange for ARM normalizer and violet curve for $k$ normalizer) and slope method (red curve) associated to the correlation coefficient (red dot, $r$ ). Scatter plots on the left test unconformity of normalizer against estimated RPI and reveal a reduced correlation for ARM. Demagnetization curves for NRM and ARM are presented on the right-hand side.....	183
Figure 51 - Comparison of the CAS16-04PC RPI variations estimated with the average ratios (superposed red, green and violet curves for ARM, IRM and $k$ respectively) and slope methods (red and green curves). Scatter plots on the left test unconformity of normalizers against estimated RPI and show a reduced correlation for $k$ and ARM. Demagnetization curves for NRM, ARM and IRM are presented on the right-hand side. ....	184
Figure 52 - Comparison of the CAS16-14PC RPI variations estimated with the average ratios (superposed red, green and violet curves for ARM, IRM and $k$ respectively) and slope methods (red and green curves). Scatter plots on the left test unconformity of normalizers against estimated RPI and show a reduced correlation for $k$ and ARM. Demagnetization curves for NRM, ARM and IRM are presented on the right-hand side. ....	185
Figure 53 - Comparison of the CAS16-36PC RPI variations estimated with the average ratios (superposed red, green and violet curves for ARM, IRM and	

k respectively) and slope methods (red and green curves). Scatter plots on the left test unconformity of normalizers against estimated RPI and show a reduced correlation for k and ARM. Demagnetization curves for NRM, ARM and IRM are presented on the right-hand side..... 186

## LISTE DES ABRÉVIATIONS, DES SIGLES ET DES ACRONYMES

**AF** *alternating field*, champ alternatif

**ARM** *anhysteretic remanent magnetisation*, aimantation rémanente anhystérétique

**DC** *direct current*, courant continu

**DRM** *detrital remanent magnetization*, aimantation rémanente détritique

**GAD** *geocentric axial dipole*, dipole axial géocentré

**Hc** *coercive force*, coercivité

**Hcr** *remanent coercive force*, coercivité rémanente

**INRS-ETE** Institut National de la Recherche Scientifique Eau Terre Environnement

**IPGP** Institut de Physique du Globe de Paris

**IRM** *isothermal remanent magnetization*, aimantation rémanente isothermale

**ISMER** Institut des Sciences de la Mer de Rimouski

**k** *magnetic susceptibility*, susceptibilité magnétique

**k<sub>ARM</sub>** *susceptibility of the anhysteretic remanent magnetisation*, susceptibilité de l'aimantation rémanente anhystérétique

**LSCE** Laboratoire des Sciences du Climat et de l'Environnement

**MAD** *maximum angular deviation*, déviation angulaire maximum

**MD** *multidomain*, domaines multiples

**MNHN** Museum national d'histoire naturel

**Mr** *saturation remanence*, rémanence à saturation

**Ms** *saturation magnetisation, aimantation à saturation*

**MSCL** *multi-sensor core logger, banc de mesures*

**NRM** *natural remanent magnetisation, aimantation naturelle rémanente*

**pDRM** *post-detrital remanent magnetization, aimantation rémanente post-déposition*

**RDL** *rapidly deposited layers, couches déposées rapidement*

**SD** *single domain, domaine simple*

**SIRM** *saturation isothermal remanent magnetization, aimantation rémanente isothermale à saturation*

**UQAR** Université du Québec à Rimouski

**VADM** *virtual axial dipole moment, moment dipolaire axial virtuel*

## INTRODUCTION GÉNÉRALE

Un tremblement de terre peut se produire en de nombreux endroits à la surface du globe terrestre soumettant ces zones à ce qu'on appelle un aléa sismique. Il existe des zones sismiquement plus actives, comme les régions volcaniques ou les limites de plaques terrestres. Cet aléa peut présenter un risque lorsqu'il a lieu à proximité de zones habitées à forte vulnérabilité, et ainsi provoquer de graves dommages tant matériels qu'humains. Il est donc essentiel de comprendre à la fois les mécanismes de déclenchement, mais aussi la fréquence et la magnitude de ces événements en un lieu donné. Pacheco et Sykes (1992) ont démontré que les séismes de plus grande magnitude ont lieu dans les zones de subduction, c'est-à-dire là où la lithosphère océanique plus froide et plus dense plonge sous l'asthénosphère d'une autre plaque tectonique (Fig. 1).

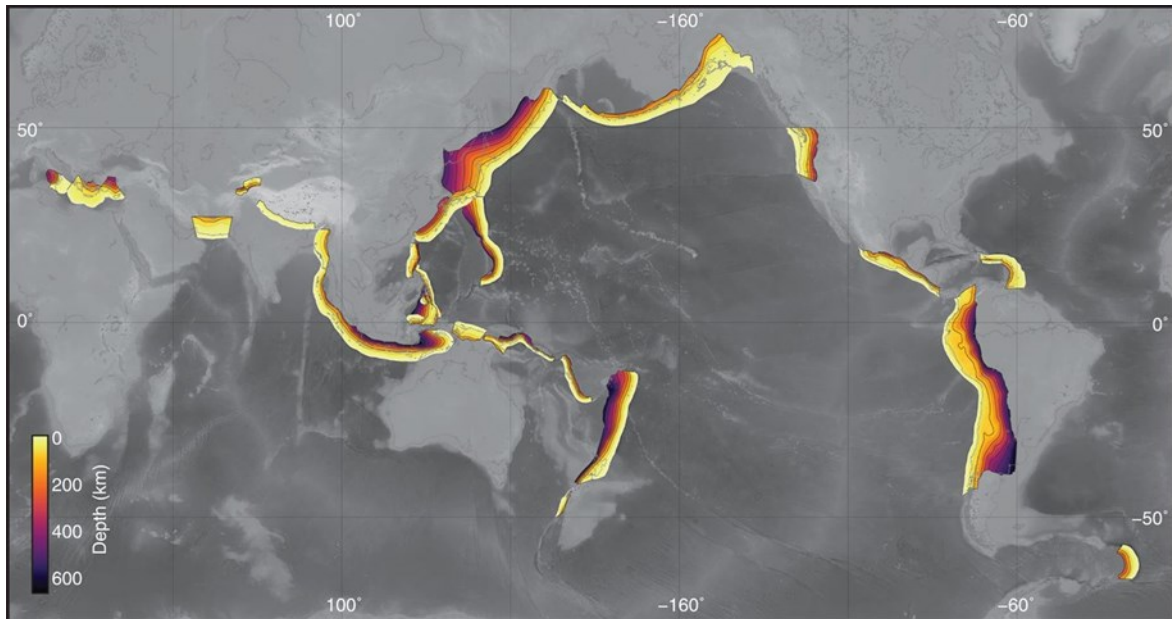


Figure 1 - Image issue du modèle Slab2 mettant en évidence la localisation des principales zones de subduction avec la géométrie de plongement des plaques subduites (modifiée de Hayes et al., 2018).

Une de ces zones de subduction se situe dans l'Atlantique et a notamment donné naissance aux îles volcaniques des Petites Antilles : il s'agit de l'unique zone de subduction présente sur le territoire français. Ce plongement des croûtes océaniques nord- et sud-américaine sous la plaque des Caraïbes a entraîné la formation d'arcs volcaniques dont l'activité sismique et volcanique est suivie en permanence par les observatoires volcanologique et sismologique de la Guadeloupe et de la Martinique (IPGP-OVSG, OVSM 2005). Bien qu'il n'y ait eu, à ce jour, aucun mégaséisme (M8-9) au cours de la période instrumentale, un certain nombre de séismes majeurs de magnitude supérieure à 7 ont été rapportés au cours de la période historique (Feuillet et al., 2011). Les deux séismes récents les plus importants ont eu lieu aux Saintes le 21 novembre 2004 (BCSF, 2005 ; Bertil et al., 2005 ; Bazin et al., 2010 ; Feuillet et al., 2011) et au nord de la Martinique le 29 novembre 2007 (Schlupp et al., 2008). Respectivement de magnitude 6,3 et 7,4, ces séismes ont provoqué de nombreux dégâts matériels, notamment sur les Saintes, Marie Galante au sud de la Guadeloupe et jusqu'en Martinique (Fig. 2).

Les mégaséismes, tel que celui à Sumatra en 2004 qui a provoqué un tragique tsunami, sont induits lors d'une rupture très grande de l'interface de subduction. Cette rupture



Figure 2 - Exemples de dégâts structurels liés au séisme des Saintes de 2004.

accommode un déficit de glissement de plusieurs mètres accumulés au cours des dizaines, centaines ou milliers d'années le long d'une interface bloquée durant la période intersismique (Bilek et Lay, 2018). Lors de la rupture, la déformation élastique soudaine du plancher océanique peut engendrer des tsunamis dévastateurs. Afin de mieux contraindre l'aléa sismique lié à ce type de séismes, il est essentiel d'obtenir des informations sur les séismes passés. Étudier les enregistrements à la fois historiques et géologiques, permettrait tout d'abord de les identifier et de montrer que ces mégaséismes sont bien un risque dans la région étudiée, mais aussi d'établir leur récurrence si une cyclicité existe.

Cette thèse de doctorat s'articule ainsi autour de la paléo-sismologie en mer basée sur des carottes sédimentaires récoltées le long de la façade atlantique des Petites Antilles. Pour réaliser et comprendre cette étude, il est donc nécessaire de poser des bases géologiques en introduction qui comprendront la géologie des Caraïbes de sa formation à aujourd'hui, du développement de l'arc antillais jusqu'au volcanisme actuel, des dépôts sédimentaires marins quaternaires des Petites Antilles : leurs origines et les processus qui interviennent, et une explication et description du paléomagnétisme comme outils pour réaliser cette étude. Enfin, après avoir développé la problématique de ce projet ainsi que les objectifs de recherche associés, nous suivrons l'extraordinaire voyage du sédiment après avoir été collecté lors de la mission CASEIS (Feuillet, 2016).

## 1. LA GEOLOGIE DES CARAÏBES, DU PACIFIQUE A L'ATLANTIQUE

La formation et la structure de la plaque Caraïbes sont à l'heure actuelle encore en débat dans la communauté scientifique. Les travaux de James (2005) et Keppie (2014) permettent de regrouper deux grandes hypothèses de cette formation : (1) la plaque serait originaire de celle du Pacifique qui sépare les plaques américaines par intrusion d'ouest en est, (2) elle aurait une origine *in situ* avec la remontée du manteau par les deux plongements des croûtes océaniques et la compression des plaques nord et sud (Fig. 3). Une troisième hypothèse a été proposée par Keppie (2013) : un modèle de piratage des lithosphères nord-

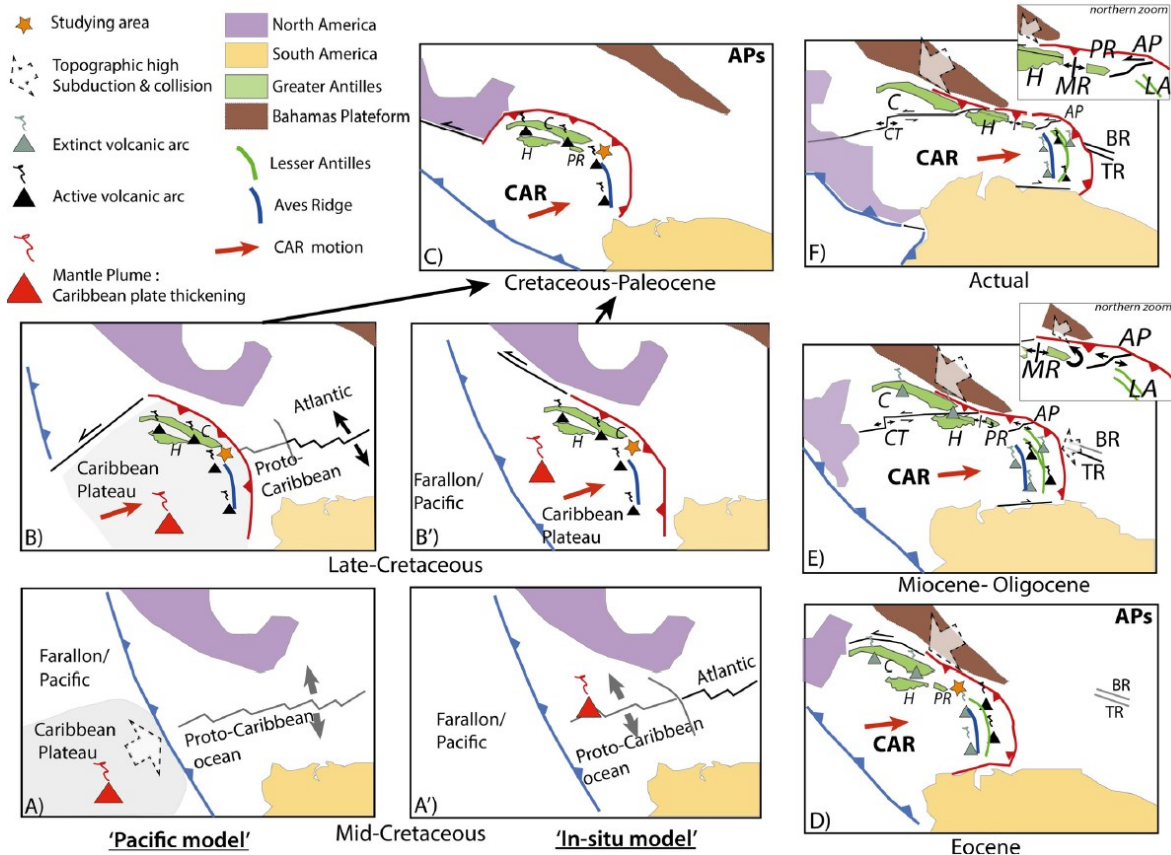


Figure 3 - Reconstruction des deux modèles géodynamiques envisagés pour la formation de la plaque Caraïbes depuis le Crétacé moyen (d'après Laurencin et al. 2018). AP: Passage d'Anegada; APs: Plaques Americaines ; BR: Ride de Barracuda ; C: Cuba; CAR: Plaque des Caraïbes ; CT: Fosse des Caïmans ; H: Hispaniola; MR: Rift de Mona ; PR: Puerto Rico ; TR: Ride de Tiburon.

et sud-américaines après l'intrusion de la plaque Pacifique. Ce modèle « Pirate » a néanmoins été regroupé avec l'origine *in situ* par James (2013). La tendance actuelle tend à considérer que ces processus se sont probablement produits à des périodes différentes de l'évolution de la plaque des Caraïbes, mais qu'ils ne sont pas exclusifs (Keppie, 2014).

Ainsi, la plaque des Caraïbes est un système complexe qui se décompose en cinq provinces géologiques (Draper et al., (1994) ; Fig. 4). L'est et l'ouest présentent respectivement une zone de subduction. À l'est de la plaque caraïbes, au niveau des Petites Antilles (composées du bassin de Grenade, la ride d'Aves, la ride de la Barbade et les Petites

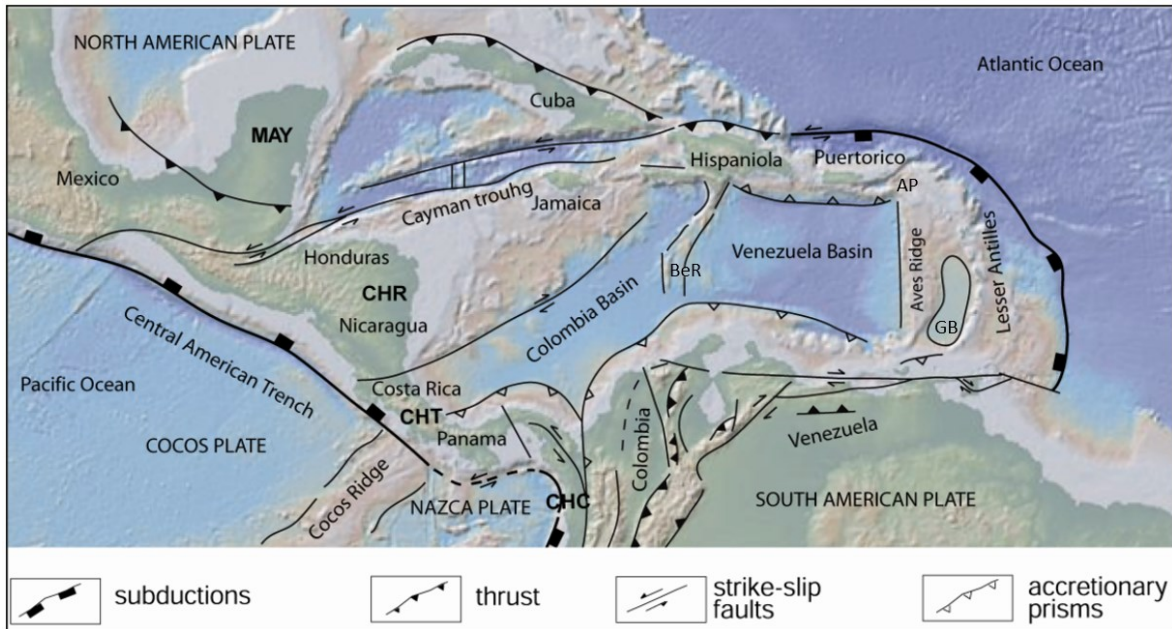


Figure 4 - Carte de la région des Caraïbes présentant les positions relatives des plaques et les différentes régions citées dans le texte (modifiée de Giunta et Orioli, 2011). AP=Passage d'Anegada ; BeR=Ride Beata ; CHC=Block Choco ; CHR=Block Chortis ; CHT=Block Chorotega ; GB=Bassin de Grenade ; MAY=Block Maya.

Antilles) il y a le plongement des plaques nord et sud-américaine selon une direction NE-SE. Tandis qu'au niveau de l'Amérique centrale (avec les blocs du Yucatan, Cortis, Chortega et Chocos) à l'ouest, il s'agit des plaques Pacifique et Coco qui plongent selon une direction SE-NE en opposition avec la façade atlantique. Les trois dernières provinces sont le nord des Caraïbes (composée du golfe du Mexique, des Antilles, du glacis de Nicaragua, de la fosse des Caïmans et du bassin du Yucatan), la mer des Caraïbes (comprenant le basin Colombien, la ride Beata, et le basin du Venezuela), et le nord de l'Amérique du Sud (avec la limite continentale du Venezuela et les Andes colombiennes). Cette étude se concentre sur la partie est des Caraïbes avec l'avant-arc des Petites Antilles et le prisme d'accrétion (Fig. 5) issu de la subduction des plaques américaines nord et sud sous la plaque des Caraïbes.

## 2. L'ARC ANTILLAIS, DE LA TECTONIQUE AUX SEISMES

La zone est des Caraïbes est très complexe au niveau structural avec des systèmes de failles de différentes natures orientées dans toutes les directions cardinales. Cette étude se

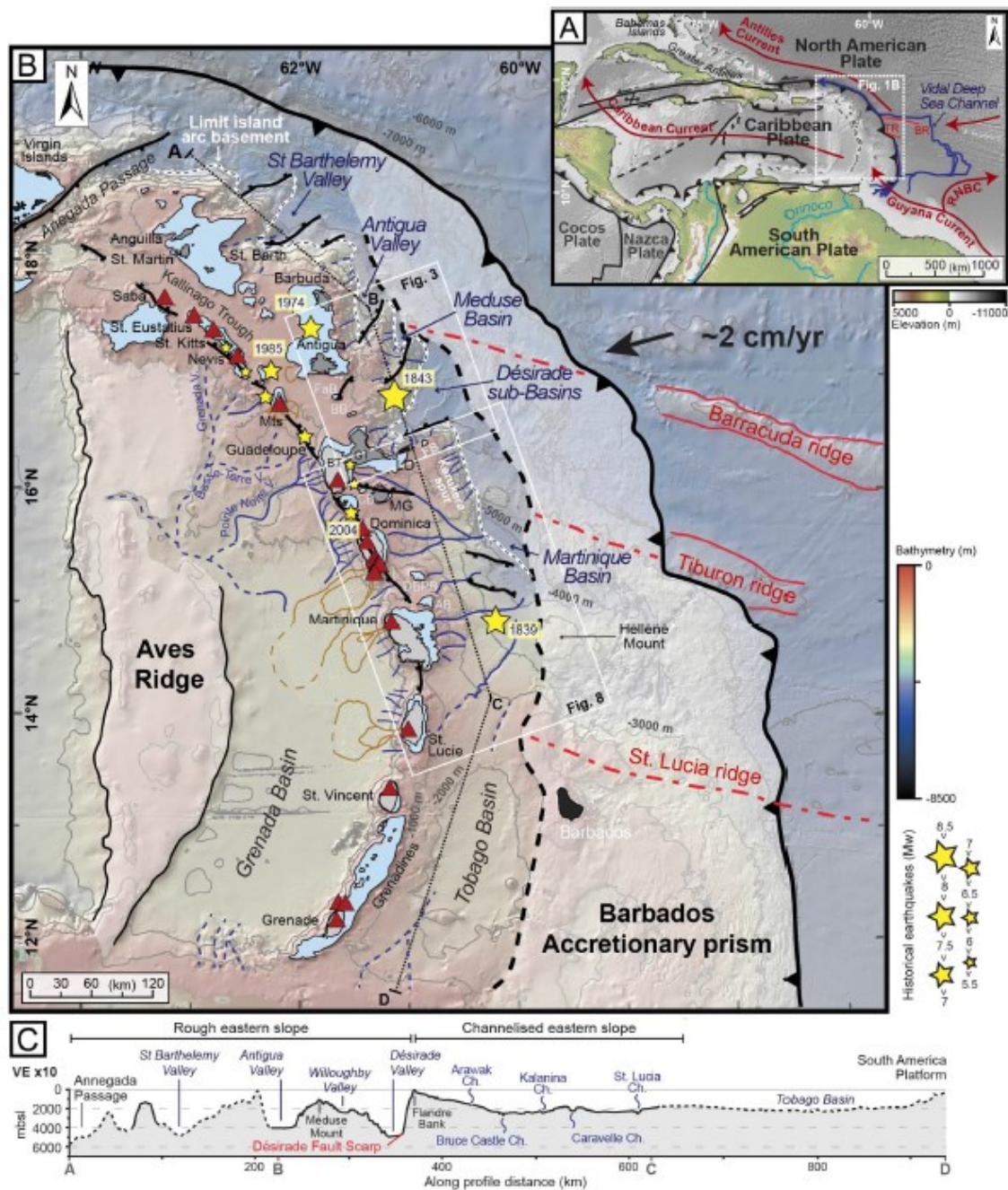


Figure 5 - A : Carte générale de la région autour de la Mer des Caraïbes avec les principaux courants marins (flèches rouges ; Johns et al., 1998; Zhang et al., 2017). B : Carte des Petites Antilles. Gris clair et gris foncé : îles respectivement de l'arc intérieur et de l'arc extérieur (Mts: Montserrat; MG: Marie-Galante; FaB: Falmouth bank, BB: Bertrand bank, FB: Flandre bank, CB: Colombia bank, DBPB: Dien Bien Phu bank, AB: Amerique Banque). Noir : îles non volcaniques. Étoiles jaunes : tremblements de terre historiques, localisation d'après Feuillet et al. (2011a). Triangles rouges : volcans actifs. Lignes brunes : Débris des dépôts d'avalanche et les glissements de terrain sous-marins de Deplus et al. (2001), Le Friant et al. (2004) et Brunet et al. (2016). Ligne noire graticulée : les systèmes de failles de Feuillet et al. (2001, 2004). Ligne noire avec triangles et ligne en pointillé noir : respectivement la poussée frontale du prisme d'accrétion et la limite supposée du prisme interne. Lignes bleues : canaux (pointillés les lignes sont des canaux supposés). Les rides asismiques sont mises en évidence par des lignes rouges et leurs parties subductées par des lignes pointillées rouges. C : profil de la bathymétrie à travers l'arc des Petites Antilles, emplacement sur la figure B. Les lignes pointillées noires correspondent à la bathymétrie Geomap et les lignes noires à la bathymétrie des missions océanographiques (figure et légende issues de Seibert et al., 2020).

concentre sur les zones morphotectoniques de l'arc, des bassins avant-arc et du prisme d'accrétion des Petites Antilles.

Cet arc volcanique est la résultante d'une subduction (voir Tatsumi (2005) pour les processus mis en jeu lors d'une subduction et l'hétérogénéité des zones de subduction). Les plaques lithosphériques océaniques américaines sont subduites sous la plaque lithosphérique océanique des Caraïbes. Ce processus entraîne parfois la formation d'îles basaltiques volcaniques, comme l'arc des Petites Antilles. Ces roches basaltiques sont le fruit de la remontée de croûtes océaniques recyclées.

La plaque Caraïbes et la lithosphère atlantique convergent sur l'ensemble de la zone de subduction à une vitesse de 2 cm/an avec respectivement une orientation NNE et SSO (Dixon et al., 1998 ; DeMets et al., 2000 ; Symithe et al., 2015). Les principaux séismes ont lieu dans la partie nord des Petites Antilles (Feuillet et al., 2002), notamment au niveau des systèmes de failles disposées en échelon. Leurs orientations SE-NO et SO-NE vont permettre d'accommoder les déplacements des plaques Caraïbes et Atlantique nord.

Il y a des séismes historiques dont les dégâts matériels et humains ont été importants et dont les épicentres se trouvaient au niveau de ces failles en échelon ou plus en profondeur

au niveau de l'interface de subduction. Par exemple, le 16 mai 1851 et le 29 avril 1897 à proximité de l'île de la Guadeloupe et de Marie-Galante, deux séismes majeurs d'intensité VII et VIII respectivement, ont été enregistrés (Feuillet et al., 2011b). La carte bathymétrique (Fig. 6) présente l'ensemble des séismes de magnitude supérieure ou égale à 5 dans la région des Petits Antilles depuis 1900. Si la mémoire historique, couplée à l'étude sismique marine de la région antillaise permet de recenser les séismes majeurs sur des périodes de temps courtes, aucune mission océanographique antérieure n'a encore été réalisée sur cette zone pour retrouver la trace de mégaséismes et leur récurrence sur des périodes géologiques plus longues.

La région des Petites Antilles s'étend du sud au nord entre Grenade et Anguilla sur plus de 800 km de distance. L'arc volcanique tel qu'il existe aujourd'hui a subi des périodes d'activité plus ou moins intense, liée à l'activation ou à la ré-activation de failles (Feuillet et al. 2002, 2004 ; Münch et al., 2014 ; Chrystèle et al., 2016) et notamment à la migration de

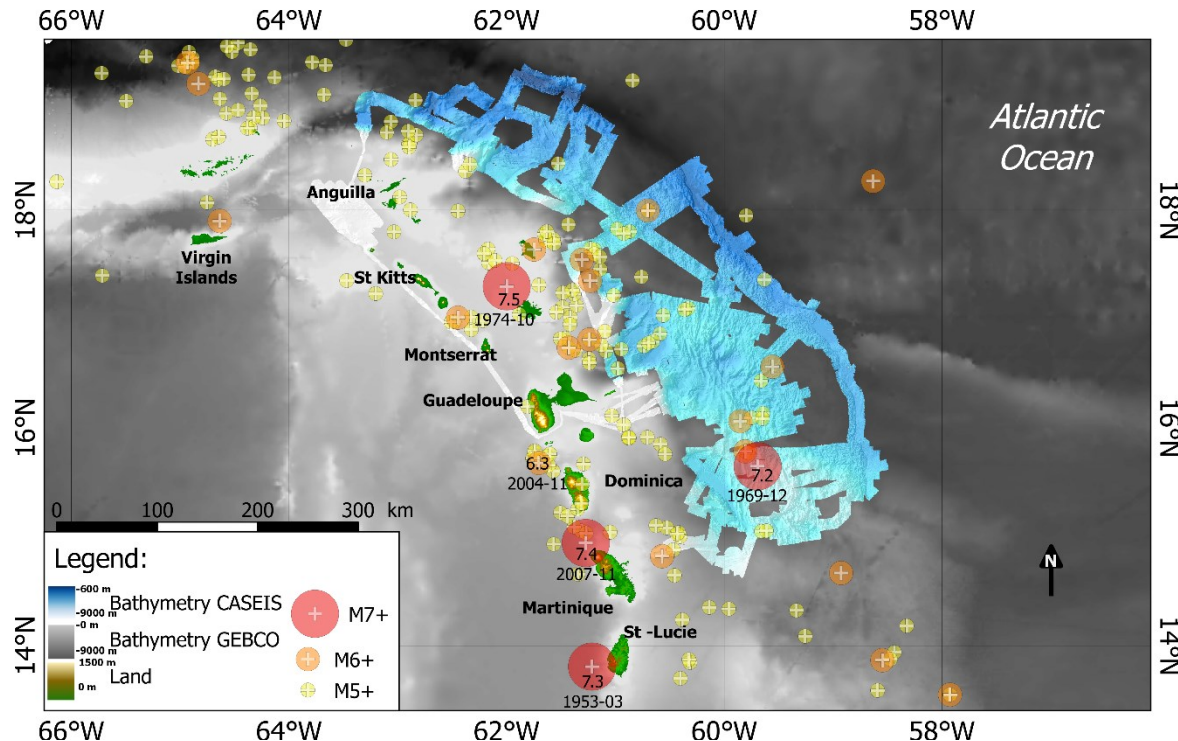


Figure 6 - Séismes historiques de magnitude supérieure à 5 depuis 1900 dans les Petites Antilles. Les étoiles orange sont les séismes de mai 1851 et avril 1897 à proximité de la Guadeloupe.

l'arc en lui-même vers l'ouest, suite à la subduction de rides asismiques (i.e., Tiburon et St Luce). Les deux périodes les plus actives de l'arc volcanique actuel ont eu lieu pendant l'Eocène-Oligocène et puis à la fin du Miocène, début du Pliocène. Ainsi, l'arc volcanique est en activité depuis environ 38 Ma (Briden et al., 1979 ; Bouysse et Westercamp, 1990).

Les éruptions volcaniques de l'arc antillais ont fait l'objet de nombreuses études, notamment sur les îles à proximité de la zone d'étude pendant la période du Quaternaire, à la fois à l'aide de l'analyse des roches magmatiques et des dépôts marins tels que les téphras (e.g., le Montserrat : Le Friant et al. (2008) ; la Guadeloupe : Samper et al. (2007, 2009) ; la Dominique : Lindsay et al. (2005) ; la Martinique : Germa et al. (2010) ; régionalement sur le Quaternaire : Sigurdsson and Carey, 1981)).

Bien que l'origine du volcanisme régional soit la subduction antillaise, il y a un lien entre les séismes et les tensions tectoniques, et donc avec les séismes et mégaséismes qui peuvent avoir lieu dans la région des Petites Antilles (Feuillet et al., 2011b; Leclerc et al., 2016). D'après Davies (1999), l'un des facteurs permettant la formation du magma des zones de subduction pourrait être les séismes de profondeur moyenne à l'interface des deux plaques convergentes qui faciliterait la libération d'eau et donc du développement d'hydrofractures du manteau.

### 3. LA SEDIMENTATION, DES PROCESSUS A LA COMPOSITION SEDIMENTAIRE

Les Petites Antilles sont caractérisées par une morphologie asymétrique est-ouest, centrée sur l'arc volcanique, et une asymétrie nord-sud sur la façade atlantique (Picard et al., 2006). Les îles des Petites Antilles sont bordées à l'ouest par le bassin de Grenade. Ce bassin d'arrière-arc se caractérise par un plateau continental très étroit et un talus continental raide. Il présente aussi un approfondissement du nord vers le sud. Cette morpho-bathymétrie et la présence des volcans sur la façade de la mer des Caraïbes, produisent des glissements et des courants turbiditiques volcano-clastiques dans le bassin de Grenade, avec une chenalisation

E-SE des canyons sous-marins. La composition minéralogique des sédiments de ce bassin est principalement d'origine volcanique et carbonatée.

En opposition, la façade atlantique présente un plateau continental beaucoup plus large (près de 250 km au sud pour 80-100 km au nord) avec un talus à pente plus faible pour former les bassins d'avant arc. Plus à l'est se trouve le prisme d'accrétion qui s'étend et s'épaissit plus largement vers le sud à cause de la charge sédimentaire transportée par les fleuves Orénoque et Amazone, tandis que la fosse plus profonde (jusqu'à 8000 m) se trouve principalement au nord. La dynamique atmosphérique des Antilles entraîne un transport des cendres volcaniques principalement d'ouest en est par les ventes d'ouest (Newell et al., 1972) avec des dépôts sur la façade atlantique. La dynamique marine, quant à elle, présente essentiellement un transport est-ouest de l'Atlantique vers la mer des Caraïbes (Johns et al., 2002).

Les dépôts sédimentaires associés au front atlantique des Petites Antilles peuvent être regroupés en trois dépôts particuliers, des sédiments argilo-silteux majoritairement de type volcanoclastique, des carbonates pélagiques et hémpélagiques et des poussières du Sahara (Reid et al., 1996 ; Picard et al., 2006 ; Fig. 7). En effet, le premier arc volcanique plus au nord a subi plusieurs cycles de transgression-régressions marines qui ont conduit à l'altération des roches magmatiques et à des dépôts sédimentaires carbonatés. Ces derniers se retrouvent aujourd'hui pour certains à l'affleurement et soumis à l'érosion (Reid et al., 1996 ; Cornée et al., 2012).

Les sédiments silto-sableux terrigènes proviennent du transport des sédiments depuis la côte par les courants de marée, les courants côtiers ou encore les courants de turbidité. De plus, certains vont directement être formés au niveau de la plateforme ou de la plaine abyssale avec une proportion plus importante de carbonate. Néanmoins, l'essentiel des éléments silicoclastiques qui se trouvent au large des côtes antillaises proviennent principalement du delta et du système turbiditique de l'Orénoque et, en moindre mesure, de celui de l'Amazone et de sa décharge partiellement transportée par le courant littoral guyanais (Westbrook et al., 1984 ; Deville et al., 2015 ; Limonta et al., 2015).

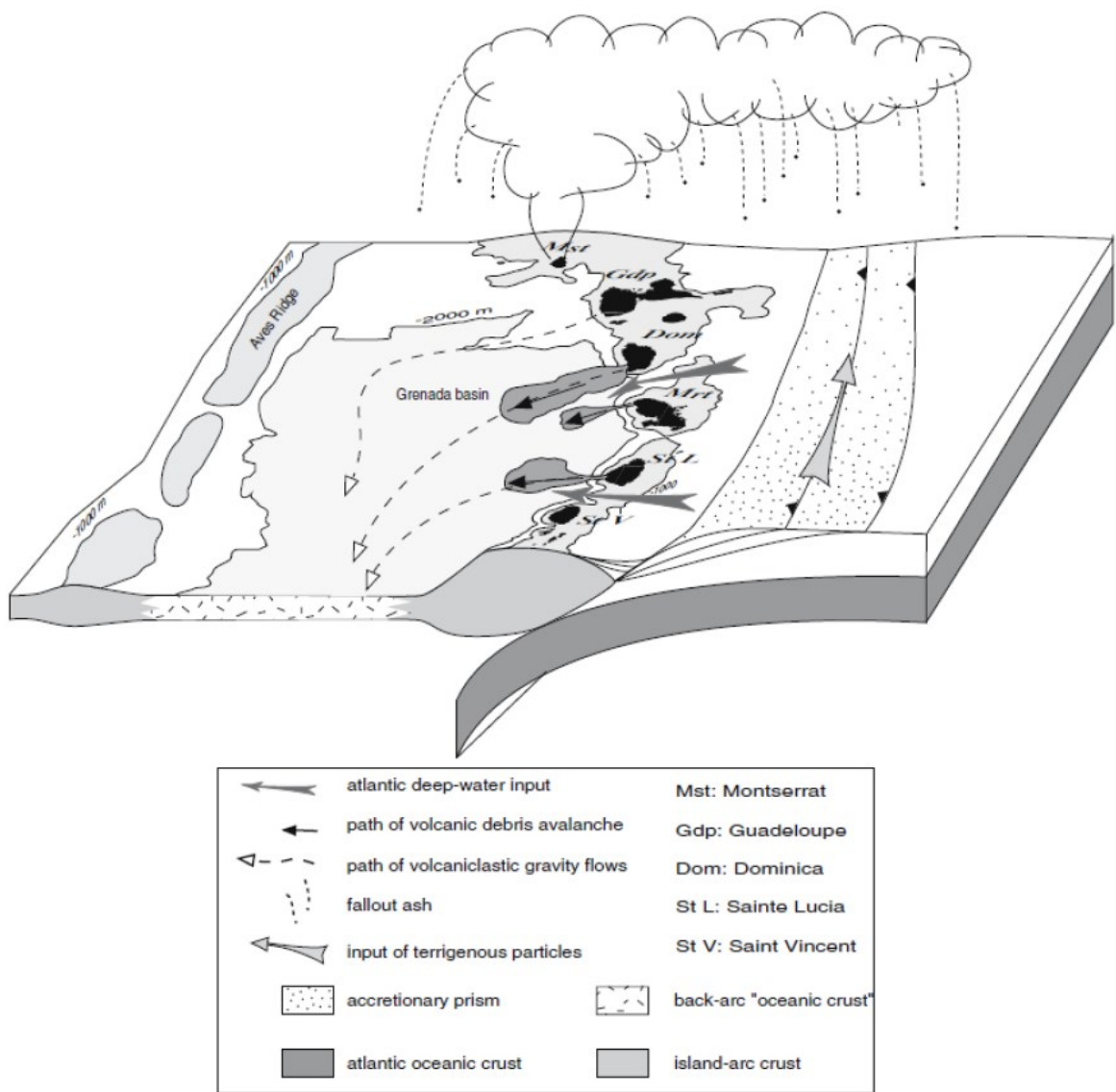


Figure 7 - Modèle des principaux processus sédimentaires existant autour de l'arc des Petites Antilles (figure modifiée d'après Picard et al. (2006), Carey (2000), Sigurdsson et al. 1981).

Les sédiments argilo-silteux volcanoclastiques peuvent être retrouvés, d'une part dans des dépôts téphras formés lors de la chute de cendres volcaniques issues des éruptions de l'arc et transportés par les vents d'ouest, d'autre part, dans des turbidites et séismo-turbidites sous forme de cendres remobilisées par des courants gravitaires liés à des instabilités sédimentaires. Les téphras sont à la fois de très bons marqueurs chronostratigraphiques (Le Friant et al., 2008) et aussi des marqueurs d'éruptions explosives (Sigurdsson et al. 1997).

Les carbonates pélagiques et hémipelagiques ont fait l'objet d'études préliminaires réalisés à bord du navire durant la mission CASEIS par prélèvement ponctuel et observations à la loupe binoculaire et/ou microscope optique. Cela a permis de mettre en évidence de grandes quantités de foraminifères (principalement planctoniques), de ptéropodes, des fragments de coquilles, bioclastes indéterminés, ou encore des fossiles de nanoplanctons. La couleur des argiles et silts issus de dépôt (hémi)pélagiques présentent des couleurs variant du brun au gris vert avec des teintes plus claires lors d'une augmentation de la proportion de carbonates. Ces observations à bord semblent correspondre aux observations déjà réalisées sur de nombreux sites de carottage pour les sédiments de l'Atlantique ouest tropicale par Damuth (1977) mais aussi Reid et al. (1996) dans les sédiments de l'arc antillais.

L'analyse des taux de sédimentation établis pour trois sites d'études au niveau de la zone d'accrétion initiale (Wright, 1984) démontre que la vitesse de sédimentation est plus forte durant le Quaternaire (entre 40 et 50 m.Ma<sup>-1</sup>) que durant le Pliocène (entre 9 et 35 m.Ma<sup>-1</sup>). Néanmoins, les carottes sédimentaires issues de la missions CASEIS qui vont être étudiées ici, se situent principalement au niveau de la zone de stabilisation du prisme d'accrétion et des bassins avant-arc. De plus, les études DSDP (Wright, 1984 ; Biju-Duval et al., 1984) et ODP (Masclé et al., 1988) se concentrent principalement sur les données anté-quaternaires de la zone d'accrétion initiale, tandis que celle de Reid et al. (1996) se concentre sur le Quaternaire récent dans l'ensemble de la zone de subduction. D'après cette dernière étude, entre Grenade au sud de l'arc et Barbuda au nord de l'arc, les taux de sédimentation varie d'un ordre de grandeur. Au sud, environ 15 cm.ka<sup>-1</sup> de sédiments se déposent avec principalement des particules fines dont 10 à 15% de carbonate de calcium (CaCO<sub>3</sub>). Tandis

qu'au nord, les taux de sédimentation sont plus faibles et compris entre 0,2 et 5 cm.ka<sup>-1</sup> avec des teneurs en CaCO<sub>3</sub> comprises entre 20 et 50 %. Ils ont ainsi pu observer une graduation sud/nord à la fois pour les taux de sédimentation et pour la proportion de carbonate. Les carottes sédimentaires ainsi prélevées présentent une alternance de dépôts hémipelagiques ou pélagiques, interrompus par des dépôts gravitaires et/ou des dépôts de cendres volcaniques (téphras).

#### 4. LE PALEOMAGNETISME, DU PRINCIPE A L'OUTIL

Le cœur de la Terre, couche la plus profonde, est composé d'un noyau interne solide et d'un noyau externe liquide. Tous deux composés principalement de fer et de nickel, ce sont les convections thermiques et compositionnelles du noyau externe qui engendrent un effet de dynamo auto-excitée dont résulte le champ magnétique terrestre (Jones, 2015). Ce bouclier qui protège la Terre et ses habitants des rayonnements cosmiques (notamment solaire ionisant) se manifeste sous forme d'un dipôle qui représenterait 90 % de l'ensemble du champ magnétique (Tauxe et al., 2018). C'est grâce à lui que de nombreuses espèces migratrices peuvent s'orienter du nord au sud et inversement (Lohmann, 2010). Ainsi, en tout point à la surface du globe terrestre, il est possible de définir le vecteur magnétique  $\vec{B}$  (Fig. 8) au travers de l'inclinaison I, la déclinaison D et sa norme B (soit son intensité). La déclinaison est l'angle mesuré entre le nord magnétique et le nord géographique, tandis que l'inclinaison est la mesure de l'angle entre le vecteur  $\vec{B}$  et sa projection sur le plan horizontal. Alors que la norme de ce vecteur représente l'intensité du champ magnétique, le sens va définir le signe positif ou négatif de I. À l'heure actuelle, le champ magnétique terrestre est positif dans l'hémisphère Nord et négatif dans l'hémisphère Sud (polarité normale). Des études ont montré que ce champ magnétique n'a pas toujours été orienté dans ce sens et que des inversions de ce champ peuvent se produire (Brunhes, 1906).

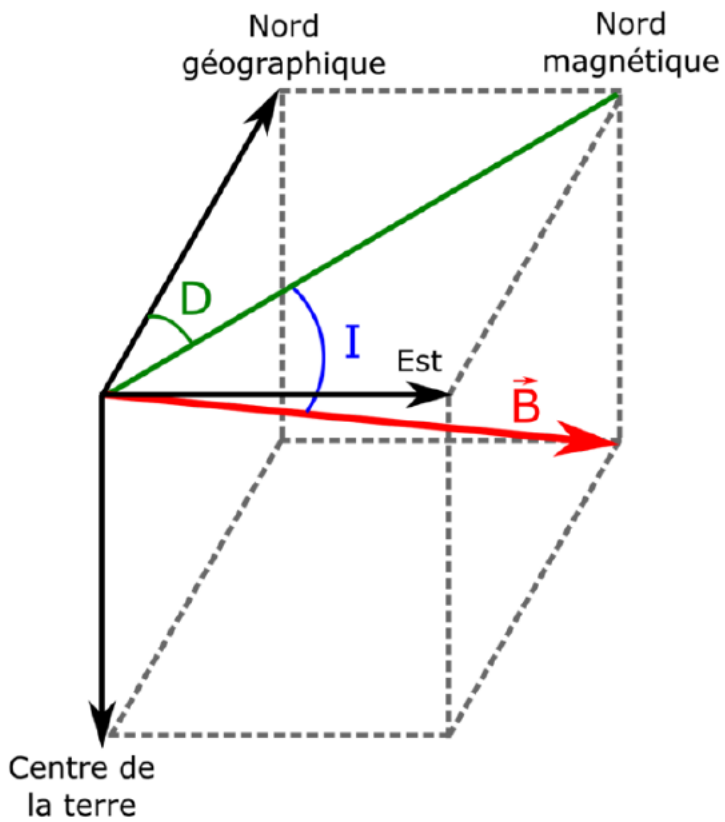


Figure 8 – Composante du champ magnétique terrestre représenté par le vecteur magnétique  $\vec{B}$  (figure de Philippe, 2019).

Cette thèse de doctorat s'intéresse plus particulièrement à l'enregistrement du champ magnétique terrestre par le sédiment. Contrairement aux roches ignées (i.e. les roches volcaniques) qui enregistrent directement le signal lors de la formation et le refroidissement des minéraux ferrimagnétique (par exemple la magnétite et la titano-magnétite), les sédiments se composent de grains magnétiques souvent incorporés dans des matrices elles-mêmes agglutinées sous forme d'agrégats ou flocs. L'enregistrement du signal se fait par ces minéraux magnétiques sous forme d'aimantation rémanente dite naturelle (NRM). Ainsi, le postulat scientifique permettant d'étudier le paléomagnétisme des sédiments est que l'aimantation rémanente détritique (DRM) est proportionnelle au champ magnétique ancien.

## 5. LA PALEOSISMOLOGIE EN MER, UN OUTIL QUI SE DEVELOPPE

Depuis la mise en évidence de courants de turbidité déclenchés par des séismes par les travaux de Heezen et Ewings (1956), de nombreuses études ont utilisé les dépôts gravitaires et plus spécifiquement les turbidites pour étudier la récurrence des séismes. C'est d'autant plus pertinent pour les zones de subductions qui présentent les séismes les plus puissants (Pacheco et Sykes, 1992) appelés mégaséismes. La zone de subduction des Cascades à l'ouest des États-Unis a particulièrement été étudiée. Elle a permis de développer une méthode basée sur l'analyse des sédiments prélevés dans des carottes sédimentaires pour réaliser de la paléosismologie marine (Adams, 1990 ; Goldfinger, 2011 ; Goldfinger et al., 2003). Les séismes et plus particulièrement les mégaséismes sont le résultat de rupture sismique affectant de grandes étendues qui sont susceptibles de générer des courants de turbidité simultanément dans différents canyons sous-marins d'une même marge. Il s'agit alors de dater des turbidites dans des chenaux ou bassins déconnectés les uns des autres et distants de plusieurs kilomètres pour éliminer les autres sources de déclenchement qu'un séisme, et de déterminer si ces dépôts ont le même âge. Un moyen complémentaire permettant d'associer des dépôts entre eux est de mettre en corrélation les paramètres physiques et lithologiques de ces dépôts (Goldfinger, 2011). En plus de la datation absolue qui n'est pas toujours évidente à cause des processus érosifs des courants de turbidité, il est possible d'utiliser les paramètres physiques et magnétiques du sédiment hé mipélagique et des couches déposées rapidement pour réaliser une corrélation stratigraphique (Fig. 9). Enfin, certains dépôts ont souvent été associés à des séismes et/ou des tsunamis, les turbidites amalgamées et les complexes homogénite-turbidites. Les turbidites amalgamées sont une succession de turbidites érosives les unes par rapport aux autres qui résulte de plusieurs courants de turbidité d'origines différentes mais déclenchés par un même événement et dont le dépôt final a lieu au même endroit (Van Daele et al., 2017). Les complexes homogénite-turbidites ont été découverts pour la première fois en mer Méditerranée (Stanley et Maldonado, 1981 ;

Kastens et Cita, 1981) et depuis référencés dans divers environnements tant marins que lacustres. Beck et al. (2012) ont aussi identifié des complexes homogenites-turbidites au nord des Petites Antilles qui pourraient être associés à des événements sismiques.

## 6. PROBLEMATIQUE DU PROJET

Les connaissances accumulées à ce jour sur les aléas naturels dans la région des Petites Antilles se concentrent essentiellement sur le volcanisme du Pléistocène à nos jours (Sigurdsson and Carey, 1981 ; Macdonald et al., 2000 ; Lindsay et al., 2005 ; Samper et al., 2009 ; Germa et al., 2010) et les séismes historiques (Feuillet et al., 2001, 2002, 2011a, 2011b). Mis à part l'étude préliminaire de Beck et al. (2012), aucune donnée antérieure à la

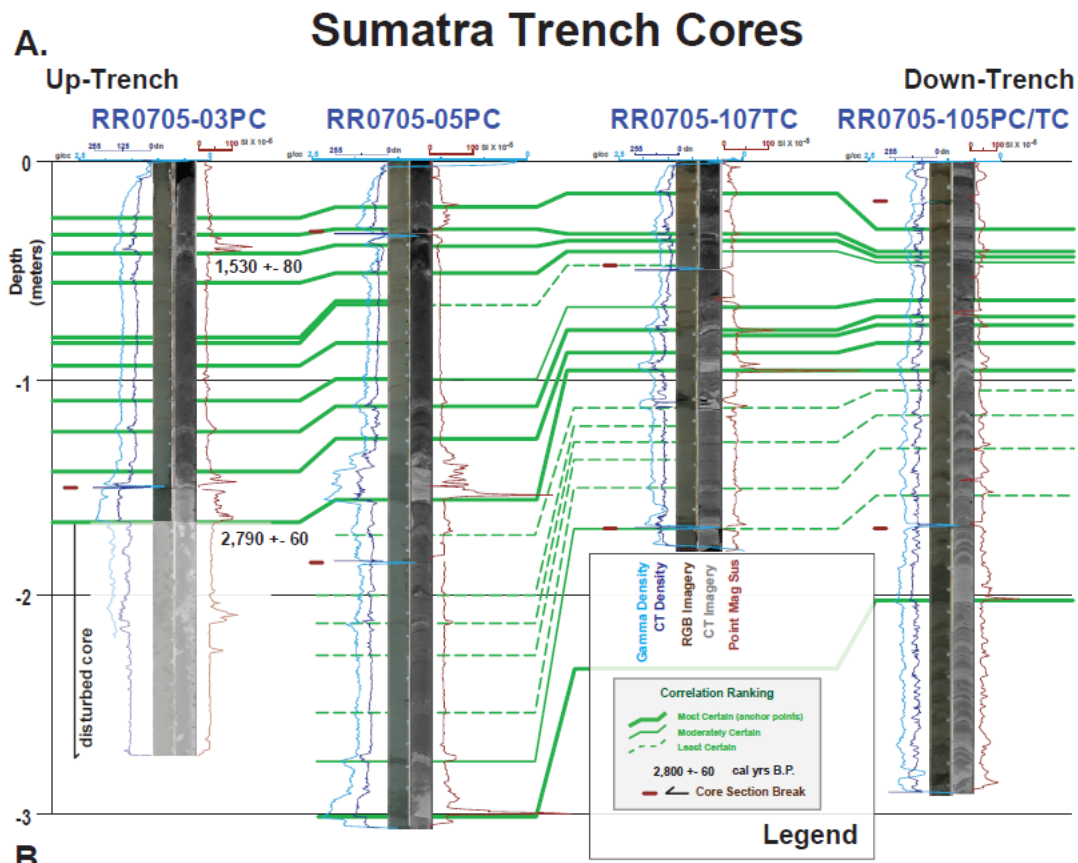


Figure 9 - Corrélation stratigraphique (traits verts) des paramètres physiques et magnétiques de quatre carottes sédimentaires prélevées dans la fosse de Sumatra. Les dates  $^{14}\text{C}$  ont été réalisées sous la base des turbidites (figure de Patton et al., 2013).

mission CASEIS n'a permis de réaliser une étude complète de paléosismologie marine des Petites Antilles. Bien que la sédimentologie quaternaire ait déjà été étudiée dans la région, notamment par Reid et al. (1996) qui ont réalisé les premières datations à partir des biozones de foraminifères et mis en évidence de nombreuses turbidites, aucune analyse n'a encore permis d'étudier les paléo-séismes associés à cette zone de subduction. Seuls les travaux préliminaires de Beck et al. (2012) entre les îles de Navis et Monserrat ont identifié des complexes homogénite-turbidites possiblement associés à des séismes. L'absence d'une chronostratigraphie solide sur le Quaternaire récent rend nécessaire d'établir un cadre chronologique bien défini, indispensable en vue d'étudier les dépôts associés à des paléo-séismes tels que les turbidites et les complexes homogénite-turbidites. Ainsi, à partir du paléomagnétisme, et plus particulièrement de la paléointensité couplée à l'analyse des isotopes stables de l'oxygène, nous souhaitons réaliser une magnétostratigraphie régionale qui sera complémentaire des études précédemment réalisées (objectif 1). Cette chronostratigraphie fait l'objet d'étude du premier chapitre de cette thèse et sera essentielle pour mieux définir temporellement les dépôts associés aux séismes. En effet, il s'agira d'identifier ces dépôts à l'aide de leurs propriétés magnétiques et physiques, et d'améliorer l'estimation de leur âge en associant les datations absolues avec les données de paléointensité relative dans le but d'établir de nouvelles informations sur la cyclicité des séismes durant le Quaternaire récent aux Petites Antilles (objectif 2). Enfin, la caractérisation magnétique et paléomagnétique des nombreuses turbidites et complexes homogénite-turbidites permettra de mieux comprendre l'enregistrement du signal paléomagnétique par ces couches déposées rapidement.

Ainsi, l'objectif principal de cette thèse **est d'étudier des dépôts sédimentaires associés à des mégaséismes encore jamais enregistrés dans les archives historiques et d'estimer la récurrence de ces événements au cours du temps en vue de mieux comprendre le fonctionnement de la zone de subduction des Petites Antilles**. L'étude de dépôts sédimentaires associés aux séismes fera l'objet d'une analyse approfondie pour mieux comprendre comment le signal magnétique terrestre peut être enregistré par le sédiment. Pour atteindre ce but, trois objectifs spécifiques ont été identifiés et feront l'objet des trois

chapitres de cette thèse sous forme d'articles scientifiques rédigés en anglais. Ces sous-objectifs sont présentés dans la section ci-après.

## 7. OBJECTIFS DE RECHERCHE

### **Objectif 1 : Magnétostratigraphie**

Le premier objectif spécifique est d'établir une magnétostratigraphie régionale à l'aide de la carotte sédimentaire de référence CAS16-24PC (chapitre 1), prélevée dans une plaine profonde (1983 m) bordée de talus à faible pente. Avec un minimum de couches déposées rapidement, cette carotte sédimentaire est principalement composée de dépôts argilo-silteux hémipélagiques capables d'enregistrer le signal paléomagnétique comprenant les paléodirections (inclinaison et déclinaison) et la paléointensité relative du champ magnétique terrestre (Tauxe, 1993 ; Stoner et St-Onge, 2007 ; Roberts et al., 2013). Il s'agira donc de répondre aux questions suivantes :

- La carotte de référence enregistre-t-elle bien de façon quasi-continue les variations d'orientation et d'intensité du champ magnétique terrestre ?
- Peut-on utiliser cette magnétostratigraphie pour dater les dépôts sédimentaires associés aux séismes dans l'ensemble des autres carottes sédimentaires étudiées ?

Pour répondre à ces questions, les données paléomagnétiques et de stratigraphie isotopique de l'oxygène seront combinées (e.g., Channell et al., 1997 ; Xuan et al., 2016). En comparant les résultats avec des enregistrements existants datés précisément (i.e., LR04 de Lisiecki et Raymo, 2005, PISO-1500 de Channell et al. 2009, et PADM2M de Ziegler et al., 2011), il sera possible d'établir un modèle d'âge en vue d'obtenir un signal paléomagnétique de référence, nécessaire pour dater les couches déposées rapidement.

### **Objectif 2 : Paléosismologie marine**

Le second objectif spécifique de cette thèse est d'étudier les cycles sismiques du Quaternaire récent associés à la zone de subduction des Petites Antilles, et ce à l'aide de dépôts associés à des séismes (i.e., turbidites et homogénite-turbidites). Il s'agira de déterminer lesquels de ces événements sont associés à des séismes et si possible de déterminer l'étendue de la zone affectée par les séismes en répondant aux questions suivantes :

- Quelles couches déposées rapidement sont associées à des séismes ?
- Peut-on estimer l'âge de ces dépôts à l'aide des données paléomagnétiques et peut-on en déduire des cycles sismiques ?

Les méthodes développées par la paléosismologie marine permettront de répondre à ces questions. En effet, l'utilisation des turbidites comme dépôt sismique a été utilisée dans différentes régions (St-Onge et al., 2004 - Fjord du Saguenay ; Gracia et al., 2010 - Portugal ; St-Onge et al., 2012 - Chili) et notamment au niveau d'autres zones de subduction (Goldfinger et al., 2003, 2007 - Cascade ; Ratzov et al., 2010 - Equateur ; Pouderoux et al., 2012 - Nouvelle-Zélande ; Patton et al., 2013 - Sumatra-Andaman).

Goldfinger et al. (2003) décrivent dans leur étude, la possibilité d'utiliser les dépôts turbiditiques synchrones sur des régions étendues, notamment avec des bassins déconnectés les uns des autres. Il est alors possible de discriminer la majorité, voire la totalité des dépôts associés à des séismes. Les travaux de Seibert et al. (soumis) et de Morena (2020) ont pu mettre en évidence que des turbidites et des complexes homogénite-turbidites pouvaient être corrélés au travers de plusieurs carottes sédimentaires dans la région. Nous utiliserons des carottes communes à ces deux études pour apporter de nouveaux éléments de réponse à l'aide des données paléomagnétiques de ces carottes.

### **Objectif 3 : Influence de la lithologie**

Le dernier objectif spécifique de cette thèse est concentré sur les variations de l'enregistrement magnétique et paléomagnétique par le sédiment en fonction des différents

types de dépôts et de l'épaisseur des couches déposées rapidement. Il s'agit de répondre aux questions suivantes :

- Les paramètres physiques et magnétiques de couches déposées rapidement peuvent-ils améliorer la compréhension des processus de dépôts ?
- Y a-t-il un lien entre la taille des grains magnétiques, l'inclinaison et la taille des turbidites enregistrés dans les Petites Antilles ?

Au cours des trois dernières décennies, les études paléomagnétiques se concentraient principalement sur l'analyse de sédiments hémipélagiques. Le paradigme du paléomagnétisme se base sur l'aimantation rémanente de (post-)dépôt (DRM – PDRM ; Kent, 1973 ; Tauxe et al., 2006). La complexité de l'enregistrement magnétique, liée aux processus sédimentaires et environnementaux, nécessite que les études se concentrent principalement sur de la modélisation et/ou des expériences de dépôts en laboratoire (Valet et al., 2017). Cependant, ces expériences de redéposition sous champ magnétique contrôlé sont semblables à des dépôts quasi-instantanés tels que les turbidites. Ainsi, Tanty et al. (2016) ont été les premiers à étudier dans le détail l'impact de 4 turbidites différentes sur le signal paléomagnétique. Ils ont montré qu'il y a une relation linéaire entre les variations d'enregistrement de l'inclinaison et la taille du dépôt gravitaire. Les carottes de la mission CASEIS offrent ainsi un potentiel très important pour étudier plus précisément ces dépôts et avec un éventail plus large de turbidites.

## 8. ÉCHANTILLONNAGE ET ANALYSES : DES FONDS MARINS JUSQU'AU LABORATOIRE

Le projet de la mission CASEIS (CAraïbes et SEISmes) est né en 2012 et a été porté par Nathalie Feuillet. Ce n'est qu'en 2015 que les financements seront finalement alloués pour réaliser la mission océanographique en mai-juin 2016. L'étude préalable de la région pour préparer les zones d'intérêt de recherche a été réalisée par Chloé Seibert (voir Chapitre 1, Seibert, 2019). À bord du navire de recherche Pourquoi Pas ? de l'IFREMER un banc de

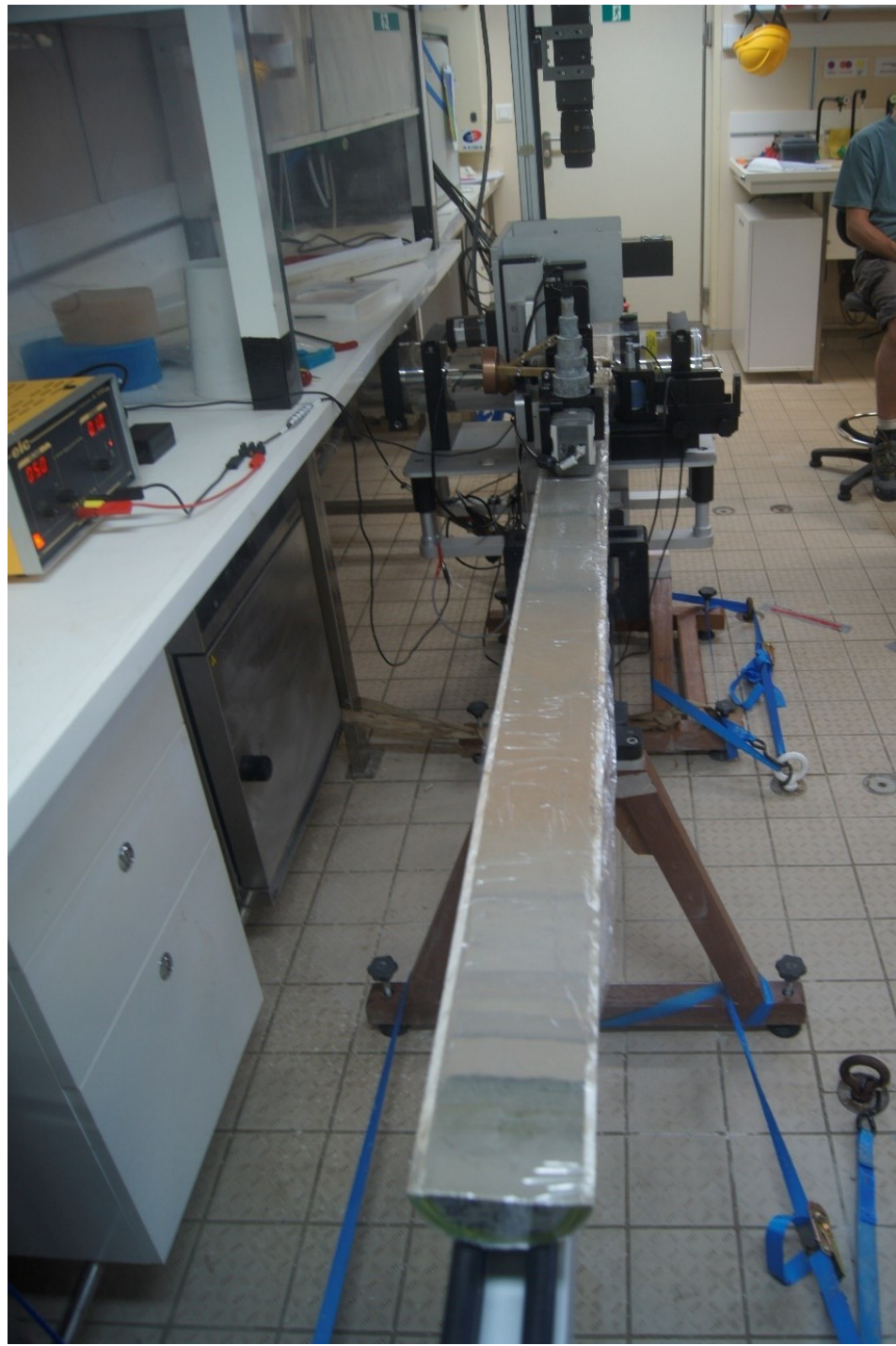


Figure 10 - Banc MSCL installé à bord du N/R Pourquoi Pas ? pendant la mission CASEIS (© Nathalie Feuillet, 2016).

découpe (fourni par le laboratoire EPOC de l’Université de Bordeaux, France) et un banc MSCL (Multi-Sensor Core Logger ; Fig. 10) GEOTEK (fourni par le laboratoire de Paléomagnétisme et sédimentologie de l’Institut des sciences de la mer de Rimouski (ISMER) de l’Université du Québec à Rimouski (UQAR)), ont été installés pour réaliser les premières mesures.

Lors de la mission océanographique, l’analyse bathymétrique par l’imagerie multifaisceaux et des profils de sondeur de sédiment ont permis de sélectionner des sites d’intérêt pour le carottage. Ainsi, 39 longues carottes à piston ont été prélevées à partir d’un carottier de type Calypso. De plus, 9 carottes à boites ont été récoltées à l’aide d’un carottier de sédiment de surface de type USNEL.

Une fois les carottes à piston (PC) à bord du navire, elles sont découpées en section de 150 cm puis numérotées pour chaque section par le nom et l’année de mission, suivi du numéro et type de carotte et enfin du numéro de section en chiffre romain. Par exemple : CAS16-01PC-IV pour la section IV (quatre) de la carotte à piston 01 (zéro un) prélevée en 2016 lors de la mission CASEIS. Au sommet (TOP) et à la base (BOT) de chaque section de carotte est indiqué TOP ou BOT, associé à la profondeur sachant que la mesure 0 cm de la carotte se trouve au sommet de la première section, c’est-à-dire le sédiment de surface, et la dernière mesure donnant la longueur de la carotte se trouve à la base de la dernière section, c’est-à-dire le sédiment le plus ancien de la carotte sédimentaire. Chaque section présentait une ligne appelée génératrice qui a permis de réaliser une découpe continue de chaque carotte, et de récolter une demi-section travail (W) et une demi-section archive (A).

Le banc MSCL (Fig. 10) a permis de mesurer la susceptibilité magnétique (Bartington, senseur MS2E1), la densité gamma du sédiment, la vitesse des ondes de compression (ondes p) qui traversent le sédiment, et de mesurer les paramètres de réflectance spectrale diffuse

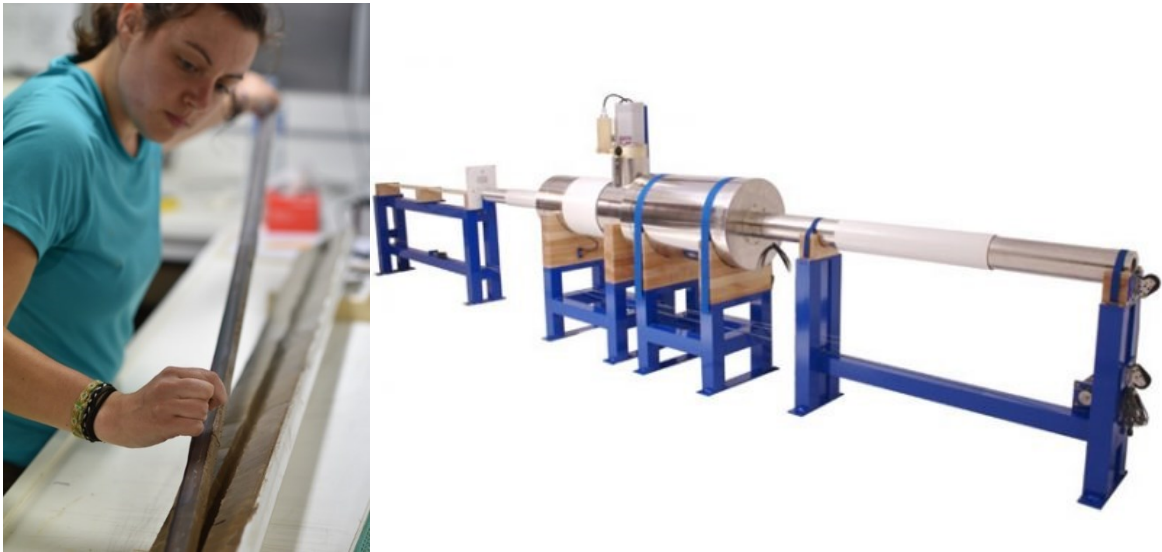


Figure 11 – A gauche, prélèvement d'un *u-channel* dans une demi-section de carotte sédimentaire. A droite, photographie d'un magnétomètre cryogénique SRM-755 de 2G Enterprise.

(Minolta CM-2600d). En plus de ces mesures physiques, le banc est équipé d'un système d'imagerie GEOTEK Geoscan IV pour prendre en photographie haute-définition les demi-sections.

En parallèle de ces mesures, l'équipe scientifique à bord du navire avait pour mission de décrire la totalité des carottes sédimentaires qui ont été ouvertes et de prélever des échantillons à l'aide de tubes de plastique en U (Fig. 11). Ces échantillons appelés « *U-channels* » ont été stockés et conservés dans la chambre froide de l'ISMER, tandis que l'ensemble des demi-sections ont été stockées dans la chambre froide de la collection marine du Muséum d'Histoire Naturelle de Paris sous la dénomination MNHN-GS-CAS16-XXPC (XX étant le numéro de la carotte).

Les *u-channels* ont été analysés à l'aide d'un magnétomètre cryogénique 2G Enterprise (Fig. 11) dans le but de réaliser une analyse paléomagnétique continue du sédiment. Pour caractériser les minéraux magnétiques, des échantillons ponctuels ont aussi été prélevés sur les *u-channels* pour être mesurés avec un magnétomètre à gradient alternatif (AGM ; Fig. 12) à l'ISMER ou prélevés sur les carottes et mesurés à l'IPGP avec un magnétomètre à

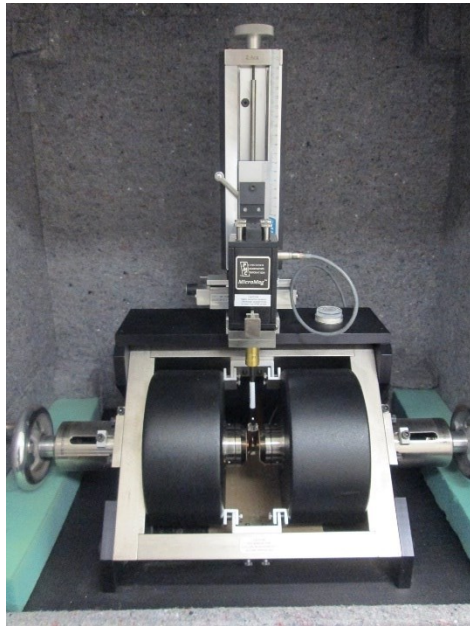


Figure 12 - Photographie du magnétomètre à gradient alternatif (MicroMag 2900 de Princeton Measurements Corp.) de l'ISMER.

échantillon vibrant (VSM). De plus, certains de ces échantillons ont été mesurés avec un susceptibilimètre Agico KLY3-CS3 Kappabridge. Enfin, quelques échantillons ont été observés au microscope électronique à balayage (SEM EVO MA10 Zeiss) couplé à un spectromètre des rayons X à dispersion d'énergie (EDS).

## 9. ORGANISATION DE LA THESE

Cette thèse de doctorat est subdivisée en trois chapitres qui répondent chacun aux objectifs spécifiques précédemment énoncés. Chacun de ces chapitres est rédigé en anglais au format d'un article, incluant les références en fin de chapitre. Les références de l'introduction générale et de la conclusion générale seront listées après les annexes.

Le premier chapitre présente une chronostratigraphie régionale détaillée, réalisée sur la carotte de référence CAS16-24PC. Cette étude a été effectuée en utilisant la combinaison

d'inversion de polarité magnétique (limite Brunhes/Matuyama et Jaramillo), des variations de paléointensité relative et de la stratigraphie des isotopes stables de l'oxygène.

Bieber, A., St-Onge, G., Feuillet, N., Carlut, J., Moreno, E., Michel, E., 2021. Regional chronostratigraphy in the eastern Lesser Antilles quaternary fore-arc and accretionary wedge sediments: Relative paleointensity, oxygen isotopes and reversals. *Quaternary Geochronology* 65, 101179. <https://doi.org/10.1016/j.quageo.2021.101179>

Le second chapitre estime l'âge des dépôts probablement associés à des séismes dans trois carottes sédimentaires (CAS16-04PC, CAS16-14PC et CAS16-36PC) en se basant sur la chronostratigraphie des carottes CAS16-24PC (chapitre 1) et CAS16-12PC. Ce chapitre met en évidence un super-cycle sismique de  $24 \pm 2$  ka avec une période de quiescence associée d'environ 6 ka.

Bieber, A., St-Onge, G., Feuillet, N., Seibert, C., Morena, P., Carlut, J., Moreno, E., Ratzov, G., Klingelhoefer, F., Cattaneo, A., Paleomagnetic analysis of rapidly deposited layers over the last 90 ka at the Lesser Antilles subduction zone: expression of earthquake super-cycle. Prochainement soumis dans le journal *Earth and Planetary Science Letters*.

Le troisième et dernier chapitre reprend l'ensemble des dépôts identifiés comme des turbidites et complexes homogénite-turbidites pour les étudier d'un point de vue paléomagnétique. Les variations d'inclinaison permettent de présenter un nouveau modèle de dépôt pour les complexes homogénite-turbidites et met en évidence la nécessité de dissocier les deux composantes (i.e., turbidite et homogénite) lorsqu'on étudie l'un ou l'autre des processus, notamment pour comprendre l'enregistrement du signal paléomagnétique.

Bieber, A., St-Onge, G., Feuillet, N., Carlut, J., Moreno, E., Influence of lithological changes on the paleomagnetic record based on Quaternary rapidly deposited layers from the Lesser Antilles: a new model for the deposition of homogenite-turbidite complexes. Prochainement soumis dans le journal *Geochemistry, Geophysics, Geosystems*.

Par ailleurs, tout au long de la réalisation de cette thèse, j'ai eu l'opportunité de présenter mes travaux lors divers congrès au format affiche ou présentation orale qui sont listés ci-après en ordre antéchronologique.

(Oral) GEOTOP2021 Bieber, A., St-Onge, G., Feuillet, N., Carlut, J., Moreno, E., Identification of a seiche effect using paleomagnetism on homogenite-turbidite complexes: example from deep basin sediments of the fore-arc Lesser Antilles. Congrès annuel du GEOTOP, Zoom-en-ligne, Québec, Canada, 16 au 18 mars (2021).

(Oral/Annulé\_COVID19) GEOTOP2020 Bieber, A., St-Onge, G., Feuillet, N., Carlut, J., Moreno, E., Identification and definition of homogenites, turbidites and hemipelagic sediments using paleomagnetism: examples from 3 giant piston cores from the Lesser Antilles accretionary wedge Quaternary sediments. Congrès annuel du GEOTOP, Québec, Canada, annulé (2020).

(Oral) AGU2019 Bieber, A., St-Onge, G., Feuillet, N., Carlut, J., Moreno, E., Identification and definition of homogenites, turbidites and hemipelagic sediments using paleomagnetism: examples from 3 giant piston cores from the Lesser Antilles accretionary wedge Quaternary sediments

(Affiche) EGU2019 Bieber, A., St-Onge, G., Feuillet, N., Carlut, J., Moreno, E., Michel, E. Quaternary magnetostratigraphy in the eastern Lesser Antilles fore-arc and accretionary wedge sediments Geophysical Research Abstracts Vol. 21, EGU2019-11261, 7-12 April 2019 (Vienna, Austria)

(Affiche) CDD2019 Bieber, A., Morena, P., St-Onge, G., Feuillet, N., Carlut, J., Moreno, E., Cattaneo, A., Ratzov, G., Klingelhoefer, F. Identification and definition of homogenites, turbidites and hemipelagic sediments using paleomagnetism: examples from the Lesser Antilles accretionary wedge Quaternary sediments Congrès des doctorants de l'IPGP (CDD2019), Paris, France, 25 au 29 mars (2019).

(Oral) ISC2018 Bieber, A., St-Onge, G., Feuillet, N., Carlut, J., Moreno, E. Impact of rapidly deposited layers on paleomagnetic records: examples from the Lesser Antilles accretionary wedge: preliminary results. I20th ISC 13-17 august 2018 (Québec, QC, Canada)

(Affiche) CDD2018 Bieber, A., St-Onge, G., Feuillet, N., Carlut, J., Moreno, E., Michel, E., St-Onge, M-P. Paleomagnetic variations in a sedimentary sequence along the lesser Antilles accretionary wedge: Preliminary results. Congrès des doctorants de l'IPGP (CDD2018), Paris, France, 25 au 30 mars (2018).

(Affiche) GEOTOP2017 Bieber, A., St-Onge, G., Feuillet, N., Carlut, J., Moreno, E., Guyard, H., Beauvais, Q., and the scientific participants of the CASEIS campaign. 2016. Magnetic and physical properties of sediment cores collected along the Lesser Antilles accretionary wedge: natural hazards and influence of lithological changes on the paleomagnetic signal. Congrès annuel du GEOTOP, Forêt Montmorency, Québec, Can., 24 au 26 mars (2017).

Finalement, une conclusion générale synthétisera les résultats des trois chapitres, cœur de cette thèse, tout en montrant de quelle manière ils ont su répondre à la problématique générale au travers des différents objectifs spécifiques. Pour étendre la discussion, quelques perspectives d'études sont proposées à la suite des connaissances acquises au travers de ce projet de recherche.



# CHAPITRE 1

## CHRONOSTRATIGRAPHIE RÉGIONALE DU PRISME D'ACCRÉTION ET DE L'AVANT-ARC À L'EST DES PETITES ANTILLES : PALÉOINTENSITÉ RELATIVE, STRATIGRAPHIE ISOTOPIQUE ET INVERSIONS

### 1.1 RESUME EN FRANÇAIS DU PREMIER ARTICLE

Le paléomagnétisme est un outil puissant pour établir une chronostratigraphie quasi-continue pour une région donnée. Lorsque cet outil est associé à d'autres méthodes de datation qu'elles soient absolues ou relatives, cela permet le développement d'un cadre chronostratigraphique régional de référence. Lors de la mission CASEIS qui a eu lieu en 2016 à bord du N/O Pourquoi Pas ?, plusieurs carottes sédimentaires ont été prélevées le long de la façade atlantique des Petites Antilles. La carotte CAS16-24PC a été dédiée à l'analyse chronostratigraphique et elle a permis le développement d'un enregistrement quasi-continu du Quaternaire. Dans cette étude et après avoir identifié et enlevé les couches déposées rapidement, telles que les turbidites et les téphras, nous avons reconstituer les variations de paléointensité relative (RPI) en normalisant l'aimantation rémanente avec l'aimantation anhydostérique rémanente. Un modèle d'âge a été développé en comparant notre enregistrement de RPI avec le stack PISO-1500 et le modèle paléomagnétique du moment dipolaire axial des dernières 2 Ma (PADM-2M), et en comparant l'enregistrement des isotopes stables de l'oxygène ( $\delta^{18}\text{O}$ ) dans des foraminifères planctoniques de la carotte CAS16-24PC avec le stack benthique LR04. En combinant la stratigraphie isotopique avec l'analyse paléomagnétique, nous avons établi un modèle d'âge avec un taux de sédimentation de  $1,7 \text{ cm.ka}^{-1}$  qui couvre la limite Brunhes/Matuyama et le Subchron Jaramillo jusqu'à  $\sim 1.15$  Ma. Ce modèle d'âge vient compléter les données paléomagnétique issues des campagnes IODP et des enregistrements volcaniques et permet d'obtenir une référence locale presque complète pour la RPI, l'inclinaison et la déclinaison.

Ce premier article, intitulé « *Regional chronostratigraphy in the eastern Lesser Antilles quaternary forearc and accretionary wedge sediments: Relative paleointensity, oxygen*

*isotopes and reversals* », fut corédigé par moi-même ainsi que mes deux directeur·es de recherche Guillaume St-Onge (ISMER-UQAR) et Nathalie Feuille (IPGP), ainsi que les chercheuses Julie Carlut (IPGP), Eva Moreno (LOCEAN/MNHN) et Élisabeth Michel (LSCE). Soumis en juillet 2020, il a été accepté pour publication en avril 2021 dans la revue scientifique *Quaternary Geochronology*. Ma contribution en tant que premier auteur a été de réaliser l'état de l'art, l'analyse en laboratoire d'une grande partie des échantillons, le développement du modèle d'âge et la rédaction de l'article. Guillaume St-Onge et Nathalie Feuillet ont participé à la recherche sur l'état de l'art, l'aide à l'analyse des données et la rédaction. Julie Carlut et Eva Moreno m'ont aidé dans la réalisation de prélèvement et d'analyse d'échantillon au sein de l'IPGP, ainsi que dans le suivi de l'analyse des données et de la rédaction. Élisabeth Michel a réalisé toutes les mesures isotopiques de l'oxygène et participer à la rédaction, notamment en rédigeant la méthodologie appliquée pour les mesures isotopiques. Une version préliminaire de cet article a été présentée au format affiche au congrès *European Geoscience Union* qui s'est déroulé à Vienne (Autriche) en 2019.

## **1.2 REGIONAL CHRONOSTRATIGRAPHY IN THE EASTERN LESSER ANTILLES QUATERNARY FOREARC AND ACCRETIONARY WEDGE SEDIMENTS: RELATIVE PALEOINTENSITY, OXYGEN ISOTOPES AND REVERSALS**

Paleomagnetism is a powerful tool for establishing an almost continuous chronostratigraphy for an entire region. When combined with other dating methods, absolute or relative, it can be used to develop a regional reference chronostratigraphic framework. During the summer of 2016, several piston cores were collected along the Atlantic side of the Lesser Antilles onboard the R/V Pourquoi pas? as part of the CASEIS Expedition. Core CAS16-24 PC was devoted to chronostratigraphic analysis and allowed development of a quasicontinuous Quaternary record. In this study, after identifying and removing rapidly deposited layers such as turbidites and tephra layers, we reconstructed the relative paleointensity (RPI) variations by normalizing the natural remanent magnetization with the laboratory induced anhysteretic remanent magnetization. An age model was developed by comparing our RPI record with the PISO-1500 stack and paleomagnetic axial dipole moment model for the past 2 Myr (PADM-2M) and the planktic oxygen isotopic record ( $\delta^{18}\text{O}$ ) for core CAS16-24 PC with the LR04 benthic stack. By combining the  $\delta^{18}\text{O}$  stratigraphy with paleomagnetic analyses, we established an age model covering the Brunhes/Matuyama boundary and Jaramillo Subchron back to  $\sim 1.15$  Ma with a mean sedimentation rate of 1.7 cm/kyr. This age model complements the paleomagnetic data from IODP campaigns and volcanic records, and offers almost complete inclination, declination and RPI records as a local reference.

### **1.2.1 Introduction**

Earth's magnetic field varies at different timescales and can undergo reversals (normal and reverse polarities) that may be globally recorded quasi-simultaneously in rocks and sediments (Lowrie, 2007). The synchronicity of reversals across different locations makes them important for stratigraphy (Hambach et al., 2008). The last reversal occurred  $773 \pm 2$  ka ago between the normal polarity Brunhes Chron and the reversed polarity Matuyama Chron (Singer, 2014; Simon et al. 2019; Channell et al., 2020). The Matuyama/Brunhes boundary (MBB) delimits the beginning of the Middle Pleistocene (International

Commission on Stratigraphy, 2020). In addition to reversals, magnetic minerals can record paleomagnetic secular variations and changes in Earth's magnetic field intensity. Full vector analysis of Quaternary oceanic sediment cores enables quasi-continuous reconstruction of the relative variations in the Earth's magnetic field (e.g., Tauxe, 1993; Weeks et al. 1993; Stoner and St-Onge, 2007; Channell et al., 2012, 2014, 2019; Roberts et al., 2013; Liu et al. 2016; Deschamps et al. 2018; Simon et al. 2020). This reconstruction is based on the assumption that magnetic minerals such as magnetite and titano-magnetite within the sediment reflect the strength and the direction of the Earth magnetic field at the time they were deposited. This non-destructive approach enables correlation of multiple cores and stratigraphic events for entire regions. While paleomagnetism has been widely used to understand past geomagnetic field fluctuations, increasing global data coverage remains a long-term challenge for understanding geomagnetic field dynamics (Korte and Mandea, 2019), and for chronostratigraphic purposes.

There is currently no complete and well-dated Quaternary magnetostratigraphic record for the Lesser Antilles. Most paleomagnetic studies have focused on volcanic rocks (Carlut and Quidelleur, 2000; Genevey et al., 2002; Tanty et al., 2015; Ricci et al., 2018) or Ocean Drilling Program (ODP) cores that cover longer geologic time intervals (DSDP Site 502: Kent and Spariosu, 1983; DSDP Leg 78A: Wilson, 1984; ODP Leg 110: Hounslow et al., 1990), but with a less detailed representation of the Quaternary.

The main objective of this study is to establish a complete regional Quaternary chronostratigraphy based on analyses of core CAS16-24PC retrieved during the CASEIS expedition (May 28 to July 4, 2016; Feuillet, 2016) onboard the R/V Pourquoi Pas?. The first step was to identify all rapidly deposited layers (RDL) using x-ray fluorescence, and physical and magnetic parameters to create a continuous composite record. The second step was to reconstruct a reliable relative paleointensity (RPI) record and to combine it to reversals and

stable oxygen isotopes ( $\delta^{18}\text{O}$ ) to derive a new Quaternary chronostratigraphic framework for the Lesser Antilles.

### 1.2.2 Regional setting

The Lesser Antilles are located in the easternmost Caribbean Sea (Fig. 13). They are composed of two volcanic arcs: the inactive early Eocene to Oligocene arc and the current arc that has been active since 38 Ma (Briden et al., 1979; Bouysse and Westercamp, 1990). These arcs resulted from subduction of the south and north Atlantic oceanic crust under Caribbean oceanic crust (McDonald et al., 2000), which led to formation of basaltic volcanic

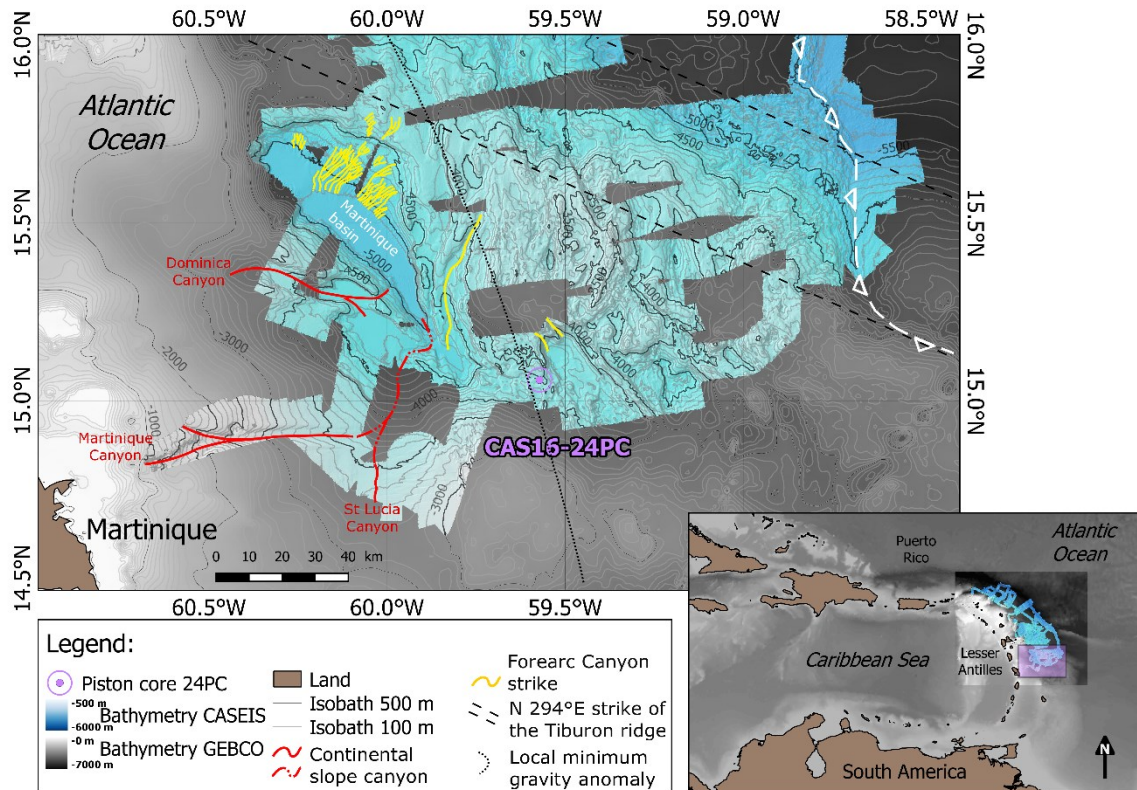


Figure 13 - Bathymetric map of the middle Lesser Antilles Arc, western Atlantic Ocean using GEBCO and CASEIS data. Red and yellow lines highlight, respectively, continental slope canyons and forearc basin canyons. The local minimum gravity anomaly limit (black dotted line), the N 294°E strike of the Tiburon ridge (dashed black lines) and the deformation front (white dashed line with teeth) are derived from Bouysse and Wastercamp (1990). The location of reference core CAS16-24PC is indicated in purple.

arcs. The current average convergence velocity is 2 cm/yr with a NNE and SSW orientation (DeMets et al., 2000; Symithe et al., 2015). The current system is the product of a western arc migration following subduction of the two aseismic ridges (i.e., Tiburon and St-Luce) beneath the Caribbean plate. The volcanic activity is probably also related to the seismic activity (Davies, 1999; Leclerc et al., 2016). Seismic fault activation or reactivation led to two periods of maximum eruptive activity during the Eocene-Oligocene and the late Miocene-early Pliocene (Bouysse and Westercamp, 1990).

The Lesser Antilles arc basement has an asymmetric shape (Picard et al., 2006). Westward of the island arc, the Grenada back-arc basin has a steep and narrow continental shelf. In contrast, eastward of the island arc, the shelf is wider and limited eastwards by the accretionary wedge and the trench. The insular shelf is 250 km wide in the south, and only 80-100 km wide in the north. Similarly, the accretionary prism has a width of 300 km in the south that decreases northward to 50 km. The trench is deeper to the north (up to 8 km below sea-level). The sedimentary fill consists of (1) shallow shelf sediment predominantly composed (up to 50 %) of river discharge volcaniclastic sediments (the proportion increases closer to islands shore, up to 50 %) and pelagic and hemipelagic carbonate sediments, (2) deep sea sediments mostly composed of pelagic, hemipelagic and remobilized carbonates, and (3) volcaniclastic turbidite and tephra deposits (Reid et al., 1996; Picard et al., 2006). However, the most important terrigenous sediment sources to the eastern Lesser Antilles are from the Orinoco delta (Deville et al., 2015) and a minor contribution from aeolian dust from Africa (Reid et al., 1996; Picard et al., 2006).

### 1.2.3 Material and methods

A bathymetric map (Fig. 13) was created with the QGIS software using the General Bathymetric Chart of the Oceans GEBCO\_08 grid, version 20100927 (<http://www.gebco.net>) and Digital Elevation Models from the 2016 CASEIS cruise (Feuillet, 2016; Seibert et al., 2020). A 100-m resolution was used with a WGS84/UTM World Mercator (15.5°N) projection. Reference core CAS16-24PC (Fig. 13) was retrieved

during the CASEIS expedition at 4023 m depth with a Calypso piston corer on board the R/V Pourquoi Pas? (IFREMER fleet). The core is stored in the marine collection of the Muséum national d'Histoire naturelle (Paris, France) under the number MNHN-GS-CAS16-24PC and is 19.90 m in length and was divided into fourteen 150 cm sections labeled with Roman numbers I to XIV (Fig. 14-A). Each section was measured on board with a Multi Sensor Core Logger (see below), then split, photographed, described and sampled with u-channels (u-shaped plastic tubes with 2 x 2 cm cross-section and up to 150 cm in length) for continuous paleomagnetic analysis (e.g., Weeks et al., 1993; Stoner and St-Onge, 2007). In 2018, the core was sampled with plastic cubes (1.9 x 1.9 x 1.9 cm) for discrete paleomagnetic analyses.

#### 1.2.3.1 Multi Sensor Core Logger analysis, CT scanning and x-ray fluorescence

The GEOTEK Multi Sensor Core Logger (MSCL) from ISMER (Institut des sciences de la mer de Rimouski) was used on board during the expedition to measure the physical and magnetic properties of the sediments (St-Onge et al., 2007). Bulk density (obtained with gamma ray attenuation), P-wave velocities and volumetric magnetic susceptibility ( $k$ ) were analysed at 1-cm intervals on whole core sections. After splitting the core, archive halves were photographed with a GEOTEK Geoscan IV imaging system and measured again at 1-cm intervals with a Bartington Instruments MS2E1 point sensor for magnetic susceptibility. Diffuse spectral reflectance data were also measured at 1-cm intervals using a Minolta CM-2600d spectrophotometer inline with the MSCL. Data were converted into the L\*a\*b\* colour space of the International Commission on Illumination (CIE): L\* ranges from black (0) to white (100), a\* ranges from green (-60) to red (+60), and b\* ranges from blue (-60) to yellow (+60). U-channel samples were scanned at the Institut national de recherche scientifique – Centre eau, terre et environnement (INRS-ETE, Québec, Canada) with a CT scanner. The resulting digital X-ray images were displayed in greyscale and expressed as CT numbers, which primarily reflect bulk density changes (e.g., St-Onge et al., 2007; Fortin et al., 2013). Major elements from Al to Ba were analysed on archive halves at the UMR CNRS 5805 EPOC laboratory (Bordeaux, France) using an X-Ray fluorescence (XRF) Avaatech core-

scanner. XRF-measurements were conducted at 1 cm intervals with two tube voltages (10 and 30 keV).

### 1.2.3.2 Paleomagnetic analysis

#### a) *CONTINUOUS MAGNETIC MEASUREMENTS*

Continuous paleomagnetic data were acquired at 1-cm intervals on u-channel samples using a 2G Enterprises 755SRM-1.65 cryogenic magnetometer at the ISMER. The natural remanent magnetization (NRM) was first measured directly and then stepwise demagnetized and measured after each of 17 alternating field (AF) demagnetization steps (0 to 80 mT, 5 mT increments) until the residual magnetization was less than 15% of the initial magnetization. An anhysteretic remanent magnetization (ARM) was then induced using a 100 mT peak AF and a 50  $\mu$ T direct current (DC) bias field. The ARM was measured following the same procedure and increment steps as the NRM. Finally, an isothermal remanent magnetization (IRM) and a saturation IRM (SIRM) were induced in DC fields of 0.3 T and 0.95 T, respectively, using a pulse magnetizer, and were then stepwise demagnetized and measured at 9 steps for IRM (0 to 80 mT, 10 mT increments) and 4 steps for SIRM (0, 10, 30, 50 mT). The data were processed with the Excel spreadsheet developed by Mazaud (2005), which provided the paleomagnetic inclination, declination and the associated maximum angular deviation (MAD) values calculated for the characteristic remanent magnetization (ChRM; 10 to 40 mT steps). The pseudo S-ratio was determined using the IRM<sub>0</sub> mT induced at 300 mT divided by SIRM<sub>0</sub> mT induced at 950 mT (IRM/SIRM). This pseudo S-ratio, alike the classical S-ratio, is an indicator of the magnetic coercivity and mineralogy (St-Onge et al., 2003). Values close to 1 (IRM  $\approx$  SIRM) indicate the preponderance of low coercivity minerals, whereas lower values are the expression of higher coercivity minerals (IRM < SIRM). The sediments from core CAS16-24PC are characterized by high values of IRM and SIRM (average value of all data  $>11$  Am<sup>-1</sup>) and the intensity of the SIRM is sometimes slightly lower than the IRM, leading to values of the pseudo-S ratio slightly higher than 1 in specific intervals. This is most likely due to the

difficulty of the cryogenic magnetometer to perform precise measurements near the dynamic range of the instrument (Roberts, 2006). As a consequence, it prevents us from using the pseudo S-ratio lonely and continuously downcore, but we still use the average value in hemipelagic facies in conjunction with the other magnetic and imaging data (SEM, see below) to assess the magnetic mineralogy. Also,  $k_{ARM}$  is calculated by normalizing the ARM with the bias field value and is used as a magnetic grain size indicator (e.g., Banerjee et al., 1981; King et al., 1982).

**b) DISCRETE MAGNETIC MEASUREMENTS**

To confirm and refine the continuous magnetic measurements results and to improve delimitation of suspected reversals, we measured paleomagnetic data on discrete samples. They were acquired at 40-cm intervals along the whole core except for the uppermost 5 m (10 cm intervals) and sections with suspected geomagnetic reversals (2 cm intervals). We used a 2G Enterprises 760SRM-3.0 cryogenic magnetometer and an ASC Scientific D-2000T AF demagnetizer for stepwise demagnetization (10 steps; 5, 10, 15, 20, 30, 40, 50, 60, 70 and 90 mT) of the NRM at the Institut de Physique du Globe de Paris (IPGP).

Twenty-five bulk samples were selected and measured using a Princeton Measurement Corporation vibrating sample magnetometer (VSM) at the IPGP to obtain hysteresis loops and derived magnetic parameters corrected for high field and mass: coercive force ( $H_c$ ), remanent coercive force ( $H_{cr}$ ), saturation magnetisation ( $M_s$ ) and saturation remanence ( $M_{rs}$ ). These data were used to estimate the relative magnetic-grain sizes domains (single domain, multidomain and vortex state; Roberts et al.; 2017) based on the Day plot (Day et al., 1977). Attention must be taken when considering these results. As Roberts et al. (2018) pointed out, the Day diagram indicates strict limits for magnetic domains, while these limits depend on multiple parameters (e.g. magnetic grain size, mineralogy, mixing, shape). Three samples with highest magnetic susceptibility values were measured using an AGICO KLY-3 Kappa bridge system to measure the low-field magnetic susceptibility ( $k_{LF}$ ) at high-temperatures.  $k_{LF}$  was measured in a heating-cooling cycle between room temperature and

700°C in a natural atmosphere. These measurements enable determination of Curie temperatures (Hrouda, 1994; Dunlop and Özdemir, 2007).

**c) SCANNING ELECTRON MICROSCOPY AND ENERGY-DISPERSIVE X-RAY SPECTROSCOPY**

The magnetic mineral fraction of five samples was manually separated from bulk powdered sediments using magnets. Imaging and energy-dispersive X-ray spectroscopy (EDS) microanalysis were observed with a EVO MA10 Zeiss scanning electron microscope (SEM).

**1.2.3.3 Stable isotopes**

One hundred seventy eight bulk samples collected at ~10 cm intervals were sieved at 150 µm. Nineteen specimens were sampled in RDL and were removed from this study.  $\delta^{18}\text{O}$  was determined on 250-315 µm sized Globigerinoides ruber planktic foraminifera using a Dual Inlet GV isoprime mass spectrometer at the Laboratoire des Sciences du Climat et de l'Environnement (LSCE). The measurements are reported versus the Vienna Pee Dee Belemnite standard (VPDB) with NBS-19 standard at  $\delta^{18}\text{O} = -2.20\text{\textperthousand}$ , with a mean external reproducibility ( $1\sigma$ ) of carbonate standards of  $\pm 0.05\text{\textperthousand}$ . Measured NBS-18  $\delta^{18}\text{O}$  values are  $-23.27 \pm 0.10\text{\textperthousand}$  VPDB.

**1.2.3.4 Age model**

The chronology of the event-free core CAS16-24PC composite record is based on paleomagnetic reversals, RPI variations and the  $\delta^{18}\text{O}$  stratigraphy (see below). In this study, the R software package Bacon 2.2 (Blaauw and Christen, 2011) was used to produce a best-fit age model using Bayesian statistics with normal distributions. The parameters used were a 5 cm depth interval (d.by=10) and a 2 cm/ka mean accumulation rate (acc.mean=500).

## 1.2.4 Results

### 1.2.4.1 Morpho-bathymetry offshore of eastern Martinique

Core CAS16-24PC was retrieved offshore of Martinique Island at the limit between forearc and accretionary wedge sediments (Fig. 13). This limit follows approximately the local minimum negative gravity anomaly (dotted black line in Fig. 13), while the deformation front (white dashed line in Fig. 13) follows the outer prism limit (Westbrook et al., 1984; Bouysse and Westercamp, 1990). The core location is surrounded eastward by a deep basin down to 4400 m below sea level (mbsl) and westward by the Martinique basin deeper down to 5100 mbsl. This basin is fed from the south by the St. Lucia, the Caravelle, the Amerique and the Kalanina canyons, together with one canyon stemming from the accretionary prism (Seibert et al., 2020). In a north-south transect, the core location is between two bathymetric highs, which protect the area from large mass wasting events and frequent turbidity currents. The core site was chosen to collect the best possible chronostratigraphic reference core from the area, with the presence of carbonates for  $\delta^{18}\text{O}$  stratigraphy (above the carbonate compensation depth) and the least possible turbidites. Nonetheless, in this volcanic setting, thin volcanoclastic layers are expected (e.g. Reid et al., 1996; Picard et al., 2000; Le Friant et al., 2008).

### 1.2.4.2 Lithology and rapidly deposited layer (RDL) determination

High-definition photographic images of the 19.90 m long piston core are presented in Fig. 14-A and confirm the overall homogeneity of brownish to greyish sediment. The associated CT-scan images have low (dark grey) to medium (light grey) density with traces of bioturbation. This background sediment is interbedded with thinner, darker sediment layers with higher density (white color) that can be related to RDL. In addition to the visual core characterization, down-core variations of physical and magnetic parameters, CT-

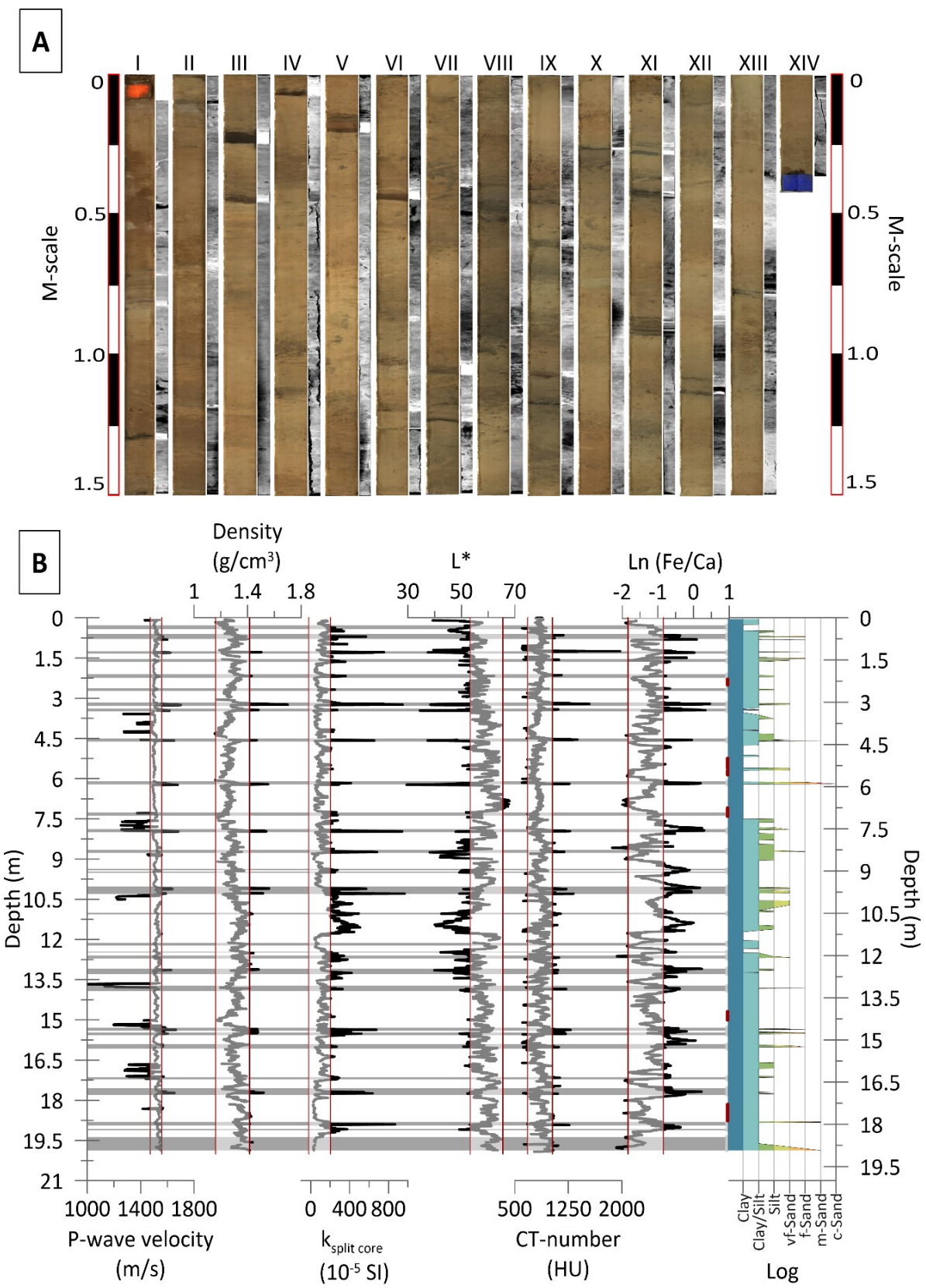


Figure 14 - A: Full core high-resolution photography with CT-scan images (left: TOP of the core, right: BOTTOM of the core). B: MSCL and XRF data comprising from left to right: P-wave velocity, density, magnetic susceptibility k, L\*, CT-number, and ln (Fe/Ca). The shipboard grain size log is also plotted on the right, including red marks that are pure hemipelagic background sediments used to delimit the background signal with  $\pm 2\sigma$  (whitened band between red straight lines). RDL are highlighted as grey horizontal intervals.

number, ln (Fe/Ca) XRF ratios and sedimentological log established onboard are shown in Fig. 14-B. The same method used by Cassidy et al. (2014) was used to decipher hemipelagic background sediments from RDL. Hemipelagic sediments are identified by traces of bioturbation, fine grains (under silt size), and relatively low and stable physical and magnetic parameter values. The mean  $\pm 2$  standard deviation ( $\sigma$ ) limits (whitened bands delimited by vertical red lines) of each parameter was calculated, which gives a 95% ( $2\sigma$ ) confidence level to delimit hemipelagic background sediments along the core, which is consistent with the photographic and CT-scan images. Outside the red lines, positive spikes in density parameters (gamma density, P-wave velocity and CT-number) and magnetic susceptibility reflect the presence of coarser grains, as well as ln (Fe/Ca) positive spikes and L\* negative spikes, which reflect darker minerals with higher iron contents. Based on this analysis, magnetic susceptibility and density are the best parameters to establish the three main facies. The first facies, hemipelagic background sediments (e.g. Fig. 15-A and -B), has low density (density around 1.29 g/cm<sup>3</sup>, CT-numbers between 600 and 1028 HU) and weaker magnetic susceptibility (between 20 to 150x10<sup>-5</sup> SI). The second facies (e.g. Fig. 15-B) has a sharp contact, coarser basal sediments with high density (up to 1.7 g/cm<sup>3</sup>), high CT-number (up to 1977 HU), P-wave velocity spikes (up to 1701 m/s) and high magnetic susceptibility (up to 966x10<sup>-5</sup> SI). The last facies is composed of silt layers with thicknesses of a few cm (e.g. Fig. 15-A) interbedded with hemipelagic background sediments with similar physical and magnetic parameters as facies 2, but without distinctive sharp contacts and normal grading. Facies 2 can be interpreted as classical turbidites because of its sharp contact and normal grading (e.g., Bouma, 1964), while facies 3 can be inferred to reflect deposition from suspended particles during a weak turbidity current with a slight normal grading at the base. Along the entire 24PC core, a total of 37 distinctive RDL were identified. Their thicknesses

vary between 1 cm and 30 cm with a mean thickness of about 6 cm and a 5 cm median value; they related mostly to cryptotephras and reworked volcaniclastic material.

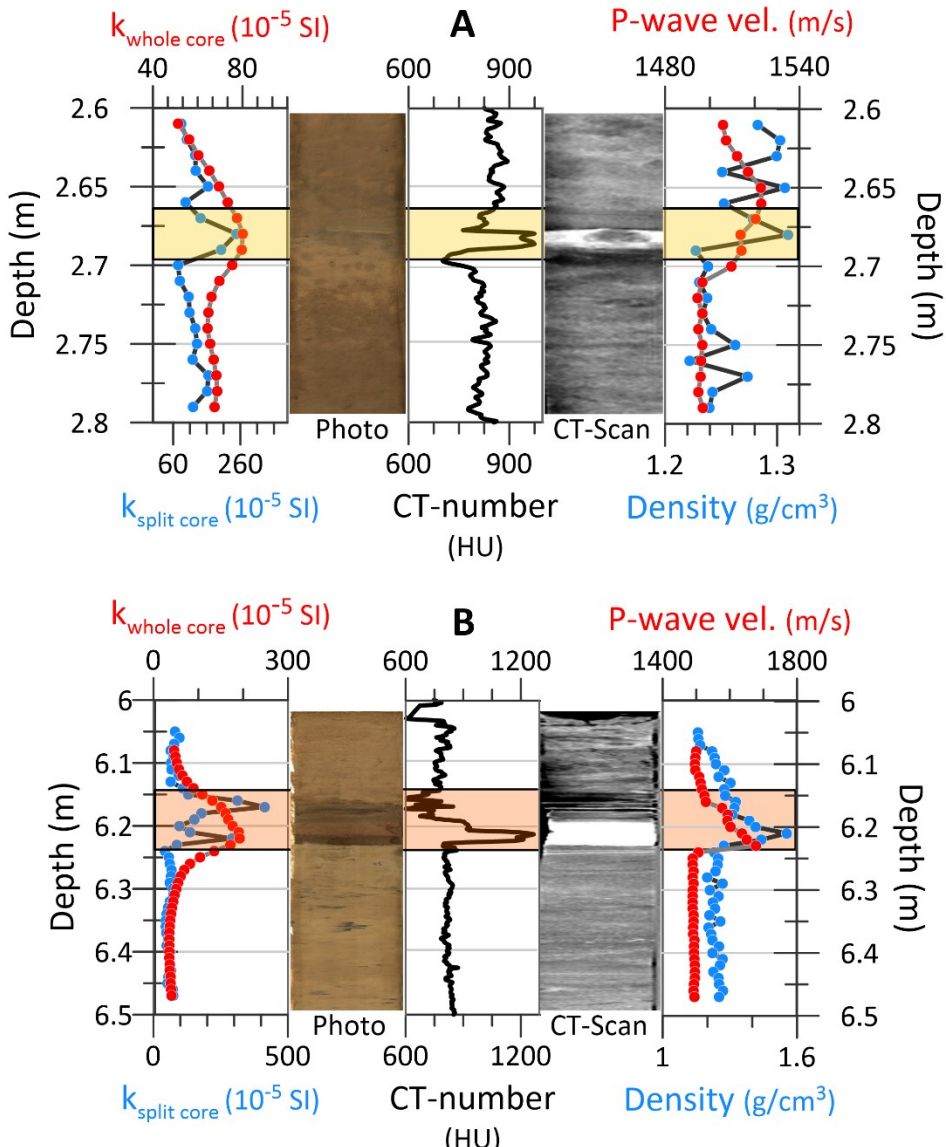


Figure 15 - A: Brownish hemipelagic background sediments defined with low and stable magnetic susceptibility ( $k$ ), CT-number, density and P-wave velocity, interbedded with a RDL ( $\approx 5$  cm) between 2.70 m and 2.65 m (yellow band). B: Light brown hemipelagic background sediments are defined by low and stable  $k$ , CT-number, density and P-wave velocity data. A well-defined RDL between 6.24 m and 6.14 m is darker (dark brown to grey color) with an erosive contact, normal grading (high CT-number, P-wave velocity, density) and high  $k$ .

#### 1.2.4.3 Creation of an event-free composite record

One part of the core, from 10.32 m to 12.01 m, presents a specific signal that is mostly not related to turbidite or mass movement deposits. This section has no high values of density indicators or P-wave velocities, but L\* and the photography (section VII132cm to IX1cm) indicate darker sediments. The XRF ratio ln (Fe/Ca) has high values, which combined with magnetic susceptibility and negative L\* spikes, could indicate the presence of cryptotephras and reworked volcaniclastic minerals (Cassidy et al., 2014). The average magnetic susceptibility is higher than the background mean + 2 standard deviations, which is the upper limit for the hemipelagic sediments. However, density parameters do not indicate coarsening grain size. This implies magnetic mineral concentration variation, but in the absence of evidence for the deposition of a RDL, we identify it as background sediment. To summarize, a total of 87.1 % (17.31 m composite depth) of the piston core is composed of background hemipelagic sediments. The following results are presented for this event-free stratigraphy as a function of meters composite depth (MCD; Table 5 in ANNEXE 1 for depth correspondence) and the magnetic mineralogy was analyzed only on these hemipelagic sediments.

#### 1.2.4.4 Magnetic mineralogy

SEM imaging and EDS of the magnetic mineral fraction (Fig. 16) enabled the identification of magnetic minerals and reveal grain sizes mostly below 5  $\mu\text{m}$ . The elemental compositions of the analyzed grains are compiled in supplementary material Table 6 (ANNEXE 1) and reveal a matrix composed mostly of alumino-silicates (Sample 4) with magnetic particles mostly consisting of low-titanium iron oxides grains (TiFeOx, samples 2, 3 and 5) and a few high-titanium iron oxide grains (not shown here). These SEM investigations are in agreement with the VSM measurements where the shapes of hysteresis loops (Fig. 17-A) are characteristic of low-coercivity ferrimagnetic minerals like magnetite or titanomagnetite (Day et al., 1977; Tauxe et al. 1996). In addition, magnetic susceptibility was measured every 18 seconds over a heating-cooling cycle from room temperature to

700°C and back to room temperature (Fig. 17-B). The presence of different magnetic minerals is revealed. High temperature curves suggest the identification of the magnetite Curie temperature (Fig. 17-B) at around 580 °C (Dunlop and Özdemir, 2007). The small peak between 300 °C and 370 °C can be interpreted as Ti-rich titanomagnetite (Gilder and Legoff, 2005). Additionally, the pseudo S-ratio in hemipelagic sediments presents an average value of 0.96. This value is typical of low coercivity minerals such as magnetite (Stoner and St-Onge, 2007). While EDS measurements only reflect mineralogy of minerals bigger than 1 µm and might be different from remanence carriers, the VSM and magnetic susceptibility measurements were made on bulk sediment. These combined results demonstrate an overall magnetic mineralogy dominated by magnetite and titanomagnetite. Such a magnetic composition is typical of volcanic settings and was previously observed for example in the Tobago Basin, Southeast Caribbean (Frank et al., 2016).

#### 1.2.4.5 Magnetic grain size and concentration

Relative magnetic grain size variations can be plotted using Day and King plots (Fig. 18). The Day-plot (Day et al., 1977), derived from hysteresis parameters (Fig. 18-A), confirms the relative prevalence of magnetic grains in a vortex state. In the King plot, data for almost all samples from the composite core range around the empirical 0.2 µm line, and

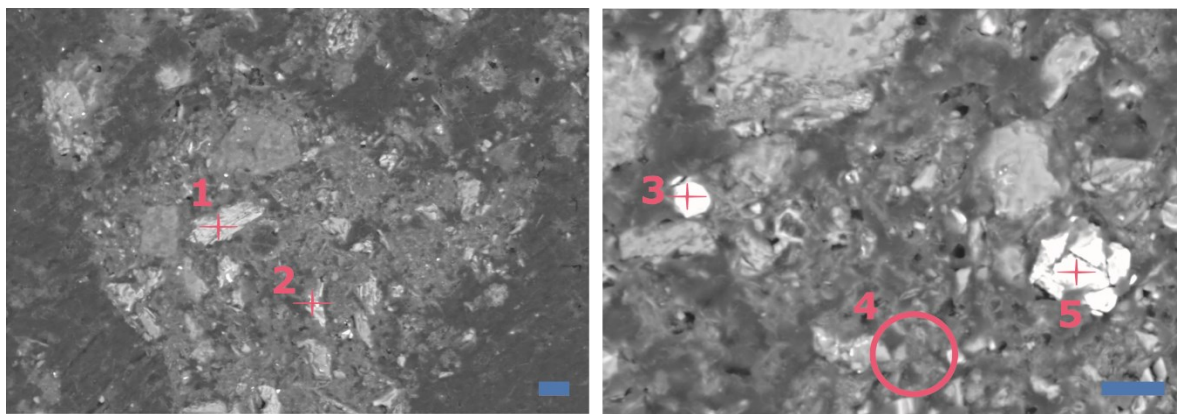


Figure 16 - SEM images for representative bulk sample VIII-1137. The left-hand image is a general view of the sample. The right-hand image is focused on small particles ( $<10\text{ }\mu\text{m}$ ) and matrix analysis. Blue bands are 10 µm scales. Red objects are elemental analyses, as referenced in Table 6 (ANNEXE 1) with the same numbers.

except for 3 samples, all are above the 5  $\mu\text{m}$  empirical line (Fig. 18-B). Even though these absolute values should be treated with caution because they were derived from synthetic magnetite (King et al., 1982), they nonetheless suggest a relatively fine magnetic grain size. These results are supported by SEM images (Fig. 16) that reveal particle sizes smaller than or equal to 5  $\mu\text{m}$ . This can explain that the NRM20 mT, ARM20 mT and IRM20 mT values vary by less than an order of magnitude along the core (Fig. 19), except from 9.24 to 10.90 MCD (10.32 m to 12.01 m) where the density parameters do not exhibit coarsening grain size, while magnetic concentration increases (Fig. 14-B). Furthermore, the  $k_{\text{ARM}}/k$  ratio (Fig.

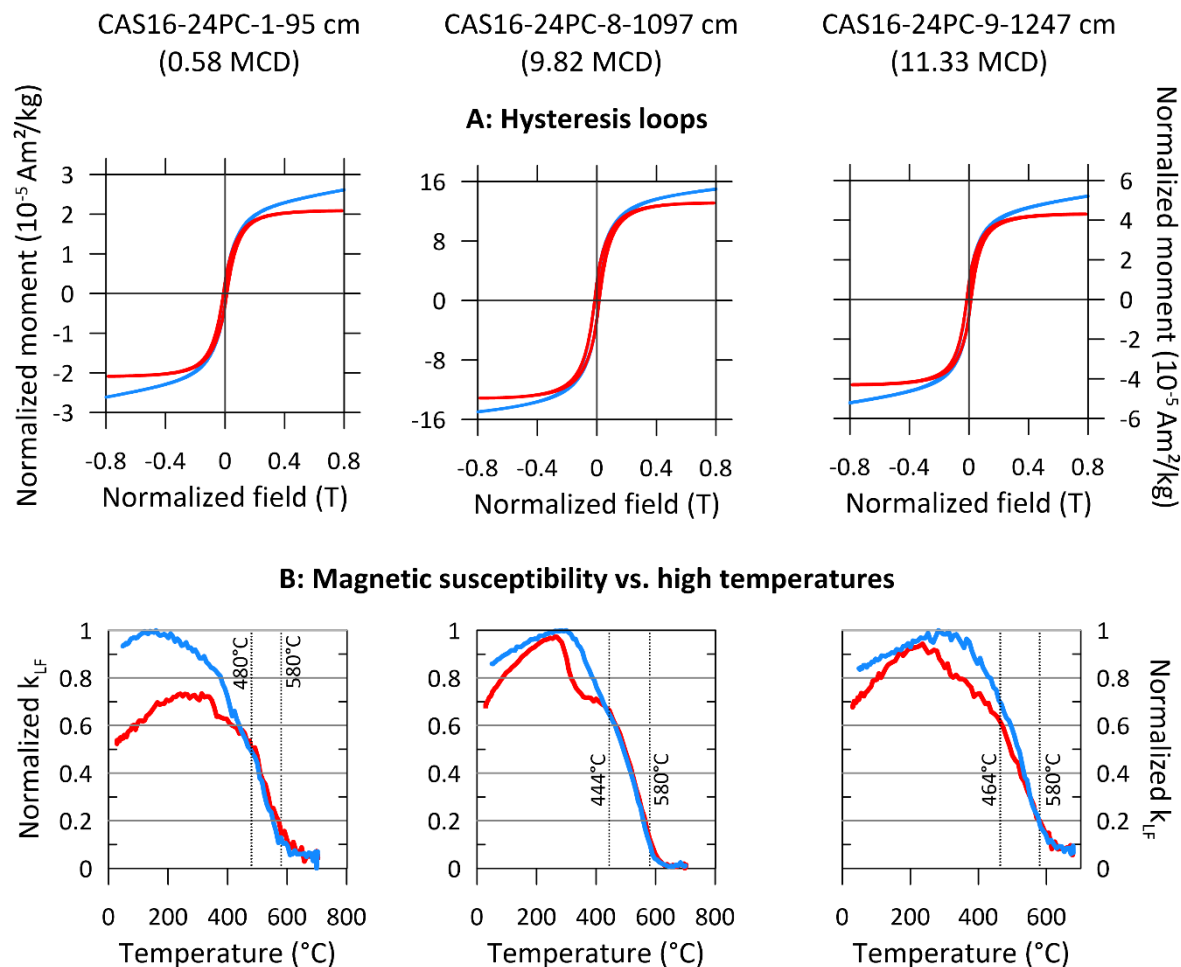


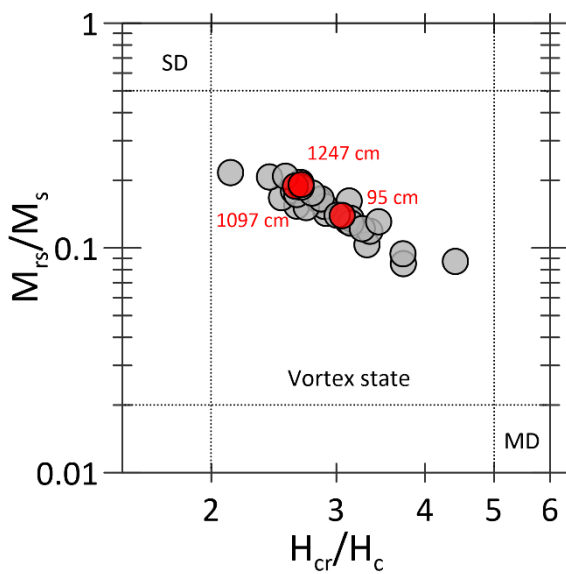
Figure 17 - A: Typical hemipelagic sediment raw hysteresis loops (blue). High-field and mass corrected loops are shown in red. B: Magnetic susceptibility vs. high temperatures. Red curves for heating, while blue curves are for cooling.

19), which reflects magnetic grain size variations (Banerjee et al., 1981; King et al., 1982; Stoner and St-Onge, 2007), has an overall constant trend.

#### 1.2.4.6 Magnetic remanence

Magnetic u-channel measurements are presented in Figs. 20 and 21. Within all the demagnetization steps, the NRM varies between  $7.95 \times 10^{-4}$  and  $2.93 \times 10^{-1}$  A/m, while induced magnetization ARM and IRM (SIRM) vary, respectively, between  $1.52 \times 10^{-4}$  and  $8.1 \times 10^{-1}$  A/m, and  $1.32 \times 10^{-1}$  and  $5.29$  A/m. From the top to 12.25 MCD, a strong and stable single-component NRM is isolated from 10 to 40 mT (7 demagnetization steps; Fig. 20) with a clear linear trend toward the origin of the orthogonal projection (Fig. 21-A and B). The viscous component is removed easily within the first 2 demagnetization steps. The mean MAD is  $7^\circ$  and the median is  $5.6^\circ$ , which are indicative of relatively good directional data. In addition, the inclination fluctuates around the expected inclination for the site latitude for a geocentric axial dipole ( $GAD = 28.28^\circ$ ) field. From 12.25 MCD to the bottom of the core, a stable single-component magnetization is isolated from 10 to 40 mT, inclinations alternate

**A: Day plot**



**B: King plot**

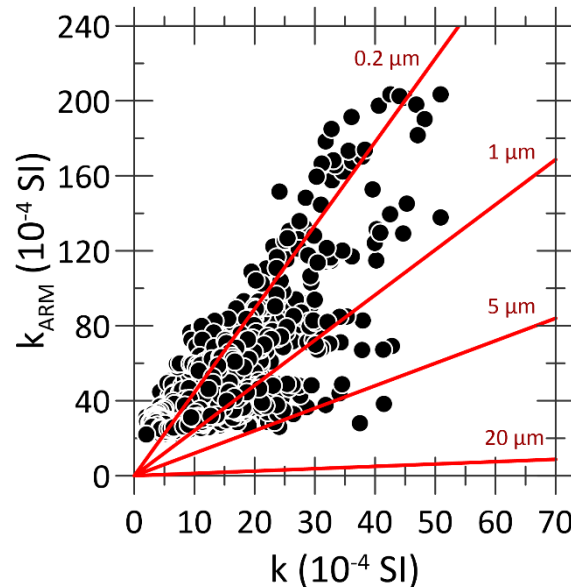


Figure 18 - A: Day plot (Day et al., 1977). Red labeled dots are data for the samples presented in Fig. 17. B: King plot (King et al., 1982).

between reversed (Fig. 21-C and D) and normal polarities and are interpreted as reversals. While the MAD values are relatively higher below 12.25 MCD (mean and median values of  $18^\circ$  and  $15.6^\circ$ , respectively), the inclinations fluctuate around the GAD values for both polarities (Fig. 20). The declination variations also mirror the inclination changes. In addition, discrete samples are coherent with u-channel data and improve the delimitation of the reversal event at 12.78 MCD (blue dots in Fig. 20). Overall, piston core CAS16-24PC has strong and stable single-component NRMs carried by PSD magnetite or titanomagnetite grains. The event-free composite record thus fulfills the criteria required for relative paleointensity (RPI) determinations (Levi and Banerjee, 1976; Tauxe, 1993; Stoner and St-Onge, 2007).

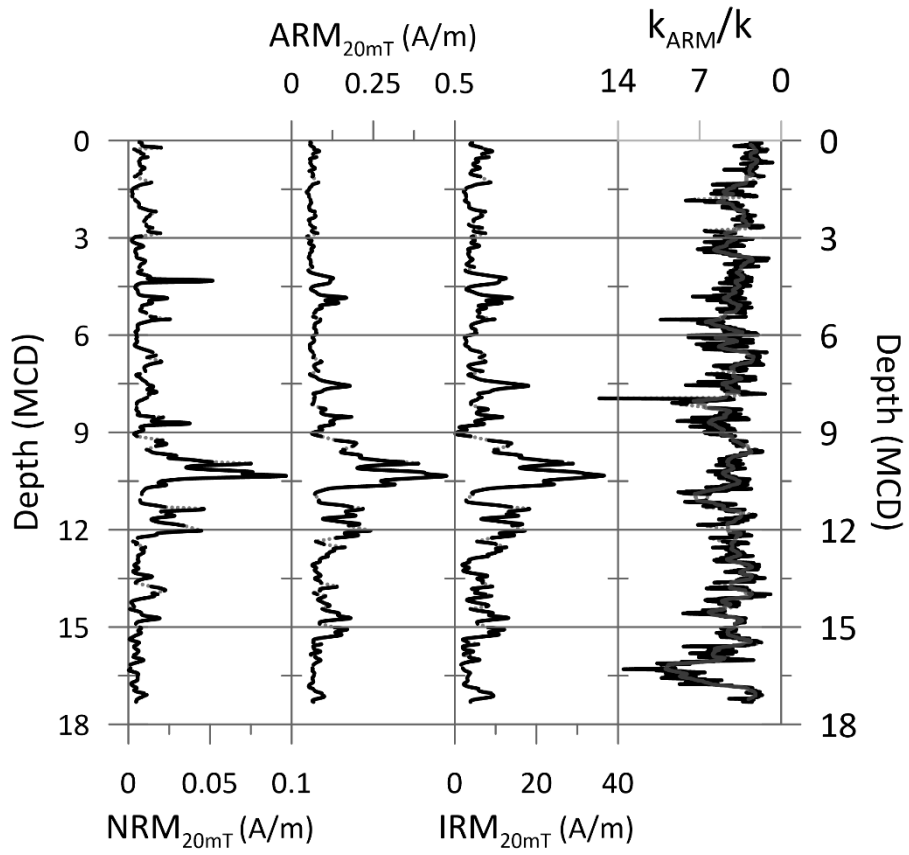


Figure 19 - Magnetic properties of the pelagic sediments (event-free composite record) with concentration, and magnetic grain size-dependent parameters on the left (NRM<sub>20 mT</sub>, ARM<sub>20 mT</sub> and IRM<sub>20 mT</sub>). k<sub>ARM/k</sub> indicates magnetic grain size variations for a magnetic assemblage dominated by magnetite.

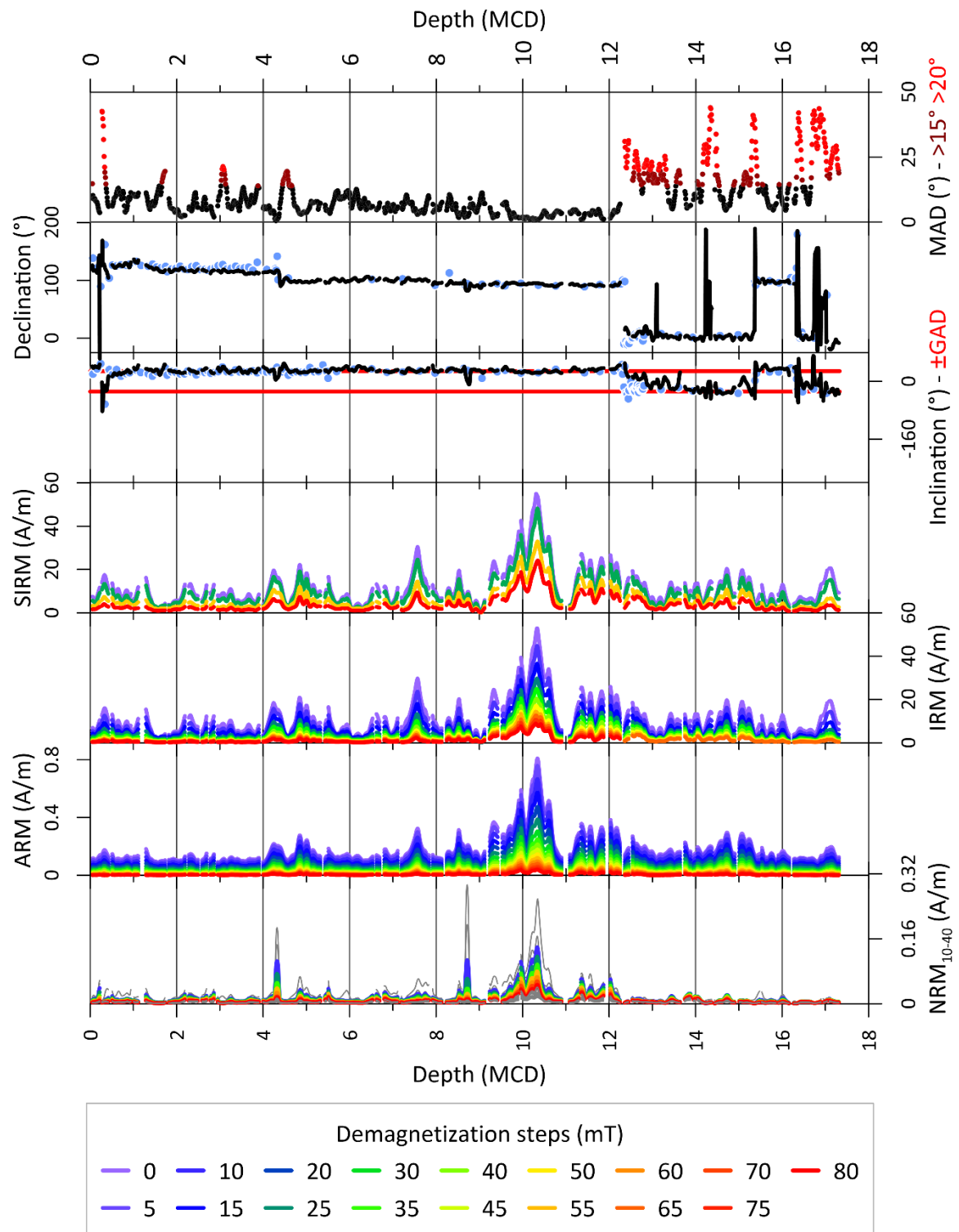


Figure 20 - Paleomagnetic data including from left to right: ChRM10-40 mT, ARM, IRM and SIRM demagnetization steps. Inclination (red line is the  $\pm$ GAD inclination at the site latitude) and declination (blue dots are data for the discrete samples). MAD values  $> 15^\circ$  are indicated in dark red and  $> 20^\circ$  in red.

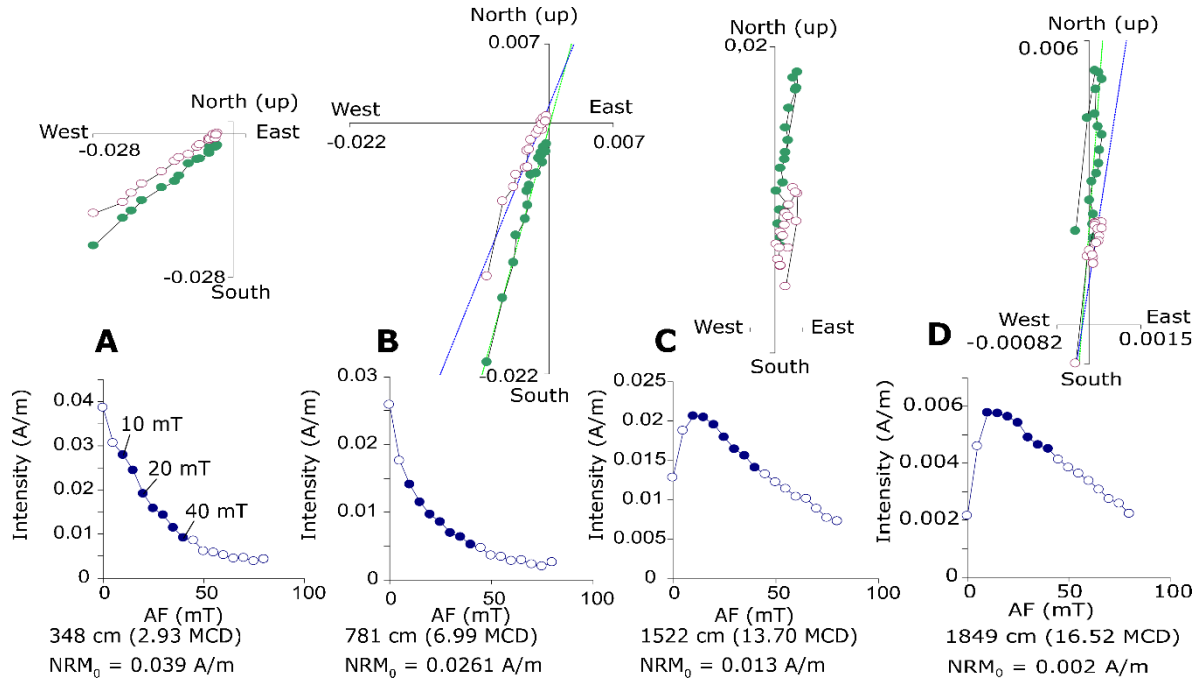


Figure 21 - Typical demagnetization curves and orthogonal projections of hemipelagic sediments. Filled blue dots represent the range of demagnetization steps used to calculate the characteristic remanent magnetization (ChRM).

#### 1.2.4.7 Relative paleointensity (RPI)

To reconstruct RPI variations, the NRM needs to be cleaned from the influence of lithological variations by using a normalizer such as ARM, IRM or  $k$  (Tauxe, 1993).  $k$  can be affected by paramagnetic grains that do not contribute to remanent magnetisation (Forster et al., 1994; Brachfeld and Banerjee, 2000), so we will not use it as a normalizer in this study. Two methods were compared to identify the best normalizer. The most used is the ratio method (e.g. Channell et al., 1997; Channell, 1999; St-Onge et al. 2003; Deschamps et al., 2018), which was calculated here using the average of seven or height demagnetization steps (10 to 40 mT or 10 to 45 mT) of the NRM normalized by ARM or IRM at the same steps (10

to 45 mT and 10 to 40 mT respectively). To evaluate the best normalizer, the normalized NRM is plotted against the normalizer and must reveal the lowest coefficient of determination ( $r^2$ ). Neither normalized remanence proxy correlates with their normalizers, but the  $r^2$  value is lower for ARM (0.0033) than for IRM (0.0201) (Fig. 22). The second method, based on the pseudo-Thellier method and recognised as the slope method (e.g. Tauxe et al., 1995; Channell, 2002; Snowball and Sandgren, 2004; Xuan and Channell, 2009), uses the slope between the NRM and the normalizer at different demagnetization steps. To evaluate the efficiency of a normalizer using the slope method, the correlation coefficient ( $r$ ) must be the highest. While ARM normalization gives the same results as for the slope

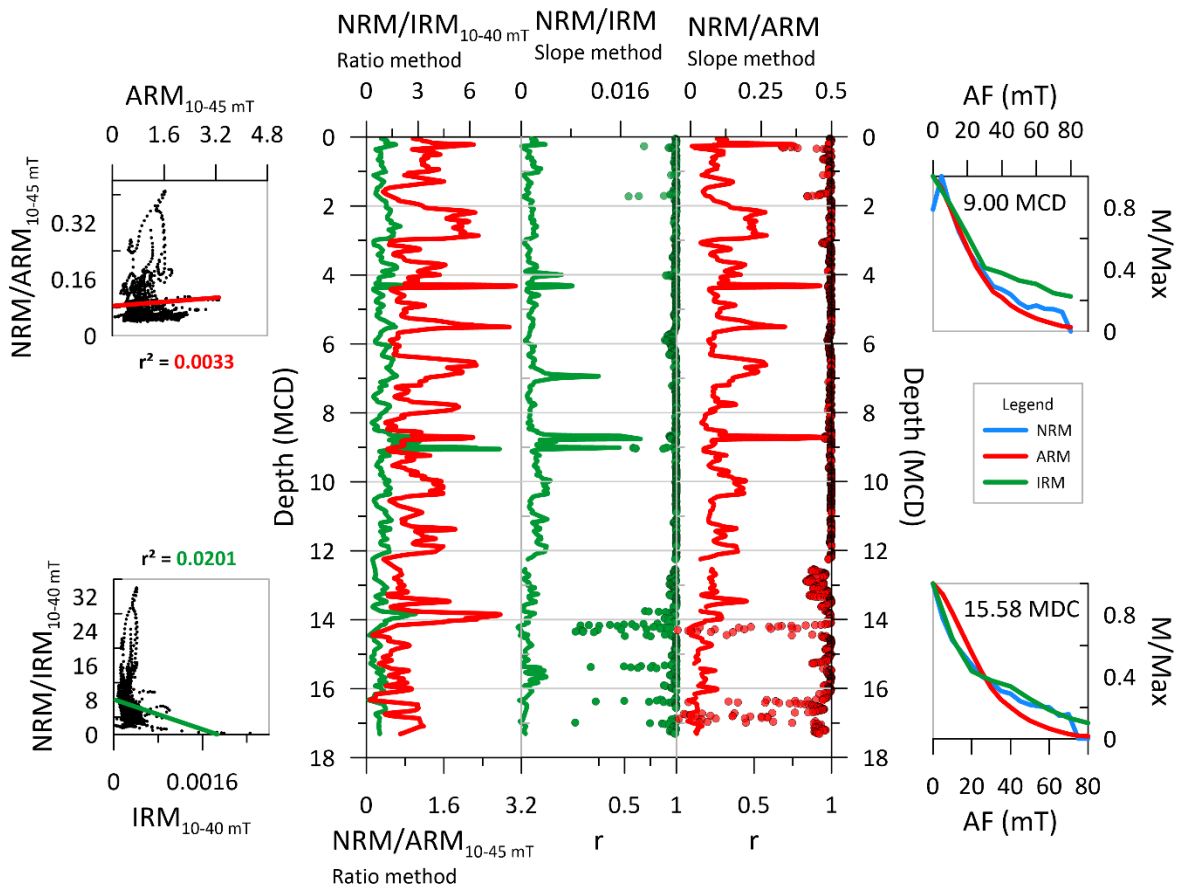


Figure 22 - Comparison of the RPI estimated with the average ratios (superposed red and green curves) and slope methods (red and green curves) in the scatter plots on the left, the correlation is reduced for ARM. Demagnetization curves for NRM, ARM and IRM are presented on the right-hand side.

method, discrepancies exist for IRM between both normalization methods. Also, the median  $r$  value is 0.99 for ARM, while it is 0.98 for IRM. Considering these arguments, ARM is here considered as the best normalizer and we use the ratio method for normalization.

### 1.2.5 Discussion

#### 1.2.5.1 $\delta^{18}\text{O}$ stratigraphy and paleomagnetic dating

Marine sediment cores usually have age models based on stratigraphic alignment of the depth-scale  $\delta^{18}\text{O}$  record with an already dated reference  $\delta^{18}\text{O}$  record. We establish a first age-model by matching the planktic  $\delta^{18}\text{O}$  record of core CAS16-24PC with the benthic reference LR04 stack (Fig. 23), which is an average of 57 globally distributed benthic  $\delta^{18}\text{O}$  records (Lisiecki and Raymo, 2005) using a graphic correlation technique with the

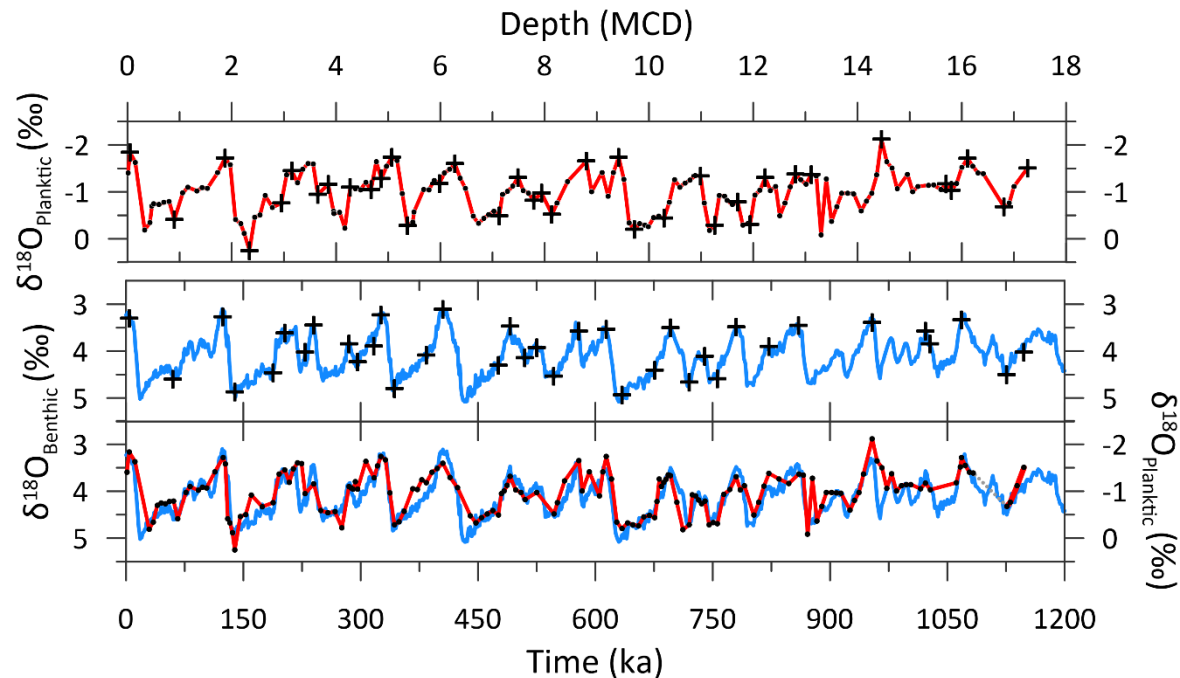


Figure 23 - Planktic foraminiferal  $\delta^{18}\text{O}$  record for core CAS16-24PC (red curve) correlated to the LR04 benthic stack in blue (Lisiecki and Raymo, 2005). Black crosses represents the tie points determined using the AnalySeries software (Paillard et al., 1996).

Analyseries software (Paillard et al., 1996). This correlation assumes a linear sedimentation rate between 2 tie-points. A total of 37 tie points (Table 1) were used and have an excellent

Table 1 - List of  $\delta^{18}\text{O}$  tie points with isotopic composition of the sample and the corresponding LR04 point with age, including the error used in the age-depth model.

Composite depth (m)	$\delta^{18}\text{O}_{\text{planktic}} (\text{\textperthousand})$	Age (ka)	LR04 $\delta^{18}\text{O}_{\text{benthic}} (\text{\textperthousand})$	Error ( $\pm \text{ ka}$ )
<b>0.05</b>	-1.84	4	3.3	3.75
<b>0.9</b>	-0.41	60	4.60	2.5
<b>1.87</b>	-1.72	124	3.27	2.5
<b>2.34</b>	0.25	139	4.87	5
<b>2.95</b>	-0.76	188	4.46	7
<b>3.15</b>	-1.45	203	3.61	4
<b>3.65</b>	-0.95	229	4.02	5
<b>3.85</b>	-1.16	240	3.44	5
<b>4.27</b>	-1.1	285	3.84	4.5
<b>4.67</b>	-1.05	296	4.23	5
<b>4.87</b>	-1.28	317	3.89	5
<b>5.07</b>	-1.74	326	3.23	3
<b>5.37</b>	-0.28	343	4.8	3.5
<b>5.98</b>	-1.18	384	4.08	3.5
<b>6.28</b>	-1.6	405	3.11	4.5
<b>7.13</b>	-0.49	476	4.3	3.5
<b>7.49</b>	-1.31	491	3.47	4.5
<b>7.79</b>	-0.82	510	4.14	3.5
<b>7.94</b>	-0.98	525	3.92	11
<b>8.14</b>	-0.52	547	4.53	11
<b>8.8</b>	-1.66	579	3.57	7
<b>9.42</b>	-1.74	614	3.53	3.5
<b>9.72</b>	-0.2	634	4.93	3.5
<b>10.29</b>	-0.44	676	4.4	3.5
<b>10.99</b>	-1.34	696	3.5	4
<b>11.26</b>	-0.29	720	4.66	4
<b>11.7</b>	-0.79	740	4.11	2.5
<b>11.94</b>	-0.31	756	4.59	4
<b>12.23</b>	-1.31	780	3.48	4
<b>12.81</b>	-1.38	822	3.9	6.5
<b>13.11</b>	-1.37	860	3.45	6.5
<b>14.46</b>	-2.12	954	3.39	3
<b>15.7</b>	-1.17	1022	3.94	3
<b>16.31</b>	-1.41	1068	3.66	8
<b>16.90</b>	-0.68	1126	4.5	4
<b>17.26</b>	-1.51	1148	4.02	9

correlation ( $r^2 = 0.75$ ). In a second stage, the age-model was refined using paleomagnetic results from core CAS16-24PC (Fig. 20). Inclination and declination variations indicate that core CAS16-24PC covers the Brunhes Chron and the end of the Matuyama Chron, including the Jaramillo Subchron. While the paleomagnetic measurements made on the u-channels were of sufficient quality to identify these reversals, discrete measurements on cubes made it possible to detect the positions of reversals more accurately, especially when sedimentation rates are below 10 cm/kyr (Philippe et al., 2018). Thus, the 3 first polarity transitions were deduced from u-channel and discrete samples. The normal polarity Jaramillo Subchron begins at around  $1069 \pm 12$  ka at 16.32 MCD and ends at around  $1001$  ka  $\pm 10$  ka at 15.38 MCD (Singer, 2014). The Matuyama/Brunhes boundary (MBB), occurred at 773 ka

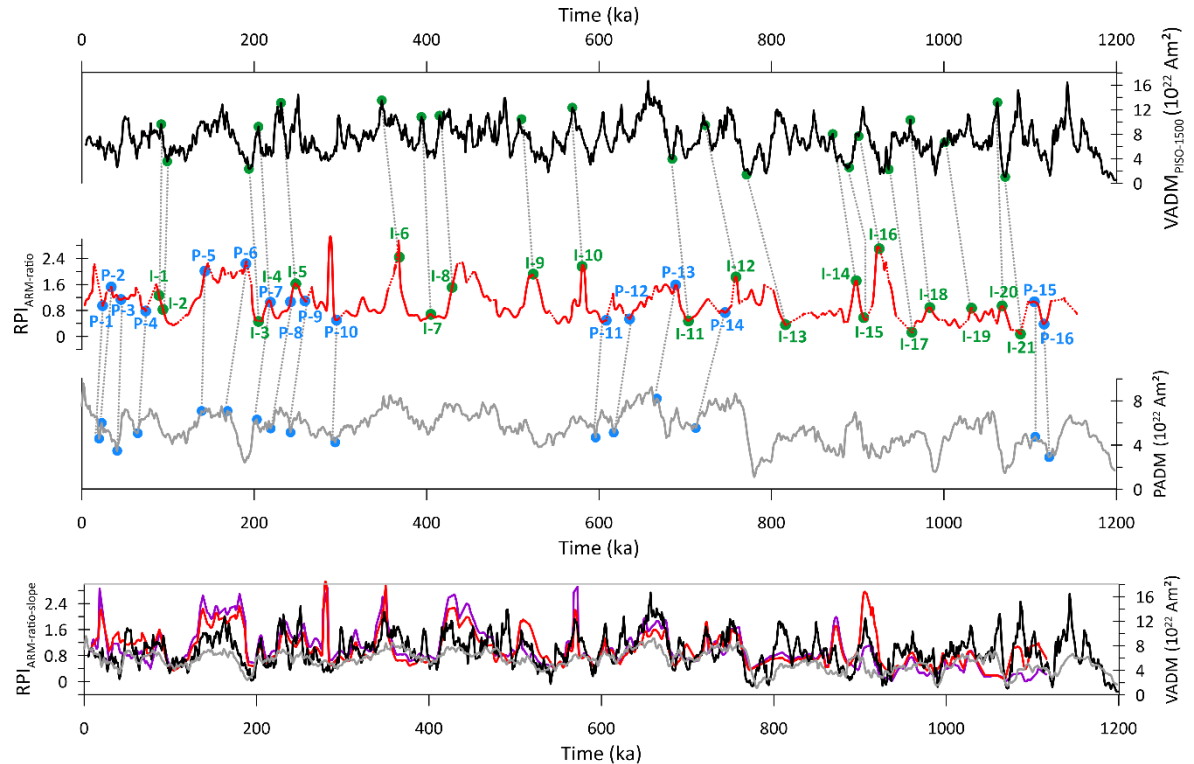


Figure 24 - Top: virtual axial dipole moment (VADM) derived from the PISO-1500 stack (Channell et al., 2009) in black. Upper middle: RPI record for core 24PC ratio-method normalized by ARM in red. Lower middle: paleomagnetic axial dipole moment (PADM2M) model (Ziegler et al., 2011) in grey. Notable tie points are indicated with green dots (I-1 to I-18) and blue dots (P-1 to P-16). Bottom: compilation of PISO-1500, PADM2M and RPI record (colors are the same as above with the violet curve derived from the developed slope method).

(Channell et al., 2010; Singer, 2014, Simon et al., 2019), and is recorded at 12.34 MCD. To increase the reliability of the age-depth model, RPI variations are plotted against the PISO-1500 paleointensity stack (Channell et al., 2009). The match between the two datasets (Fig. 24) is reasonable for the Brunhes Chron ( $r^2 = 0.45$ ), while for the Matuyama Chron part it is

Table 2 - List of RPI tie points determined against PISO-1500 (I1-18) and against PADM2M (P1-16), including the error used in the age-depth model.

Composite depth (m)	RPI	Age (ka)	Models ( $10^{22}$ Am $^2$ )	Error ( $\pm$ ka)
<b>0.36 P-1</b>	0.94	20	4.59	2
<b>0.51 P-2</b>	1.52	23	6.01	2
<b>0.68 P-3</b>	1.13	41	3.48	2
<b>1.11 P-4</b>	0.78	65	5.07	2
<b>1.34 I-1</b>	1.26	92	9.62	1
<b>1.41 I-2</b>	0.83	99	3.59	1
<b>2.14 P-5</b>	2.01	139	7.10	2
<b>2.85 P-6</b>	2.23	169	7.10	2
<b>3.07 I-3</b>	0.46	194	2.34	2
<b>3.28 P-7</b>	1.05	203	6.32	1
<b>3.28 I-4</b>	1.05	205	9.24	1
<b>3.63 P-8</b>	1.07	219	5.52	2
<b>3.72 I-5</b>	1.62	231	13.11	1
<b>3.88 P-9</b>	1.10	242	5.16	2
<b>4.43 P-10</b>	0.50	294	4.25	1
<b>5.52 I-6</b>	2.45	348	13.51	2
<b>6.07 I-7</b>	0.68	394	10.81	1
<b>6.44 I-8</b>	1.51	415	11.04	2
<b>7.85 I-9</b>	1.92	510	10.46	2
<b>8.70 I-10</b>	2.16	569	12.34	1
<b>9.12 P-11</b>	0.50	596	4.69	1
<b>9.53 P-12</b>	0.53	617	5.14	2
<b>10.33 P-13</b>	1.59	667	8.21	1
<b>10.55 I-11</b>	0.48	685	3.97	1
<b>11.19 P-14</b>	0.73	712	5.55	1
<b>11.38 I-12</b>	1.83	723	9.48	1
<b>12.24 I-13</b>	0.36	771	1.41	2
<b>13.47 I-14</b>	1.72	871	8.06	1
<b>13.60 I-15</b>	0.58	890	2.62	2
<b>13.87 I-16</b>	2.70	901	7.68	1
<b>14.44 I-17</b>	0.13	936	2.30	2
<b>14.75 I-18</b>	0.88	961	10.32	1

<b>15.48 I-19</b>	0.87	1001	11.27	2
<b>16.01 I-20</b>	0.94	1062	13.21	1
<b>16.33 I-21</b>	0.08	1071	1.05	2
<b>16.57 P-15</b>	1.07	1106	4.76	1
<b>16.74 P-16</b>	0.38	1122	2.92	2

weaker ( $r^2 = 0.33$ ). To complement these results, we also match our RPI curve against the PADM2M model (Ziegler et al., 2011). Within the Brunhes Chron, two intervals are more difficult to match. The first is between 100 and 150 ka, while the second interval is between 300 and 500 ka. However, 37 tie points (Fig. 24, green and blue dots) were derived from these two correlations and are listed in Table 2 and error estimations are described in ANNEXE 1, Fig. 45. The discrepancies between the reference curves and Lesser Antilles RPI before the MBB are likely to be the result of the lower quality data, as illustrated by the demagnetization curves (Fig. 21-D) and high MAD values (Fig. 20). From 900 to 1151 ka, the lack of continuous data points does not permit use of the RPI record as a sole chronostratigraphic marker.

#### 1.2.5.2 Final age model and paleomagnetic record

Quaternary sediments can contain numerous time constraints such as geomagnetic polarity reversals, geomagnetic excursions,  $\delta^{18}\text{O}$  and RPI stratigraphy (Richards and Andersen, 2013). The combination of RPI and  $\delta^{18}\text{O}$  stratigraphy has been used in several studies to establish a stronger age model than with RPI or  $\delta^{18}\text{O}$  alone (e.g., Channell et al., 1997, 2009, 2012; Stoner and St-Onge, 2007; Xuan et al., 2016). Our age model (Fig. 25) was generated using 3 reversals, 37 tie points derived from the reconstructed RPI record and 37 tie points derived from the  $\delta^{18}\text{O}$  stratigraphy. This age model has an age of  $\sim 1.15$  Ma at the base of the core (17.33 MCD). The mean sedimentation rate varies around 1.67 cm/kyr, ranging from 1.70 cm/kyr during the Brunhes Chron and 1.58 cm/kyr during the Matuyama Chron. This change between the Matuyama and Brunhes Chrons might reflect change in the astronomical control of paleoclimate across the mid-Pleistocene transition (Schmieder et al., 2000). The sedimentation rate in this age-depth model is almost linear, but it is not well-constrained before the MBB because of the presence of thicker RDL ( $> 5$  cm), and fewer

$\delta^{18}\text{O}$  and paleomagnetic tie points. Nonetheless, the low sedimentation rates are similar to published data from the accretionary prism sediments with Brunhes Chron sedimentation rates between 1 and 3 cm/kyr (Damuth, 1977; Reid et al., 1996) and they are slightly lower than the sedimentation rate reported at 3 km landward of the Barbados subduction deformation front DSDP Site 541 (Wright, 1984), which is about 5 cm/kyr for the Quaternary

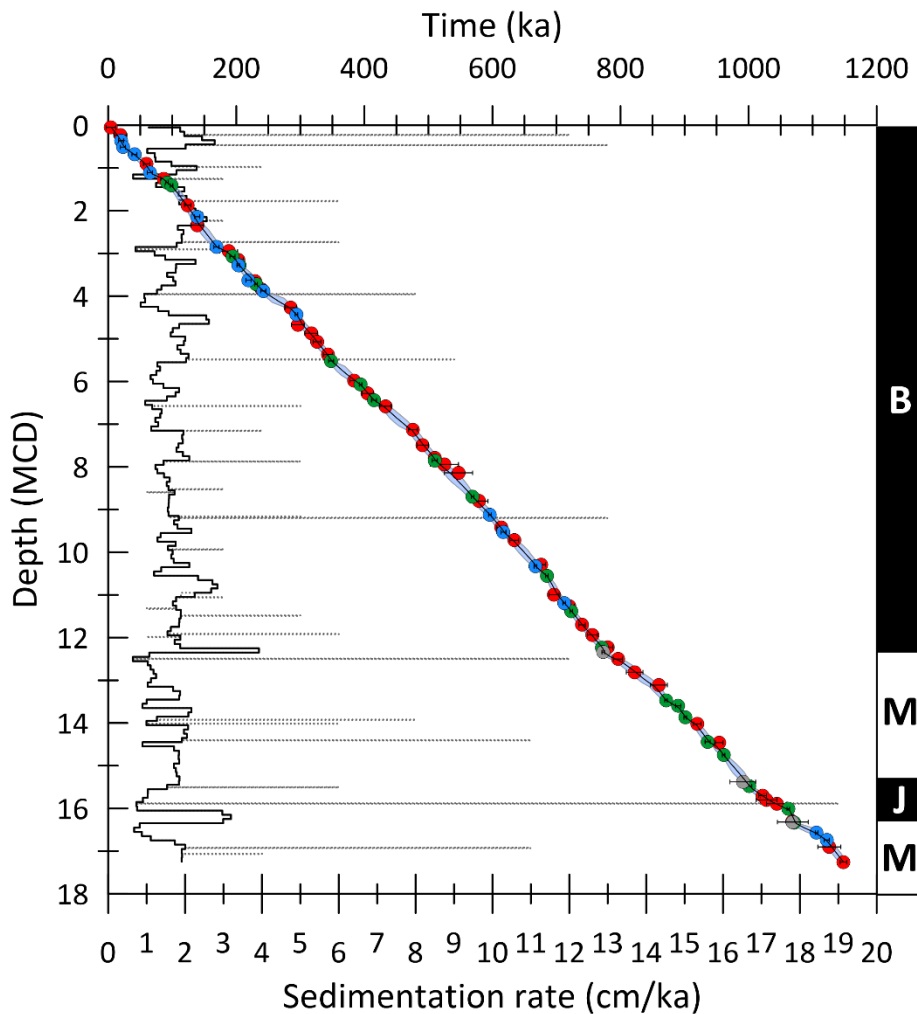


Figure 25 - Age-depth model developed using the R package Bacon 2.2 (Blaauw and Christen, 2011) with linear interpolation using 3 paleomagnetic reversals (grey dots) and 37 tie points (blue and green dots) from RPI (see Fig. 24) and 37 tie points (red dots) from  $\delta^{18}\text{O}$  stratigraphy (see Fig. 23). Age-errors used for each tie point correspond to half the distance samples (see Fig. 46 in ANNEXE 1). Sedimentation rates are derived from the age-depth model, including RDL (grey dotted lines). B = Brunhes Chron, M = Matuyama Chron, J = Jaramillo Subchron.

epoch. This age-depth model is validated by comparison of our data with the stacks mentioned above (Fig. 26).

Long sedimentary paleomagnetic records have been published in the equatorial to sub-equatorial Indian Ocean (e.g. Meynadier et al., 1994; Oda et al., 2000) and Pacific Ocean (e.g. Shackleton et al., 1990; Yamazaki and Oda, 2005), and in the North and South Atlantic Ocean (e.g. Haag, 2000; Stoner et al., 2003; Hofmann and Fabian, 2007). We establish here a new chronostratigraphy for the sub-equatorial Atlantic Ocean based on reconstruction of RPI, geomagnetic polarity reversals and  $\delta^{18}\text{O}$  stratigraphy for the last  $\sim 1.15$  Ma (Fig. 25). The low sedimentation rates prevent for detailed study of the MBB or the Jaramillo Subchron,

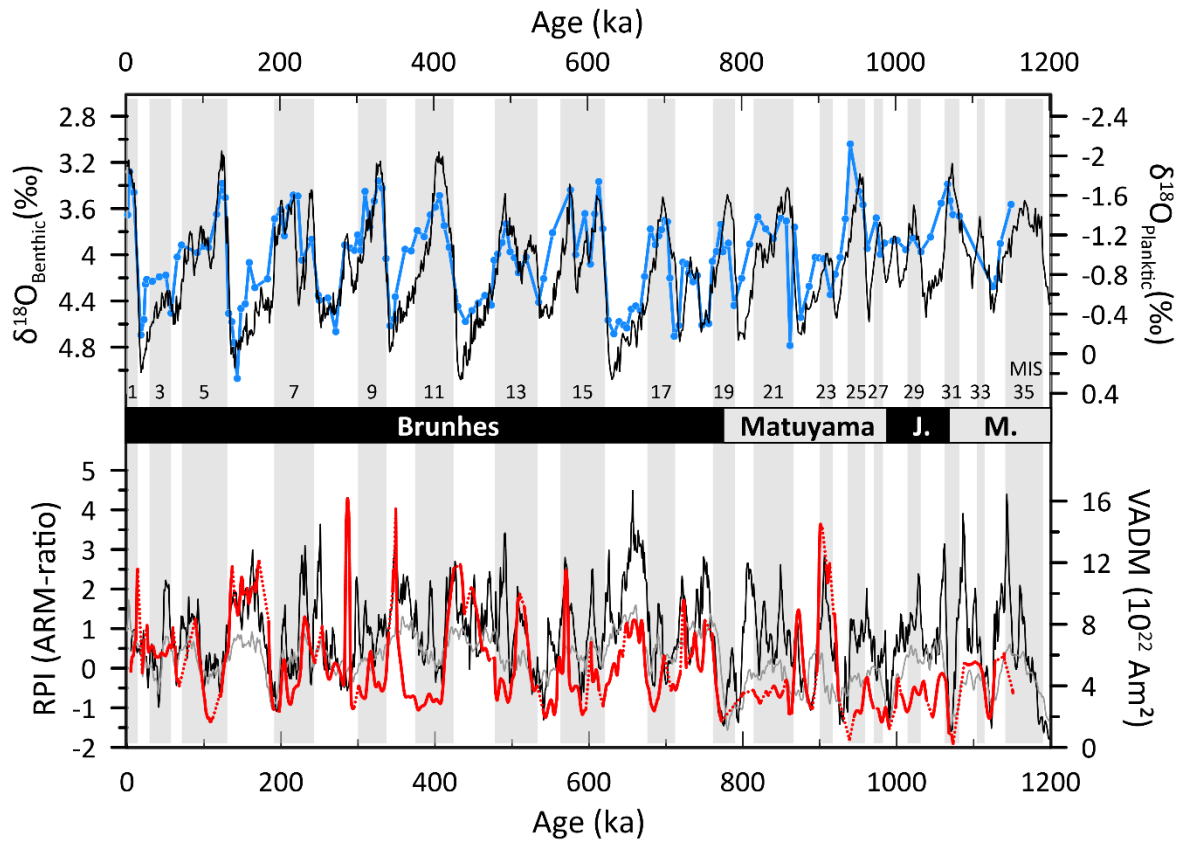


Figure 26 - Planktic foraminiferal  $\delta^{18}\text{O}$  record for core CAS16-24PC (blue curve) and RPI record (red curve) using the age-depth model developed in this study (Fig. 25) compared with the LR04 benthic (upper black curve), PISO-1500 (lower black curve) and PADM2M (grey curve) stacks. Odd-numbered MIS are highlighted with grey bands. B = Brunhes Chron, M = Matuyama Chron, J = Jaramillo Subchron.

but the composite record provides the first late Quaternary magnetostratigraphy (Fig. 26, red curve, and Fig. 46 in ANNEXE 1) in this area and complements younger (Frank et al., 2016) and older (Wilson, 1984; Hounslow et al., 1990) records.

Our results make a new contribution to the global coverage of paleomagnetic data by adding a detailed and almost continuous late Quaternary paleomagnetic record from the Lesser Antilles subduction zone. The chronostratigraphy established here will be useful to correlate and date numerous cores from the CASEIS campaign from this area (Seibert et al., 2020), as well as to date the RDL triggered by earthquakes (e.g. seismo-turbidites, Heezen and Ewing, 1952) and tsunamis (e.g. turbidite-homogenite complexes, San Pedro et al., 2017) in these cores.

#### 1.2.5.3 Age-depth model limitations

The combination of strong chronostratigraphic markers based on two magnetic reversals and indirect dating methods based on  $\delta^{18}\text{O}$  and RPI correlation enable the construction of an age model for core CAS16-24PC. However, in spite of the quality of the chronology proposed, our study has three limitations. First, we did not use any absolute dating methods (such as radiometric or luminescence dating). Second, reference records used in our study already have their own limitations and uncertainties. For the benthic LR04 stack, the uncertainties are about 6 ka from 3 to 1 Ma and 4 ka for the last Ma (Lisiecki and Raymo, 2005). The PISO-1500 stack is comparable to LR04 (Channell et al., 2009), while the PADM2M age model has an estimated uncertainty of 5-10 ka (Ziegler et al., 2011). Third, low sedimentation rate can limit the resolution of the record. However, the mean sedimentation rate in core CAS16-24PC is 1.7 cm/kyr what is similar to cores MD97-2140 and MD97-2143 used in the construction of the PISO-1500 stack (Channel et al. 2009). Considering these three limitations, the uncertainty of the reconstructed RPI is estimated at 10 ka on continuous measurements. Some periods of time were not recorded (for example in core breaks or between the sections) and some tie-points were found at the limit of these hiatuses and imply a greater uncertainty.

### **1.2.6 Conclusion**

Magnetic, physical and chemical properties of the sediments enable identification of rapidly deposited layers and makes it able to build an event-free 1.51 Ma composite record for core CAS16-24PC. This sediment acquired a natural remanent magnetization characterized by a strong, well-defined, stable single component magnetization carried by fine-grained magnetite and titanomagnetite. These results allow for reconstructing a reliable relative paleointensity record for the last 900 ka, including the Brunhes/Matuyama boundary. This geomagnetic reversal is also recorded by inclination and declination data from u-channel and discrete samples, which also record the limits of the Jaramillo Subchron.

The  $\delta^{18}\text{O}$  stratigraphy combined with the reconstructed relative paleointensity and 3 reversal events recorded in core CAS16-24PC allow establishment of an age-depth model for the last  $\sim$ 1.15 Ma. This age model will be used to investigate earthquakes and tsunami recurrence in Lesser Antilles forearc and accretionary wedge sediments. Finally, even though the reference core was selected to avoid the recording of rapidly deposited layers, we have established a rapid and non-destructive method to identify thin turbidites and tephra layers based on the combination of several magnetic, physical and geochemical properties.

### **Acknowledgments**

We thank the captain, officers and crew of the R/V Pourquoi Pas?, and the scientific participants in the CASEIS Expedition for the quality of the acquired shipboard data. This work was supported by grants from the Natural Sciences and Engineering Research Council of Canada (NSERC) and the French National Research Agency (ANR-17-CE03-0006; DS01 – CARQUAKES). We also thank Quentin Beauvais, Hervé Guyard, Lola Johannes and Marie-Pier St-Onge for their help on board the ship and/or in the laboratory. We thank MNHN for CASEIS cores storage in the marine collection. A. Bieber acknowledges scholarships from the Institut des sciences de la mer de Rimouski (ISMER) and Institut de

physique du globe de Paris (IPGP). Finally, we thank Andrew Roberts and an anonymous reviewer for their constructive comments that helped improving the manuscript.

## References

- Banerjee, S.K., King, J., Marvin, J., 1981. A rapid method for magnetic granulometry with applications to environmental studies. *Geophys. Res. Lett.* 8, 333–336. <https://doi.org/10.1029/GL008i004p00333>
- Blaauw, M., Christen, J.A., 2011. Flexible paleoclimate age-depth models using an autoregressive gamma process. *Bayesian Analysis* 6, 457–474. <https://doi.org/10.1214/11-BA618>
- Bouma, A.H., 1964. Turbidites, in: *Developments in Sedimentology*. Elsevier, pp. 247–256. [https://doi.org/10.1016/S0070-4571\(08\)70967-1](https://doi.org/10.1016/S0070-4571(08)70967-1)
- Bouysse, P., Westercamp, D., 1990. Subduction of Atlantic aseismic ridges and Late Cenozoic evolution of the Lesser Antilles island arc. *Tectonophysics* 175, 349–355, 357–380.
- Brachfeld, S.A., Banerjee, S.K., 2000. A new high-resolution geomagnetic relative paleointensity record for the North American Holocene: A comparison of sedimentary and absolute intensity data. *Journal of Geophysical Research: Solid Earth* 105, 821–834. <https://doi.org/10.1029/1999JB900365>
- Briden, J.C., Rex, D.C., Faller, A.M., Tomblin, J.F., 1979. K-Ar Geochronology and Palaeomagnetism of Volcanic Rocks in the Lesser Antilles Island Arc. *Philosophical Transactions of the Royal Society A: Mathematical, Physical and Engineering Sciences* 291, 485–528. <https://doi.org/10.1098/rsta.1979.0040>

- Carlut, J., Quidelleur, X., 2000. Absolute paleointensities recorded during the Brunhes chron at La Guadeloupe Island. *Physics of the Earth and Planetary Interiors* 120, 255–269.
- Cassidy, M., Watt, S.F.L., Palmer, M.R., Trofimovs, J., Symons, W., MacLachlan, S.E., Stinton, A.J., 2014. Construction of volcanic records from marine sediment cores: A review and case study (Montserrat, West Indies). *Earth-Science Reviews* 138, 137–155. <https://doi.org/10.1016/j.earscirev.2014.08.008>
- Channell, J.E.T., 2002. Geomagnetic excursions and paleointensities in the Matuyama Chron at Ocean Drilling Program Sites 983 and 984 (Iceland Basin). *Journal of Geophysical Research* 107. <https://doi.org/10.1029/2001JB000491>
- Channell, J.E.T., 1999. Geomagnetic paleointensity and directional secular variation at Ocean Drilling Program (ODP) Site 984 (Bjorn Drift) since 500 ka: Comparisons with ODP Site 983 (Gardar Drift). *Journal of Geophysical Research: Solid Earth* 104, 22937–22951. <https://doi.org/10.1029/1999JB900223>
- Channell, J.E.T., Hodell, D.A., Curtis, J.H., 2012. ODP Site 1063 (Bermuda Rise) revisited: Oxygen isotopes, excursions and paleointensity in the Brunhes Chron: ODP SITE 1063 REVISITED. *Geochemistry, Geophysics, Geosystems* 13. <https://doi.org/10.1029/2011GC003897>
- Channell, J.E.T., Hodell, D.A., Lehman, B., 1997. Relative geomagnetic paleointensity and  $\delta^{18}\text{O}$  at ODP Site 983 (Gardar Drift, North Atlantic) since 350 ka. *Earth and Planetary Science Letters* 153, 103–118. [https://doi.org/10.1016/S0012-821X\(97\)00164-7](https://doi.org/10.1016/S0012-821X(97)00164-7)
- Channell, J.E.T., Hodell, D.A., Singer, B.S., Xuan, C., 2010. Reconciling astrochronological and  $^{40}\text{Ar}/^{39}\text{Ar}$  ages for the Matuyama-Brunhes boundary and late Matuyama Chron: MATUYAMA-BRUNHES REVERSAL AGES. *Geochemistry, Geophysics, Geosystems* 11. <https://doi.org/10.1029/2010GC003203>

Channell, J.E.T., Singer, B.S., Jicha, B.R., 2020. Timing of Quaternary geomagnetic reversals and excursions in volcanic and sedimentary archives. *Quaternary Science Reviews* 228, 106114. <https://doi.org/10.1016/j.quascirev.2019.106114>

Channell, J.E.T., Wright, J.D., Mazaud, A., Stoner, J.S., 2014. Age through tandem correlation of Quaternary relative paleointensity (RPI) and oxygen isotope data at IODP Site U1306 (Eirik Drift, SW Greenland). *Quaternary Science Reviews* 88, 135–146. <https://doi.org/10.1016/j.quascirev.2014.01.022>

Channell, J.E.T., Xuan, C., Hodell, D.A., 2009. Stacking paleointensity and oxygen isotope data for the last 1.5 Myr (PISO-1500). *Earth and Planetary Science Letters* 283, 14–23. <https://doi.org/10.1016/j.epsl.2009.03.012>

Channell, J.E.T., Xuan, C., Hodell, D.A., Crowhurst, S.J., Larter, R.D., 2019. Relative paleointensity (RPI) and age control in Quaternary sediment drifts off the Antarctic Peninsula. *Quaternary Science Reviews* 211, 17–33. <https://doi.org/10.1016/j.quascirev.2019.03.006>

Damuth, J.E., 1977. Late Quaternary sedimentation in the western equatorial Atlantic. *Geological Society of America Bulletin* 88, 695. [https://doi.org/10.1130/0016-7606\(1977\)88<695:LQSITW>2.0.CO;2](https://doi.org/10.1130/0016-7606(1977)88<695:LQSITW>2.0.CO;2)

Davies, J.H., 1999. The role of hydraulic fractures and intermediate-depth earthquakes in subduction-zone magmatism. *Nature* 398, 142–145. <https://doi.org/10.1038/18202>

Day, R., Fuller, M., Schmidt, V.A., 1977. Hysteresis properties of titanomagnetites: Grain-size and compositional dependence. *Physics of the Earth and Planetary Interiors* 13, 260–267. [https://doi.org/10.1016/0031-9201\(77\)90108-X](https://doi.org/10.1016/0031-9201(77)90108-X)

DeMets, C., Jansma, P.E., Mattioli, G.S., Dixon, T.H., Farina, F., Bilham, R., Calais, E., Mann, P., 2000. GPS geodetic constraints on Caribbean-North America Plate Motion. *Geophysical Research Letters* 27, 437–440. <https://doi.org/10.1029/1999GL005436>

- Deschamps, C.-E., St-Onge, G., Montero-Serrano, J.-C., Polyak, L., 2018. Chronostratigraphy and spatial distribution of magnetic sediments in the Chukchi and Beaufort seas since the last deglaciation. *Boreas* 47, 544–564. <https://doi.org/10.1111/bor.12296>
- Deville, E., Masclé, A., Callec, Y., Huyghe, P., Lallement, S., Lerat, O., Mathieu, X., Padron de Carillo, C., Patriat, M., Pichot, T., Loubrieux, B., Granjeon, D., 2015. Tectonics and sedimentation interactions in the east Caribbean subduction zone: An overview from the Orinoco delta and the Barbados accretionary prism. *Marine and Petroleum Geology* 64, 76–103. <https://doi.org/10.1016/j.marpetgeo.2014.12.015>
- Dunlop, D.J., Özdemir, Ö., 2007. Magnetizations in Rocks and Minerals, in: Treatise on Geophysics. Elsevier, pp. 277–336. <https://doi.org/10.1016/B978-044452748-6.00093-6>
- Feuillet, N., 2016. CASEIS cruise, RV Pourquoi pas ? <https://doi.org/10.17600/16001800>
- Forster, Th., Evans, M.E., Heller, F., 1994. The frequency dependence of low field susceptibility in loess sediments. *Geophysical Journal International* 118, 636–642. <https://doi.org/10.1111/j.1365-246X.1994.tb03990.x>
- Fortin, D., Francus, P., Gebhardt, A.C., Hahn, A., Kliem, P., Lisé-Pronovost, A., Roychowdhury, R., Labrie, J., St-Onge, G., 2013. Destructive and non-destructive density determination: method comparison and evaluation from the Laguna Potrok Aike sedimentary record. *Quaternary Science Reviews* 71, 147–153. <https://doi.org/10.1016/j.quascirev.2012.08.024>
- Frank, U., Nowaczyk, N.R., Frederichs, T., Korte, M., 2016. Paleo- and rock magnetic investigations on Late Quaternary sediments from low latitudes I: Geomagnetic paleosecular variation and relative paleointensity records from the Tobago Basin, Southeast Caribbean. *Geophysical Journal International* ggw481. <https://doi.org/10.1093/gji/ggw481>

Genevey, A., Gallet, Y., Boudon, G., 2002. Secular variation study from non-welded pyroclastic deposits from Montagne Pelée volcano, Martinique (West Indies). *Earth and Planetary Science Letters* 201, 369–382. [https://doi.org/10.1016/S0012-821X\(02\)00713-6](https://doi.org/10.1016/S0012-821X(02)00713-6)

Gilder, S.A., LeGoff, M., 2005. Pressure dependence on the magnetic properties of titanomagnetite using the reversible susceptibility method, in: *Advances in High-Pressure Technology for Geophysical Applications*. Elsevier, pp. 315–335. <https://doi.org/10.1016/B978-044451979-5.50017-X>

Haag, M., 2000. Reliability of relative palaeointensities of a sediment core with climatically-triggered strong magnetisation changes. *Earth and Planetary Science Letters* 180, 49–59. [https://doi.org/10.1016/S0012-821X\(00\)00145-X](https://doi.org/10.1016/S0012-821X(00)00145-X)

Hambach, U., Rolf, C., Schnepp, E., 2008. Magnetic dating of Quaternary sediments, volcanites and archaeological materials: an overview. <https://doi.org/10.3285/eg.57.1-2.2>

Heezen, B.C., Ewing, W.M., 1952. Turbidity currents and submarine slumps, and the 1929 Grand Banks [Newfoundland] earthquake. *American Journal of Science* 250, 849–873. <https://doi.org/10.2475/ajs.250.12.849>

Hofmann, D.I., Fabian, K., 2007. Rock magnetic properties and relative paleointensity stack for the last 300 ka based on a stratigraphic network from the subtropical and subantarctic South Atlantic. *Earth and Planetary Science Letters* 260, 297–312. <https://doi.org/10.1016/j.epsl.2007.05.042>

Hounslow, M.W., Bootes, P.A., Whyman, G., 1990. 25. Remanent magnetization of sediments undergoing deformation in the Barbados accretionary prism: ODP LEG110. <https://doi.org/10.2973/odp.proc.sr.110.155.1990>

Hrouda, F., 1994. A technique for the measurement of thermal changes of magnetic susceptibility of weakly magnetic rocks by the CS-2 apparatus and KLY-2

Kappabridge. Geophysical Journal International 118, 604–612.  
<https://doi.org/10.1111/j.1365-246X.1994.tb03987.x>

Kent, D.V., Spariosu, D.J., 1983. High resolution magnetostratigraphy of Caribbean Plio-Pleistocene deep-sea sediments. Palaeogeography, Palaeoclimatology, Palaeoecology 42, 47–64. [https://doi.org/10.1016/0031-0182\(83\)90038-X](https://doi.org/10.1016/0031-0182(83)90038-X)

King, J., Banerjee, S.K., Marvin, J., Özdemir, Ö., 1982. A comparison of different magnetic methods for determining the relative grain size of magnetite in natural materials: Some results from lake sediments. Earth and Planetary Science Letters 59, 404–419. [https://doi.org/10.1016/0012-821X\(82\)90142-X](https://doi.org/10.1016/0012-821X(82)90142-X)

Korte, M., Mandea, M., 2019. Geomagnetism: From Alexander von Humboldt to Current Challenges. Geochemistry, Geophysics, Geosystems 20, 3801–3820. <https://doi.org/10.1029/2019GC008324>

Le Friant, A., Lock, E.J., Hart, M.B., Boudon, G., Sparks, R.S.J., Leng, M.J., Smart, C.W., Komorowski, J.C., Deplus, C., Fisher, J.K., 2008. Late Pleistocene tephrochronology of marine sediments adjacent to Montserrat, Lesser Antilles volcanic arc. Journal of the Geological Society 165, 279–289. <https://doi.org/10.1144/0016-76492007-019>

Leclerc, F., Feuillet, N., Deplus, C., 2016. Interactions between active faulting, volcanism, and sedimentary processes at an island arc: Insights from Les Saintes channel, Lesser Antilles arc: FAULTING, VOLCANISM, AND TURBIDITY SYSTEMS. Geochemistry, Geophysics, Geosystems 17, 2781–2802. <https://doi.org/10.1002/2016GC006337>

Levi, S., Banerjee, S.K., 1976. On the possibility of obtaining relative paleointensities from lake sediments. Earth and Planetary Science Letters 29, 219–226. [https://doi.org/10.1016/0012-821X\(76\)90042-X](https://doi.org/10.1016/0012-821X(76)90042-X)

Lisiecki, L.E., Raymo, M.E., 2005. A Pliocene-Pleistocene stack of 57 globally distributed benthic  $\delta^{18}\text{O}$  records: PLIOCENE-PLEISTOCENE BENTHIC STACK. *Paleoceanography* 20. <https://doi.org/10.1029/2004PA001071>

Liu, Jianxing, Liu, Q., Zhang, X., Liu, Jian, Wu, Z., Mei, X., Shi, X., Zhao, Q., 2016. Magnetostratigraphy of a long Quaternary sediment core in the South Yellow Sea. *Quaternary Science Reviews* 144, 1–15. <https://doi.org/10.1016/j.quascirev.2016.05.025>

Lowrie, W., 2007. Magnetostratigraphy, in: Gubbins, D., Herrero-Bervera, E. (Eds.), *Encyclopedia of Geomagnetism and Paleomagnetism*. Springer Netherlands, Dordrecht, pp. 664–670. [https://doi.org/10.1007/978-1-4020-4423-6\\_206](https://doi.org/10.1007/978-1-4020-4423-6_206)

Macdonald, R., Hawkesworth, C.J., Heath, E., 2000. The Lesser Antilles volcanic chain: a study in arc magmatism. *Earth-Science Reviews* 49, 1–76.

Meynadier, L., Valet, J.-P., Bassinot, F.C., Shackleton, N.J., Guyodo, Y., 1994. Asymmetrical saw-tooth pattern of the geomagnetic field intensity from equatorial sediments in the Pacific and Indian Oceans. *Earth and Planetary Science Letters* 126, 109–127. [https://doi.org/10.1016/0012-821X\(94\)90245-3](https://doi.org/10.1016/0012-821X(94)90245-3)

Oda, H., Shibuya, H., Hsu, V., 2000. Palaeomagnetic records of the Brunhes/Matuyama polarity transition from ODP Leg 124 (Celebes and Sulu seas). *Geophysical Journal International* 142, 319–338. <https://doi.org/10.1046/j.1365-246x.2000.00130.x>

Paillard, D., Labeyrie, L., Yiou, P., 1996. Macintosh Program performs time-series analysis. *Eos, Transactions American Geophysical Union* 77, 379–379. <https://doi.org/10.1029/96EO00259>

Philippe, É.G.H., Valet, J., St-Onge, G., Thevarasan, A., 2018. Are Paleomagnetic Records From U-Channels Appropriate for Studies of Reversals and Excursions? *Geochemistry, Geophysics, Geosystems* 19, 4130–4142. <https://doi.org/10.1029/2018GC007803>

- Picard, M., Schneider, J.-L., Boudon, G., 2006. Contrasting sedimentary processes along a convergent margin: the Lesser Antilles arc system. *Geo-Marine Letters* 26, 397–410. <https://doi.org/10.1007/s00367-006-0046-y>
- Reid, R.P., Carey, S.N., Ross, D.R., 1996. Late Quaternary sedimentation in the Lesser Antilles island arc. *Geological Society of America Bulletin* 108, 78–100. [https://doi.org/10.1130/0016-7606\(1996\)108<0078:LQSITL>2.3.CO;2](https://doi.org/10.1130/0016-7606(1996)108<0078:LQSITL>2.3.CO;2)
- Ricci, J., Carlut, J., Valet, J.-P., 2018. Paleosecular variation recorded by Quaternary lava flows from Guadeloupe Island. *Scientific Reports* 8. <https://doi.org/10.1038/s41598-018-28384-z>
- Richards, D.A., Andersen, M.B., 2013. Time Constraints and Tie-Points in the Quaternary Period. *Elements* 9, 45–51. <https://doi.org/10.2113/gselements.9.1.45>
- Roberts, A.P., 2006. High-resolution magnetic analysis of sediment cores: Strengths, limitations and strategies for maximizing the value of long-core magnetic data. *Physics of the Earth and Planetary Interiors* 156, 162–178. <https://doi.org/10.1016/j.pepi.2005.03.021>
- Roberts, A.P., Almeida, T.P., Church, N.S., Harrison, R.J., Heslop, D., Li, Y., Li, J., Muxworthy, A.R., Williams, W., Zhao, X., 2017. Resolving the Origin of Pseudo-Single Domain Magnetic Behavior: Origin of PSD Behavior. *J. Geophys. Res. Solid Earth* 122, 9534–9558. <https://doi.org/10.1002/2017JB014860>
- Roberts, A.P., Tauxe, L., Heslop, D., 2013. Magnetic paleointensity stratigraphy and high-resolution Quaternary geochronology: successes and future challenges. *Quaternary Science Reviews* 61, 1–16. <https://doi.org/10.1016/j.quascirev.2012.10.036>
- Roberts, A.P., Tauxe, L., Heslop, D., Zhao, X., Jiang, Z., 2018. A Critical Appraisal of the “Day” Diagram. *J. Geophys. Res. Solid Earth* 123, 2618–2644. <https://doi.org/10.1002/2017JB015247>

San Pedro, L., Babonneau, N., Gutscher, M.-A., Cattaneo, A., 2017. Origin and chronology of the Augias deposit in the Ionian Sea (Central Mediterranean Sea), based on new regional sedimentological data. *Marine Geology* 384, 199–213. <https://doi.org/10.1016/j.margeo.2016.05.005>

Schmieder, F., von Dobeneck, T., Bleil, U., 2000. The Mid-Pleistocene climate transition as documented in the deep South Atlantic Ocean: initiation, interim state and terminal event. *Earth and Planetary Science Letters* 179, 539–549. [https://doi.org/10.1016/S0012-821X\(00\)00143-6](https://doi.org/10.1016/S0012-821X(00)00143-6)

Seibert, C., Feuillet, N., Ratzov, G., Beck, C., Cattaneo, A., 2020. Seafloor morphology and sediments transfers in the mixed carbonated-siliciclastic environment of the Lesser Antilles forearc along Barbuda and St. Lucia. *Marine Geology* 106242. <https://doi.org/10.1016/j.margeo.2020.106242>

Shackleton, N.J., Berger, A., Peltier, W.R., 1990. An alternative astronomical calibration of the lower Pleistocene timescale based on ODP Site 677. *Transactions of the Royal Society of Edinburgh: Earth Sciences* 81, 251–261. <https://doi.org/10.1017/S0263593300020782>

Simon, Q., Ledru, M.-P., Sawakuchi, A.O., Favier, C., Mineli, T.D., Grohmann, C.H., Guedes, M., Bard, E., Thouveny, N., Garcia, M., Tachikawa, K., Rodríguez-Zorro, P.A., 2020. Chronostratigraphy of a  $1.5 \pm 0.1$  Ma composite sedimentary record from Colônia basin (SE Brazil): Bayesian modeling based on paleomagnetic, authigenic  $^{10}\text{Be}/^{9}\text{Be}$ , radiocarbon and luminescence dating. *Quaternary Geochronology* 58, 101081. <https://doi.org/10.1016/j.quageo.2020.101081>

Simon, Q., Suganuma, Y., Okada, M., Haneda, Y., 2019. High-resolution  $^{10}\text{Be}$  and paleomagnetic recording of the last polarity reversal in the Chiba composite section: Age and dynamics of the Matuyama–Brunhes transition. *Earth and Planetary Science Letters* 519, 92–100. <https://doi.org/10.1016/j.epsl.2019.05.004>

- Singer, B.S., 2014. A Quaternary geomagnetic instability time scale. *Quaternary Geochronology* 21, 29–52. <https://doi.org/10.1016/j.quageo.2013.10.003>
- Snowball, I., Sandgren, P., 2004. Geomagnetic field intensity changes in Sweden between 9000 and 450 cal BP: extending the record of “archaeomagnetic jerks” by means of lake sediments and the pseudo-Thellier technique. *Earth and Planetary Science Letters* 227, 361–376. <https://doi.org/10.1016/j.epsl.2004.09.017>
- Stoner, J.S., Channell, J.E.T., Hodell, D.A., Charles, C.D., 2003. A ~580 kyr paleomagnetic record from the sub-Antarctic South Atlantic (Ocean Drilling Program Site 1089): PALEOMAGNETIC RECORD FROM THE SOUTH ATLANTIC. *Journal of Geophysical Research: Solid Earth* 108. <https://doi.org/10.1029/2001JB001390>
- Stoner, J.S., St-Onge, G., 2007. Chapter Three Magnetic Stratigraphy in Paleoceanography: Reversals, Excursions, Paleointensity, and Secular Variation, in: Developments in Marine Geology. Elsevier, pp. 99–138. [https://doi.org/10.1016/S1572-5480\(07\)01008-1](https://doi.org/10.1016/S1572-5480(07)01008-1)
- St-Onge, G., Mulder, T., Francus, P., Long, B., 2007. Chapter Two Continuous Physical Properties of Cored Marine Sediments, in: Developments in Marine Geology. Elsevier, pp. 63–98. [https://doi.org/10.1016/S1572-5480\(07\)01007-X](https://doi.org/10.1016/S1572-5480(07)01007-X)
- St-Onge, G., Stoner, J.S., Hillaire-Marcel, C., 2003. Holocene paleomagnetic records from the St. Lawrence Estuary, eastern Canada: centennial- to millennial-scale geomagnetic modulation of cosmogenic isotopes. *Earth and Planetary Science Letters* 209, 113–130. [https://doi.org/10.1016/S0012-821X\(03\)00079-7](https://doi.org/10.1016/S0012-821X(03)00079-7)
- Symithe, S., Calais, E., de Chabalier, J.B., Robertson, R., Higgins, M., 2015. Current block motions and strain accumulation on active faults in the Caribbean: CURRENT CARIBBEAN KINEMATICS. *Journal of Geophysical Research: Solid Earth* 120, 3748–3774. <https://doi.org/10.1002/2014JB011779>

Tanty, C., Carlut, J., Valet, J.-P., Germa, A., 2015. Palaeosecular variation recorded by 9 ka to 2.5-Ma-old lavas from Martinique Island: new evidence for the La Palma aborted reversal 617 ka ago. *Geophysical Journal International* 200, 915–932. <https://doi.org/10.1093/gji/ggu423>

Tauxe, L., 1993. Sedimentary records of relative paleointensity of the geomagnetic field: Theory and practice. *Reviews of Geophysics* 31, 319. <https://doi.org/10.1029/93RG01771>

Tauxe, L., Mullender, T.A.T., Pick, T., 1996. Potbellies, wasp-waists, and superparamagnetism in magnetic hysteresis. *Journal of Geophysical Research: Solid Earth* 101, 571–583. <https://doi.org/10.1029/95JB03041>

Tauxe, L., Pick, T., Kok, Y.S., 1995. Relative paleointensity in sediments: A Pseudo-Thellier Approach. *Geophysical Research Letters* 22, 2885–2888. <https://doi.org/10.1029/95GL03166>

Weeks, R., Laj, C., Endignoux, L., Fuller, M., Roberts, A., Manganne, R., Blanchard, E., Goree, W., 1993. Improvements in long-core measurement techniques: applications in palaeomagnetism and palaeoceanography. *Geophysical Journal International* 114, 651–662. <https://doi.org/10.1111/j.1365-246X.1993.tb06994.x>

Westbrook, G.K., Mascle, A., Biju-Duval, B., 1984. Geophysics and the structure of the Lesser Antilles Forearc. *Initial Reports Deep Sea Drilling Program, LXXVIIIA* 23–38.

Wilson, D.S., 1984. Paleomagnetic results from Deep Sea Drilling Project Leg 78A. *Init. Repts DSDP* 78, 583 –591.

Wright, A., 1984. Sediment accumulation rates of the Lesser Antilles intraoceanic island arc, Deep Sea Drilling Project leg 78A. *Init. Repts DSDP* 78, 583 –591.

Xuan, C., Channell, J.E.T., 2009. UPmag: MATLAB software for viewing and processing u channel or other pass-through paleomagnetic data: TECHNICAL BRIEF. *Geochemistry, Geophysics, Geosystems* 10. <https://doi.org/10.1029/2009GC002584>

Xuan, C., Channell, J.E.T., Hodell, D.A., 2016. Quaternary magnetic and oxygen isotope stratigraphy in diatom-rich sediments of the southern Gardar Drift (IODP Site U1304, North Atlantic). *Quaternary Science Reviews* 142, 74–89. <https://doi.org/10.1016/j.quascirev.2016.04.010>

Yamazaki, T., Oda, H., 2005. A geomagnetic paleointensity stack between 0.8 and 3.0 Ma from equatorial Pacific sediment cores: PALEOINTENSITY STACK. *Geochemistry, Geophysics, Geosystems* 6. <https://doi.org/10.1029/2005GC001001>

Ziegler, L.B., Constable, C.G., Johnson, C.L., Tauxe, L., 2011. PADM2M: a penalized maximum likelihood model of the 0-2 Ma palaeomagnetic axial dipole moment: PADM2M revised. *Geophysical Journal International* 184, 1069–1089. <https://doi.org/10.1111/j.1365-246X.2010.04905.x>



## CHAPITRE 2

# ANALYSE PALEOMAGNETIQUE DES COUCHES DEPOSEES RAPIDEMENT AU COURS DES DERNIERS 90 KA DANS LA ZONE DE SUBDUCTION DES PETITES ANTILLES : EXPRESSION D'UN SUPER-CYCLE SISMIQUE

### 2.1 RESUME EN FRANÇAIS DU DEUXIEME ARTICLE

Les Petites Antilles font partie de l'unique marge active de l'Océan Atlantique, mais reste l'une des zones de subduction les moins étudiées par la paléo-séismologie. Bien qu'aucun mégaséisme n'ait été enregistré durant les derniers siècles, deux séismes de magnitude 8-8.5 ont été documentés le 11 janvier 1839 et le 8 février 1843. Ces deux événements majeurs ont entraîné la destruction des villes de Pointe-à-Pitre (île de la Guadeloupe) et Fort-de-France (île de la Martinique). Plus récemment, en 2007, un séisme de magnitude 7,4 dont l'épicentre se situait entre la Dominique et la Guadeloupe, a engendré la destruction de certains bâtiments et certaines routes sur ces îles. Les risques sismiques liés à ce type de séisme ont donc motivé la campagne CASEIS et le prélèvement de plusieurs carottes sédimentaires à piston dans les bassins avant-arc pour obtenir des informations sur la paléo-sismicité régionale. Cette étude offre un nouvel enregistrement paléomagnétique pour les derniers 400 ka (CAS16-12PC) et permet d'identifier des complexes homogénite-turbidites qui sont associés à des mégaséismes dans trois carottes à piston. Les carottes CAS16-04PC et CAS16-14PC ont été prélevées au large de la Guadeloupe, alors que la carotte CAS16-36PC a été prélevée au large d'Anguilla.

Ce deuxième article, intitulé « *Paleomagnetic analysis of rapidly deposited layers over the last 90 ka at the Lesser Antilles subduction zone: expression of earthquake super-cycle* », fut corédigé par moi-même ainsi que mes deux directeurs de recherche Guillaume St-Onge (ISMER-UQAR) et Nathalie Feuille (IPGP), ainsi que huit collaborateurs incluant Chloé Seibert (IPGP), Pierre Morena (IFREMER), Julie Carlut (IPGP), Eva Moreno (LOCEAN/MNHN) Gueorguy Ratzov (IRD), Frauke Klingelhoefer (IFREMER) et Antonio Cattaneo (IFREMER). Ce manuscrit sera soumis à la revue *Earth and Planetary Science*

*Letter* (EPSL). Ma contribution en tant que premier auteur a été de réaliser l'état de l'art, l'analyse en laboratoire d'une grande partie des échantillons, le développement du modèle d'âge et la rédaction de l'article. Guillaume St-Onge a participé à la recherche sur l'état de l'art, supervisé les travaux analytiques, aidé dans l'analyse et l'interprétation des données et la rédaction. Nathalie Feuillet a participé à la recherche sur l'état de l'art, élaboré et dirigé le projet de la mission océanographique qui a permis la collecte des carottes sédimentaire, aidé dans l'analyse des données et la rédaction. Chloé Seibert et Pierre Morena ont tous deux réaliser des analyses en laboratoire, sont les auteurs des différentes datations radiocarbone et ont participé à l'interprétation et la rédaction. Julie Carlut et Eva Moreno m'ont aidé dans la réalisation de prélèvement et d'analyse d'échantillon au sein de l'IPGP, ainsi que dans le suivi de l'analyse des données et de la rédaction. Gueorguy Ratzov, Frauke Klingelhoefer, et Antonio Cattaneo ont participé à la rédaction et l'amélioration du manuscrit. Une partie des résultats a été présentée lors d'une présentation orale à l'*International Sedimentology Congress* (ISC) qui s'est déroulé à Québec (Canada) en 2018, et au format affiche au Congrès des Doctorants (CDD) en 2019 à Paris (France).

## **2.2 PALEOMAGNETIC ANALYSIS OF RAPIDLY DEPOSITED LAYERS OVER THE LAST 90 KA AT THE LESSER ANTILLES SUBDUCTION ZONE: EXPRESSION OF EARTHQUAKE SUPER-CYCLE**

The Lesser Antilles is an active margin in the Atlantic Ocean, but one of the less studied subduction zones in term of paleo-seismicity over the last decades. While no major earthquakes occurred in the last centuries, records of  $M \geq 8$  earthquakes were reported on January 11, 1839, and February 8, 1843. These two major events resulted into the destruction of Pointe-à-Pitre and Fort-de-France in the Guadeloupe and the Martinique islands. More recently a  $M = 7.4$  earthquake occurred between the Dominica and Guadeloupe islands in the subducting slab and promoted the destruction of several buildings and roads. A better understanding of the seismic hazards induced by earthquakes along the subduction zone motivated a submarine paleoseismological study in the Lesser Antilles fore-arc basins. To this goal, we collected 38 up to 29 m-long piston cores during the CASEIS expedition. This study presents new exceptionally long (up to 400 ka) paleomagnetic and sedimentary records from four piston cores that reveal the occurrence of several rapidly deposited layers (RDL) in the fore-arc basins. Those RDL includes homogenite-turbidite complexes that may have been triggered by megathrust earthquakes. To establish the chronology of the RDL, we first construct a composite record for each core by isolating and removing those RDL from hemipelagic background sediments on the basis of physical and magnetic parameters. We then used those composite cores to reconstruct relative paleointensity (RPI) variations and to compare them to both the NAPIS-75 stack and the core CAS16-24PC regional reference record to derive several chronostratigraphic tie-points. By combining these tie-points with radiocarbon ages, we developed four age-depth models to temporally constrain all the RDL. We evidenced that those RDL are emplaced in a cyclic manner. They cluster over  $\sim 18$  ka long active period separated by  $\sim 7$  ka long quiescent period during which almost no RDL are observed. Those RDL may be triggered by earthquakes that cluster to form a  $\sim 25$  ka long seismic super-cycle in the Lesser Antilles subduction.

## 2.2.1 Introduction

Heezen and Ewing (1952) were the first to clearly link turbidite deposits to earthquakes with the 1929 Grand Banks earthquake. After decades of marine paleo-seismological studies, several criteria and methods have been established to assume earthquake as trigger mechanism for turbidite deposits (Goldfinger, 2011; Talling, 2014). Amalgamated turbidites (as defined by Van Daele et al., 2017) were also reported as a paleo-earthquake sediment signature (Nakajima and Kanai, 2000; Noda et al., 2008). In addition to such deposits, Kasten and Cita (1981) described homogenous sediment that would be induced by a tsunami following an earthquake in the Mediterranean Sea. Combined turbidite and homogenite were found in different locations and environments, and they were sometimes linked to earthquakes (e.g. Lacustrine environment: Chapron et al., 1999; Beck, 2009; Kong et al., 2019; marine environment: Beck et al., 2012; McHugh et al., 2020; Seibert et al., submitted). Pacheco and Sykes (1992) demonstrated that the largest earthquakes mostly occur in subduction zones. Since then, many of subduction regions have been studied using turbidity current deposits to investigate paleo-earthquakes. For the past three decades, research have been conclusive in areas such as Cascadia (e.g., Goldfinger et al., 2003, 2007), Equator (e.g., Ratzov et al., 2010), New Zealand (e.g., Pouderoux et al., 2012), Japan (e.g., Ikehara et al., 2016), Chile (e.g., St-Onge et al., 2012) and Sumatra-Andaman (e.g., Patton et al., 2013). In the same manner, we performed a sedimentological study to understand the sedimentary processes resulting from strong earthquakes and to determine the recurrence of such events in the Lesser Antilles. The seismological behavior of this slow tectonic boundary is highly debated. Several studies used continuous record of global navigation satellite system (GNSS) associated with interseismic coupling modelisation to identify a very slow strain accumulation in favor of an uncoupled subduction interface (Symithe et al., 2015; van Rijsingen et al., 2020, 2022 PREPRINT). In opposition, studying coral microatolls of the Lesser Antilles gives crucial information for long-term vertical motion and reveal strain accumulation consistent with a subduction plate interface coupling (Weil-Accardo et al., 2016; Leclerc and Feuillet, 2019; Philibosian et al., 2022 PREPRINT). Two large and strong

earthquakes occurred for years apart in 1839 and 1843 ( $M \geq 8$ , Feuillet et al., 2011, Hough, 2013) but their origin is still debate. Indeed, up to now no megathrust earthquake have been firmly reported in the historical report.

A better understanding of the seismic activity during the Late Quaternary in the eastern Caribbean subduction zone motivated the CASEIS expedition (May 28th to July 4th 2016; Feuillet, 2016) onboard the R/V Pourquoi Pas?. We collected forty-three sediment cores (including thirty-four CALYPSO long piston cores and nine box cores) at depths varying between 1100 and 7000 mbsl (meter below sea level). In this study, we used three piston cores retrieved offshore Guadeloupe Island (CAS16-04PC and CAS16-14PC), and offshore Anguilla Island (CAS16-36PC). A fourth core (CAS16-12PC) sampled in a deep basin of the Barbados accretionary prism off-shore Guadeloupe is used to improve the chronostratigraphic framework. As regional sedimentation rate is slow (Reid et al., 1996; Bieber et al., 2021; Seibert et al., 2022 SUBMITTED), develop a good age-depth model remain challenging. We conducted paleomagnetic analysis of the sediment in order to estimate the age of RDL possibly triggered by seismic event, as it has been successfully used in Japan (Usami et al., 2018; Kanamatsu et al., 2022). Using physical and magnetic parameters, we first establish the main sedimentary facies, which include hemipelagite (HMPL), turbidite (TU) and homogenite-turbidite complexes (HmTu). We then remove the RDL to construct event-free composite records and compared them to both a reference record CAS16-24PC (Bieber et al., 2021) and well known paleomagnetic stack to constrain the chronology of those RDL. More precisely age-depth models were derived from the combination of radiocarbon dating ( $^{14}\text{C}$ ) and relative paleointensity (RPI) records. By analysing the chronology of the 63 distinct RDL (including 22 HmTu), we finally discussed their origin and the occurrence of possible seismic super-cycles along the northern Lesser Antilles over the last 80 ka.

## 2.2.2 Regional setting

The Lesser Antilles subduction zone is located at the extreme east of the Caribbean region (Fig. 27-A) where the Caribbean asthenosphere scavenges the Atlantic oceanic sinking plate (Macdonald et al., 2000) at  $2 \text{ cm.yr}^{-1}$  in a NNE-SSW orientation (DeMets et al., 2000; Symithe et al., 2015). The trench is 8000 mbsl next to an accretionary prism of 300 km (south) to 50 km (north) of width. The insular shelf presents the same south-north dissymmetry and is 250 km to 100-80 km wide (Picard et al., 2006). Two periods of eruptive activity during the Eocene-Oligocene and the late Miocene-early Pliocene to present (Bouysse and Westercamp, 1990) shaped the morphology of the Lesser Antilles arc. It is composed of an active volcanic arc (volcanic caribbees) along which are growing the main active volcanoes (Montagne Pelée, Soufrière, Montserrat) to the west and an old, nowadays inactive, volcanic arc composed of abraded volcanic islands now covered by Plio-Pleistocene carbonate platform to the east (limestone caribbes). The westward migration of the volcanism may have resulted from a change in the dip of the subducting slab promoted by the subduction of the Tiburon and St-Lucia ridges (Briden et al., 1979; Bouysse and Westercamp, 1990). In addition to the megathrust fault zone at the subduction plate interface, the overriding Caribbean plate is cut by numerous active faults that form two different families: arc perpendicular graben in the fore-arc and arc-parallel sinistral en-echelon oblique faults along the arc which result from slip partitioning of the convergence (Feuillet et al., 2001, 2002, 2004, 2011).

A long-term strain accumulation at the megathrust might have been responsible for large and strong earthquakes as those recorded in 1839 and 1843 ( $M \geq 8$ ; Feuillet et al., 2011; Hough, 2013). The oldest large historical earthquake occurred in April 1690 offshore Monserrat (intensity between VIII and IX; Feuillet et al., 2011). In the last decades, the two most recent large earthquakes occurred in 2004 in Les Saintes ( $Mw = 6.3$ ; Zahibo et al. 2005, Feuillet et al. 2011a) and 2007 in Martinique ( $Mw = 7.4$ ; Schlupp et al. 2008).

Beck et al. (2012) were the first to use piston cores (4 to 7 m long) in addition to seismic-reflection survey to study the paleo-seismology offshore Montserrat and Nevis Islands. They reveal the presence of homogenite-turbidite complexes probably associated to historical earthquakes. Seibert et al. (2022; SUBMITTED) and Morena et al. (in prep) produced the first analysis of respectively the middle and the north of Lesser Antilles fore-arc basins paleo-seismology. These studies reveal a seismic recurrence time between 2 and 5 ka and about 1.5 ka respectively. Recurrence of major event seems larger (about 30 ka); however, those studies are limited by their age models developed with radiocarbon dating and biozones. We propose here to complement these two studies with a paleomagnetic analysis to better constrain the age model and link the two geographic locations. We also

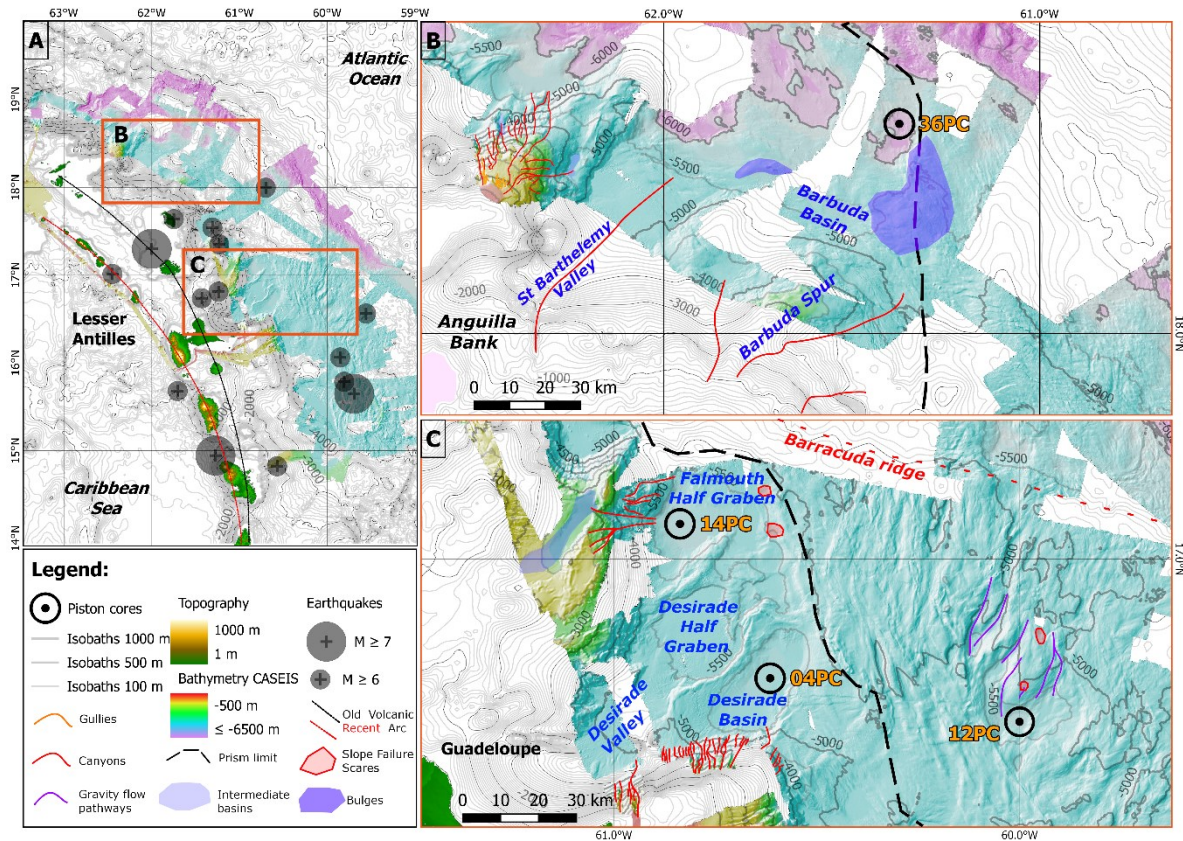


Figure 27 - Bathymetric map of the Lesser Antilles Arc, western Atlantic Ocean (A), north of Barbuda island (B) and east of Antigua and Guadeloupe islands (C), using GEBCO and CASEIS data. Maps also reveal the core location in orange for CAS16-04, -14 and -36PC, and purple for core CAS16-12PC.

develop a new model of super-cycle in the Lesser Antilles based on the identification of clustering events.

### 2.2.3 Material and methods

The four cores CAS16-04PC, CAS16-12PC, CAS16-14PC and CAS16-36PC were collected on board the R/V Pourquoi Pas ?. They were retrieved at respectively 5706, 5827, 5821 and 6100 mbsl with a Calypso piston corer. These cores are stored in the marine collection of the Muséum national d'Histoire naturelle (Paris, France) under the number MNHN-GS-CAS16-##PC (# = core number). Each section has been measured on board with a GEOTEK Multi Sensor Core Logger (MSCL, see below), then split, photographed, described and sampled with u-channels (u-shaped plastic tubes with a section of 2 x 2 cm and up to 150 cm in length) for continuous paleomagnetic analysis (e.g., Stoner and St-Onge, 2007).

#### 2.2.3.1 Physical property analysis

Whole core sections were analyzed on board with a MSCL from ISMER (*Institut des sciences de la mer de Rimouski*) in order to measure bulk density (obtained with gamma ray attenuation), P-wave velocity and volumetric magnetic susceptibility ( $k$ ). Split cores were also analysed on the MSCL in order to obtain images from the GEOTEK Geoscan IV imaging system, magnetic susceptibility with a Bartington MS2E1 point sensor, as well as diffuse spectral reflectance using a Minolta CM-2600d spectrophotometer. All these parameters were analyzed at a 1-cm intervals. Red-green-blue data were converted into the L\*a\*b\* colour space of the International Commission on Illumination (CIE). These parameters range from black (0) to white (100) for L\*, from green (-60) to red (+60) for a\* and from blue (-60) to yellow (+60) for b\*. U-channel samples were scanned at the Institut national de recherche scientifique – Centre eau, terre et environnement (INRS-ETE, Québec, Canada) with a Siemens SOMATOM definition AS+ 128 CT-scanner. The resulting digital X-ray

images were displayed in greyscale and expressed as CT numbers, which primarily reflect bulk density changes (e.g., St-Onge et al., 2007; Fortin et al., 2013).

### 2.2.3.2 Magnetic analysis

#### a) PALEOMAGNETIC ANALYSIS

Continuous paleomagnetic data were acquired at 1-cm intervals on u-channel samples using a 2G Enterprises 755SRM-1.65 cryogenic magnetometer at ISMER. The natural remanent magnetization (NRM) was first measured directly followed by stepwise demagnetization (5 mT increments) with an alternative field (AF) and measured at each 17 steps (0 to 80 mT) until the residual magnetization was less than 15% of the initial magnetization, except for coarser grain sections where demagnetization at the higher steps might have induced a remagnetization. An anhysteretic remanent magnetization (ARM) was secondly induced using a 100 mT peak AF and a 50  $\mu$ m direct current (DC) biasing field. These measurements were made following the same stepwise demagnetization as the NRM. Finally, using a pulse magnetizer, an isothermal remanent magnetization (IRM) and a saturated IRM (SIRM) were induced in a DC field of 0.3 T and 0.95 T and then stepwise demagnetized (10 mT increments) and measured at 9 steps for IRM (0 to 80 mT) and 4 steps for SIRM (0, 10, 30 and 50 mT). The data were processed with the Excel spreadsheet developed by Mazaud (2005) in order to derive the paleomagnetic inclination and declination, as well as the associated median destructive field (MDF) and maximum angular deviation (MAD) values calculated for the characteristic remanent magnetization interval (ChRM) using the steps from 10 to 40 mT. Using the  $IRM_{0 \text{ mT}}$  induced at 300 mT normalized by  $SIRM_{0 \text{ mT}}$  induced at 950 mT, we determined the pseudo S-ratio. Alike the classical S-ratio, it is an indicator of the magnetic coercivity and mineralogy (St-Onge et al. 2003). Closer to 1 ( $IRM \approx SIRM$ ), this parameter indicates the preponderance of low coercivity minerals, whereas lower values ( $IRM < SIRM$ ) express higher coercivity minerals. The  $k_{ARM}$  used as a magnetic grain size indicator is calculated by normalizing the ARM with the biasing field (e.g., Barnerjee et al., 1981; King et al., 1982).

## **b) BULK MAGNETIC PROPERTIES**

In order to obtain hysteresis loops of the different facies 16, 10, 13 and 21, samples from core 04PC, 12PC, 14PC and 36PC (ANNEXE 2: Table 7) were analyzed on a MicroMag 2900 alternating gradient force magnetometer (AGM) from Princeton Measurements Corporation. Magnetic parameters including the coercive force ( $H_c$ ), the remanent coercive force ( $H_{cr}$ ), the saturation magnetisation ( $M_s$ ) and the saturation remanence ( $M_{rs}$ ) were derived from these hysteresis loops in order to identify the magnetic grain size range (single domain, vortex state or multi domain) based on the Day plot from its original publication Day et al. (1977).

### 2.2.3.3 Age model

The chronology of core CAS16-12PC composite record was made by comparing RPI with the regional paleointensity record CAS16-24PC (Bieber et al., 2021) and the North Atlantic paleointensity stack since 75 ka (NAPIS-75, Laj et al., 2000). The chronology of cores CAS16-04PC, CAS16-14PC and CAS16-36PC composite records were established by using previously published radiocarbon ages ( $^{14}C$ ) in Seibert et al. (submitted) and Morena et al., (in prep) combined to several tie points established with the CAS16-12PC RPI and NAPIS-75 RPI stacks. For this study, we used the R software package Bacon 2.2 (Blaauw and Christen, 2011) to produce a best fit age model using Bayesian statistics with normal distributions for each core. The parameters used for cores CAS16-12PC, CAS16-04PC, CAS16-14PC and CAS16-36PC were a 1-cm depth interval ( $d.\text{by} = 1$ ) and a 5 cm/ka mean accumulation rate ( $\text{acc.mean} = 200$ ), except core CAS16-14PC for which a 2 cm/ka mean accumulation rate ( $\text{acc.mean} = 500$ ) was used.

## **2.2.4 Results**

### 2.2.4.1 Morphobathymetry offshore of eastern Lesser Antilles

Core CAS16-12PC was retrieved in a deep basin of the accretionary wedge sediment (Fig. 27-C) completely isolated from continental and shallow carbonaceous inputs ( $\approx 109$  km

from the platform). The basin is at the bottom of fold-and-thrust structures that shaped privileged pathways for density currents. Therefore, sedimentary inputs are mostly composed of pelagic and hemipelagic mud interbedded with few thin RDLs originating from the surrounding accretionary prism slopes or tephra falls. Cores CAS16-04PC and CAS16-14PC were respectively collected offshore Guadeloupe island from the Desirade basin (DB) and Falmouth half-graben (FHG). While both are disconnected from continental inputs, the DB is linked to the carbonate shelve by a 50 km-long canyons and channels system. The DB is near the accretionary prism internal limit and might receive sediments originating from slope destabilization as well as from the carbonate platform. Platform inputs to the FHG are interrupted by an intermediate basin. FHG north and west sides lean against the accretionary prism. Therefore, hemipelagic sedimentation represents the major input interbedded by RDL originating from slope failures and tephra fall deposits. Core CAS16-36PC was retrieved offshore the north-eastern Barbuda Island in a 6500-m deep fore-arc basin bordered by the Barbados accretionary wedge (Fig. 27-B). It is in the continuity of the Barbuda basin, which is mainly fed by canyons from the Barbuda spur and the Anguilla bank through the St-Barthelemy Valley. However, two bulges (probably interconnected) are limiting density currents to travel straight forward to this basin. Readers are referred to Seibert et al. (2020) and Morena (2020) for a detailed description of the morpho-bathymetry of the two locations presented in Fig. 27-B and -C.

#### 2.2.4.2 Sedimentary Facies

Sedimentary facies were described using the three fore-arc basins cores. They are characterized by physical and magnetic parameters reflecting grain size variability and sedimentary structures related to processes, and the presence or absence of traces of bioturbation (Fig. 28). As the color is varying from dark brown to light grey to yellowish and greenish sediments in all type of facies, we do not use the sediment color as a parameter to distinguish each of them but as lithostratigraphic marker. Three main facies were identified and described thereafter: 1) hemipelagic sediment, 2) turbidites and 3) homogenite-turbidite complexes. One last facies called unidentified RDL groups all other instantaneous deposits

that does not fulfill other facies criteria. Extreme, mean and median values are reported in Table 1.

### a) HEMIPELAGIC BACKGROUND SEDIMENT

The three top graphs on Fig. 29 present the physical and magnetic parameters of hemipelagic background sediments for cores CAS16-04PC, -14PC and -36PC. High-definition photographic and CT-scan images do not exhibit any sedimentary structures, but faint traces of bioturbation characteristic of hemipelagic sediments are observed. The physical and magnetic parameters are consistent within each core. CT-number, P-wave velocity and

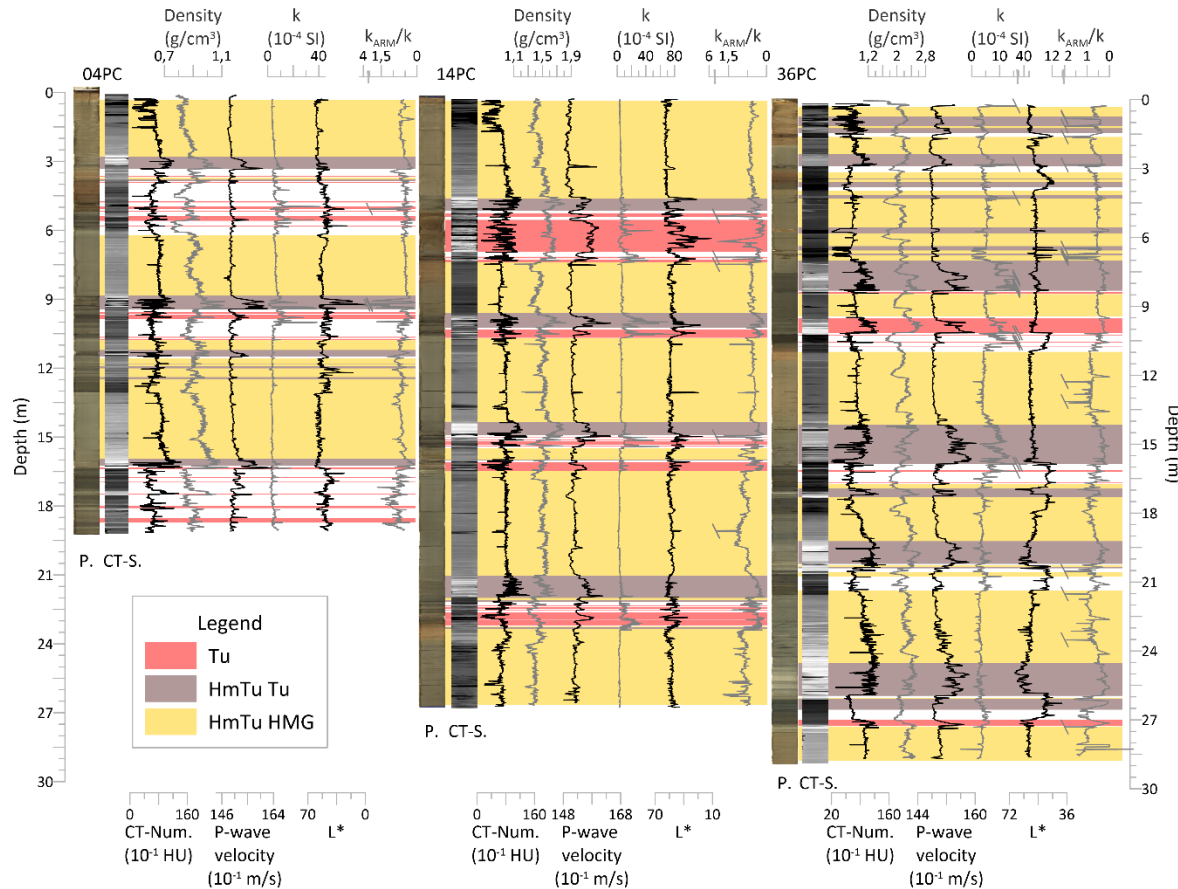


Figure 28 - Physical and magnetic parameter as a function of depth (m) comprising from left to right: high-resolution photography (P.), CT-scan images (CT-S.), CT-number, density, P-wave velocity, magnetic susceptibility, white (100) to black (0) color space ( $L^*$ ) and magnetic susceptibilities ratio ( $k_{ARM}/k$ ). RDL are highlighted as light red (turbidite), light brown and yellow-sand (HmTu complexes).

density, as well as magnetic susceptibility ( $k$ ) and  $k_{ARM}/k$  are stable along the cores and also between the cores (Fig. 28 and 29; Table 3).  $L^*$  values exhibit varying values between different hemipelagic sections within a core and between each core and thus do not express a specific trend associated to such deposit, however, this parameter generally drops or rises between facies. This background hemipelagic sedimentation is interbedded by RDL (such as turbidites and homogenite-turbidite complexes) and represent 27.1% of the sediment in core CAS16-04PC and only 4.4% and 10.4% in core CAS16-14PC and core CAS16-36PC respectively. Fig. 30-A presents a King plot (King et al., 1982) with empirical lines established using synthetic magnetite of known size and are used as an indicator of magnetic

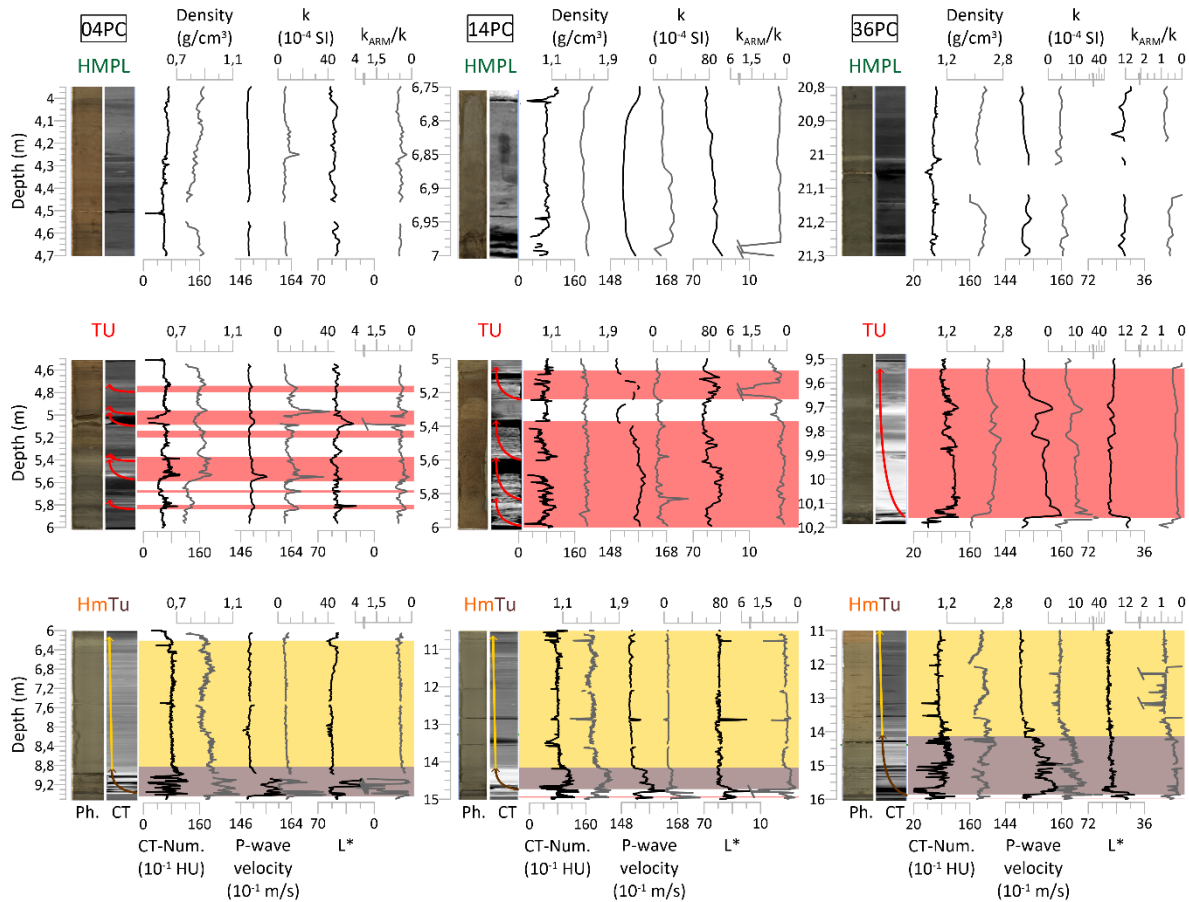


Figure 29 - Examples for each facies of each core with the same parameters as Fig. 28. Top: hemipelagic background sediments (HMPL). Middle: Turbidite facies highlighted in light red with fining upward red arrows on CT-scan images. Bottom: Homogenite-turbidite complexes (HmTu) facies highlighted in light brown (Tu) and sandy-yellow (Hm) with fining upward brown arrows and vertical yellow arrows on CT-scan images.

grain size variations of bulk sediment measurement. This plot highlights that the hemipelagic background sediments does not cross the empirical line  $0.2 \mu\text{m}$  except for few centimeters in each core.

**b) TURBIDITES**

In the middle of Fig. 29, three examples of turbidites or set of turbidites are presented, one for each core studied. These events are identified by a fining-upward grain size and most of the time by a sharp contact with the underlying sediments. This fining-upward grading is highlighted by the density parameters CT-number, density and P-wave velocity, as well as by the magnetic measurements  $k$  and  $k_{\text{ARM}}/k$ . Each of these parameters is slightly different from another, which is why we consider here that a minimum of two parameters must exhibit the same fining-upward behavior to validate the facies. In addition, a visual identification of such deposit with the high-definition photographic and CT-scan images is required. As a example of this facies, we will now describe in details the turbidite observed in core CAS16-36PC. On the high-definition photographic picture, a basal sharp contact is observed and all the physical and magnetic parameters exhibit higher basal values which slightly decrease upward. Two others increases are pictured at around 9.85 MCD and 9.70 MCD with again a fining upward behavior. These parameters and their visual identification are also supported by CT-scan images (and associated CT-number) with high intensities (white) at the base of each coarser deposit, while intensities diminished upward (darkening images). As the CAS16-36PC examples, some of these TU are a succession of interrupted turbidite known as amalgamated turbidite, while some others are associated to a thick homogenous layer known as an homogenite that differs from the the “e” term of the Bouma (1961) sequence ( $T_e$ ). The latter deposits are described as a specific facies in the next section. In Fig. 30-B, as expected from  $k$  and  $k_{\text{ARM}}$  measurements, most of turbidite sediments are at right of the  $0.2 \mu\text{m}$  empirical line, which delimits HMPL from TU. In each core few TU present lower magnetic susceptibility and are thus plotted lower than this empirical line. However, it is easily explained by the absence of magnetic minerals in some turbidite deposits mostly composed of shell fragments and foraminiferal tests, or in some cases to the  $T_e$ , which might

be composed of mud to silty-mud settling sediments (similar to hemipelagic background sediment).

**c) HOMOGENITE-TURBIDITE COMPLEXES**

At the bottom of the Fig. 29, one homogenite-turbidite complex (HmTu) is shown for each core. This facies can be divided into two subgroup: (1) Turbidite-like basal deposition, which generally began with a well-defined sharp contact on the high-definition photographic picture and CT-scan images. At the base of the facies, CT-number, density and P-wave velocity show high value in each core. In addition to the physical parameters, the magnetic parameters also reveal a fining upward behavior. (2) Sediments become homogenous on all precedent parameters, as well as on high-definition photographic and CT-scan pictures, and the L\* color space. Fig. 30-C show similar values as turbidite facies for turbidite-like sediment (brown) which mainly are above the 0.2  $\mu\text{m}$  empirical line, while homogenite (yellow) values are below the 0.2  $\mu\text{m}$  empirical line and looks quite similar to hemipaligic background sediment facies. However, hemipelagic background sediment can be easily identified at the top of the homogenite with higher magnetic susceptibility amplitudes than for the underlying homogenous layers.

**d) UNIDENTIFIED RDL**

This facies groups all RDL that are not clearly identified as turbidites or homogenite-turbidite complexes. It includes tephra deposits, mass transport deposits or thin silty layers that may be the extension of turbidite fan deposits with only the uppermost finer sediments of a turbidite. All these RDL are mainly associated with high intensities CT-scan images (and high CT-number), and high physical and magnetic parameters.

Table 3 - Physical properties of the three main facies hemipelagic (HMPL), turbidite (Tu) including turbidite from homogenite-turbidite complexes (HmTu) and homogenite (HMG) for cores CAS16-04PC, -14PC and 36PC.

Facies	Core	Stat	P-wave velocity (m/s)	Density (g/cm <sup>3</sup> )	Magnetic susceptibility (10 <sup>-5</sup> SI)	L*	k <sub>ARM</sub> /k
HMPL	CAS16-04PC	Min	1482	0.74	14	25.7	1.8
		Max	1563	1.05	386	62.1	16.8
		Mean	1497	0.87	53	48.4	7.1
		Median	1493	0.87	47	48.0	6.8
	CAS16-14PC	Min	1499	1.29	18	20.4	2.1
		Max	1782	1.77	296	64.3	42.5
		Mean	1535	1.49	95	49.8	6.5
		Median	1527	1.51	74	49.4	5.3
	CAS16-36PC	Min	1453	1.68	5	43.8	3.1
		Max	1541	2.46	169	62.7	58.1
		Mean	1490	2.03	52	50.1	7.8
		Median	1488	2.04	48	49.2	7.2
Tu (HmTu)	CAS16-04PC	Min	1486 (1483)	0.76 (0.86)	20 (5)	22.6 (0.1)	1.1 (0.8)
		Max	1634 (1618)	1.14 (1.14)	411 (381)	60.1 (61.8)	20.1 (39.4)
		Mean	1508 (1533)	0.90 (0.98)	103 (74)	47.3 (51.6)	4.3 (5.5)
		Median	1500 (1533)	0.89 (0.98)	103 (63)	47.2 (54.8)	3.8 (3.7)
	CAS16-14PC	Min	1500 (1504)	1.26 (1.33)	8 (28)	11.2 (22.8)	0.6 (0.9)
		Max	1603 (1747)	1.77 (1.83)	818 (704)	65.5 (60.8)	32.4 (8.2)
		Mean	1553 (1556)	1.533 (1.58)	126 (112)	46.7 (52.1)	4.2 (3.4)
		Median	1557 (1556)	1.55 (1.58)	93 (85)	47.2 (53.8)	3.2 (3.2)
	CAS16-36PC	Min	1480 (1477)	1.76 (1.70)	34 (1.8)	43.0 (39.1)	0.7 (0.2)
		Max	1598 (1602)	2.72 (2.80)	379 (456)	65.6 (68.7)	9.7 (81.5)
		Mean	1524 (1524)	2.32 (2.24)	89 (62)	55.7 (57.2)	3.4 (4.5)
		Median	1524 (1527)	2.39 (3.25)	84 (46)	56.9 (57.2)	3.0 (3.5)
HMG	CAS16-04PC	Min	1468	0.78	11	15.0	1.3
		Max	1527	1.04	87	62.4	10.6
		Mean	1493	0.90	44	54.4	6.1

		Median	1491	0.90	38	54.9	6.0
CAS16-14PC	Min	1482	1.10	5	24.7	2.8	
	Max	1597	1.71	94	63.4	51.0	
	Mean	1511	1.47	43	54.3	7.1	
	Median	1511	1.48	41	53.8	6.6	
CAS16-36PC	Min	1471	1.57	2	43.6	3.4	
	Max	1552	2.59	86	66.6	109.2	
	Mean	1489	2.19	39	56.8	7.7	
	Median	1485	2.20	39	57.7	3.4	

#### 2.2.4.3 Event-free composite record

In order to use paleomagnetic dating, reconstructing the event-free composite record is a requirement, especially in such a setting where turbidites and homogenite-turbidite complexes were recorded. The above facies determination (Fig. 28, 29 and 30) allows the creation of the event-free composite record for cores CAS16-04PC, -14PC and -36PC. Construction of the event-free composite record of core CAS16-12PC was made following the same process: identifying (ANNEXE 2, Fig. 47) and removing all RDL using the physical and magnetic parameters. All the following figures will be plotted in meter composite depth (MCD; ANNEXE 2, Table 8 for depth correspondence). Fig. 31 displays the paleomagnetic records including NRM, ARM and IRM, as well as inclination, declination and MAD variations as a function of MCD. The ChRM presents clear linear trend towards the origin of the orthogonal projection (ANNEXE 2, Fig. 48). A viscous component is removed easily within the first three demagnetization steps. As a comparison, TU and HmTu orthogonal projections are shown in ANNEXE 2, Fig. 48. Inclination is following the GAD value except for CAS16-36PC that presents a shallowing inclination error increasing as a function of MCD. MAD values are almost always under 5° for all cores with a mean value of 2.0°, 1.8°, 4.9° and 1.3° for cores CAS16-04PC, -12PC, -14PC and -36PC respectively.

#### 2.2.4.4 Magnetic carriers and relative paleointensity (RPI) reconstruction

Considering MDF calculation with a mean value of 24, 24, 20 and 26 mT for cores CAS16-04PC, -12PC, -14PC and -36PC respectively, and considering their (except CAS16-

12PC) average pseudo S-ratio values 0.99, 1.04 and 0.94, magnetic carriers of the remanent magnetization are expected to consist of low coercivity minerals such as magnetite or titanomagnetite. High value over 1 found in core CAS16-14PC is most likely due to the difficulty of the cryogenic magnetometer to perform precise measurements near the dynamic range of the instrument (Roberts, 2006), especially when turbidites affect surrounding HMPL sediment. Hemipelagic background sediments of each core present normalized moments  $< 0.1 \times 10^{-5} \text{ Am}^2$  with the shape of the hysteresis loops characteristic of magnetite and titanomagnetite minerals (ANNEXE 2, Fig. 49-A to F), while turbidite-like silt to sand sediments from the HmTu complexes display greater normalized moments (ANNEXE 2, Fig. 49-D to F doted lines) with maximum values  $> 0.1 \times 10^{-5} \text{ Am}^2$ . Parameters derived from these hysteresis curves are used to construct the Day diagrams. The Day diagram (ANNEXE 2, Fig. 49-G) allows to distinguish turbidite-like deposits with high Hcr/Hc and low Mrs/Ms values from the hemipelagic background sediments with lower Hcr/Hc and higher Mrs/Ms values (parameters derived from HMPL hysteresis loops are plotted in the ANNEXE 2, Fig. 49-H). Homogenite sediments range between these two facies.

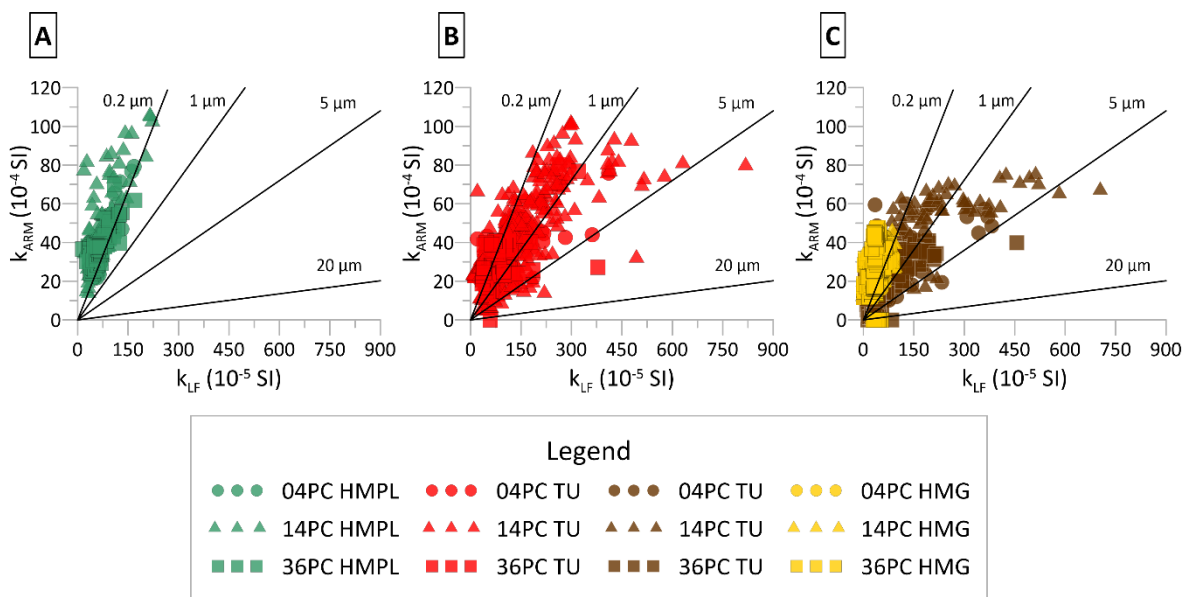


Figure 30 - King plot (King et al., 1982). A: hemipelagic (HMPL) background sediments (green symbols). B: turbidite (TU) sediments (red symbols). C: homogenite (yellow) turbidite (brown symbols) complexes (HmTu).

Considering all the above arguments, the NRM is most probably carried by low coercivity minerals such as magnetite and titano-magnetite and the hemipelagic sediments of the composite records fulfill recommended criteria to reconstruct a reliable RPI (Levi and Banerjee, 1976; Tauxe, 1993; Stoner and St-Onge, 2007).

The reconstruction of the RPI requires to correct the NRM from the lithological influence using a normalizer such as ARM, IRM or k (Tauxe, 1993). The use of different methods to normalize the NRM is a requirement to evaluate the robustness of the RPI reconstructions (coherence between each normalization results). Two main methods are commonly used to identify the best normalizer. The most used is the ratio method (e.g. Channel et al., 1997; St-Onge et al., 2003; Bieber et al. 2021), which was calculated here using eight demagnetization steps (10-45 mT) of the NRM for core CAS16-12PC and nine demagnetization steps (10-50 mT) for the other cores, each of them normalized by ARM, IRM and k. The normalized NRM is plotted against each normalizer and the best one must reveal the lowest coefficient of determination ( $r^2$ ). For the top twelve meters, CAS16-12PC presents the lowest  $r^2 = 0.04$  with ARM as a normalizer (ANNEXE 2, Fig. 50), while for the other cores, the lowest  $r^2$  is found to be with k as the normalizer. Because k might be affected by paramagnetic grains that do not contribute to remanent magnetization (Forter et al., 1994; Brachfeld and Banerjee, 2000) and because ARM or IRM better mimics the coercivity spectra of the NRM (right-end graphs in figures S4-S7), we will further investigate the use of ARM or IRM as the best normalizer. Cores CAS16-04PC, CAS16-14PC and CAS16-36PC show the lowest  $r^2$  with ARM as normalizer with respective values of 0.18, 0.07 and 0.10 (ANNEXE 2, Fig. 51 to 53). A second method to reconstruct the RPI is based on the pseudo-Thellier approach developed by Tauxe et al. (1995) and recognizes as the slope method (e.g. Channell, 2002; Snowball and Sandgren, 2004; Xuan and Channel, 2009). It uses the slope between NRM and normalizer at different demagnetization steps. To assess the efficiency of a normalizer using the slope method, a correlation coefficient (r) must be the highest. In all cores, ARM normalizer presents the best r median values  $> 0.99$ . Coherence between both methods is strongest with ARM than with IRM normalization, which raises

visual discrepancies. All these arguments are in favor to use ARM as the normalizer for all the cores studied here, and we use the ratio method for normalization.

#### 2.2.4.5 Age-depth models

##### a) CAS16-12PC

To reconstruct a reliable age-depth model for core CAS16-12PC, we compared it to the regional reference record CAS16-24PC RPI (Bieber et al., 2021; Fig. 32-A;  $r = 0.44$ ) and identify seven tie points between 100 ka and 400 ka (Table 2). We additionally compare the top of the core with the North Atlantic paleointensity stack (NAPIS-75; Laj et al., 2000,  $r =$

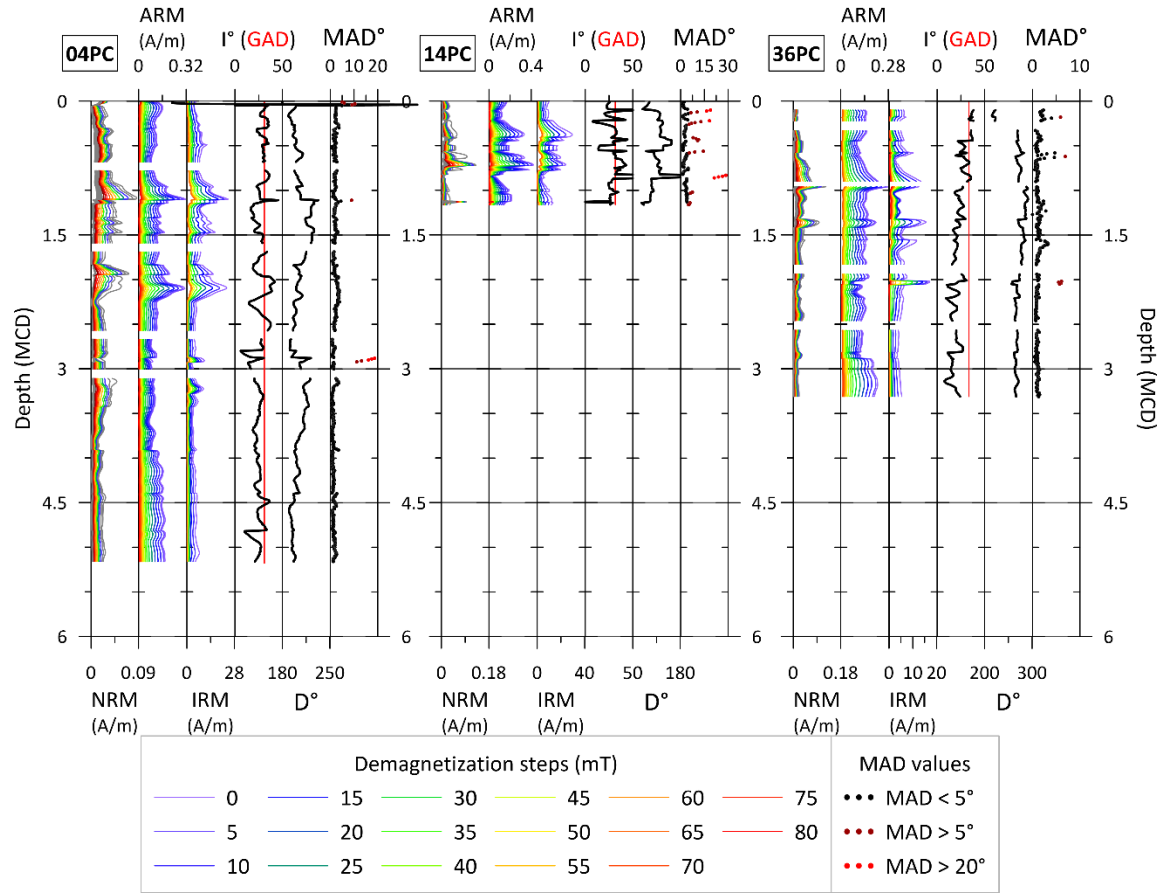


Figure 31 - Paleomagnetic data including from left to right: NRM, ARM and IRM demagnetization steps, inclination ( $I^\circ$ ; red line is the GAD inclination at the site latitude), declination and MAD angles for cores CAS16-04PC, -14PC and -36PC.

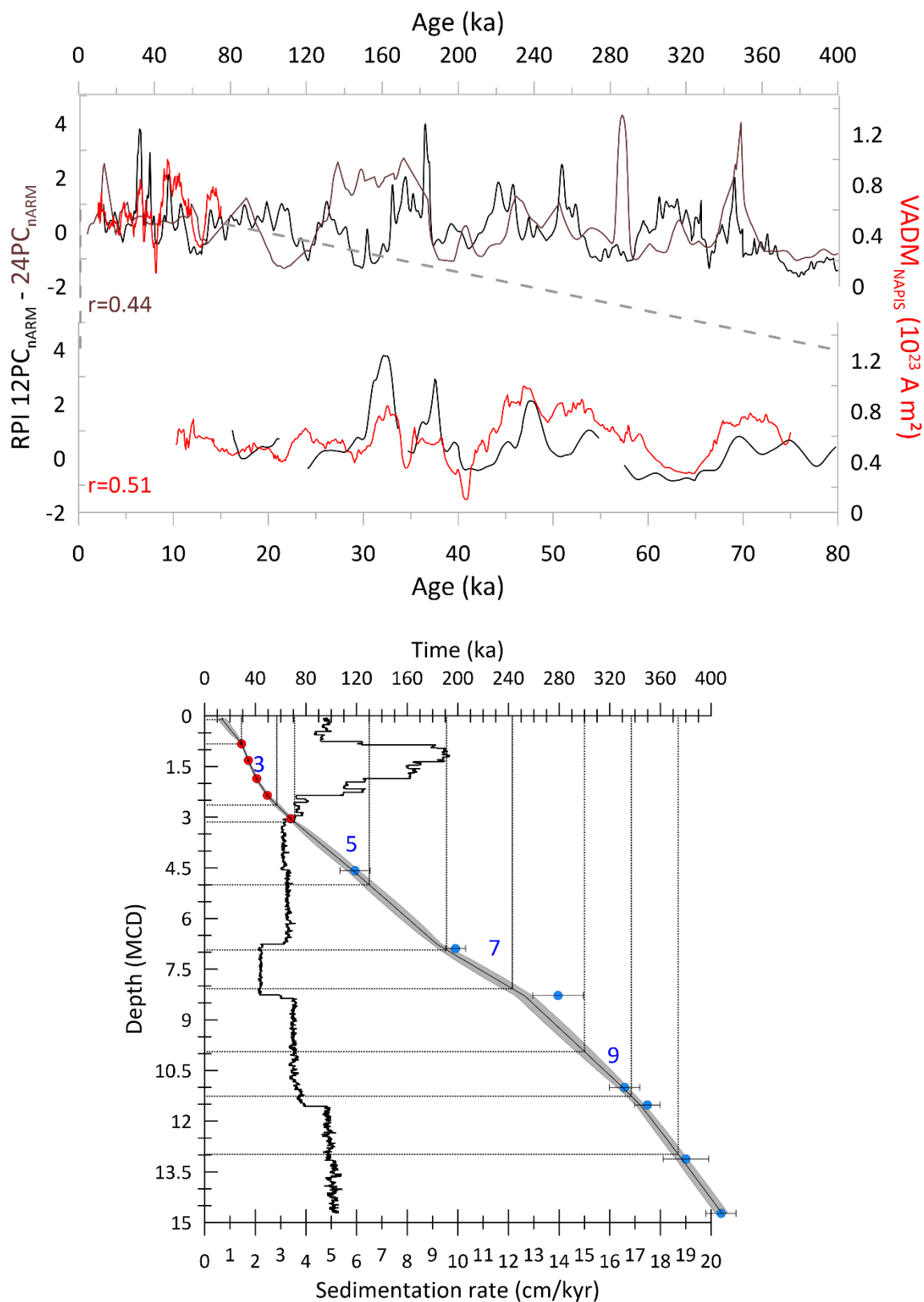


Figure 32 - A) Comparison of CAS16-12PC RPI (black curves) with reference records CAS16-24PC (brown curve) and NAPIS-75 (red curves), including coefficient of correlation ( $r$ ). B) Age-depth model of core CAS16-12PC developed using R Package Bacon 2.2 (Blaauw and Christen, 2011), with linear interpolation using five NAPIS-75 tie points (red dots) and seven CAS16-24PC tie points (blue dots). Sedimentation rates are derived from the age-depth model. Interglacial marine isotopic stages (MIS) from 3 to 9 are in blue roman number and all MIS delimited by straight lines from linear interpolation curve to axis.

0.51), which allows to establish five more tie points to better constrain the age-depth model (Fig. 32-B). Mean sedimentation rate is about 3.7 cm/kyr between MIS 11 and MIS 4. Sedimentation rate increases rapidly at the beginning of MIS 3 to reach a sedimentation rate of about 7.7 cm/kyr. Core is estimated to be  $407 \text{ ka} \pm 9 \text{ ka}$  old.

### **b) CAS16-04PC, -14PC AND -36PC**

Each core was compared to the CAS16-12PC RPI record and to NAPIS-75 stack (Fig. 33-A). These age-depth models also used radiocarbon dating, RPI tie points and the Laschamps geomagnetic excursion. The CAS16-04PC model was constructed using three  $^{14}\text{C}$  ages combined with twelve tie points ( $r = 0.50$  with the CAS16-12PC and  $r = 0.44$  with NAPIS-75 RPI records; Table 4) and one geomagnetic excursion (Laschamps at  $\sim 41 \text{ ka}$ ; Channel et al., 2020). Mean sedimentation rate is about 6.8 cm/kyr with the highest sedimentation rate during MIS 3 (as for core CAS16-12PC). The age of cores CAS16-14PC and CAS16-36PC were more difficult to establish because of a very low sedimentation rate on the first one and the presence of numerous turbidites and HMTU complexes on the second one (both present less than 15 % of background hemipelagic sedimentation). The CAS16-14PC age model was established with three  $^{14}\text{C}$  ages, two tie points (Table 4) from core CAS16-12PC ( $r = 0.49$ ) and the Laschamps excursion, while CAS16-36PC age model was determined using three  $^{14}\text{C}$  ages, and one tie-point ( $r = 0.54$ ) from core CAS16-12PC and two tie points from NAPIS-75 ( $r = 0.32$ ). Cores are estimated to respectively be  $95 \pm 15 \text{ ka}$ ,  $65 \pm 5 \text{ ka}$  and  $85 \pm 5 \text{ ka}$  old (Fig. 33-B).

Table 4 - List of RPI tie-points determined using <sup>1</sup>NAPIS-75 (Laj et al., 2000); reference record <sup>2</sup>CAS16-24PC (Bieber et al., 2021) and CAS16-12PC, with MCD and age, including the error used in the age-depth model.

Sample	MCD (m)	Age (ka)	Error (ka)	Reference
CAS16-04PC	23	16.465	0.2	NAPIS-75 <sup>1</sup>
CAS16-04PC	43	21.797	0.2	NAPIS-75 <sup>1</sup>
CAS16-04PC	112	29.548	0.2	NAPIS-75 <sup>1</sup>
CAS16-04PC	137	32.205	0.2	NAPIS-75 <sup>1</sup>
CAS16-04PC	257	45.476	1	CAS16-12PC
CAS16-04PC	380	58.002	0.2	CAS16-12PC
CAS16-04PC	391	66.167	2.9	CAS16-12PC
CAS16-04PC	398	70.283	1.4	CAS16-12PC
CAS16-04PC	418	75.547	1.8	CAS16-12PC
CAS16-04PC	470	90.612	4.4	CAS16-12PC
CAS16-04PC	496	101.506	6.3	CAS16-12PC
CAS16-04PC	515	102.309	6.9	CAS16-12PC
CAS16-14PC	77	49.667	0.2	NAPIS-75 <sup>1</sup>
CAS16-14PC	112	62.532	2.3	CAS16-12PC
CAS16-36PC	132	40.9	0.2	NAPIS-75 <sup>1</sup>
CAS16-36PC	137	46.542	0.4	NAPIS-75 <sup>1</sup>
CAS16-36PC	228	65.135	2	CAS16-12PC

CAS16-12PC	83	29.1	0.2	NAPIS-75 <sup>1</sup>
CAS16-12PC	132	34.5	0.2	NAPIS-75 <sup>1</sup>
CAS16-12PC	186	41	0.2	NAPIS-75 <sup>1</sup>
CAS16-12PC	235	49.4	0.2	NAPIS-75 <sup>1</sup>
CAS16-12PC	304	67.9	0.2	NAPIS-75 <sup>1</sup>
CAS16-12PC	458	118.8	6	CAS16-24PC <sup>2</sup>
CAS16-12PC	689	198.1	4	CAS16-24PC <sup>2</sup>
CAS16-12PC	828	279.2	10	CAS16-24PC <sup>2</sup>
CAS16-12PC	1100	331.7	6	CAS16-24PC <sup>2</sup>
CAS16-12PC	1152	349.8	5	CAS16-24PC <sup>2</sup>
CAS16-12PC	1312	380.1	9	CAS16-24PC <sup>2</sup>
CAS16-12PC	1473	407.9	6	CAS16-24PC <sup>2</sup>

## 2.2.5 Discussion

### 2.2.5.1 Age model limitations

The initial age models of cores CAS16-04PC, -14PC and -36PC based on radiocarbon dating and foraminifera paleoclimatic biozone were previously established by Morena et al. (in prep) and by Seibert et al. (2022, SUBMITTED). To improve and better constrain the age-depth models, we used paleomagnetism as complementary dating method. While RPI variations offer the opportunity to establish an almost continuous record, the presence of many RDL probably led to some erosion and likely led to some RPI record gaps. Gap sizes are difficult to estimate but could likely explain some abrupt drops and rises in sedimentation

rates, which prevent us to use sedimentation rates as paleo-environmental marker in our study. We recommend to keep in mind this possible erosive bias in our age-depths models.

Another limitation is the fact that the age model of core CAS16-12PC is only based on RPI comparison with the reference record CAS16-24PC and the NAPIS-75 stack. Nonetheless, the correlations made with the reference core CAS16-24PC and the NAPIS-75 stack are strong enough to endorse the reliability of this age-depth model, with age error about 5.6 ka for the first 300 ka based on the uncertainty of the CAS16-24PC record (Bieber et al. 2021), while it is about 2.2 ka for the last 100 ka based on the NAPIS-75 uncertainty (Laj et al. 2000). The increase in sedimentation rates during MIS 3 was found in association with a strong incorporation of carbonaceous content (Bouchet, 2017) probably of a detrital origin considering the core location below the carbonate compensation depth. In brief, while the chronology presented in this paper has some limitations, it is nonetheless a major step forward in order to date RDL and sediments below the carbonate compensation depths.

#### 2.2.5.2 Trigger mechanism of each sediment facies

A major task in marine paleo-seismology is to determine the trigger mechanism of turbidites. Talling (2021) pointed out how tricky it can be to assess a seismogenic initiation of a turbidite, as it could also originate from tsunamis, storms or continental floods (mentioning external events only). During the CASEIS cruise, core locations have been selected in order to be disconnected from continental discharge, which refutes a continental origin. Each coring site is deeper than 5 km deep, which is below storm oceanic influence (e.g. Black and Dickey, 2008). However, turbidites triggered by storm have been recorded in several location by cable destruction (e.g. Pope et al., 2017). Storm waves might trigger turbidity current in shallow area that can be export sediments in the deep ocean. While the Falmouth half graben (core CAS16-14PC) is a basin also isolated from shallow input, the Desirade basin (core CAS16-04PC) is connected to the carbonate platform by several canyons and might receive high density current from density cascading or storm events (Seibert et al., 2020). Core CAS16-36PC basin, which is connected to the Anguilla Bank and

Antigua Bank by canyons (Morena et al., in prep), might record shallow carbonate input linked to density cascading or storm events as well. In that respect, RDL recorded in the core CAS16-14PC is more likely to be triggered by an earthquake than in the cores CAS16-04PC and CAS16-36PC that might also be induced by shallow input, especially during sea level low stands. However, unlike several studies (Reeder et al. 2000; Rothwell et al., 2000; Leynayd et al., 2009;), no specific trend can be correlated to sea-level variations. Indeed, by comparing the number of RDL per 5 ka intervals to the global sea level stack (Spratt and Lisiecki, 2015), it appears that the minimum number of deposits is found at the last glacial maximum during the marine isotopic stage two (MIS 2; Fig. 34-A) , but no drastic increasing amount of turbidite is identified during the MIS 2-1 transition, nor is at sea-level highstand as it has been reported in other carbonate platform context (e.g., Droxler and Schlager, 1985; Jorry et al., 2010; Tournadour et al., 2014). Ion addition, homogenite-turbidite complexes were previously associated to tsunamis or earthquakes (e.g. Chapron et al. 1999 ; Beck et al., 2007 ; Çagatay et al., 2012 ; St-Onge et al. 2012 ; Campos et al., 2013 ; Polonia et al., 2013 ; San Pedro et al., 2016 ; McHugh et al., 2020 ; Polonia et al. 2021). The distance between the carbonate platforms and the basins studied is probably too long ( $> 60$  km) to collect tsunami backwash deposits, which limit the main trigger mechanism to be paleo-earthquake for HmTu deposits. The thick size of the homogenous part might reflect the remobilization of bottom sediments by ground-shaking and or S-waves resulting from earthquakes as it has been suggested by Mc Hugh et al. (2020). In summary, HmTu are most probably triggered by earthquakes exceeding the magnitude of historical records (Seibert et al., submitted), while turbidite deposits might also be triggered by local destabilisation or by density cascading. Undefined RDL are not necessarily resulting from a gravity current but might be the end tail of a turbidity current that could have been initiated by earthquakes. Considering the occurrence of turbidite and homogenite-turbidite complexes we will consider these deposits as the result of paleoearthquakes.

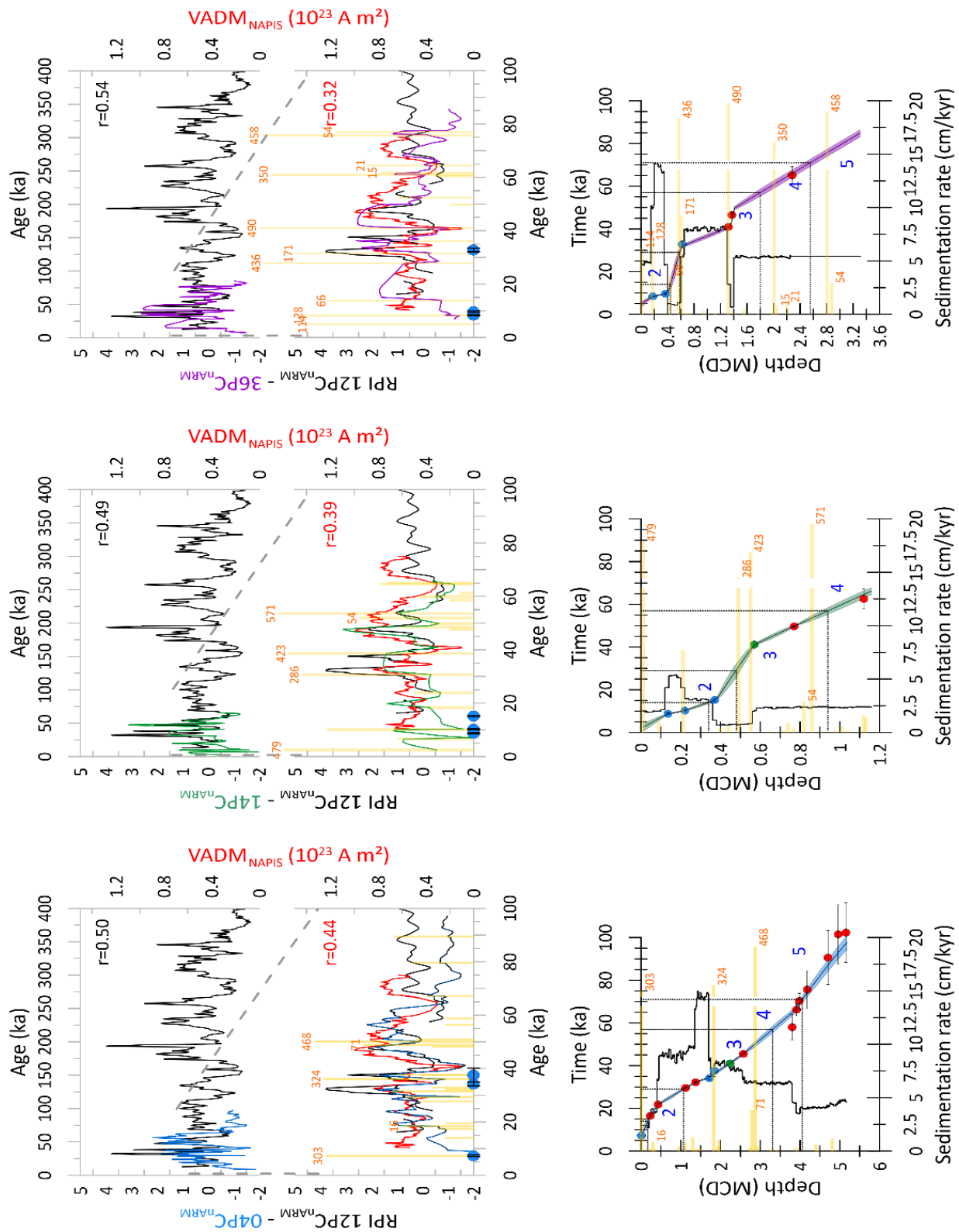


Figure 33 - Same figure as Fig. 32 but for cores CAS16-04PC (blue curves), -14PC (green curves) and -36PC (purple curves). Blue dots are  $^{14}\text{C}$  dates while red dots are RPI tie points and green dots reflect the Laschamps geomagnetic excursion. RDL are additionally plotted as chart bar (yellow) with HmTu labeled with event size.

### 2.2.5.3 RDL dating and seismic super-cycle

Using the three age-depth models established previously allows to estimate the ages of each RDL including the HmTu complexes (Table 5, ANNEXE 1). However, we will not attempt to correlate the deposits from a basin to another one as proposed by Seibert et al. (submitted), instead we will estimate the age of each RDL as a possible distinct seismic event. The resulting chronology allows evaluating the number of RDL as a function of time for each core (Fig. 34-A and -B). Several studies mentioned large earthquakes that do not completely release the strain accumulated. This strain would be released during several clustered events and associated to seismic supercycles (Goldfinger et al., 2013; Ratzov et al., 2015; Noccquet et al., 2016; Salditch et al., 2020). Considering the RDL not as a solely event, but as a group of clustered events, we identified four possible groups labeled CE-1 to CE-4 (stacked stick diagram in Fig. 34-B and boxplot in Fig. 34-C). These clustered events are defined by the presence of at least one HmTu event, while their extent is estimated by successive overlapping RDL (minimum and maximum limits). This clustering makes possible to establish a recurrence time of  $23 \pm 2$  ka between each median's age with an average extent of  $18 \pm 2$  ka. Moreover, the data permit the estimation of a  $6.8 \pm 0.1$  ka quiescence time between each cluster. The recurrence time of HmTu (related to strong earthquakes) inside the three most recent CE is about  $2.8 \pm 0.4$  ka. Considering the last strong earthquake recorded occurred  $2.4 \pm 1.6$  ka ago (age of the most recent HmTu), maximum probability for a major seismic event occurring in the Lesser Antilles will be reached in the next four hundred years. In brief, the Lesser Antilles subduction zone is currently at the limit between a seismic super-cycle and its following quiescence period. The Lesser Antilles megathrust might hold enough strain

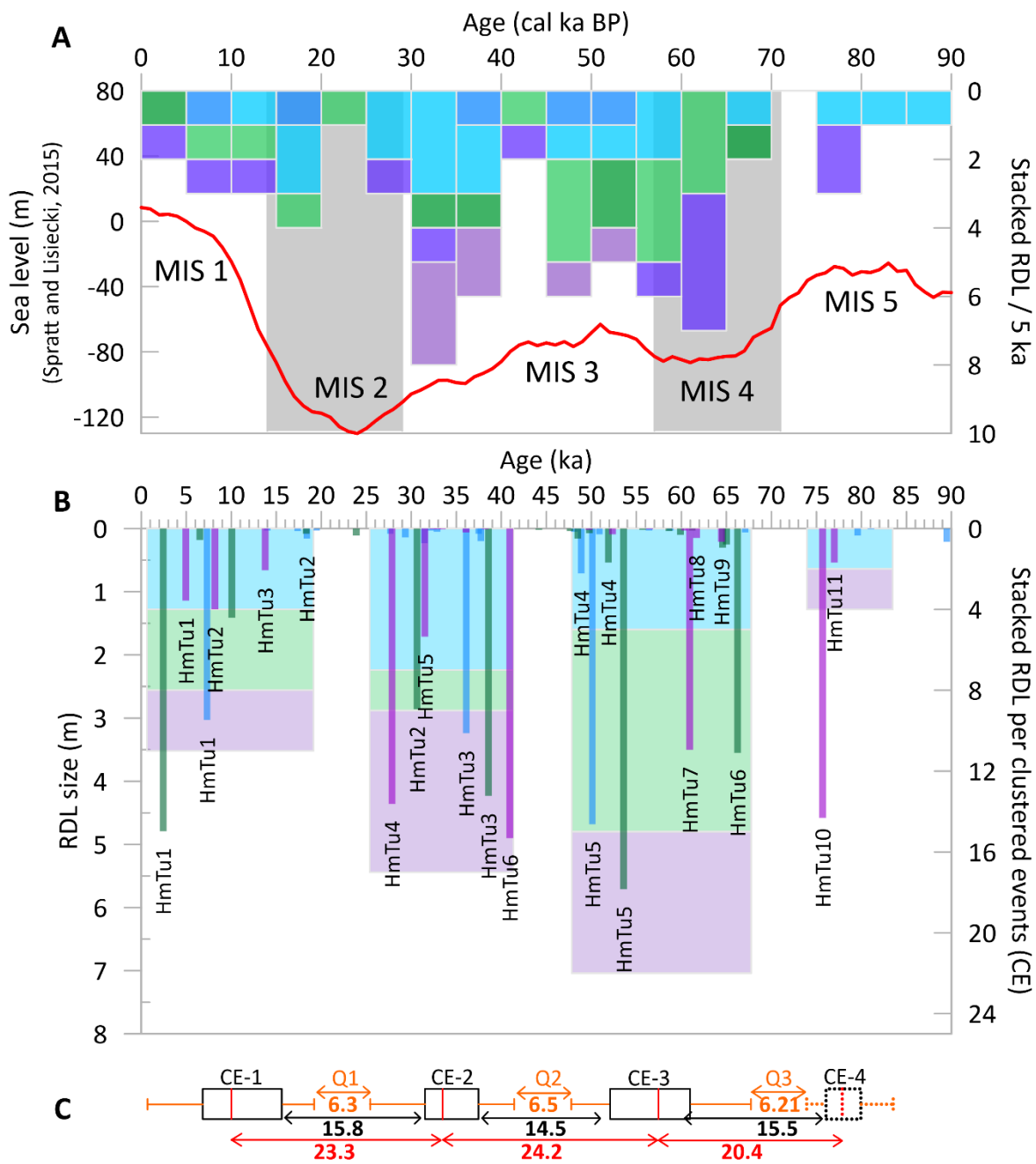


Figure 34 - A) Bar chart of 5 ka grouped and stacked RDL with blue bar for CAS16-04PC RDL (deep blue for HmTu), green bar for CAS16-14PC RDL (deep green for HmTu) and violet bar for CAS16-36PC RDL (deep violet for HmTu) compared to global sea level variations (Spratt and Lisiecki, 2015). B) Bar chart of RDL size function of time. HmTu are labeled from 1 to 11 for each core ante-chronologically. Background bar chart stacked RDL as clustered defined by C. C: box plots of each clustered event (CE-1 to CE-4) with associated quiescence time Q1 to Q3. Red arrows reveal time between each average age of CE.

to release it into a strong earthquake that have never been recorded in the recent historical archives.

## 2.2.6 Conclusions

Records of large historical earthquakes ( $M \geq 8$ ) support the need to better understand the Lesser Antilles subduction zone and megathrust earthquakes that can affect the region. Paleo-seismology has already demonstrated its effectiveness in several subduction zones, including offshore the Guadeloupe island (Seibert et al.; 2022, SUBMITTED). This study offers a novel paleoseismological framework in the Lesser Antilles based on the combination of radiocarbon dating and RPI variations. Identifying all the RDL from the cores enables to construct their event-free composite record and establish age-depth models covering the last 90 ka, as well as dating each sedimentary event.

A total of seventy-three RDL most probably triggered by paleo-earthquakes (including thirty-one turbidites and twenty-two homogenite-turbidite complexes) were identified. Based on the estimated age of these RDL, we found a  $24 \pm 2$  ka-long seismic super-cycle including a  $6.8 \pm 0.1$  ka quiescence period. The present time might be at the limit between two seismic super-cycles.

Further investigations on the carbonate platform and canyon systems of the Lesser Antilles could provide complementary data and help characterize RDL not triggered by seismic events. Finally, shallower sediments collected closer to the shoreline might record tsunami back-wash deposits that could be associated to HmTu events.

## Acknowledgments

We thank the captain, officers and crew of the R/V Pourquoi Pas?, and the scientific participants in the CASEIS Expedition for the quality of the acquired shipboard data. This work was supported by grants from the Natural Sciences and Engineering Research Council of Canada (NSERC) and the French National Research Agency (ANR-17-CE03-0006; DS01 – CARQUAKES). We also thank Quentin Beauvais, Hervé Guyard, Lola Johannes and

Marie-Pier St-Onge for their help on board the ship and/or in the laboratory. We thank MNHN for CASEIS cores storage in the marine collection. A. Bieber acknowledges scholarships from the Institut des sciences de la mer de Rimouski (ISMER) and Institut de physique du globe de Paris (IPGP).

## References

- Banerjee, S.K., King, J., Marvin, J., 1981. A rapid method for magnetic granulometry with applications to environmental studies. *Geophys. Res. Lett.* 8, 333–336. <https://doi.org/10.1029/GL008i004p00333>
- Beck, C., 2009. “Late Quaternary lacustrine paleo-seismic archives in north-western Alps: Examples of earthquake-origin assessment of sedimentary disturbances.” *Earth-Science Reviews* 96, 327–344. <https://doi.org/10.1016/j.earscirev.2009.07.005>
- Beck, C., Reyss, J.-L., Leclerc, F., Moreno, E., Feuillet, N., Barrier, L., Beauducel, F., Boudon, G., Clément, V., Deplus, C., Gallou, N., Lebrun, J.-F., Le Friant, A., Nercessian, A., Paterne, M., Pichot, T., Vidal, C., 2012. Identification of deep subaqueous co-seismic scarps through specific coeval sedimentation in Lesser Antilles: implication for seismic hazard. *Natural Hazards and Earth System Science* 12, 1755–1767. <https://doi.org/10.5194/nhess-12-1755-2012>
- Bieber, A., St-Onge, G., Feuillet, N., Carlut, J., Moreno, E., Michel, E., 2021. Regional chronostratigraphy in the eastern Lesser Antilles quaternary fore-arc and accretionary wedge sediments: Relative paleointensity, oxygen isotopes and reversals. *Quaternary Geochronology* 65, 101179. <https://doi.org/10.1016/j.quageo.2021.101179>
- Bilek, S.L., Lay, T., 2018. Subduction zone megathrust earthquakes. *Geosphere* 14, 1468–1500. <https://doi.org/10.1130/GES01608.1>
- Blaauw, M., Christen, J.A., 2011. Flexible paleoclimate age-depth models using an autoregressive gamma process. *Bayesian Analysis* 6, 457–474. <https://doi.org/10.1214/11-BA618>

Black, W.J., Dickey, T.D., 2008. Observations and analyses of upper ocean responses to tropical storms and hurricanes in the vicinity of Bermuda. *J. Geophys. Res.* 113, C08009. <https://doi.org/10.1029/2007JC004358>

Bouchet, O., 2017. Essai de caractérisation par Anisotropie de Susceptibilité Magnétique de séquences turbiditiques déposées au front de l'arc des Petites Antilles. Institut de physique du globe de Paris.

Bouma, A.H., 1964. Turbidites, in: *Developments in Sedimentology*. Elsevier, pp. 247–256. [https://doi.org/10.1016/S0070-4571\(08\)70967-1](https://doi.org/10.1016/S0070-4571(08)70967-1)

Bouysse, P., Westercamp, D., 1990. Subduction of Atlantic aseismic ridges and Late Cenozoic evolution of the Lesser Antilles island arc. *Tectonophysics* 175, 349–355, 357–380.

Brachfeld, S.A., Banerjee, S.K., 2000. A new high-resolution geomagnetic relative paleointensity record for the North American Holocene: A comparison of sedimentary and absolute intensity data. *Journal of Geophysical Research: Solid Earth* 105, 821–834. <https://doi.org/10.1029/1999JB900365>

Briden, J.C., Rex, D.C., Faller, A.M., Tomblin, J.F., 1979. K-Ar Geochronology and Palaeomagnetism of Volcanic Rocks in the Lesser Antilles Island Arc. *Philosophical Transactions of the Royal Society A: Mathematical, Physical and Engineering Sciences* 291, 485–528. <https://doi.org/10.1098/rsta.1979.0040>

Çağatay, M.N., Erel, L., Bellucci, L.G., Polonia, A., Gasperini, L., Eriş, K.K., Sancar, Ü., Biltekin, D., Uçarkuş, G., Ülgen, U.B., Damcı, E., 2012. Sedimentary earthquake records in the İzmit Gulf, Sea of Marmara, Turkey. *Sedimentary Geology* 282, 347–359. <https://doi.org/10.1016/j.sedgeo.2012.10.001>

Campos, C., Beck, C., Crouzet, C., Demory, F., Van Welden, A., Eris, K., 2013. Deciphering hemipelagites from homogenites through anisotropy of magnetic susceptibility.

Paleoseismic implications (Sea of Marmara and Gulf of Corinth). *Sedimentary Geology* 292, 1–14. <https://doi.org/10.1016/j.sedgeo.2013.03.015>

Channell, J.E.T., 2002. Geomagnetic excursions and paleointensities in the Matuyama Chron at Ocean Drilling Program Sites 983 and 984 (Iceland Basin). *Journal of Geophysical Research* 107. <https://doi.org/10.1029/2001JB000491>

Channell, J.E.T., Hodell, D.A., Lehman, B., 1997. Relative geomagnetic paleointensity and  $\delta^{18}\text{O}$  at ODP Site 983 ŽGardar Drift, North Atlantic/ since 350 ka 16.

Channell, J.E.T., Singer, B.S., Jicha, B.R., 2020. Timing of Quaternary geomagnetic reversals and excursions in volcanic and sedimentary archives. *Quaternary Science Reviews* 228, 106114. <https://doi.org/10.1016/j.quascirev.2019.106114>

Chapron, E., Beck, C., Pourchet, M., Deconinck, J.-F., 1999. 1822 earthquake-triggered homogenite in Lake Le Bourget (NW Alps). *Terra Nova* 11, 86–92. <https://doi.org/10.1046/j.1365-3121.1999.00230.x>

Davies, J.H., 1999. The role of hydraulic fractures and intermediate-depth earthquakes in subduction-zone magmatism. *Nature* 398, 142–145. <https://doi.org/10.1038/18202>

Day, R., Fuller, M., Schmidt, V.A., 1977. Hysteresis properties of titanomagnetites: Grain-size and compositional dependence. *Physics of the Earth and Planetary Interiors* 13, 260–267. [https://doi.org/10.1016/0031-9201\(77\)90108-X](https://doi.org/10.1016/0031-9201(77)90108-X)

DeMets, C., Jansma, P.E., Mattioli, G.S., Dixon, T.H., Farina, F., Bilham, R., Calais, E., Mann, P., 2000. GPS geodetic constraints on Caribbean-North America Plate Motion. *Geophysical Research Letters* 27, 437–440. <https://doi.org/10.1029/1999GL005436>

Droxler, A.W., Schlager, W., 1985. Glacial versus interglacial sedimentation rates and turbidite frequency in the Bahamas. *Geol* 13, 799. [https://doi.org/10.1130/0091-7613\(1985\)13<799:GVISRA>2.0.CO;2](https://doi.org/10.1130/0091-7613(1985)13<799:GVISRA>2.0.CO;2)

Feuillet, N., 2016. CASEIS cruise, RV Pourquoi pas ? <https://doi.org/10.17600/16001800>

Feuillet, N., Beauducel, F., Jacques, E., Tapponnier, P., Delouis, B., Bazin, S., Vallée, M., King, G.C.P., 2011a. The  $M_w = 6.3$ , November 21, 2004, Les Saintes earthquake (Guadeloupe): Tectonic setting, slip model and static stress changes. *Journal of Geophysical Research* 116. <https://doi.org/10.1029/2011JB008310>

Feuillet, N., Beauducel, F., Tapponnier, P., 2011b. Tectonic context of moderate to large historical earthquakes in the Lesser Antilles and mechanical coupling with volcanoes. *Journal of Geophysical Research* 116. <https://doi.org/10.1029/2011JB008443>

Feuillet, N., Leclerc, F., Tapponnier, P., Beauducel, F., Boudon, G., Le Friant, A., Deplus, C., Lebrun, J.-F., Nercessian, A., Saurel, J.-M., Clément, V., 2010. Active faulting induced by slip partitioning in Montserrat and link with volcanic activity: New insights from the 2009 GWADASEIS marine cruise data: ACTIVE FAULTING IN MONTSERRAT. *Geophysical Research Letters* 37, n/a-n/a. <https://doi.org/10.1029/2010GL042556>

Forster, Th., Evans, M.E., Heller, F., 1994. The frequency dependence of low field susceptibility in loess sediments. *Geophysical Journal International* 118, 636–642. <https://doi.org/10.1111/j.1365-246X.1994.tb03990.x>

Fortin, D., Francus, P., Gebhardt, A.C., Hahn, A., Kliem, P., Lisé-Pronovost, A., Roychowdhury, R., Labrie, J., St-Onge, G., 2013. Destructive and non-destructive density determination: method comparison and evaluation from the Laguna Potrok Aike sedimentary record. *Quaternary Science Reviews* 71, 147–153. <https://doi.org/10.1016/j.quascirev.2012.08.024>

Goldfinger, C., 2011. Submarine Paleoseismology Based on Turbidite Records. *Annu. Rev. Mar. Sci.* 3, 35–66. <https://doi.org/10.1146/annurev-marine-120709-142852>

Goldfinger, C., Morey, A.E., Nelson, C.H., Gutiérrez-Pastor, J., Johnson, J.E., Karabanov, E., Chaytor, J., Eriksson, A., 2007. Rupture lengths and temporal history of significant earthquakes on the offshore and north coast segments of the Northern San Andreas

Fault based on turbidite stratigraphy. *Earth and Planetary Science Letters* 254, 9–27. <https://doi.org/10.1016/j.epsl.2006.11.017>

Goldfinger, C., Nelson, C.H., Johnson, J.E., The Shipboard Scientific Party, 2003. Holocene earthquake records from the Cascadia subduction zone and northern San Andreas fault based on precise dating of offshore turbidites. *Annual Review of Earth and Planetary Sciences* 31, 555–577. <https://doi.org/10.1146/annurev.earth.31.100901.141246>

Heezen, B.C., Ewing, W.M., 1952. Turbidity currents and submarine slumps, and the 1929 Grand Banks [Newfoundland] earthquake. *American Journal of Science* 250, 849–873. <https://doi.org/10.2475/ajs.250.12.849>

Hough, S.E., 2013. Missing great earthquakes: MISSING GREAT EARTHQUAKES. *J. Geophys. Res. Solid Earth* 118, 1098–1108. <https://doi.org/10.1002/jgrb.50083>

Ikehara, K., Kanamatsu, T., Nagahashi, Y., Strasser, M., Fink, H., Usami, K., Irino, T., Wefer, G., 2016. Documenting large earthquakes similar to the 2011 Tohoku-oki earthquake from sediments deposited in the Japan Trench over the past 1500 years. *Earth and Planetary Science Letters* 445, 48–56. <https://doi.org/10.1016/j.epsl.2016.04.009>

Jorry, S.J., Droxler, A.W., Francis, J.M., 2010. Deepwater carbonate deposition in response to re-flooding of carbonate bank and atoll-tops at glacial terminations. *Quaternary Science Reviews* 29, 2010–2026. <https://doi.org/10.1016/j.quascirev.2010.04.016>

Kanamatsu, T., Ikehara, K., Hsiung, K.-H., 2022. Stratigraphy of deep-sea marine sediment using paleomagnetic secular variation: Refined dating of turbidite relating to giant earthquake in Japan Trench. *Marine Geology* 443, 106669. <https://doi.org/10.1016/j.margeo.2021.106669>

Kastens, K.A., Cita, M.B., 1981. Tsunami-induced sediment transport in the abyssal Mediterranean Sea. *Geol Soc America Bull* 92, 845. [https://doi.org/10.1130/0016-7606\(1981\)92<845:TSTITA>2.0.CO;2](https://doi.org/10.1130/0016-7606(1981)92<845:TSTITA>2.0.CO;2)

King, J., Banerjee, S.K., Marvin, J., Özdemir, Ö., 1982. A comparison of different magnetic methods for determining the relative grain size of magnetite in natural materials: Some results from lake sediments. *Earth and Planetary Science Letters* 59, 404–419. [https://doi.org/10.1016/0012-821X\(82\)90142-X](https://doi.org/10.1016/0012-821X(82)90142-X)

Kong, X., Jiang, Z., Han, C., Li, H., Li, Q., Zheng, L., Yang, Y., Zhang, J., Xiao, F., 2019. Sedimentary characteristics and depositional models of two types of homogenites in an Eocene continental lake basin, Shulu Sag, eastern China. *Journal of Asian Earth Sciences* 179, 165–188. <https://doi.org/10.1016/j.jseaes.2019.04.023>

Laj, C., Kissel, C., Mazaud, A., Channell, J.E.T., Beer, J., 2000. North Atlantic palaeointensity stack since 75ka (NAPIS-75) and the duration of the Laschamp event. *Philosophical Transactions of the Royal Society A: Mathematical, Physical and Engineering Sciences* 358, 1009–1025. <https://doi.org/10.1098/rsta.2000.0571>

Leclerc, F., Feuillet, N., Deplus, C., 2016. Interactions between active faulting, volcanism, and sedimentary processes at an island arc: Insights from Les Saintes channel, Lesser Antilles arc: FAULTING, VOLCANISM, AND TURBIDITY SYSTEMS. *Geochemistry, Geophysics, Geosystems* 17, 2781–2802. <https://doi.org/10.1002/2016GC006337>

Levi, S., Banerjee, S.K., 1976. On the possibility of obtaining relative paleointensities from lake sediments. *Earth and Planetary Science Letters* 29, 219–226. [https://doi.org/10.1016/0012-821X\(76\)90042-X](https://doi.org/10.1016/0012-821X(76)90042-X)

Leynaud, D., Mienert, J., Vanneste, M., 2009. Submarine mass movements on glaciated and non-glaciated European continental margins: A review of triggering mechanisms and preconditions to failure. *Marine and Petroleum Geology* 26, 618–632. <https://doi.org/10.1016/j.marpetgeo.2008.02.008>

Macdonald, R., Hawkesworth, C.J., Heath, E., 2000. The Lesser Antilles volcanic chain: a study in arc magmatism. *Earth-Science Reviews* 49, 1–76.

- Manaker, D.M., Calais, E., Freed, A.M., Ali, S.T., Przybylski, P., Mattioli, G., Jansma, P., Prépetit, C., de Chabalier, J.B., 2008. Interseismic Plate coupling and strain partitioning in the Northeastern Caribbean. *Geophysical Journal International* 174, 889–903. <https://doi.org/10.1111/j.1365-246X.2008.03819.x>
- Mazaud, A., 2005. User-friendly software for vector analysis of the magnetization of long sediment cores: SOFTWARE FOR VECTOR ANALYSIS. *Geochemistry, Geophysics, Geosystems* 6, n/a-n/a. <https://doi.org/10.1029/2005GC001036>
- McHugh, C.M., Seeber, L., Rasbury, T., Strasser, M., Kioka, A., Kanamatsu, T., Ikebara, K., Usami, K., 2020. Isotopic and sedimentary signature of megathrust ruptures along the Japan subduction margin. *Marine Geology* 428, 106283. <https://doi.org/10.1016/j.margeo.2020.106283>
- Morena, P., 2020. Paléosismologie et potentiel sismogène de la zone de subduction des Petites Antilles à partir de l'enregistrement sédimentaire. L'UNIVERSITE DE BRETAGNE OCCIDENTALE.
- Münch, Ph., Cornee, J.-J., Lebrun, J.-F., Quillevere, F., Verati, C., Melinte-Dobrinescu, M., Demory, F., Smith, B., Jourdan, F., Lardeaux, J.-M., De Min, L., Leticee, J.-L., Randrianasolo, A., 2014. Pliocene to Pleistocene vertical movements in the forearc of the Lesser Antilles subduction: insights from chronostratigraphy of shallow-water carbonate platforms (Guadeloupe archipelago). *Journal of the Geological Society* 171, 329–341. <https://doi.org/10.1144/jgs2013-005>
- Nakajima, T., Kanai, Y., 2000. Sedimentary features of seismoturbidites triggered by the 1983 and older historical earthquakes in the eastern margin of the Japan Sea. *Sedimentary Geology* 135, 1–19. [https://doi.org/10.1016/S0037-0738\(00\)00059-2](https://doi.org/10.1016/S0037-0738(00)00059-2)
- Nocquet, J.-M., Jarrin, P., Vallée, M., Mothes, P.A., Grandin, R., Rolandone, F., Delouis, B., Yepes, H., Font, Y., Fuentes, D., Régnier, M., Laurendeau, A., Cisneros, D., Hernandez, S., Sladen, A., Singauchon, J.-C., Mora, H., Gomez, J., Montes, L., Charvis,

- P., 2017. Supercycle at the Ecuadorian subduction zone revealed after the 2016 Pedernales earthquake. *Nature Geosci* 10, 145–149. <https://doi.org/10.1038/ngeo2864>
- Noda, A., TuZino, T., Kanai, Y., Furukawa, R., Uchida, J., 2008. Paleoseismicity along the southern Kuril Trench deduced from submarine-fan turbidites. *Marine Geology* 254, 73–90. <https://doi.org/10.1016/j.margeo.2008.05.015>
- Pacheco, J.F., Sykes, L.R., 1992. Seismic moment catalog of large shallow earthquakes, 1900 to 1989. *Bulletin of the Seismological Society of America* 82, 1306–1349.
- Patton, J.R., Goldfinger, C., Morey, A.E., Romsos, C., Black, B., Djadjadihardja, Y., Udrehk, 2013. Seismoturbidite record as preserved at core sites at the Cascadia and Sumatra–Andaman subduction zones. *Natural Hazards and Earth System Science* 13, 833–867. <https://doi.org/10.5194/nhess-13-833-2013>
- Philibosian, B., Feuillet, N., Weil-Accardo, J., Jacques, E., Guihou, A., Mériaux, A.-S., Anglade, A., Saurel, J.-M., Deroussi, S., 2022. 20th-century strain accumulation on the Lesser Antilles megathrust based on coral microatolls. *Earth and Planetary Science Letters* 579, 117343. <https://doi.org/10.1016/j.epsl.2021.117343>
- Picard, M., Schneider, J.-L., Boudon, G., 2006. Contrasting sedimentary processes along a convergent margin: the Lesser Antilles arc system. *Geo-Marine Letters* 26, 397–410. <https://doi.org/10.1007/s00367-006-0046-y>
- Polonia, A., Bonatti, E., Camerlenghi, A., Lucchi, R.G., Panieri, G., Gasperini, L., 2013. Mediterranean megaturbidite triggered by the AD 365 Crete earthquake and tsunami. *Sci Rep* 3, 1285. <https://doi.org/10.1038/srep01285>
- Polonia, A., Bonetti, C., Bonetti, J., Çağatay, M.N., Gallerani, A., Gasperini, L., Nelson, C.H., Romano, S., 2021. Deciphering Co-Seismic Sedimentary Processes in the Mediterranean Sea Using Elemental, Organic Carbon, and Isotopic Data. *Geochem Geophys Geosyst* 22. <https://doi.org/10.1029/2020GC009446>

- Pope, E.L., Talling, P.J., Carter, L., Clare, M.A., Hunt, J.E., 2017. Damaging sediment density flows triggered by tropical cyclones. *Earth and Planetary Science Letters* 458, 161–169. <https://doi.org/10.1016/j.epsl.2016.10.046>
- Pouderoux, H., Proust, J.-N., Lamarche, G., Orpin, A., Neil, H., 2012. Postglacial (after 18ka) deep-sea sedimentation along the Hikurangi subduction margin (New Zealand): Characterisation, timing and origin of turbidites. *Marine Geology* 295–298, 51–76. <https://doi.org/10.1016/j.margeo.2011.11.002>
- Ratzov, G., Cattaneo, A., Babonneau, N., Déverchère, J., Yelles, K., Bracene, R., Courboulex, F., 2015. Holocene turbidites record earthquake supercycles at a slow-rate plate boundary. *Geology* 43, 331–334. <https://doi.org/10.1130/G36170.1>
- Ratzov, G., Collot, J.-Y., Sosson, M., Migeon, S., 2010. Mass-transport deposits in the northern Ecuador subduction trench: Result of frontal erosion over multiple seismic cycles. *Earth and Planetary Science Letters* 296, 89–102. <https://doi.org/10.1016/j.epsl.2010.04.048>
- Reeder, M.S., Rothwell, R.G., Stow, D.A.V., 2000. Influence of sea level and basin physiography on emplacement of the late Pleistocene Herodotus Basin Megaturbidite, SE Mediterranean Sea. *Marine and Petroleum Geology* 20.
- van Rijsingen, E.M., Calais, E., Jolivet, R., de Chabalier, J.-B., Jara, J., Symithe, S., Robertson, R., Ryan, G.A., 2021. Inferring Interseismic Coupling Along the Lesser Antilles Arc: A Bayesian Approach. *J Geophys Res Solid Earth* 126. <https://doi.org/10.1029/2020JB020677>
- van Rijsingen, E., Calais, E., Jolivet, R., de Chabalier, J.-B., Robertson, R., Ryan, G., Symithe, S., 2021. Vertical tectonic motions in the Lesser Antilles: linking short- and long-term observations (preprint). *Earth Sciences*. <https://doi.org/10.31223/X5360D>
- Roberts, A.P., 2006. High-resolution magnetic analysis of sediment cores: Strengths, limitations and strategies for maximizing the value of long-core magnetic data. *Physics*

of the Earth and Planetary Interiors 156, 162–178.  
<https://doi.org/10.1016/j.pepi.2005.03.021>

Rothwell, R.G., Reeder, M.S., Anastasakis, G., Stow, D.A.V., Thomson, J., Kähler, G., 2000. Low sea-level stand emplacement of megaturbidites in the western and eastern Mediterranean Sea. *Sedimentary Geology* 135, 75–88. [https://doi.org/10.1016/S0037-0738\(00\)00064-6](https://doi.org/10.1016/S0037-0738(00)00064-6)

Salditch, L., Stein, S., Neely, J., Spencer, B.D., Brooks, E.M., Agnon, A., Liu, M., 2020. Earthquake supercycles and Long-Term Fault Memory. *Tectonophysics* 774, 228289. <https://doi.org/10.1016/j.tecto.2019.228289>

San Pedro, L., Babonneau, N., Gutscher, M.-A., Cattaneo, A., 2017. Origin and chronology of the Augias deposit in the Ionian Sea (Central Mediterranean Sea), based on new regional sedimentological data. *Marine Geology* 384, 199–213. <https://doi.org/10.1016/j.margeo.2016.05.005>

Schlupp, A., n.d. C. Sira, M. Cara, S. Bazin, C. Michel, J. Régnier, C. Beauval, N. Feuillet, J.-B. De Chabalier, A.-V. Barras, S. Auclair, M.-P. Bouin, C. Duclos, M. Granet (2008) - Séisme de Martinique du 29 novembre 2007, rapport du BCSF : synthèse sismologique et étude macrosismique, BCSF2008-R1, 132 p., 266 figures, 3 tableaux, 5 annexes.

Seibert, C., Feuillet, N., Ratzov, G., Beck, C., Cattaneo, A., 2020. Seafloor morphology and sediments transfers in the mixed carbonated-siliciclastic environment of the Lesser Antilles forearc along Barbuda and St. Lucia. *Marine Geology* 106242. <https://doi.org/10.1016/j.margeo.2020.106242>

Snowball, I., Sandgren, P., 2004. Geomagnetic field intensity changes in Sweden between 9000 and 450 cal BP: extending the record of “archaeomagnetic jerks” by means of lake sediments and the pseudo-Thellier technique. *Earth and Planetary Science Letters* 227, 361–376. <https://doi.org/10.1016/j.epsl.2004.09.017>

- Spratt, R.M., Lisiecki, L.E., 2015. A Late Pleistocene sea level stack (preprint). *Ice Dynamics/Marine Archives/Pleistocene*. <https://doi.org/10.5194/cpd-11-3699-2015>
- Stoner, J.S., St-Onge, G., 2007. Chapter Three Magnetic Stratigraphy in Paleoceanography: Reversals, Excursions, Paleointensity, and Secular Variation, in: *Developments in Marine Geology*. Elsevier, pp. 99–138. [https://doi.org/10.1016/S1572-5480\(07\)01008-1](https://doi.org/10.1016/S1572-5480(07)01008-1)
- St-Onge, G., Chapron, E., Mulsow, S., Salas, M., Viel, M., Debret, M., Foucher, A., Mulder, T., Winiarski, T., Desmet, M., Costa, P.J.M., Ghaleb, B., Jaouen, A., Locat, J., 2012. Comparison of earthquake-triggered turbidites from the Saguenay (Eastern Canada) and Reloncavi (Chilean margin) Fjords: Implications for paleoseismicity and sedimentology. *Sedimentary Geology* 243–244, 89–107. <https://doi.org/10.1016/j.sedgeo.2011.11.003>
- St-Onge, G., Mulder, T., Francus, P., Long, B., 2007. Chapter Two Continuous Physical Properties of Cored Marine Sediments, in: *Developments in Marine Geology*. Elsevier, pp. 63–98. [https://doi.org/10.1016/S1572-5480\(07\)01007-X](https://doi.org/10.1016/S1572-5480(07)01007-X)
- St-Onge, G., Stoner, J.S., Hillaire-Marcel, C., 2003. Holocene paleomagnetic records from the St. Lawrence Estuary, eastern Canada: centennial- to millennial-scale geomagnetic modulation of cosmogenic isotopes. *Earth and Planetary Science Letters* 209, 113–130. [https://doi.org/10.1016/S0012-821X\(03\)00079-7](https://doi.org/10.1016/S0012-821X(03)00079-7)
- Symithe, S., Calais, E., de Chabalier, J.B., Robertson, R., Higgins, M., 2015. Current block motions and strain accumulation on active faults in the Caribbean: CURRENT CARIBBEAN KINEMATICS. *Journal of Geophysical Research: Solid Earth* 120, 3748–3774. <https://doi.org/10.1002/2014JB011779>
- Talling, P.J., 2021. Fidelity of turbidites as earthquake records. *Nat. Geosci.* 14, 113–116. <https://doi.org/10.1038/s41561-021-00707-2>

Talling, P.J., 2014. On the triggers, resulting flow types and frequencies of subaqueous sediment density flows in different settings. *Marine Geology* 352, 155–182.  
<https://doi.org/10.1016/j.margeo.2014.02.006>

Tauxe, L., 1993. Sedimentary records of relative paleointensity of the geomagnetic field: Theory and practice. *Reviews of Geophysics* 31, 319.  
<https://doi.org/10.1029/93RG01771>

Tauxe, L., Pick, T., Kok, Y.S., 1995. Relative paleointensity in sediments: A Pseudo-Thellier Approach. *Geophysical Research Letters* 22, 2885–2888.  
<https://doi.org/10.1029/95GL03166>

Usami, K., Ikehara, K., Kanamatsu, T., McHugh, C.M., 2018. Supercycle in great earthquake recurrence along the Japan Trench over the last 4000 years. *Geosci. Lett.* 5, 11.  
<https://doi.org/10.1186/s40562-018-0110-2>

Van Daele, M., Meyer, I., Moernaut, J., De Decker, S., Verschuren, D., De Batist, M., 2017. A revised classification and terminology for stacked and amalgamated turbidites in environments dominated by (hemi)pelagic sedimentation. *Sedimentary Geology* 357, 72–82. <https://doi.org/10.1016/j.sedgeo.2017.06.007>

Xuan, C., Channell, J.E.T., 2009. UPmag: MATLAB software for viewing and processing u channel or other pass-through paleomagnetic data: TECHNICAL BRIEF. *Geochemistry, Geophysics, Geosystems* 10, n/a-n/a.  
<https://doi.org/10.1029/2009GC002584>

Zahibo, N., Pelinovsky, E., Okal, E., Yalçiner, A., Kharif, C., Talipova, T., Kozelkov, A., 2005. The earthquake and tsunami of November 21, 2004 at Les Saintes, Guadeloupe, Lesser Antilles. *Science of Tsunami Hazards* 23, 25–39.

# **CHAPITRE 3**

## **INFLUENCE DES CHANGEMENTS LITHOLOGIQUES SUR**

### **L'ENREGISTREMENT DU SIGNAL PALEOMAGNETIQUE BASEE SUR DES**

### **COUCHES QUATERNAIRES DEPOSEES RAPIDEMENT DANS LES PETITES**

### **ANTILLES : UN NOUVEAU MODELE DE DEPOT POUR LES COMPLEXES**

### **HOMOGENITE-TURBIDITES**

#### **3.1 RESUME EN FRANÇAIS DU TROISIEME ARTICLE**

Les océans représentent plus de 70 % de la surface de la Terre, ce qui fait des sédiments marins des archives idéales pour étudier le champ géomagnétique au cours du temps. Cependant, la manière dont le champ ambiant est enregistré lors de la sédimentation des particules magnétiques reste mal comprise. Pour améliorer notre compréhension de cet enregistrement, plusieurs études ont mené des expériences de redéposition de sédiment en champ magnétique contrôlé. Étant donné que ces expériences reflètent des dépôts rapides de sédiments, les turbidites ont commencé à avoir de l'intérêt pour les études paléomagnétiques. Cependant, ces études ne dissocient pas les turbidites des complexes homogénite-turbidites (HmTu), alors que ces derniers, associés à des séismes et/ou des tsunamis, présentent une couche supérieure homogène qui ne peut pas être le fruit d'un courant de turbidité uniquement. L'étude paléomagnétique de vingt HmTu identifiés dans trois carottes sédimentaires prélevées dans des bassins de l'avant-arc des Petites Antilles a permis de mieux comprendre comment ces couches sédimentaires se sont déposées. Les aimantations rémanentes naturelle et anhydostérique ont été mesurées et utilisées pour obtenir les données de paléodirection incluant l'angle de déviation maximale (MAD) et les variations de la taille des grains magnétiques. Les MAD ont été utilisés pour déterminer la qualité de l'enregistrement paléomagnétique et pour dissocier les HmTu en deux processus hydrodynamiques distincts. En utilisant les variations de l'inclinaison, cet article développe un nouveau modèle de déposition des HmTu et explore l'impact des turbidites sur l'enregistrement du signal paléomagnétique. Pour étudier cet impact, quatorze turbidites ont

été ajoutées aux vingt HmTu tronqués de leur partie homogène. Une relation quasi-logarithmique est identifiée entre la taille des grains magnétiques et l'épaisseur des turbidites, alors que l'inclinaison présente une relation linéaire avec l'épaisseur. Ces deux relations peuvent être l'identification de processus différents, et en particulier que les variations d'inclinaison sont moins affectées par la flocculation que la turbulence du milieu marin. Cette étude suggère donc que les homogénites soient à privilégier plutôt que les turbidites comme élément de comparaison avec les expériences de dépôt étant donné que pas ou peu de turbulence affecte la section homogène.

Ce troisième article intitulé « *Influence of lithological changes on the paleomagnetic record based on Quaternary rapidly deposited layers from the Lesser Antilles: a new model for the deposition of homogenite-turbidite complexes* », fut corédigé par moi-même ainsi que mon directeur de recherche Guillaume St-Onge (UQAR-ISMER) et ma directrice de recherche Nathalie Feuillet (IPGP), ainsi que les chercheuses Julie Carlut (IPGP) et Eva Moreno (LOCEAN/MNHN). Ce manuscrit sera soumis dans la revue *Geochemistry, Geophysics, Geosystems* (G<sup>3</sup>). Ma contribution en tant que premier auteur a été de réalisé l'état de l'art, l'analyse en laboratoire d'une grande partie des échantillons, le développement du modèle de dépôt, l'analyse statistique et la rédaction de l'article. Guillaume St-Onge a participé à la recherche sur l'état de l'art, supervisé les travaux analytiques et statistiques, aidé dans l'analyse et l'interprétation des données et la rédaction. Nathalie Feuillet a participé à la recherche sur l'état de l'art, élaboré et dirigé le projet de la mission océanographique qui a permis la collecte des carottes sédimentaire, aidé dans l'analyse des données et la rédaction. Julie Carlut et Eva Moreno m'ont aidé dans la réalisation de prélèvement et d'analyse d'échantillon au sein de l'IPGP, ainsi que dans le suivi de l'analyse des données et de la rédaction. Une partie des résultats ont été exposés lors de présentations orales à l'*International Sedimentology Congress* (ISC) qui s'est déroulé à Québec (Canada) en 2018, et au congrès des étudiants du GEOTOP en 2021 à Québec (Canada) en conférences virtuelles.

### **3.2 INFLUENCE OF LITHOLOGICAL CHANGES ON THE PALEOMAGNETIC RECORD BASED ON QUATERNARY RAPIDLY DEPOSITED LAYERS FROM THE LESSER ANTILLES: A NEW MODEL FOR THE DEPOSITION OF HOMOGENITE-TURBIDITE COMPLEXES.**

Oceans represent over 70 % of Earth's surface, which makes marine sediment an ideal archive to study the geomagnetic field through time. However, how the ambient field is recorded by settling magnetic particles remains incomplete. To improve this knowledge, several studies realized redeposition experiments. Given that such experiments reflect the deposition of rapidly deposited layers, turbidites began to gain paleomagnetic interest. However, turbidites and homogenite-turbidite complexes (HmTu) were used indistinctively. While turbidites are the result of a turbidity current, HmTu were previously associated to tsunami and earthquakes events with a generally thick homogenous uppermost layer that cannot be the result of a sole turbidity current. The paleomagnetic study of twenty HmTu identified on three cores collected in Lesser Antilles fore-arc basins enable us to better understand how such layers have settled. Natural remanent and anhysteretic remanent magnetizations were measured and used to recover directional data including maximum angular deviation (MAD), and magnetic grain size variations. The MAD was used to assess the quality of the paleomagnetic data and enabled us to dissociate HmTu into two hydrodynamic processes. Based on the inclination variations, this paper develops a new depositional model of HmTu in deep marine bounded basins and explores the impact of turbidite deposits on the paleomagnetic data. Fourteen turbidites have been added to the basal HmTu dataset for a total of thirty-four beds available. A quasi-logarithmic relationship was found between magnetic grain size and turbidite thickness, while inclination reveals a linear relationship with thickness. These two different trends might be the reflection of distinct processes and, in particular, turbidite inclination variations are less affected by flocculation than by turbulence. This study suggests analyzing homogenite rather than turbidite to compare with redeposition experiments, as no turbulence occurs during the latter.

### **3.2.1 Introduction**

Sediments are of great interest for paleomagnetic studies, in particular for their global coverage and possible continuous record of past Earth's magnetic field behavior (e.g. Stoner and St-Onge, 2007; Mazaud et al., 2012; Liu et al., 2016; Deschamps et al., 2018; Channell et al., 2019; Bieber et al., 2021; Hatfield et al., 2021; Lisé-Pronovost et al., 2021). Most of paleomagnetic studies avoided instantaneous deposits as they do not record high fidelity paleomagnetic variations. The key point of sediment paleomagnetism is the acquisition of a natural remanent magnetization (NRM), which is the sum of a detrital remanent magnetization (DRM) and a post-DRM (pDRM). Understanding the process behind the acquisition of DRM and pDRM remains imperfect (Tauxe et al., 2006). Over the last decades, several studies tried to better constrain this remanent magnetization acquisition through redeposition experiments (e.g. Tauxe and Kent, 1983; Spasov and Valet, 2012; Valet et al., 2017; Chang et al., 2021). However, such experiments are analogous to turbidity current deposits, but not to hemipelagic background sediment deposits. Therefore, a few (paleo) magnetic studies began to investigate turbidite data (e.g. Piguet et al., 2000; St-Onge et al., 2004; Campos et al. 2013; Tanty et al., 2016; Philippe, 2019). Turbidites are well studied by sedimentologists, and many specific characteristics were identified after the ideal Bouma sequence was defined (Bouma, 1961). The most common facies were summarized by several papers including Mulder et al. (1996), and Stow and Smilie (2020) to mention a few. One peculiar deposit reveals a homogenous thick uppermost layer called megaturbidite (Mulder et al., 2009) or complex homogenite-turbidite (Beck et al., 2012; Seibert et al., 2021). From three giant piston cores recovered during the CASEIS cruise in July 2016 (Feuillet, 2016), twenty homogenite-turbidite complexes (HmTu) were identified (Bieber et al., in prep.). Based on the paleomagnetic analysis of these HmTu, the present study will present a new depositional model using variations in paleomagnetic inclination. The differentiation of the turbidite and homogenite part of these complexes allows for investigating a total of thirty-four turbidites and how their depositional processes affect the magnetic grain size variations and inclination variations. The identification of two depositional processes within one event

including one strongly affected by hydrodynamic forces (i.e. turbidite), while the other one that is driven by gravity settling with a standing seiche-like wave (i.e. homogenite), makes the HmTu complex a perfect candidate to better understand how sediment acquires a NRM.

### 3.2.2 Materials and methods

Core CAS16-04PC, CAS16-14PC, and CAS16-36PC were collected by the R/V Pourquoi Pas? (French oceanographic fleet) during the CASEIS cruise in 2016 (Feuillet, 2016) in fore-arc basins (Fig. 35) of the Lesser Antilles volcanic arc system at a water depth of 5706, 5821, and 6100 meters below sea level respectively. These cores are stored in the marine collection of the Muséum national d'Histoire naturelle (Paris, France) under the number MNHN-GS-CAS16-##PC (# = core number). Core locations were selected specifically to be disconnected from the continental terrigenous input (Seibert et al., 2020; Morena et al., in prep). Each core was analyzed on-board using a GEOTEK multi-sensor core logger to determine the physical and magnetic parameters of the sediments including bulk magnetic susceptibility ( $k$ ). Lithologic description and analysis of each core have been interpreted and published in Bieber et al. (in prep). where all turbidite and homogenite-turbidite complexes (HmTu) recorded over the past  $\approx 70$  ka were reported. Paleomagnetic and rock magnetic analyses were performed at the Institut des sciences de la mer de Rimouski, ISMER (Rimouski, QC, Canada) of the Université du Québec à Rimouski (UQAR). Natural remanent magnetization (NRM) of each core was measured on a 2G Enterprises 755SRM-1.65 cryogenic magnetometer. Thereafter, sediment was stepwise demagnetized at 5-mT increments using an alternative field (5 to 100 mT maximum). For sections mostly composed of rapidly deposited layers (RDL, St-Onge et al., 2012), stepwise demagnetization was performed from 5 to 60 mT. Following the same stepwise demagnetization, an anhysteretic remanent magnetization (ARM) was secondly induced using a 100 mT peak AF and a 50  $\mu\text{m}$  direct current (DC) biasing field.  $k_{\text{ARM}}$  was calculated by normalizing the ARM with the bias field value and is used in the  $k_{\text{ARM}}/k$  ratio as a magnetic grain size indicator (e.g., Banerjee et al., 1981; King et al., 1982). The present study focuses on inclination ( $I^\circ$ ) and maximum angular deviation (MAD), as well as  $k$  and  $k_{\text{ARM}}$  of

RDL,  $I^{\circ}$  and MAD values result from the principal component analysis (Kirschvink, 1980) of the NRM using demagnetization steps from 10 to 45 mT and the Excel spreadsheet developed by Mazaud (2005). MAD values can be used to assess the quality of the directional data (i.e., inclination and declination, e.g., Stoner and St-Onge 2007). Several subsamples were analyzed on a MicroMag 2900 alternating gradient force magnetometer (AGM) from Princeton Measurements Corporation to measure the progressive acquisition of isothermal remanent magnetization (IRM). These curves are used to analyze the coercivity distribution based on the first derivative of this progressive acquisition.

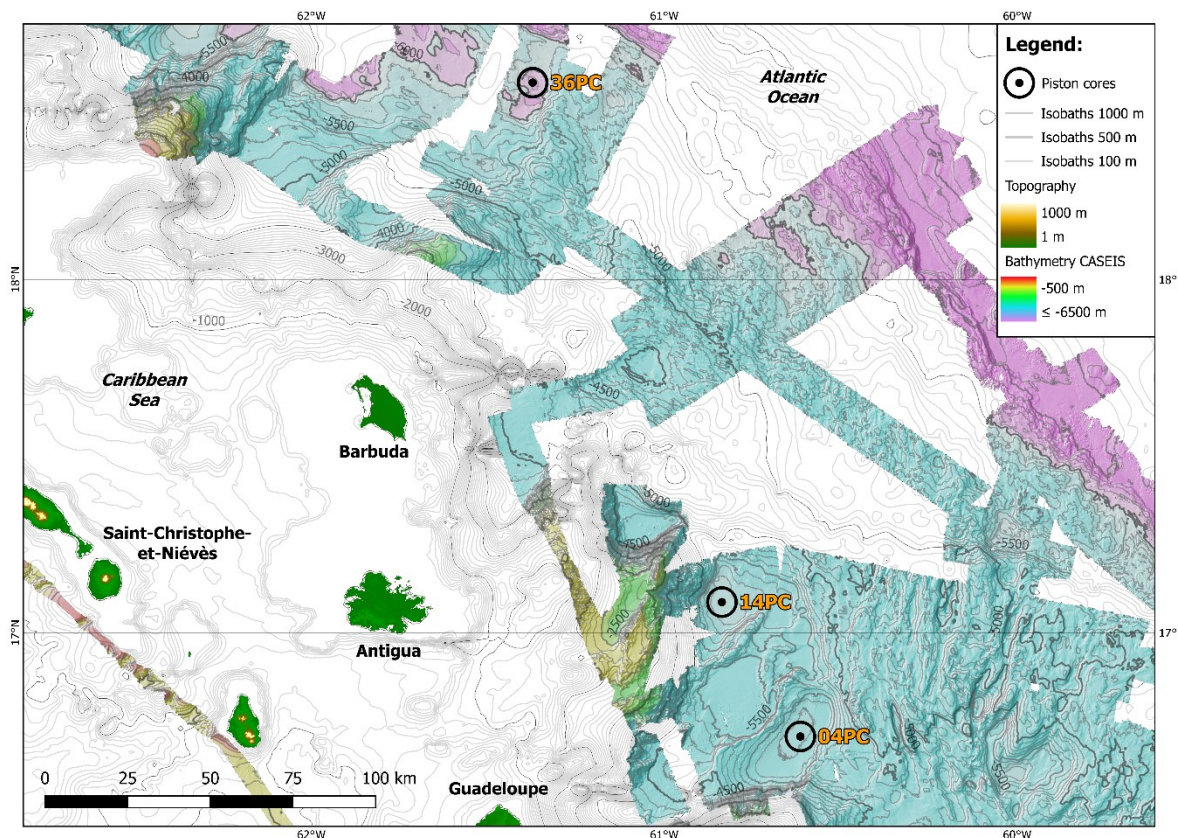


Figure 35 - Location of cores CAS16-04PC, -14PC, and -36PC in the western Atlantic Ocean (Lesser Antilles fore-arc basins).

### 3.2.3 Results

#### 3.2.3.1 Turbidite characterization

Thirteen turbidites were identified on cores CAS16-04PC, CAS16-14PC, and CAS16-36PC (Bieber et al. in prep). Twelve present a fining upward magnetic grain size variations based on the  $k_{ARM}/k$  parameter (Fig. 36). This magnetic grain size variation is consistent with the analysis of density parameters. The four cm-thick turbidite observed in core CAS16-14PC is the only one with decreasing  $k_{ARM}/k$  values. The mean range ( $\Delta$ ) of  $k_{ARM}/k$  is 3.7 for core CAS16-04PC, while it is 5.7 and 5.0 for cores CAS16-14PC and CAS-36PC.

For each core, two demagnetization diagrams from a single turbidite (10-cm interval) are shown in Figure 37. Their associated orthogonal projections present a well-defined single component magnetization passing through the origin. These samples also reveal that 90 % of the demagnetization is already removed before the 50 mT step, which is typical of low coercivity minerals with larger grains.  $\Delta I$  show similar variations between cores with a mean value of  $8.8^\circ$  for the core CAS16-04PC, while the two other cores depict higher values of  $39.0^\circ$  and  $16.4^\circ$  respectively. Range data are shown in Figure 36 with left-right gray arrows. All MAD values range from  $1^\circ$  to  $40^\circ$  with the highest values found at the base and the lowest in the uppermost parts of turbidites. Small turbidites (< 5 cm) reveal MAD values <  $5^\circ$ .

#### 3.2.3.2 Homogenite-Turbidite complexes (HmTu) characterization

Twenty HmTu's were identified and analyzed on the three cores presented in this paper. Turbidite basal parts range from 6 to 173 cm in thickness with an average of 58 cm. They are defined as turbidites with normal grading and similar mean  $\Delta k_{ARM}/k$  values of 3.7, 4.7, and 5.0 for cores CAS16-04PC, -14PC, and -36PC (Fig. 38). In contrast with turbidite,  $\Delta I$  is more important with mean values of  $37.0^\circ$ ,  $48.0^\circ$ , and  $77.6^\circ$  for the respective cores, however, like the turbidites, MAD values are ranging from  $1^\circ$  to  $29^\circ$  with higher values at the base of the event and lowest values at the top. Typical demagnetization diagrams and orthogonal

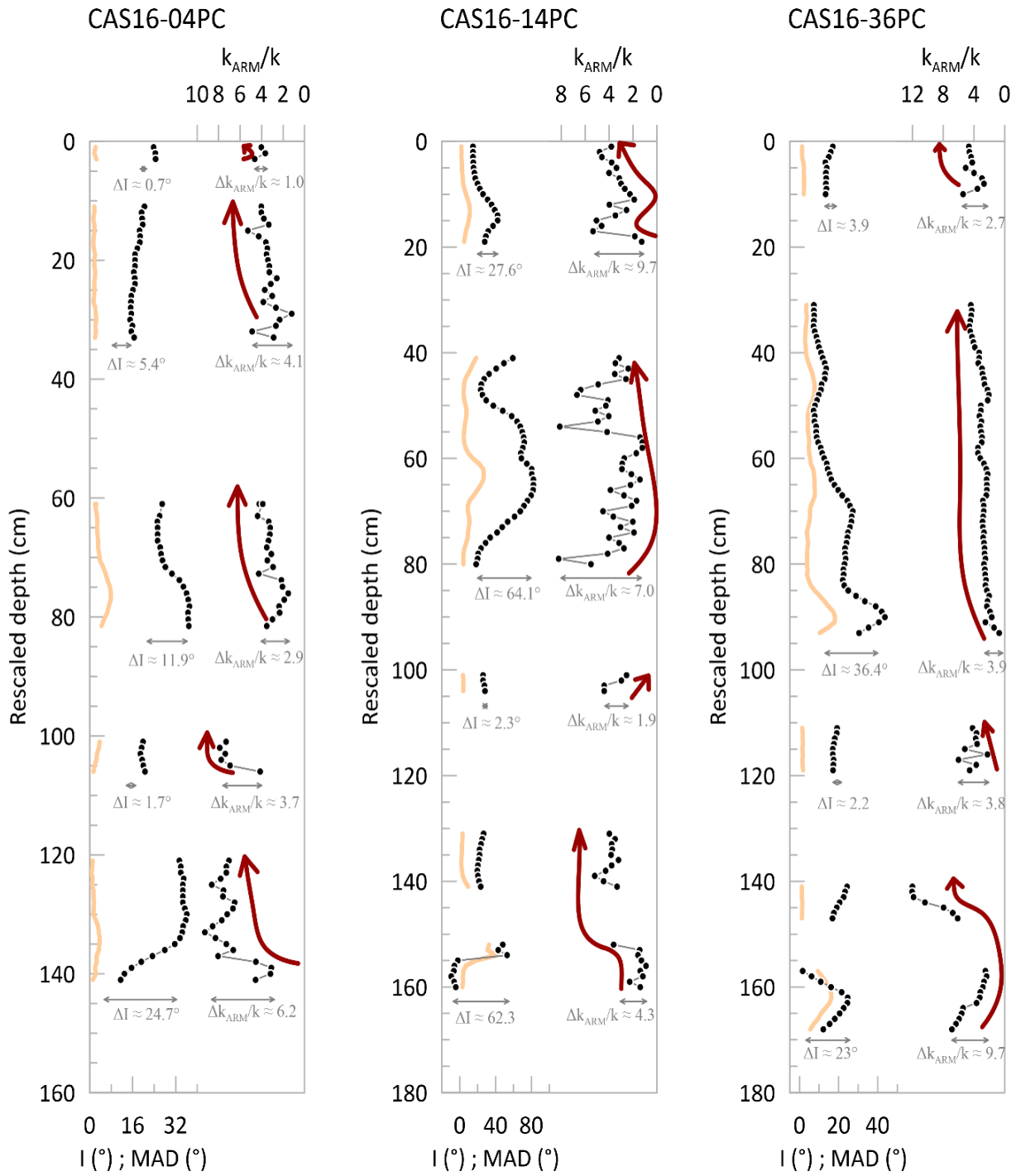


Figure 36 - Inclination (including MAD values in orange)) and magnetic grain size parameter ( $k_{ARM}/k$ ) as a function of rescaled depth (cm) from turbidites identified in each core. Dark red arrows follow grains size variations from the bottom to top of each deposit. Grey arrows represent the range in inclination and  $k_{ARM}/k$ .

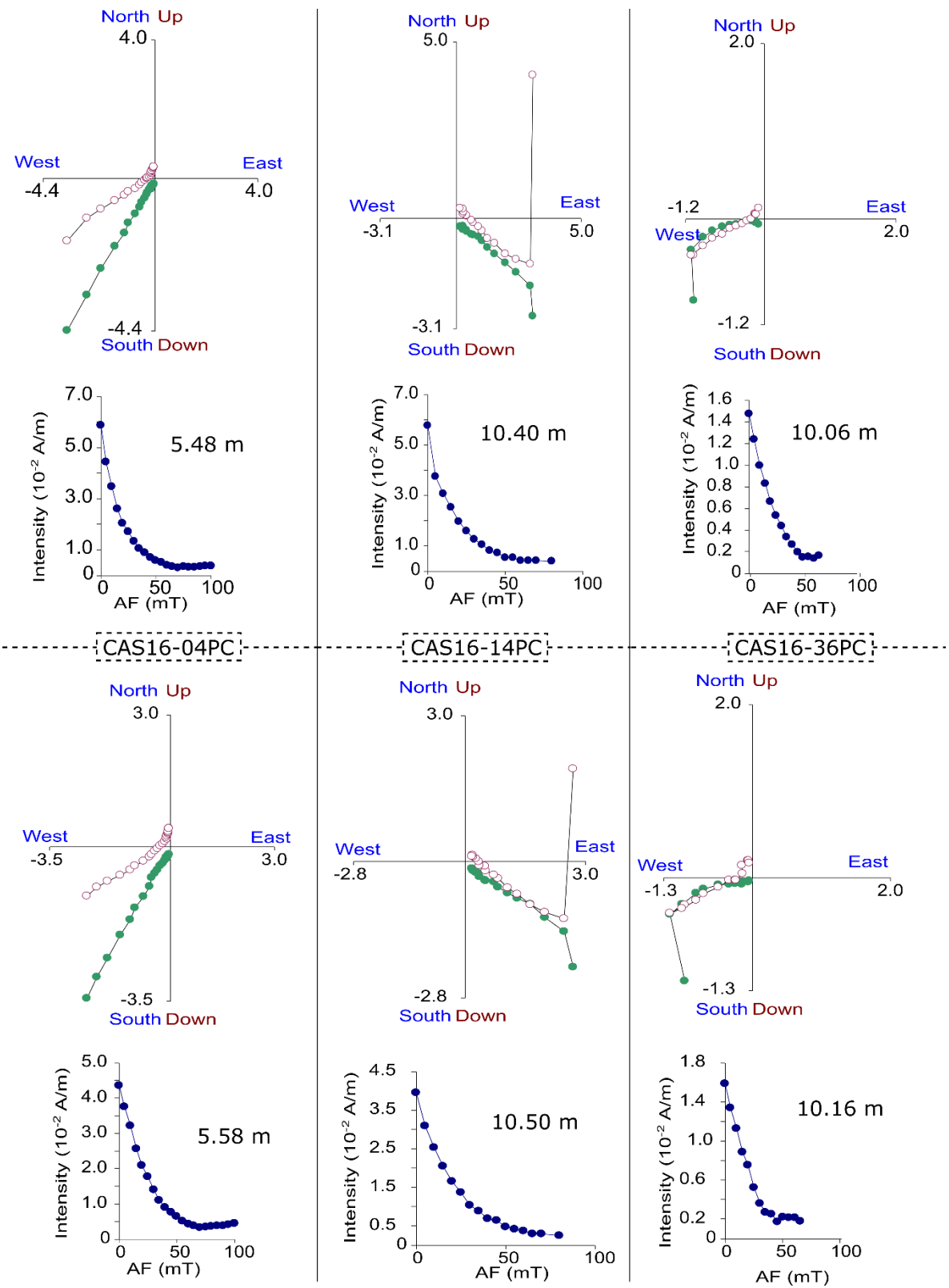


Figure 37 - Two typical orthogonal projections with the associated demagnetization curves for one turbidite example in each core.

projections are shown in Figure 38. Homogenite (Hm) sections reveal a well-defined single component behavior passing through the origin, while the turbidite (Tu) sections acquire a new remanence magnetization after the 50 mT step for core CAS16-04PC and core CAS16-36PC. A minimum of 90 % of the magnetization is lost before the 50 mT step for all Tu sections. Normalized coercivity distributions (Fig. 40) reveal a higher proportion of low coercivity minerals in Tu (brown curves) than Hm (yellow curves) and that Hm progressively reaches similar coercivity distribution as hemipelagic background sediment (HMPL, green curves).

Considering that the Tu and Hm sections of these complexes show very different values, they have been separated into two sections (Fig. 41-A for homogenite and Fig. 41-B for turbidite). The homogenite reveals a sinusoidal variation of inclination and declination with MAD values similar to hemipelagic background sediments (HMPL; Bieber et al., in prep), while the turbidite sections reveal high inclination and declination at the base that decreases sinusoidally to values closer to the homogenite section. We calculated the standard deviation ( $\sigma$ ) of inclination, declination, and MAD angles for the three types of deposits of each core.  $\sigma$  variations reveal two major patterns (Fig. 42): 1) MAD value of HMPL and Hm are quite similar with a mean  $\sigma$  respectively equal to 2.6 and 1.6, while it is about 5.5 for Tu. 2) Inclination and declination  $\sigma$  show the same behavior for each sediment type with  $\sigma_{\text{HMPL}} < \sigma_{\text{Hm}} < \sigma_{\text{Tu}}$ . Core CAS16-14PC is the only one that shows high inclination  $\sigma$  variations that can be inferred to the very small amount of hemipelagic background sediments available (composite record of 0.81 MCD long) with more RDL affecting this HMPL.

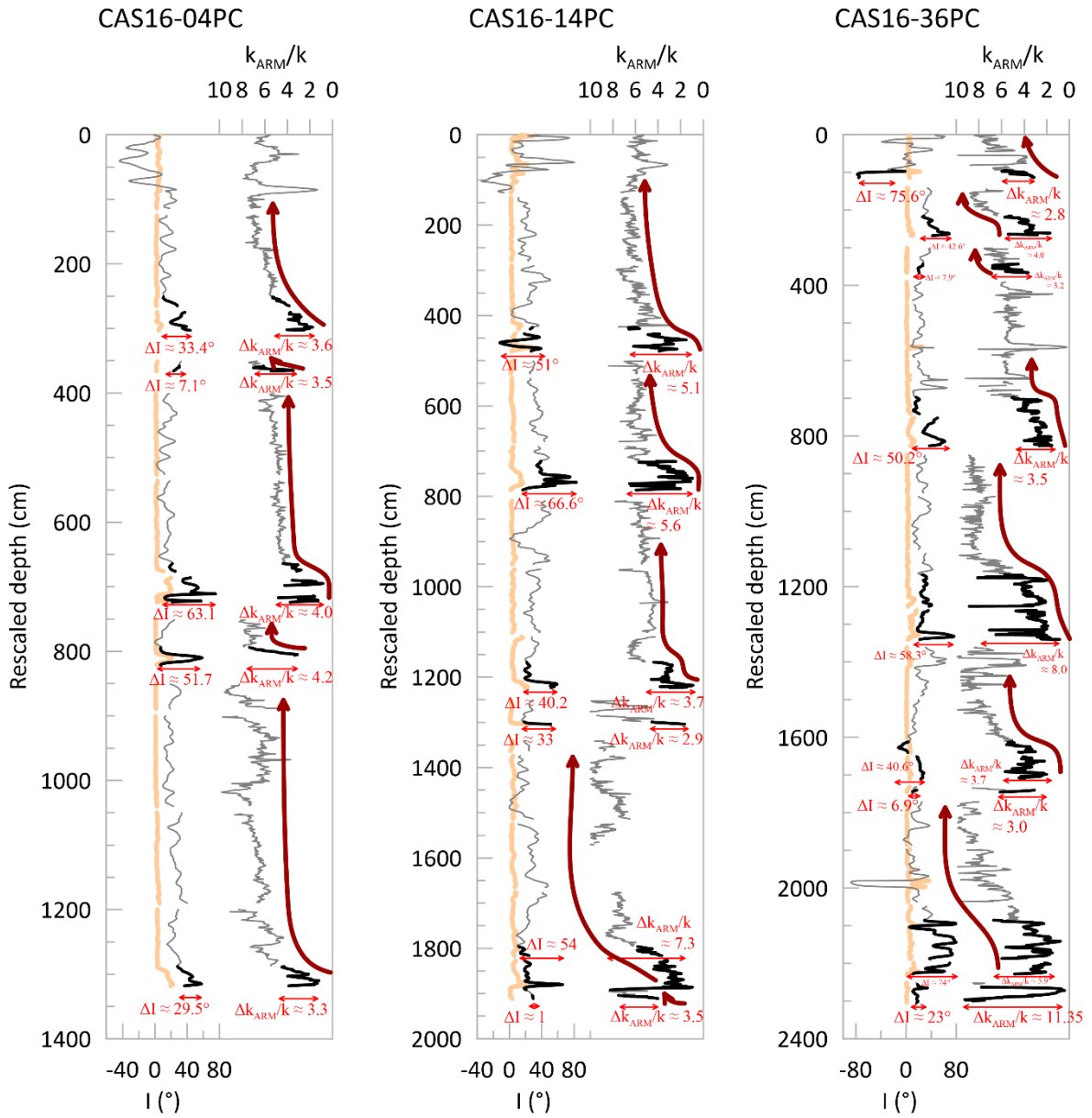


Figure 38 - Inclination (including MAD values in orange) and magnetic grain size parameter ( $k_{ARM}/k$ ) as a function of rescaled depth (cm) from homogenite-turbidite complexes identified in each core. Dark red arrows follow grains size variations from bottom to the top of each deposit. Grey arrows represent the range of inclination and  $k_{ARM}/k$ .

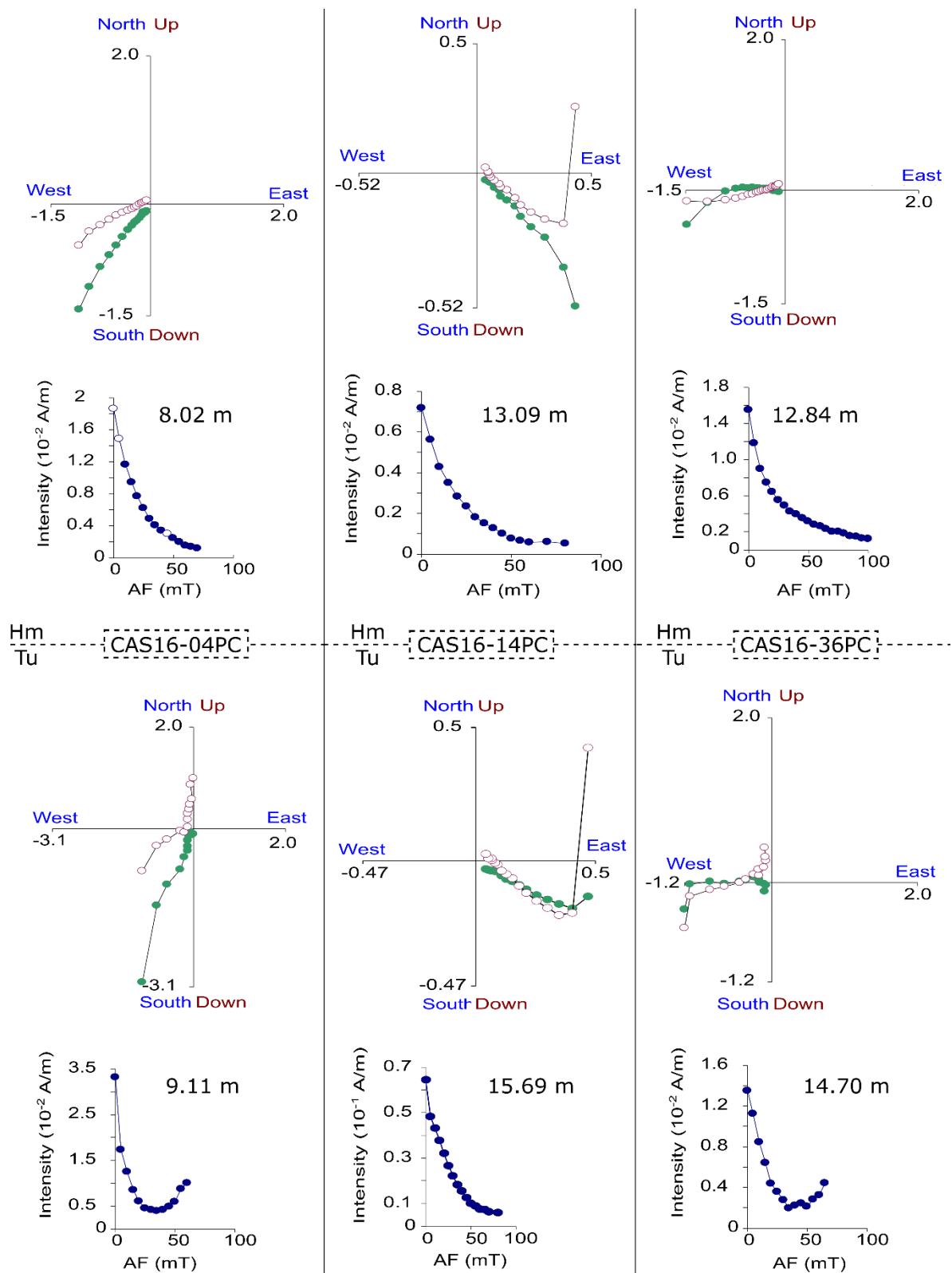


Figure 39 - Typical orthogonal projection (Zijderveld, 1967) with the associated demagnetization curve for one homogenite-turbidite complex in each core. Top: homogenite part; bottom: turbidite part. White circles (green circles) represent projections on the vertical plane (horizontal plane).

### 3.2.4 Discussion

#### 3.2.4.1 HmTu magnetic mineral deposition model

Turbidite and HmTu show similar physical and magnetic parameters except that HmTu has a thick homogenous upper section (up to 6-meter in thickness) with a magnetic grain size sequence slightly fining upward (Fig. 38). Depositional processes associated with homogenite-turbidite are not well constrained despite several attempts. Kastens and Cita (1981) were the first to introduce the term homogenite for a sediment deposit triggered by tsunamis in the Mediterranean Sea. Siegenthaler (2021) explains homogenites with slide/seiche dynamics occurring in large lakes after earthquake-triggered mass movement. Mulder et al. (2009) proposed a depositional model based on a seiche-effect induced by the classical turbidity current that will keep finer particles in the water column, while Beck (2009) proposed a seiche-like water motion induced by an earthquake to maintain and segregate suspended load after an hyperpycnal flow. More recently, Polonia et al. (2017) suggest a depositional model in which a structureless homogenite underly a laminated seiche unit induced by an earthquake surface-wave and/or the surge of a tsunami. Similarly, homogenites observed in the present study are structureless, but with slight variations of density according to CT-scan images. While physical parameters are consistent with previous studies – homogenous over thickness –, paleomagnetic inclination and MAD provide new insight on the depositional process. The mean of the inclination's standard deviation varies by a factor of 1.3 and 1.5 between HMPL and Hm, and between Hm and Tu. This  $\sigma$  inclination variation in such rapidly deposited layers indicates that the sediment is not recording paleomagnetic secular variations, but rather some depositional processes.  $\sigma$  values of the MAD (Fig. 42) indicate that HMG deposits in a relatively slow hydrodynamic environment close to background hemipelagic sediment. In addition, MAD

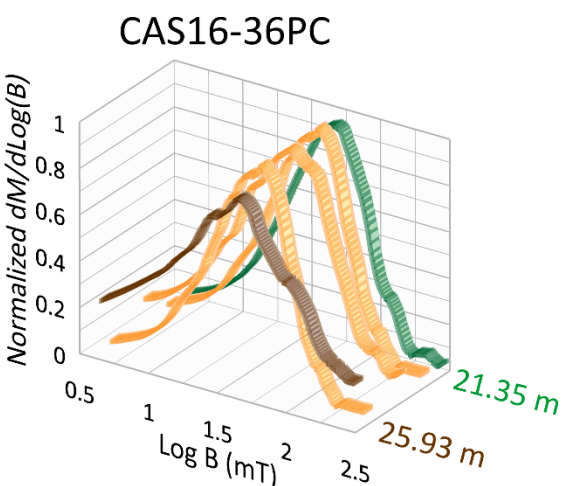
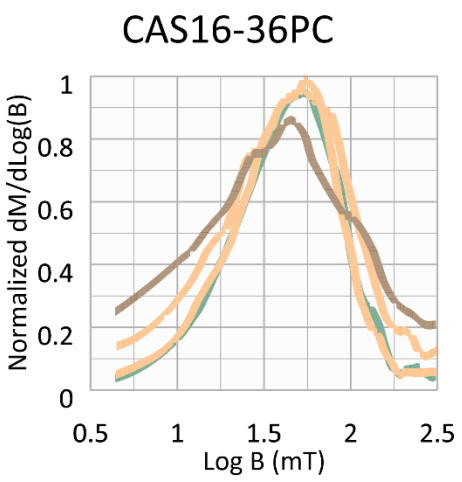
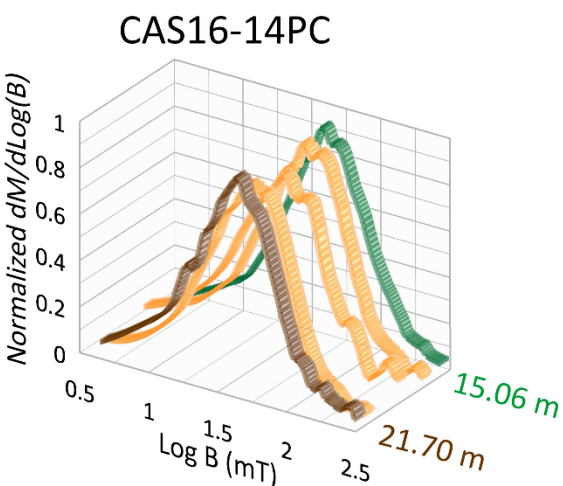
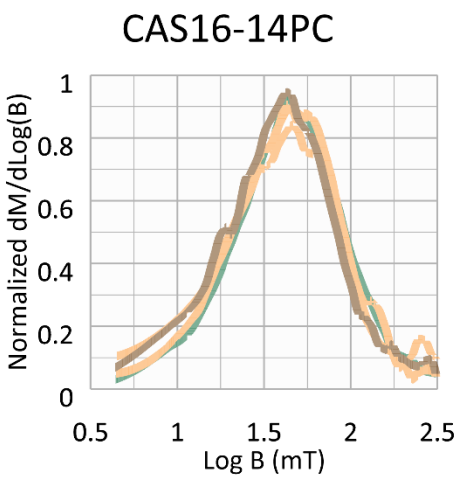
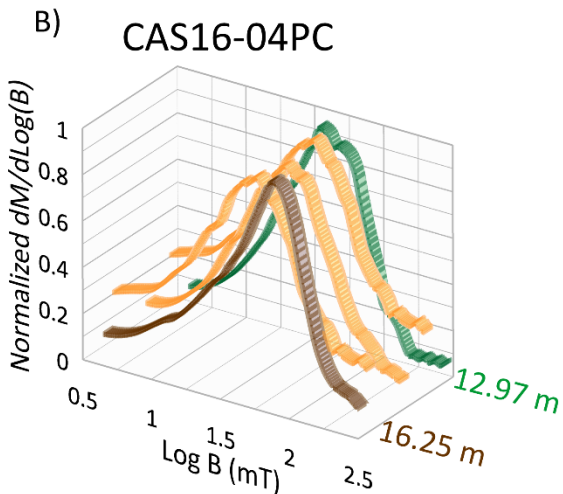
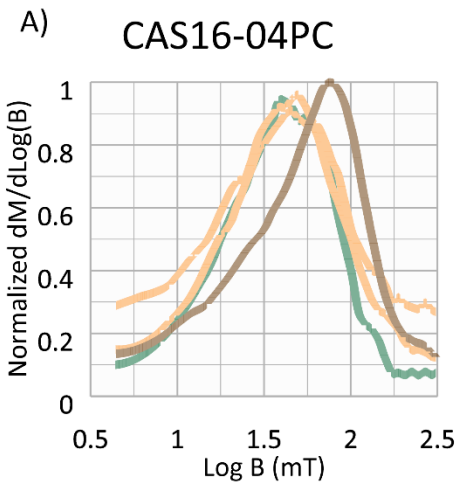


Figure 40 - A) Normalized coercivity distribution made from the first derivative of IRM acquisition curves. Brown, yellow and green curves represent Tu, Hm, and hemipelagite respectively. B) Same figure as A) but with a 3D rotation. The depth of each turbidite and hemipelagite are in their respective color

values of HMG and HMPL are below  $5^\circ$ , indicating a record of high-quality data in these environments. By focusing on one example from core CAS16-04PC (Fig. 43), it is possible to follow the magnetic grain journey during the deposition of the HmTu complex. The basal turbidite motion is easily observed with the highest MAD values of the deposit, along with inclination values with the largest offset from the GAD values. These data indicate a combination of turbulent conditions during the deposition of the basal turbidite along with

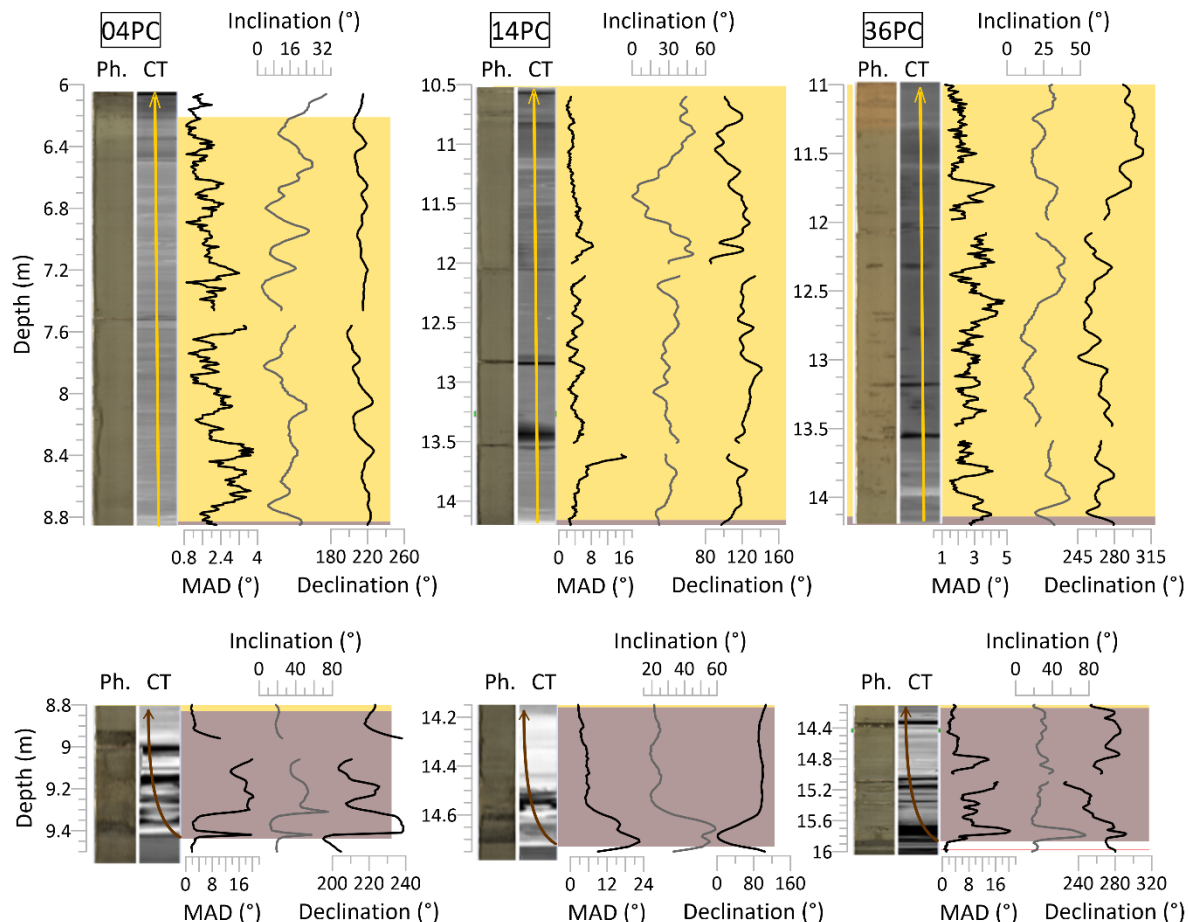


Figure 41 - Top: Homogenite part of HmTu with from left to right high-definition photography, CT-scan images, MAD ( $^\circ$ ), inclination ( $^\circ$ ), and declination ( $^\circ$ ). Bottom: Same parameters for the turbidite part of HmTu deposits.

the presence of coarser grains that are unreliable for the recording of a coherent paleomagnetic signal. However, a generalized oscillatory record of inclination is found in the basal HmTu record (Fig. 38 and 41), while it is not with the inclination of strict turbidite (Fig. 36). Following the basal Tu deposit, inclination oscillation increases along the homogenite section. MAD values are low and express a good portion of the paleomagnetic record over the sequence. While the homogenites of cores CAS16-04PC, -14PC, and -36PC are structureless on high-resolution photography and CT-scan images (Bieber et al., in prep), we interpret the oscillatory record of inclination as the result of a seiche-like effect on the water column with fluctuating bottom water to seabed pressure. Analysis of bottom pressures was previously performed in the coastal environment (Suhayda, 1977, 1984) and linked with crest and trough of surface waves as well as internal waves, which explain the ability of homogenite sediments to record inclination variations. This oscillatory motion cannot systematically affect the declination record because the oscillatory system might be aligned

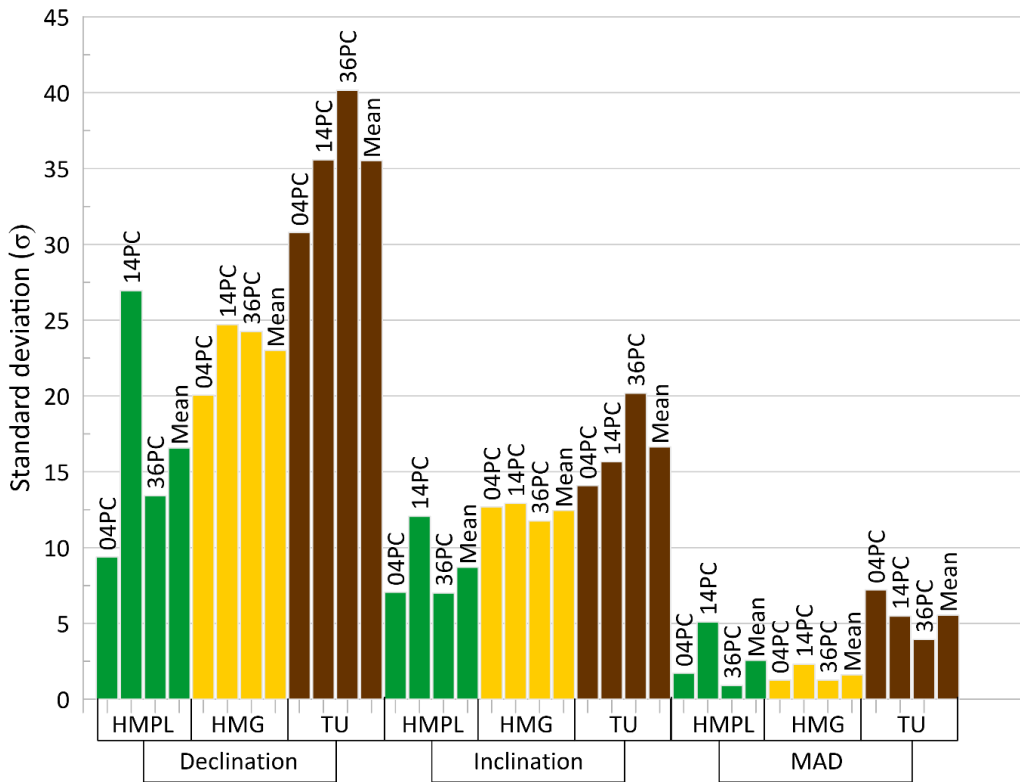


Figure 42 - Bar chart of HMPL (green), HMG (yellow) and TU (brown) declination, inclination, and MAD standard deviation ( $\sigma$ ) for each core and total mean values.

to the paleomagnetic vector, which prevents from using the declination. Finally, hydrodynamic conditions of the seiche-like effect drop and stop to affect the deposition of the magnetic grains as they are mainly influenced by Earth's magnetic field. This is reflected in the values typical of the GAD observed in the hemipelagic sediments immediately above the homogenite deposit. This oscillatory nature of the paleomagnetic signal is observed in all the homogenites found in cores CAS16-04PC, CAS16-14PC, and CAS16-36PC.

### 3.2.4.2 Natural remanent magnetization acquisition in turbidites

Based on the above section, the homogenous section of HmTu cannot be considered for magnetic and paleomagnetic analyses of turbidites as they are influenced by the oscillatory nature of the seiche effect. As such only the basal section of HmTu will be considered, along with strict turbidites for the following statistical analysis (a total of fourteen deposits). Magnetic grain size variations ( $\Delta k_{ARM}/k$ ) show a close logarithmic relationship with turbidite thickness (Fig. 44), which is consistent with previous work on bulk sediment of Potter and Scheidegger (1966) that links maximum grain size relation to bed thickness with the turbulence of the turbidity current. The linear trend found on small turbidites (< 20 cm) probably reflects the grain size distribution while a threshold effect occurs between 30 and 40 cm in thickness where sediment concentration increases more than particle size. The logarithmic growth of magnetic grains size might be linked to sediment concentration and the turbulence of the turbidity currents. As the largest turbidites (> 80 cm) correspond to HmTu and as homogenite layer has been associated with local hemipelagic remobilization by seismic waves (Hughes et al. 2020; Bieber et al., in prep), turbidity currents flowing through this hemipelagic sediment increases their sediment concentration, which led to the build-up of flocculation and growth of larger flocs.

Finally, a linear relationship is observed between turbidite thickness and inclination range (Fig. 44). Such a link has been previously established by Tanty et al. (2016) and Philippe (2019). They attribute this relation to turbulence. Undoubtedly, the magnetic torque of magnetic minerals is unable to align with the geomagnetic ambient field because of

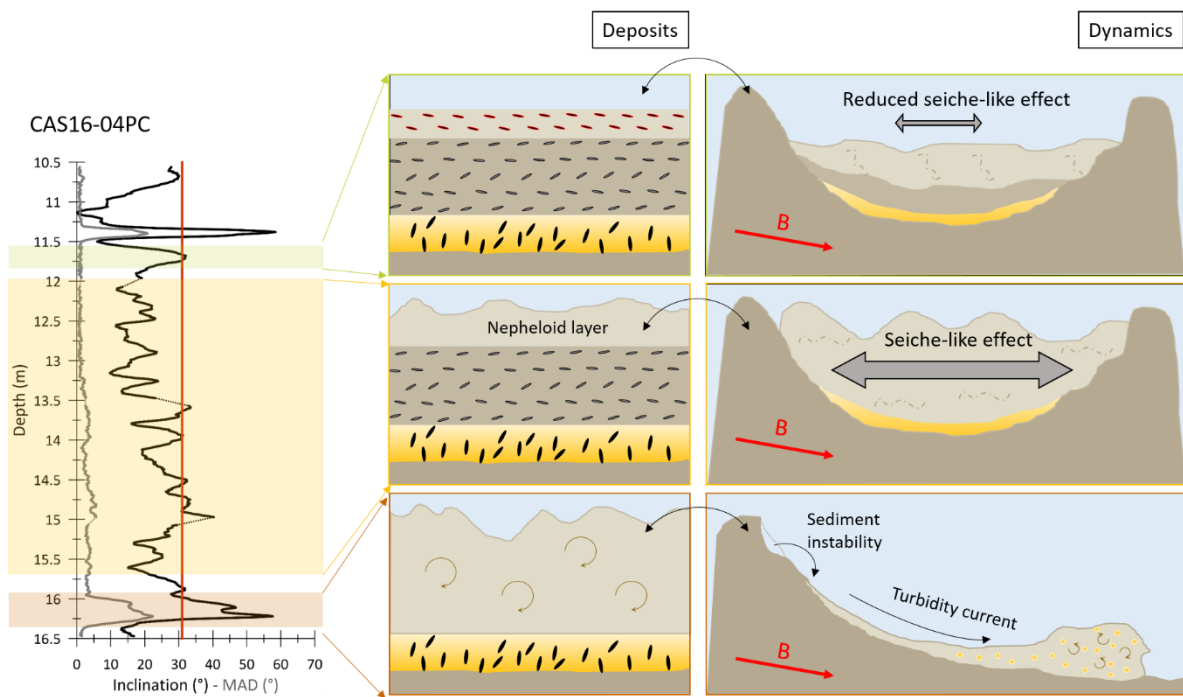


Figure 43 - A) HmTu example from core CAS16-04PC with inclination ( $^{\circ}$ , black line), GAD ( $^{\circ}$ , red line), and MAD ( $^{\circ}$ , grey line) as a function of depth. Transparent rectangles represent Tu (brown), Hm (yellow), and HMPL (green). B) The right side of the figure presents the dynamics, while the left side presents the resulting deposits.

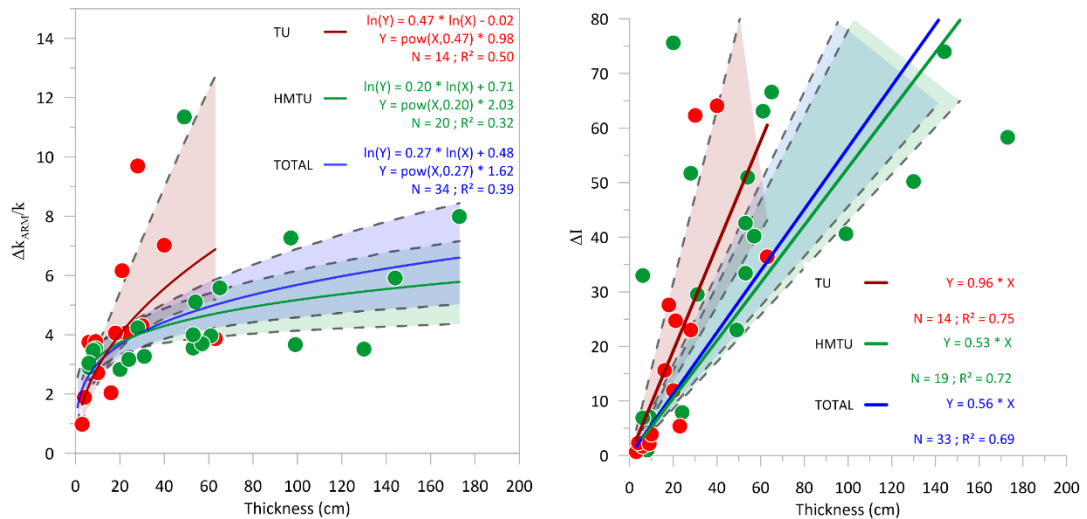


Figure 44 – Left plot is a power-law relationship between magnetic grain size range and turbidite thickness. Right plot is a linear relationship between  $\Delta I$  and turbidite thickness. Red dots are strictly turbidite, while green dots are turbidite basal parts of HmTu. Their respective fit curves are in red and blue lines (with a 90 % confidence range) while the blue line is the fit curve of the combination of both datasets.

associated turbulence, particle interactions, and extremely fast sedimentation rates. However, within the thirty-four turbidites of this study, no clear shallowing effect is systematically recorded, on the contrary, larger deposits present rising inclination at the base that shallows closer to the top. This result suggests that turbulence only cannot explain inclination deviation, nor can the effect of compaction by a high sedimentation rate. However, the maximum deviation of inclination observed in turbidites occurs at the basal part of deposits (Fig. 36, 38, and 41), which link the linear relationship between inclination and bed thickness to the initial turbidity current hydrodynamics rather than lithologic composition.

### 3.2.5 Conclusion

Paleomagnetic analyses and more specifically paleodirections (inclination and declination) are often derived from hemipelagic sediments and used as a magnetostratigraphic tool, while turbidites are avoided. This study uses paleodirections as a sedimentological marker of hydrodynamic conditions. Using three cores collected in deep marine fore-arc basins of the Lesser Antilles subduction zone, several HmTu were identified. These specific deposits are related to one event but can be differentiated into two hydrodynamic modes. The basal turbulent gravity current led to fining upward turbidite deposits with unreliable paleodirections ( $MAD > 20^\circ$ ). The upper homogenous section presents larger standard deviations of paleodirections than the background hemipelagic sediments, but with a similar high-quality record ( $MAD < 5^\circ$ ). Sinusoidal variations of inclinations are most probably the imprint of a seiche-like effect induced by the combination of seismic waves and (multi) turbidite flow into the basin. Subsequently, to study the impact of turbidite on the acquisition of the remanent magnetization, we studied 34 turbidites together with the basal Tu section of HmTu. We identified a power-law relationship between magnetic grain size variation as a function of turbidite thickness that we infer to the increasing particle concentration. The link between the size and the inclination's range of the deposit follows a linear trend. The more turbulent the flow, the larger is the  $\Delta I$ . However, most of the thickest deposits do not reveal a shallowing effect on the most turbulent basal

deposits but on the upper part, which does not associate a linear relation between turbulence and shallowing inclination.

Turbidite remanent magnetization acquisition turned out to be more complex and might not be a good comparison to redeposition experiments. Thus, homogenite emerged to be the most similar natural deposit to laboratory redeposition experiments.

### Acknowledgments

We thank the captain, officers and crew of the R/V Pourquoi Pas?, and the scientific participants in the CASEIS Expedition for the quality of the acquired shipboard data. This work was supported by grants from the Natural Sciences and Engineering Research Council of Canada (NSERC) and the French National Research Agency (ANR-17-CE03-0006; DS01 – CARQUAKES). We also thank Quentin Beauvais, Hervé Guyard, Lola Johannes and Marie-Pier St-Onge for their help on board the ship and/or in the laboratory. We thank MNHN for CASEIS cores storage in the marine collection. A. Bieber acknowledges scholarships from the Institut des sciences de la mer de Rimouski (ISMER) and Institut de physique du globe de Paris (IPGP).

### References

- Banerjee, S.K., King, J., Marvin, J., 1981. A rapid method for magnetic granulometry with applications to environmental studies. *Geophys. Res. Lett.* 8, 333–336. <https://doi.org/10.1029/GL008i004p00333>
- Beck, C., 2009. “Late Quaternary lacustrine paleo-seismic archives in north-western Alps: Examples of earthquake-origin assessment of sedimentary disturbances.” *Earth-Science Reviews* 96, 327–344. <https://doi.org/10.1016/j.earscirev.2009.07.005>
- Beck, C., Reyss, J.-L., Leclerc, F., Moreno, E., Feuillet, N., Barrier, L., Beauducel, F., Boudon, G., Clément, V., Deplus, C., Gallou, N., Lebrun, J.-F., Le Friant, A., Nercessian, A., Paterne, M., Pichot, T., Vidal, C., 2012. Identification of deep subaqueous co-seismic scarps through specific coeval sedimentation in Lesser Antilles:

- implication for seismic hazard. *Natural Hazards and Earth System Science* 12, 1755–1767. <https://doi.org/10.5194/nhess-12-1755-2012>
- Bieber, A., St-Onge, G., Feuillet, N., Carlut, J., Moreno, E., Michel, E., 2021. Regional chronostratigraphy in the eastern Lesser Antilles quaternary fore-arc and accretionary wedge sediments: Relative paleointensity, oxygen isotopes and reversals. *Quaternary Geochronology* 65, 101179. <https://doi.org/10.1016/j.quageo.2021.101179>
- Bouma, A.H., 1964. Turbidites, in: *Developments in Sedimentology*. Elsevier, pp. 247–256. [https://doi.org/10.1016/S0070-4571\(08\)70967-1](https://doi.org/10.1016/S0070-4571(08)70967-1)
- Campos, C., Beck, C., Crouzet, C., Demory, F., Van Welden, A., Eris, K., 2013. Deciphering hemipelagites from homogenites through anisotropy of magnetic susceptibility. Paleoseismic implications (Sea of Marmara and Gulf of Corinth). *Sedimentary Geology* 292, 1–14. <https://doi.org/10.1016/j.sedgeo.2013.03.015>
- Chang, L., Hong, H., Bai, F., Wang, S., Pei, Z., Paterson, G.A., Heslop, D., Roberts, A.P., Huang, B., Tauxe, L., Muxworthy, A.R., 2020. Detrital remanent magnetization of single-crystal silicates with magnetic inclusions: constraints from deposition experiments. *Geophysical Journal International* 224, 2001–2015. <https://doi.org/10.1093/gji/ggaa559>
- Channell, J.E.T., Xuan, C., Hodell, D.A., Crowhurst, S.J., Larter, R.D., 2019. Relative paleointensity (RPI) and age control in Quaternary sediment drifts off the Antarctic Peninsula. *Quaternary Science Reviews* 211, 17–33. <https://doi.org/10.1016/j.quascirev.2019.03.006>
- Deschamps, C.-E., St-Onge, G., Montero-Serrano, J.-C., Polyak, L., 2018. Chronostratigraphy and spatial distribution of magnetic sediments in the Chukchi and Beaufort seas since the last deglaciation. *Boreas* 47, 544–564. <https://doi.org/10.1111/bor.12296>
- Feuillet, N., 2016. CASEIS cruise, RV Pourquoi pas ? <https://doi.org/10.17600/16001800>

Hatfield, R.G., Stoner, J.S., Fraass, A.J., 2021. Relative Paleointensity Record of Integrated Ocean Drilling Program Site U1396 in the Caribbean Sea: Geomagnetic and Chronostratigraphic Observations in the Pliocene. *Geochem Geophys Geosyst* 22. <https://doi.org/10.1029/2021GC009677>

Kastens, K.A., Cita, M.B., 1981. Tsunami-induced sediment transport in the abyssal Mediterranean Sea. *Geol Soc America Bull* 92, 845. [https://doi.org/10.1130/0016-7606\(1981\)92<845:TSTITA>2.0.CO;2](https://doi.org/10.1130/0016-7606(1981)92<845:TSTITA>2.0.CO;2)

King, J., Banerjee, S.K., Marvin, J., Özdemir, Ö., 1982. A comparison of different magnetic methods for determining the relative grain size of magnetite in natural materials: Some results from lake sediments. *Earth and Planetary Science Letters* 59, 404–419. [https://doi.org/10.1016/0012-821X\(82\)90142-X](https://doi.org/10.1016/0012-821X(82)90142-X)

Kirschvink, J.L., 1980. The least-squares line and plane and the analysis of palaeomagnetic data. *Geophys J Int* 62, 699–718. <https://doi.org/10.1111/j.1365-246X.1980.tb02601.x>

Lisé-Pronovost, A., Fletcher, M.-S., Simon, Q., Jacobs, Z., Gadd, P.S., Heslop, D., Herries, A.I.R., Yokoyama, Y., team, A., 2021. Chronostratigraphy of a 270-ka sediment record from Lake Selina, Tasmania: Combining radiometric, geomagnetic and climatic dating. *Quaternary Geochronology* 62, 101152. <https://doi.org/10.1016/j.quageo.2021.101152>

Liu, Jianxing, Liu, Q., Zhang, X., Liu, Jian, Wu, Z., Mei, X., Shi, X., Zhao, Q., 2016. Magnetostratigraphy of a long Quaternary sediment core in the South Yellow Sea. *Quaternary Science Reviews* 144, 1–15. <https://doi.org/10.1016/j.quascirev.2016.05.025>

Mazaud, A., 2005. User-friendly software for vector analysis of the magnetization of long sediment cores: SOFTWARE FOR VECTOR ANALYSIS. *Geochemistry, Geophysics, Geosystems* 6, n/a-n/a. <https://doi.org/10.1029/2005GC001036>

Mazaud, A., Channell, J.E.T., Stoner, J.S., 2012. Relative paleointensity and environmental magnetism since 1.2Ma at IODP site U1305 (Eirik Drift, NW Atlantic). *Earth and*

Planetary Science Letters 357–358, 137–144.  
<https://doi.org/10.1016/j.epsl.2012.09.037>

McHugh, C.M., Seeber, L., Rasbury, T., Strasser, M., Kioka, A., Kanamatsu, T., Ikebara, K., Usami, K., 2020. Isotopic and sedimentary signature of megathrust ruptures along the Japan subduction margin. Marine Geology 428, 106283.  
<https://doi.org/10.1016/j.margeo.2020.106283>

Mulder, T., Cochonat, P., 1996. Classification of Offshore Mass Movements. SEPM JSR Vol. 66. <https://doi.org/10.1306/D42682AC-2B26-11D7-8648000102C1865D>

Mulder, T., Zaragosi, S., Razin, P., Grelaud, C., Lanfumey, V., Bavoil, F., 2009. A new conceptual model for the deposition process of homogenite: Application to a cretaceous megaturbidite of the western Pyrenees (Basque region, SW France). Sedimentary Geology 222, 263–273. <https://doi.org/10.1016/j.sedgeo.2009.09.013>

Philippe, E., 2019. ACQUISITION DE L'AIMANTATION REMANENTE DANS LES SÉDIMENTS. Université du Québec à Rimouski.

Piguet, B., McNeill, D.F., Kindler, P., 2000. Tectonic rotation and diverse remanence carriers revealed by the paleomagnetism of Eo-Oligocene turbidites from two Ultrahelvetic units (Western Alps, Haute-Savoie, France). Tectonophysics 321, 359–375.  
[https://doi.org/10.1016/S0040-1951\(00\)00071-8](https://doi.org/10.1016/S0040-1951(00)00071-8)

Polonia, A., Nelson, C.H., Romano, S., Vaiani, S.C., Colizza, E., Gasparotto, G., Gasperini, L., 2017. A depositional model for seismo-turbidites in confined basins based on Ionian Sea deposits. Marine Geology 384, 177–198.  
<https://doi.org/10.1016/j.margeo.2016.05.010>

Potter, P.E., Scheidegger, A.E., 1966. Bed thickness and grain size: graded beds. Sedimentology 7, 233–240. <https://doi.org/10.1111/j.1365-3091.1966.tb01596.x>

Seibert, C., Feuillet, N., Ratzov, G., Beck, C., Cattaneo, A., 2020. Seafloor morphology and sediments transfers in the mixed carbonated-siliciclastic environment of the Lesser Antilles forearc along Barbuda and St. Lucia. *Marine Geology* 106242. <https://doi.org/10.1016/j.margeo.2020.106242>

Siegenthaler, C., 2021. Seiches and the slide/seiche dynamics; subcritical and supercritical subaqueous mass flows and their deposits. Examples from Swiss Lakes. *Swiss J Geosci* 114, 17. <https://doi.org/10.1186/s00015-021-00394-6>

Spassov, S., Valet, J.-P., 2012. Detrital magnetizations from redeposition experiments of different natural sediments. *Earth and Planetary Science Letters* 351–352, 147–157. <https://doi.org/10.1016/j.epsl.2012.07.016>

Stoner, J.S., St-Onge, G., 2007. Chapter Three Magnetic Stratigraphy in Paleoceanography: Reversals, Excursions, Paleointensity, and Secular Variation, in: Developments in Marine Geology. Elsevier, pp. 99–138. [https://doi.org/10.1016/S1572-5480\(07\)01008-1](https://doi.org/10.1016/S1572-5480(07)01008-1)

St-Onge, G., Chapron, E., Mulsow, S., Salas, M., Viel, M., Debret, M., Foucher, A., Mulder, T., Winiarski, T., Desmet, M., Costa, P.J.M., Ghaleb, B., Jaouen, A., Locat, J., 2012. Comparison of earthquake-triggered turbidites from the Saguenay (Eastern Canada) and Reloncavi (Chilean margin) Fjords: Implications for paleoseismicity and sedimentology. *Sedimentary Geology* 243–244, 89–107. <https://doi.org/10.1016/j.sedgeo.2011.11.003>

St-Onge, G., Mulder, T., Piper, D.J.W., Hillaire-Marcel, C., Stoner, J.S., 2004. Earthquake and flood-induced turbidites in the Saguenay Fjord (Québec): a Holocene paleoseismicity record. *Quaternary Science Reviews* 23, 283–294. <https://doi.org/10.1016/j.quascirev.2003.03.001>

Stow, D., Smillie, Z., 2020. Distinguishing between Deep-Water Sediment Facies: Turbidites, Contourites and Hemipelagites. *Geosciences* 10, 68. <https://doi.org/10.3390/geosciences10020068>

Suhayda, J.N., 1986. Interaction Between Surface Waves and Muddy Bottom Sediments, in: Mehta, A.J. (Ed.), *Estuarine Cohesive Sediment Dynamics, Lecture Notes on Coastal and Estuarine Studies*. Springer New York, New York, NY, pp. 401–428. [https://doi.org/10.1007/978-1-4612-4936-8\\_18](https://doi.org/10.1007/978-1-4612-4936-8_18)

Suhayda, J.N., 1977. Surface waves and bottom sediment response. *Marine Geotechnology* 2, 135–146. <https://doi.org/10.1080/10641197709379775>

Tanty, C., Valet, J.-P., Carlut, J., Bassinot, F., Zaragozi, S., 2016. Acquisition of detrital magnetization in four turbidites: MAGNETIC STUDY OF TURBIDITES. *Geochemistry, Geophysics, Geosystems* 17, 3207–3223. <https://doi.org/10.1002/2016GC006378>

Tauxe, L., Kent, D.V., 1984. Properties of a detrital remanence carried by haematite from study of modern river deposits and laboratory redeposition experiments. *Geophys J Int* 76, 543–561. <https://doi.org/10.1111/j.1365-246X.1984.tb01909.x>

Tauxe, L., Steindorf, J.L., Harris, A., 2006. Depositional remanent magnetization: Toward an improved theoretical and experimental foundation. *Earth and Planetary Science Letters* 244, 515–529. <https://doi.org/10.1016/j.epsl.2006.02.003>

Valet, J.-P., Tanty, C., Carlut, J., 2017. Detrital magnetization of laboratory-redeposited sediments. *Geophysical Journal International* 210, 34–41. <https://doi.org/10.1093/gji/ggx139>



## CONCLUSION GÉNÉRALE

À travers l'étude de cinq carottes sédimentaires prélevées sur la façade atlantique des Petites Antilles, cette thèse de doctorat répond à l'objectif principal qui est d'étudier les aléas naturels au cours du Quaternaire récent, et plus particulièrement les séismes dans la région des Petites Antilles. À l'aide d'une chronostratigraphie régionale, nous avons mis en évidence l'existence d'un super-cycle sismique sur les quatre-vingt derniers milliers d'années avec une récurrence de vingt-quatre mille ans. Pour atteindre ce résultat, les dépôts sédimentaires caractéristiques des séismes ont été analysés au travers de paramètres physiques et magnétiques, ce qui a amené à l'établissement d'un modèle de dépôt sédimentaire des complexes homogénite-turbidites. Ces dépôts sont liés à des événements sismiques majeurs qui n'ont encore jamais été enregistrés dans l'histoire récente des Petites Antilles. Ainsi, cette dernière section sera l'occasion de rappeler les principaux résultats et conclusions des trois chapitres de cette thèse, tout en ouvrant sur des perspectives qui pourraient compléter les limites de cette étude et enrichir ce projet.

### Chapitre 1

Dans ce chapitre, une magnétostratigraphie régionale a été établie à l'aide d'une carotte sédimentaire dédiée à ces travaux. En effet, alors que les îles volcaniques ont fait l'objet de plusieurs études paléomagnétiques (e.g. Carlut et Quidilieur, 2000 ; Tanty et al., 2015 ; Ricci et al., 2018) et que certaines études de l'*Ocean Drilling Program* (ODP) ont cherché à mieux comprendre les processus de formation et d'évolution de la zone de subduction des Petites Antilles et de l'arc volcanique résultant (Kent et Spariosu, 1983 ; Wilson, 1984 ; Hounslow et al., 1990), aucune étude n'a encore permis d'établir une magnétostratigraphie détaillée du Quaternaire récent dans cette région. Par conséquent, lors de la mission océanographique CASEIS à bord du N/R Pourquoi Pas ?, un site spécifique a été choisi pour prélever la carotte CAS16-24PC. À l'est de la Dominique, un haut-bathymétrique séparant deux bassins

profonds - dont le Bassin de la Martinique - a été un endroit privilégié pour obtenir une carotte sédimentaire peu perturbée, isolée des apports fluviaux des îles et des apports de la plateforme carbonatée. Ainsi, à l'aide des paramètres physiques et magnétiques du sédiment, la totalité des couches déposées rapidement (RDL) ont été identifiées et retirées des données pour obtenir une carotte composite avec un signal quasi-continu.

L'analyse paléomagnétique du sédiment a permis de mettre en évidence l'enregistrement de la dernière inversion paléomagnétique que la Terre ait connue : l'inversion Brunhes-Matuyama datée à environ 773 ka (Simon et al., 2019 ; Channell et al., 2020) ainsi que le subchron Jaramillo dont les limites temporelles sont approximativement 1.01 Ma et 1.069 Ma (Singer et al, 2014). L'établissement de la chronostratigraphie complète a été permise par la combinaison de ces données avec celles des variations isotopiques de l'oxygène et des variations de paléointensité relative (RPI). En effet, ces dernières ont été comparées à des compilations (*stacks*) globaux bien contraints temporellement pour obtenir de nombreux *tie-points* (i.e., LR04, Lisiecky et Raimo, 2005 ; PISO1500, Channel et al., 2009 ; PADM2M, Ziegler et al., 2011).

Il résulte de cette analyse un taux de sédimentation particulièrement faible (environ 3 cm/ka au cours des derniers 1150 Ma), mais tout à fait cohérent avec la littérature (Reid et al. 1996). L'étendue de cette chronostratigraphie fait de la carotte CAS16-24PC une très bonne référence pour estimer l'âge de dépôts sédimentaires associés à des phénomènes naturels tels que des séismes dans la région. Les variations de RPI de cette carotte de référence ont permis de déterminer l'âge de la carotte CAS16-12PC étudiée dans le chapitre suivant et pourra ainsi servir de carotte de référence pour de futures études sur la période quaternaire des Petites Antilles.

## Chapitre 2

Ce second chapitre a permis de mettre en valeur un super-cycle sismique associé à la zone de subduction des Petites Antilles sur un secteur qui s'étend des bassins avant-arc de la Guadeloupe jusqu'à ceux de Saint-Barthélemy. Pour identifier la récurrence sismique de

cette région, trois carottes prélevées dans des bassins profonds ( $> 5000$  mètres de profondeur) et une carotte provenant d'un bassin du prisme d'accrétion ont été étudiées. Cette dernière, la carotte CAS16-12PC, a été analysée à l'aide des paramètres physiques et magnétiques pour obtenir une carotte composite dont la RPI a pu être mise en corrélation à la fois avec la carotte de référence CAS16-24PC (Bieber et al., 2021) et avec le stack de RPI Nord-Atlantique (NAPIS-75 ; Laj et al., 2000).

Les trois autres carottes, CAS16-04PC, CAS16-14PC et CAS16-36PC, ont aussi été étudiées au travers des paramètres physiques et magnétiques pour l'établissement des carottes composites. Contrairement aux deux précédentes carottes, celles-ci sont principalement composées de couches déposées rapidement (RDL) dont deux types majoritaires ont été identifiées : les turbidites et les complexes homogénite-turbidites. Les turbidites présentent un contact franc, souvent érosif, et sont identifiées avec un granoclassement normal mis en évidence à l'aide des paramètres de densité et de taille des grains magnétiques. L'épaisseur de ces turbidites varie de quelques centimètres à plusieurs décimètres. Les complexes homogénite-turbidites (HmTu) présentent une structure similaire aux turbidites avec une base à contact franc et érosif suivit d'un granoclassement normal, mais avec une partie supérieure homogène généralement très épaisse (plusieurs décimètres jusqu'à quatre mètres d'épaisseur). Cette partie homogène ne présente aucune structure lithologique identifiable sur les photographies à haute-résolution ou les images à rayon-X, mais présente un granoclassement normal très léger tout le long du dépôt. Alors que les turbidites ont déjà fait l'objet de nombreuses études dans d'autres zones de subduction comme marqueur paléosismologique (e.g. Goldfinger et al., 2003, 2007 - Cascade ; Ratzov et al., 2010 - Equateur ; Pouderoux et al., 2012 - Nouvelle-Zélande ; Ikehara et al., 2016 – Japan ; St-Onge et al., 2012 - Chile ; Patton et al., 2013 - Sumatra-Andaman), les HmTu ont principalement été identifiées comme des dépôts associés à des séismes ou à des tsunamis dans des milieux confinés tels que des lacs (e.g., Chapron et al., 1999) ou des mers (e.g., Cita, 2008) mais très peu comme marqueur stratigraphique dans les zones de subduction (e.g., McHugh et al. 2020).

L’isolement des bassins, leur profondeur et leur faible connexion aux plateformes carbonatées ont fait de ces carottes des candidates idéales pour réaliser une étude paléosismologique. Le développement d’un modèle d’âge pour chacune de ces carottes, basé sur des datations au radiocarbone (Seibert et al., soumis ; Morena, 2020) et les variations de paléointensité comparées au stack NAPIS-75 et à la RPI de la carotte CAS16-12PC ont permis de dater l’ensemble des RDL. Considérant la localisation des bassins, ces dépôts sédimentaires sont le plus probablement issus d’événements sismiques, notamment de mégaséismes qui n’ont encore jamais été répertoriés dans des archives historiques des Petites Antilles. Les travaux réalisés au cours de ce second chapitre ont permis d’identifier au cours des derniers 90 ka, un super-cycle sismique de  $24 \pm 2$  ka comprenant une période de quiescence de 7 ka. Ces résultats viennent enrichir les récentes études de Seibert et al., (soumis) et Morena (2020). Il s’agit aussi de la première étude où les variations de RPI sont utilisées pour déterminer l’âge des dépôts sédimentaires d’origine sismique. Les mesures de RPI étant continues, tout le sédiment hémpélagique conservé permet d’améliorer la datation du sommet et de la base des turbidites et des HmTu, et donc d’obtenir une estimation plus précise de l’âge de ces dépôts.

### Chapitre 3

Au travers des nombreuses RDL caractérisées dans le chapitre 2, quatorze turbidites et vingt complexes homogénite-turbidites (HmTu) ont composé l’objet d’étude du troisième et dernier chapitre de cette thèse. Alors que la grande majorité des études paléomagnétiques cherchent à obtenir des enregistrements sédimentaires quasi-continus avec le moins possible de ces dépôts (e.g. Lisé-Pronovost et al., 2014 ; Deschamps et al., 2016 ; Caron et al., 2019 ; Bieber et al., 2021), ce sont ces couches sédimentaires qui peuvent aider à mieux comprendre les processus qui gouvernent l’enregistrement d’une aimantation rémanente par le sédiment. En effet, l’analyse paléomagnétique des HmTu a confirmé la succession d’un dépôt très turbulent à la base (la turbidite) avec un dépôt particulièrement homogène d’un point de vue sédimentaire (Cita et al. 1981 ; Beck et al. 2009), mais dont l’inclinaison magnétique montre une oscillation le long du dépôt. Cette oscillation est confirmée par des écarts types plus

importants sur ces dépôts d'homogénites que pour les hémiplégites. De plus, les déviations angulaires maximales et leurs écarts types sont du même ordre de grandeur que ceux des dépôts hémiplégique. Les homogénites sont donc le fruit d'une sédimentation avec un faible hydrodynamisme, mais sous l'effet d'une onde stationnaire qui modifie l'orientation verticale des grains magnétiques.

Un modèle de dépôt a ainsi pu être établi pour les HmTu et révèle que les processus hydrodynamiques affectant les sédiments sont très différents entre les parties turbidites et homogénites. Il devient donc nécessaire de séparer ces deux dépôts pour étudier le comportement des turbidites ou des homogénites, même s'il s'agit d'un seul et même événement. Cette dissociation avait déjà été suggérée par Beck et al., 2009 en nommant ces dépôts « turbidites/homogénites ». Ainsi, en analysant des turbidites strictes et des turbidites issues des HmTu, il a été possible de mettre en évidence une corrélation quasi-logarithmique entre l'épaisseur de ces dépôts et l'étendue granulométrique de la fraction magnétique ( $\Delta k_{ARM}/k$ ), et une corrélation linéaire entre l'épaisseur de ces couches et l'étendue de la déviation de l'inclinaison ( $\Delta I$ ). Il est cependant notable que sur l'ensemble de ces trente turbidites, seulement deux présentent des inclinaisons négatives. Il est donc envisageable que même au travers d'un hydrodynamisme aussi important qu'un dépôt gravitaire, le champ magnétique terrestre conserve une importance non-négligeable dans l'orientation des grains magnétiques. Cependant, l'orientation attendue (inclinaison) n'est pas retrouvée et semble particulièrement variable d'un dépôt à un autre. Il semble donc que les HmTu seraient de très bons candidats pour l'étude de l'acquisition de l'aimantation rémanente naturelle (NRM), notamment la partie homogène qui serait plus assimilable aux expériences de redéposition de sédiment naturel et artificiel (e.g. Tauxe et Kent, 1983 ; Spasov et Valet, 2012 ; Valet et al., 2017 ; Chang et al., 2020).

### Paléomagnétisme et paléosismologie marine dans les Petites Antilles, avancées et limitations

Comme résumé ci-dessus, l'ensemble des chapitres de cette thèse répond aux trois grands objectifs initialement établis et offre de nouveaux éléments de réponse à la

problématique générale. En effet, l'étude des propriétés physiques, magnétiques et paléomagnétiques des cinq carottes analysées, ainsi que de leur enregistrement paléomagnétique, a permis non seulement d'établir une magnétostratigraphie des Petites Antilles qui répond au premier objectif de cette thèse (chapitre 1), mais également d'étudier et estimer l'âge des dépôts sédimentaires associés à des séismes pour répondre au second objectif (chapitre 2), et finalement d'analyser l'impact des turbidites sur le signal paléomagnétique et d'établir un modèle de dépôt des complexes homogénite-turbidites à partir des variations paléomagnétiques en réponse au troisième objectif (chapitre 3).

Nous avons ainsi mis en évidence qu'au travers de l'enregistrement sédimentaire de carottes prélevées dans des bassins avant-arc de la zone de subduction des Petites Antilles, il est possible de réaliser une étude paléoseismologique robuste. Cependant, certaines limitations nécessitent d'être relevées pour les futures études. Premièrement, l'étendue et le nombre de carottes étudiées au travers de cette thèse ne permettent pas de faire des corrélations évidentes de dépôts associés à des séismes entre ces archives sédimentaires. Contrairement aux études de Seibert et al. (soumis) et Morena (2020) qui ont réalisé des corrélations stratigraphiques basées sur le même procédé que les études antérieures de Goldfinger et al. (2007, 2008) et Goldfinger (2011) sur la marge des Cascades, nous avons associé ces dépôts à des clusters d'événements. Une des principales raisons étant que l'utilisation du paléomagnétisme pour dater des carottes avec des RDL n'avait encore jamais été réalisée. Deux carottes, les CAS16-04PC et CAS16-14PC ont été sélectionnées pour leur proximité et donc permettent de retrouver plus facilement des événements synchrones, tandis que la CAS16-36PC prélevée bien plus au nord a été sélectionnée pour sa distanciation avec les deux autres carottes, et pour tenter de faire une corrélation stratigraphique entre les deux zones. Les taux de sédimentation particulièrement faibles de la région (Reid et al., 1996 ; Bieber et al., 2021) – variant de 2 à 10 cm/ka,- associés au potentiel érosif des courants de turbidité, n'ont pas permis d'estimer plus précisément l'âge des RDL et donc de faire une corrélation temporelle événement par événement. Deuxièmement, si les complexes homogénite-turbidites sont facilement associés aux séismes, les turbidites et les autres RDL, plus fines, ne peuvent pas y être associées avec certitude. Néanmoins, l'absence de corrélation directe entre le niveau

marin global observé dans le chapitre 2 et la présence de ces RDL permettent de supposer qu'un certain « bruit de fond » de ces couches déposées rapidement existe (e.g., déstabilisation d'origine passive) et est présent dans les périodes d'activité sismique plus importante. L'utilisation des clusters permet de s'affranchir de l'existence de ce bruit fond. Troisièmement, bien que cette étude ait permis d'améliorer la compréhension des dépôts de complexes homogénite-turbidites grâce aux variations de l'enregistrement paléomagnétique, ces résultats ne présentent pas de données sur la fabrique magnétique qui pourrait parfaire la compréhension de ces dépôts comme son utilisation par Campos et al. (2013) pour discerner la limite entre homogénite et hémipelagite.

### Perspectives

Cette thèse de doctorat s'inscrit dans le projet ANR CARQUAKES et vient s'ajouter aux résultats obtenus dans les thèses de doctorat de Chloé Seibert (2019) et Pierre Morena (2020) qui traitent respectivement de la paléosismologie marine des zones Martinique-Antigua et Barbuda-Anguilla. En démontrant que le paléomagnétisme peut être utilisé pour améliorer la précision des datations, il semble évident que cet outil devrait être intégré dans les prochaines études paléosismologiques, d'autant plus qu'il s'agit d'une méthode de mesure continue et non destructive. L'analyse paléomagnétique de carottes complémentaires issues des résultats des thèses susmentionnées permettrait d'améliorer les corrélations stratigraphiques en précisant l'âge de chacun des dépôts. Par exemple, l'analyse paléomagnétique des carottes CAS16-01PC, CAS16-07PC, CAS16-31PC, CAS16-39PC et CAS16-42PC permettrait de couvrir la totalité du segment nord de l'arc des Petites Antilles, de la Martinique jusqu'à Anguilla et de préciser le fonctionnement de cette zone de subduction, notamment sur sa segmentation (Seibert et al., soumis). De plus, un projet de post-doctorat basé sur des carottes sédimentaires prélevées dans l'environnement côtier des îles de la Guadeloupe et de la Martinique (mission CARESSE, été 2021) pourra établir une corrélation entre les dépôts marins peu profonds avec l'ensemble des données paléosismologiques établies sur le milieu marin profond.

Enfin, comme relevé pour le troisième chapitre, une analyse plus poussée des complexes homogénite-turbidites permettrait de spécifier si l'effet de seiche est présent tout le long du dépôt, notamment en étudiant la fabrique magnétique de la totalité d'un complexe homogénite-turbidite. Des expériences de redéposition de turbidite et/ou HmTu pourraient être envisagées sous l'influence d'un champ magnétique contrôlé pour mieux définir la part des différents processus physiques qui affectent l'enregistrement du signal paléomagnétique.

Pour résumé, cette thèse démontre l'utilité de l'analyse paléomagnétique des carottes sédimentaires utilisées dans les études de paléosismologie marine et du potentiel théorique qu'apporte l'analyse des dépôts spécifiques tels que les complexes homogénite-turbidite. L'ensemble combiné des limitations et des perspectives de cette études sont autant de sources à explorer pour de futurs travaux combinant le paléomagnétisme et la sédimentologie marine par le laboratoire de paléomagnétisme et géologie marine de l'institut des sciences de la mer (ISMER), et de futures collaborations avec les différentes équipes de l'institut de physique du globe de paris (IPGP).

## ANNEXES

### Annexe 1 : Chapitre 1

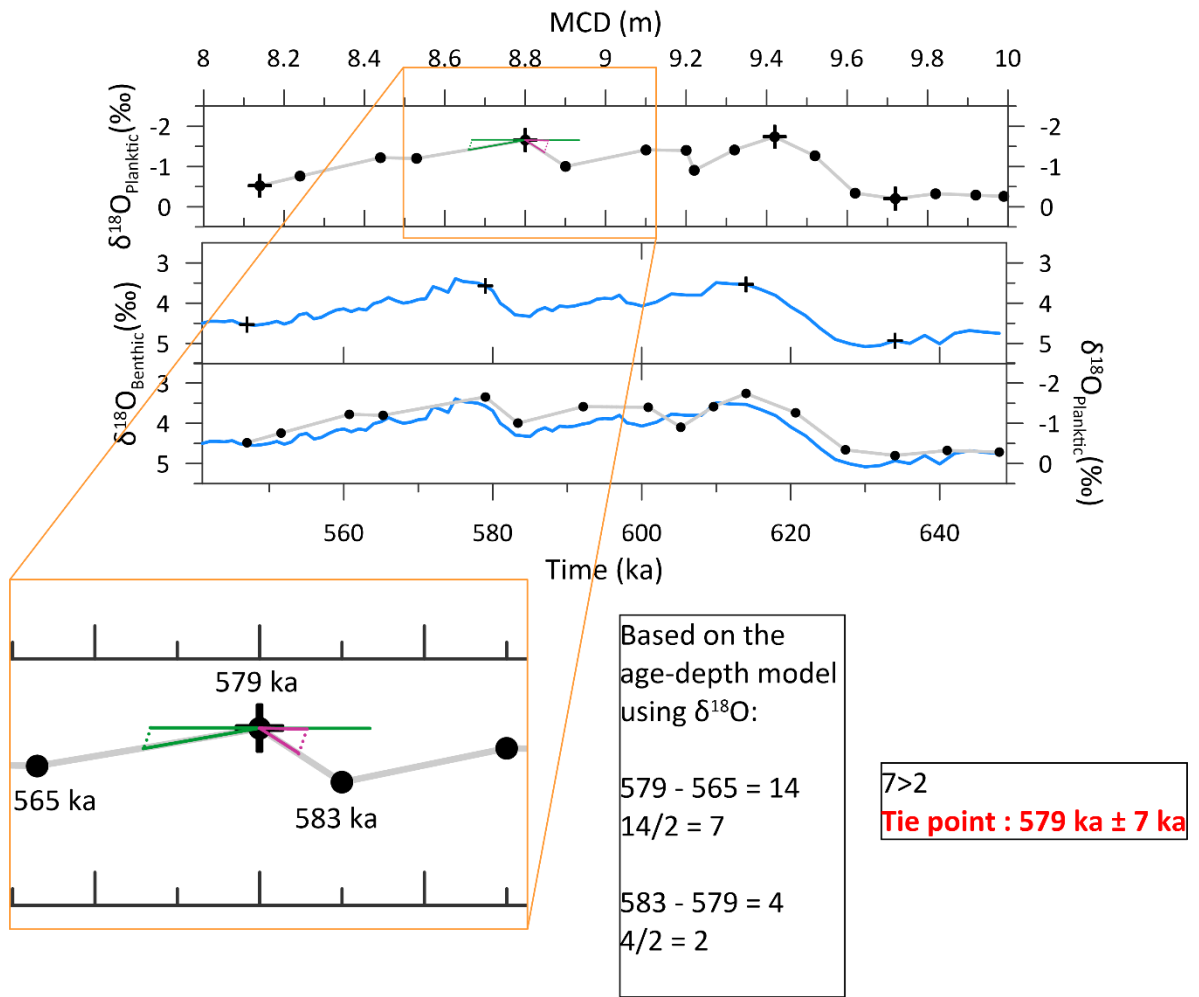


Figure 45 - Schematic explanation of age-error used for the age-depth model. The half-time gap between a tie-point and its surrounding values is represented in green and purple segments. The longest half-time gap (green segments) is set as this specific tie-point age-error.

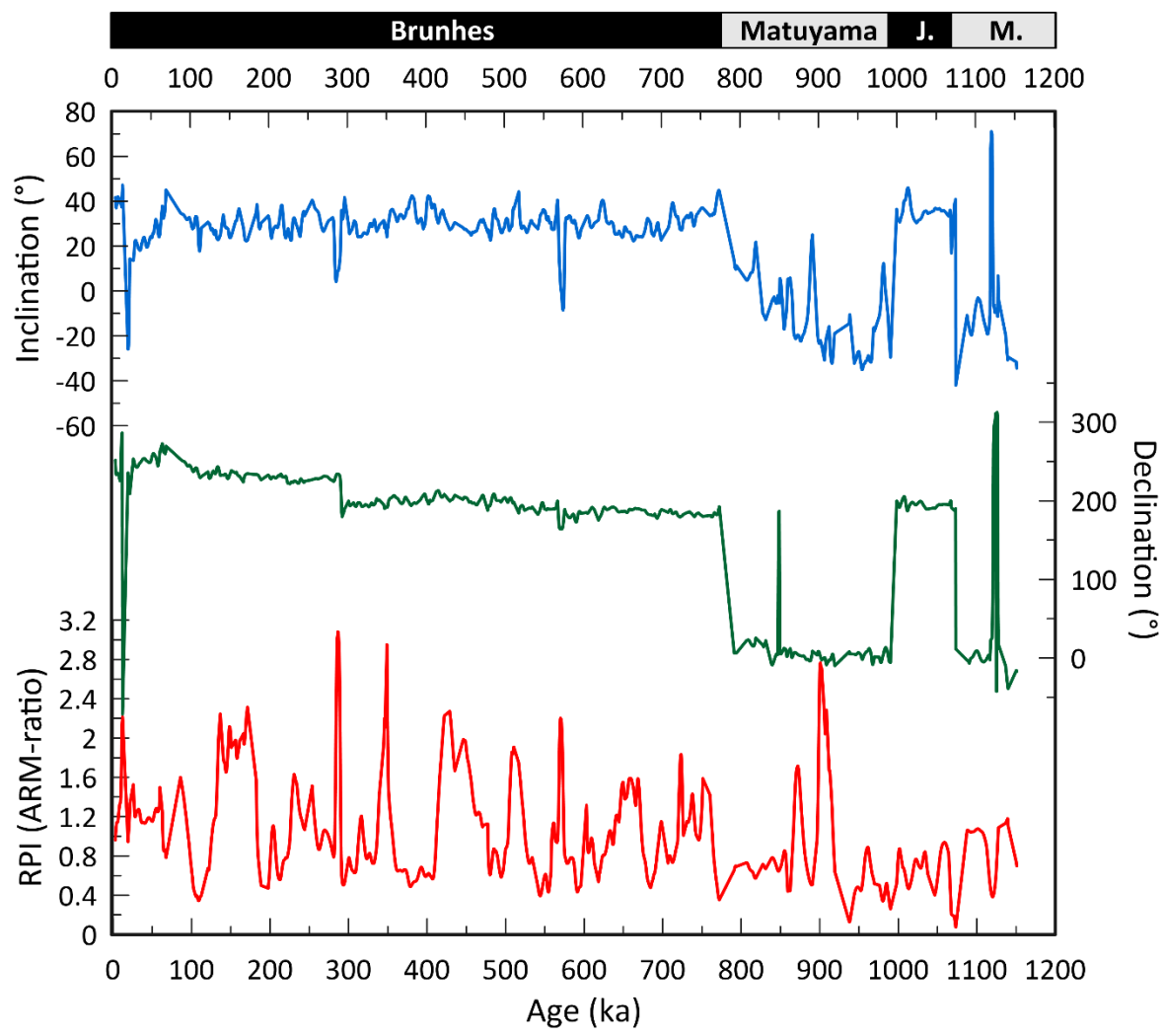


Figure 46 - Inclination, declination and relative paleointensity records for core CAS16-24PC.

Table 5 - Meter composite depth (MCD) correspondence with original coring depth in meters.

Depth (m)	MCD (m)	Depth (m)	MCD (m)	Depth (m)	MCD (m)
<b>0.05</b>	0	7.35	6.58	13.18	11.92
<b>0.27</b>	0.22	7.92	7.15	13.24	11.98
<b>0.4</b>	0.23	7.97	7.16	13.26	11.99
<b>0.63</b>	0.46	8.68	7.87	13.76	12.49
<b>0.77</b>	0.47	8.74	7.88	13.89	12.5
<b>1.27</b>	0.97	9.38	8.52	15.31	13.92
<b>1.32</b>	0.98	9.42	8.53	15.4	13.93
<b>1.58</b>	1.24	9.48	8.59	15.48	14.01
<b>1.62</b>	1.25	9.5	8.6	15.55	14.02
<b>2.14</b>	1.77	10.06	9.16	15.93	14.4
<b>2.21</b>	1.78	10.12	9.17	16.05	14.41
<b>2.66</b>	2.23	10.14	9.19	17.14	15.5
<b>2.7</b>	2.24	10.28	9.2	17.21	15.51
<b>3.19</b>	2.73	11.01	9.93	17.58	15.88
<b>3.26</b>	2.74	11.05	9.94	17.78	15.89
<b>3.42</b>	2.9	12.15	11.04	18.81	16.92

<b>3.46</b>	2.91	12.19	11.05	18.93	16.93
<b>4.5</b>	3.95	12.46	11.32	19.06	17.06
<b>4.59</b>	3.96	12.48	11.33	19.11	17.07
<b>6.11</b>	5.48	12.63	11.48	19.37	17.33
<b>6.21</b>	5.49	12.69	11.49		
<b>7.29</b>	6.57	13.11	11.91		

Table 6 - Major elemental percentages obtained by energy dispersive X-ray spectroscopy (EDS) in samples indicated in Fig. 16.

Element	Sample 1	Sample 2	Sample 3	Sample 4	Sample 5
Boron	<b>25.35</b>	<b>20.35</b>	0	0	0
Sodium	0	1.02	0.43	2.21	0
Magnesium	10.02	1.58	0.45	2.38	0.94
Aluminium	1.37	6.45	1.51	<b>15.31</b>	0.81
Silicon	<b>39.85</b>	<b>35.14</b>	<b>1.94</b>	<b>58.89</b>	<b>1.69</b>
Potassium	0	0.48	0	1.32	0
Calcium	6.88	1.61	0.26	<b>10.55</b>	0.27
Iron	<b>15.09</b>	<b>29.05</b>	<b>87.8</b>	7.91	<b>88.82</b>
Chlorine	0	0	0	0.78	0
Titanium	0	4.32	<b>7.62</b>	0.65	<b>7.47</b>
Manganese	1.44	0	0	0	0

## Annexe 2 : Chapitre 2

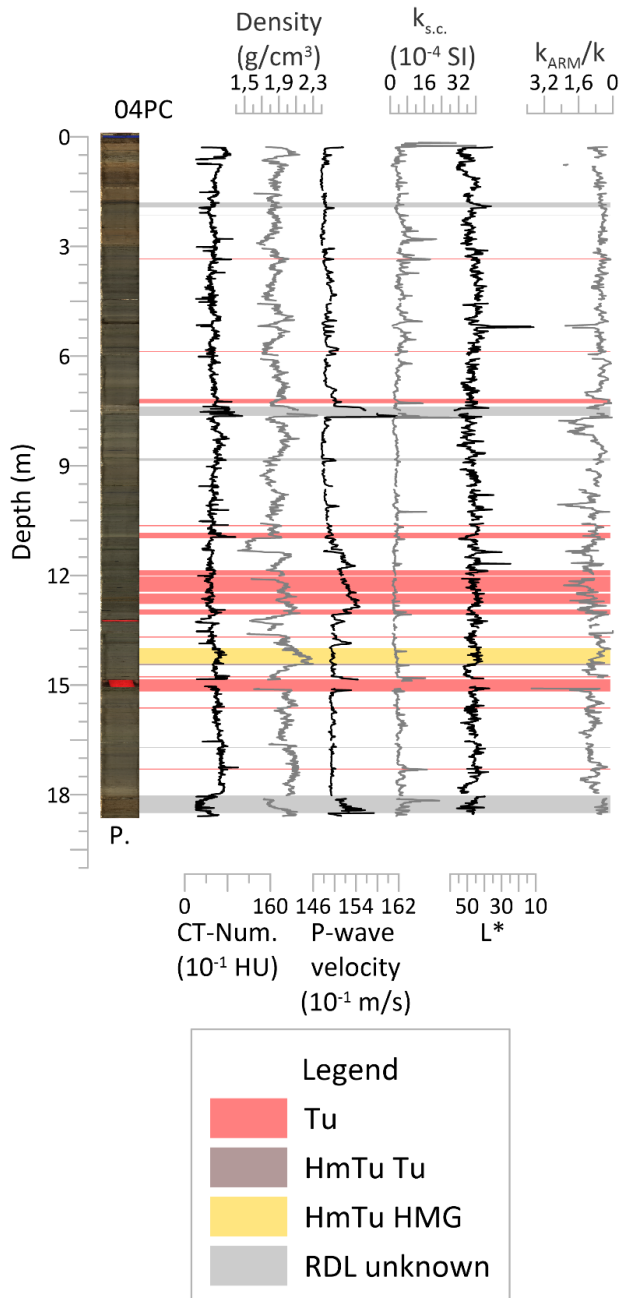


Figure 47 - Physical and magnetic parameter as a function of depth (m) comprising from left to right: high-resolution photography (P.), CT-scan images (CT-S.), CT-number, density, P-wave velocity, magnetic susceptibility, white (100) to black (0) color space ( $L^*$ ) and magnetic susceptibilities ratio ( $k_{ARM}/k$ ). RDL are highlighted as light red (turbidite), light brown and yellow-sand (HmTu complexes).

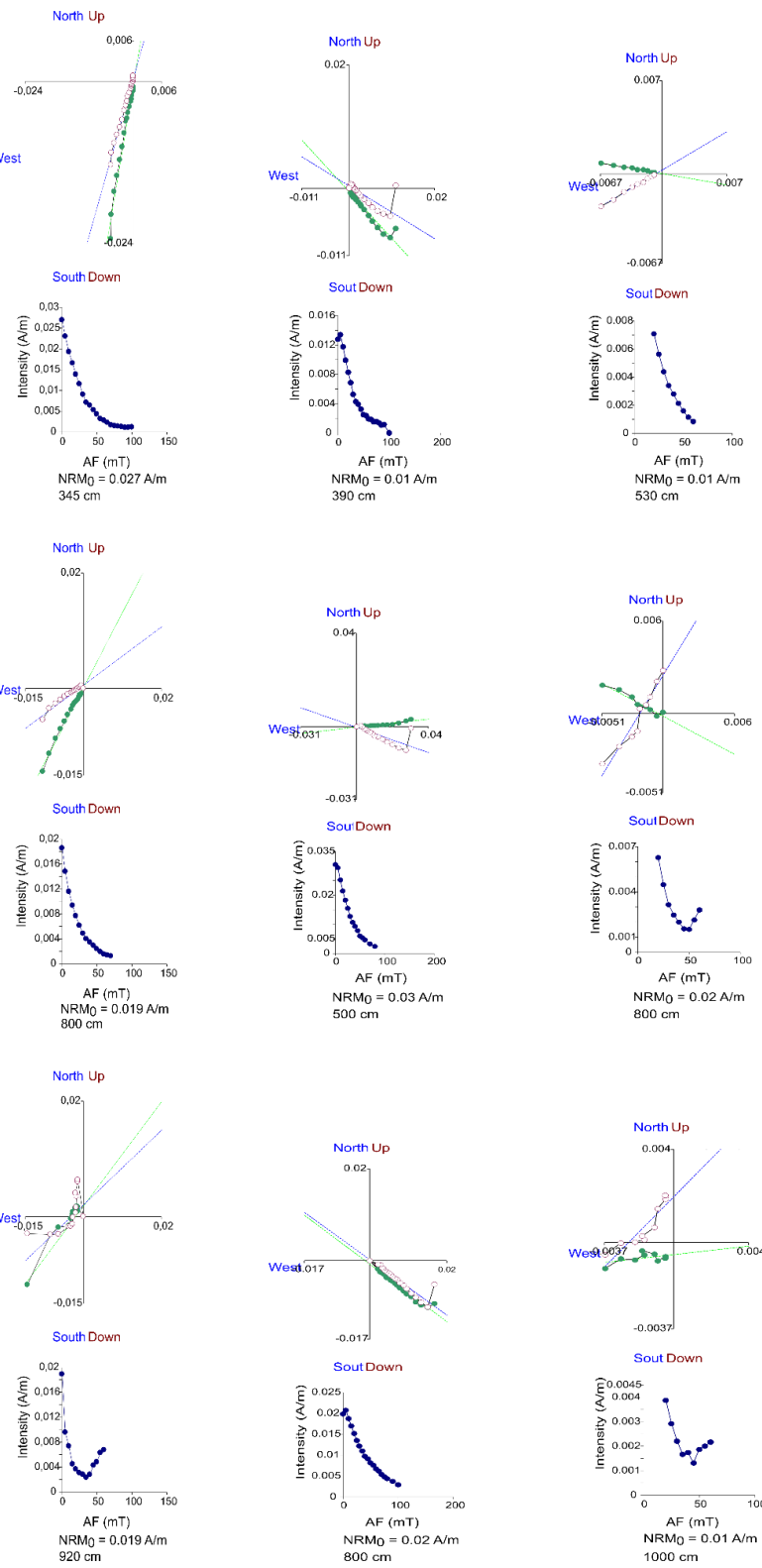


Figure 48 - Typical demagnetization curves and orthogonal projections of hemipelagic background sediment (HMPL), turbidite (TU) and homogenite (HMG) for cores CAS16-04PC, -14PC and -36PC.

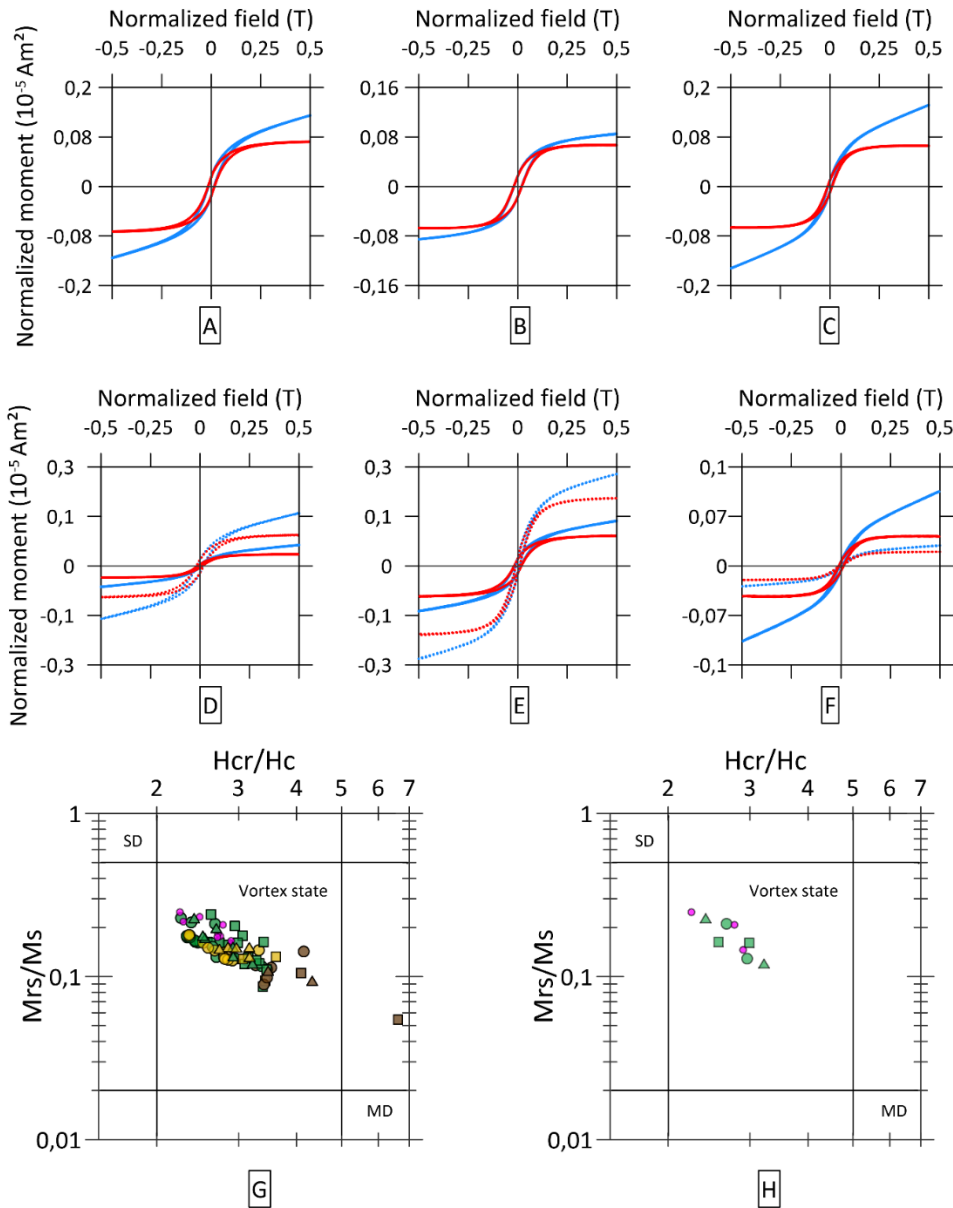


Figure 49 - Typical raw hysteresis loops (blue) and high-field corrected loops (red) of hemipelagic sediment (solid line) and turbidite (dotted line) for core CAS16-12PC (A, B and C) and cores CAS16-04PC (D), CAS16-14PC (E) and CAS16-36PC (F). G and H are King plot (King et al., 1982) of respectively all the sample listed on Table 7 (ANNEXE 2) and the six hemipelagite hysteresis loops (A to F).

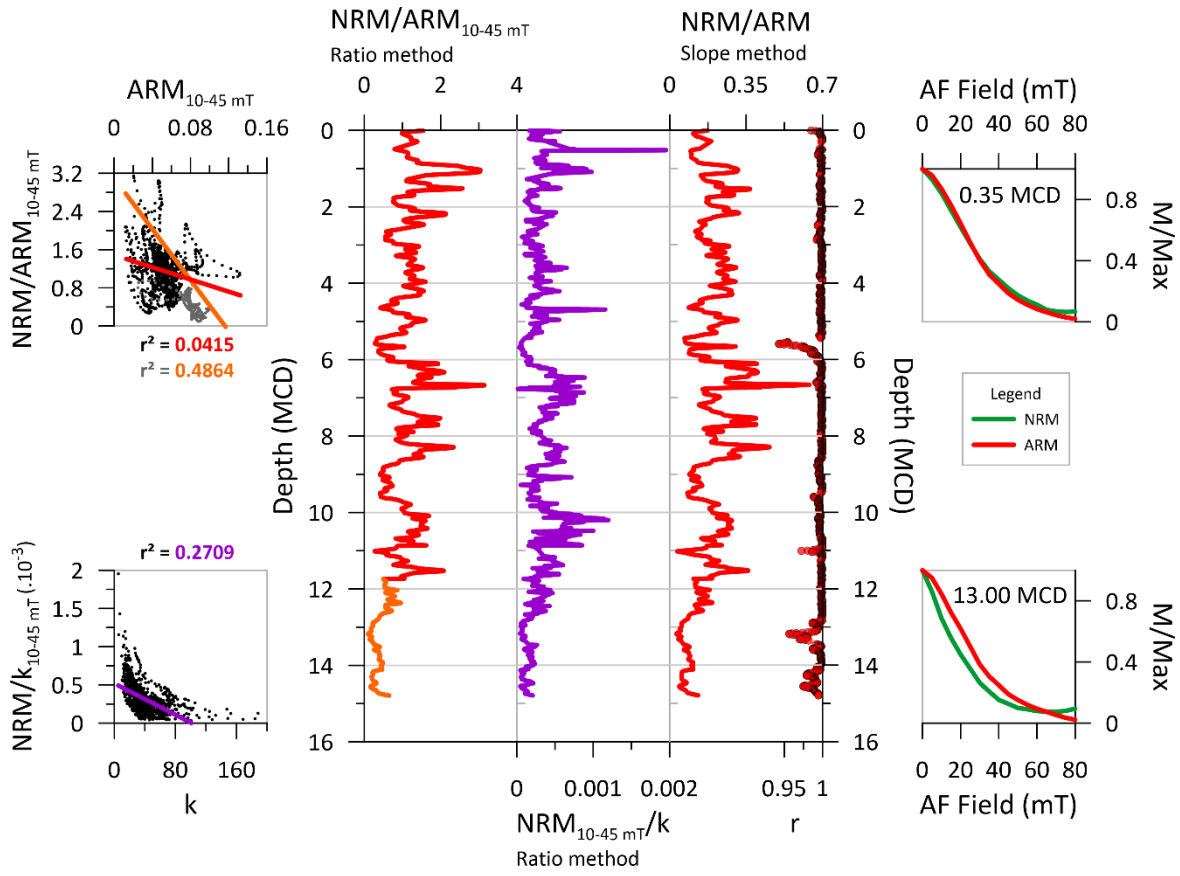


Figure 50 - Comparison of the CAS16-12PC RPI variations estimated with the average ratios (Red + orange for ARM normalizer and violet curve for  $k$  normalizer) and slope method (red curve) associated to the correlation coefficient (red dot,  $r$ ). Scatter plots on the left test un conformity of normalizer against estimated RPI and reveal a reduced correlation for ARM. Demagnetization curves for NRM and ARM are presented on the right-hand side.

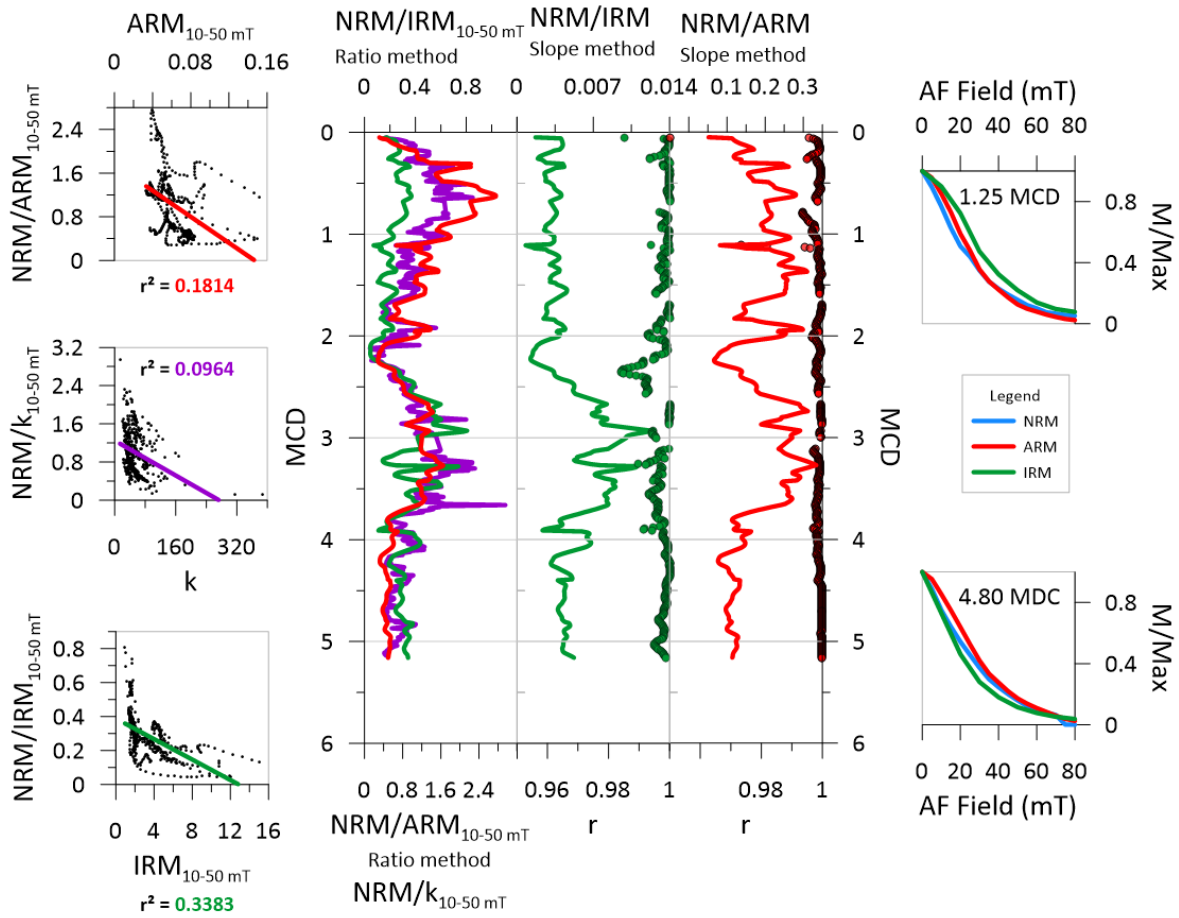


Figure 51 - Comparison of the CAS16-04PC RPI variations estimated with the average ratios (superposed red, green and violet curves for ARM, IRM and k respectively) and slope methods (red and green curves). Scatter plots on the left test unconformity of normalizers against estimated RPI and show a reduced correlation for k and ARM. Demagnetization curves for NRM, ARM and IRM are presented on the right-hand side.

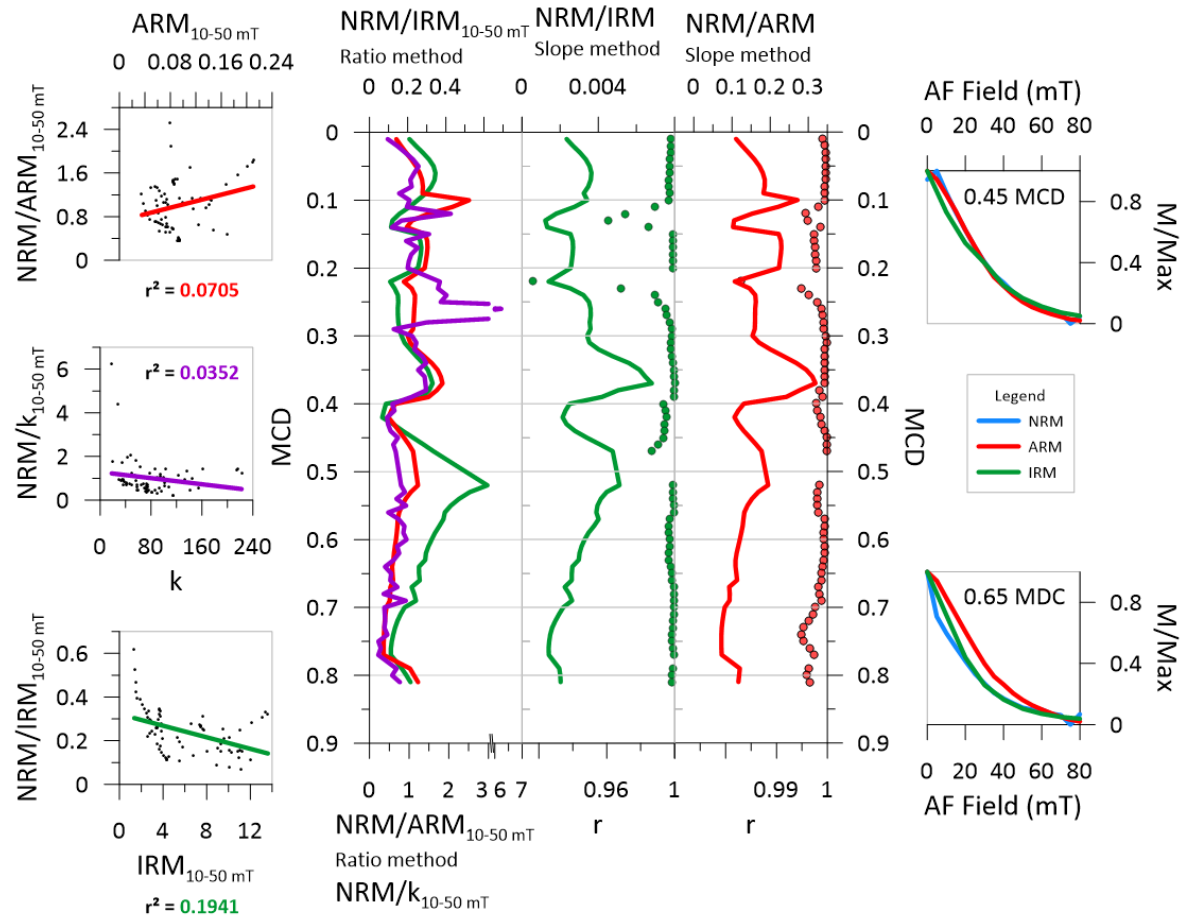


Figure 52 - Comparison of the CAS16-14PC RPI variations estimated with the average ratios (superposed red, green and violet curves for ARM, IRM and k respectively) and slope methods (red and green curves). Scatter plots on the left test unconformity of normalizers against estimated RPI and show a reduced correlation for k and ARM. Demagnetization curves for NRM, ARM and IRM are presented on the right-hand side.

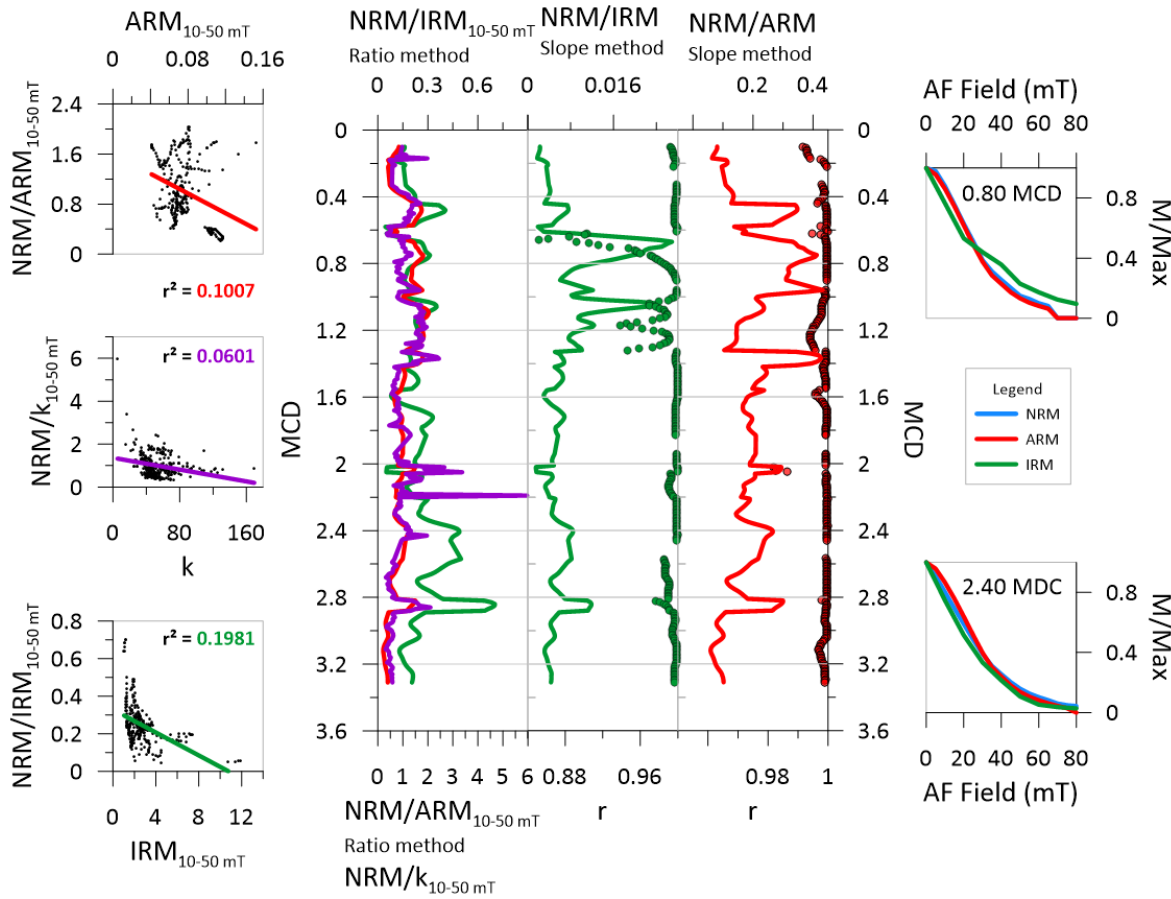


Figure 53 - Comparison of the CAS16-36PC RPI variations estimated with the average ratios (superposed red, green and violet curves for ARM, IRM and k respectively) and slope methods (red and green curves). Scatter plots on the left test unconformity of normalizers against estimated RPI and show a reduced correlation for k and ARM. Demagnetization curves for NRM, ARM and IRM are presented on the right-hand side.

Table 7 - List of all samples collected and analyzed on AGM with depth in meter and respective magnetic parameters in tesla.

Sample	Depth (m)	Ms (T)	Mr (T)	Hc (T)	Hcr (T)	Type
CAS16-04PC	3.5	2.34E-06	2.95E-07	1.16E-02	3.63E-02	HMPL
CAS16-04PC	4.4	9.42E-07	1.98E-07	1.82E-02	4.86E-02	HMPL
CAS16-04PC	4.85	1.53E-06	3.49E-07	1.92E-02	4.34E-02	HMPL
CAS16-04PC	5.25	1.64E-06	2.55E-07	1.29E-02	3.48E-02	HMPL
CAS16-04PC	5.64	3.01E-06	3.97E-07	1.07E-02	2.87E-02	HMPL
CAS16-04PC	5.75	1.54E-06	3.30E-07	1.72E-02	4.07E-02	HMPL
CAS16-04PC	10.73	4.71E-07	5.98E-08	1.08E-02	3.16E-02	HMPL
CAS16-04PC	12.85	3.52E-07	4.53E-08	1.04E-02	3.08E-02	HMPL
CAS16-04PC	13.02	2.82E-07	3.31E-08	9.50E-03	3.10E-02	MIX
CAS16-04PC	13.09	1.10E-07	1.68E-08	1.13E-02	3.20E-02	HMG
CAS16-04PC	13.53	2.37E-07	3.43E-08	1.07E-02	3.55E-02	HMG
CAS16-04PC	15.94	2.86E-07	3.17E-08	9.23E-03	3.19E-02	HMG
CAS16-04PC	15.99	2.38E-07	2.70E-08	8.99E-03	3.17E-02	MIX
CAS16-04PC	16.325	4.98E-07	5.76E-08	9.49E-03	3.20E-02	HMPL
CAS16-04PC	16.5	2.73E-07	4.25E-08	1.11E-02	3.19E-02	HMPL
CAS16-04PC	17.1	2.34E-06	2.95E-07	1.16E-02	4.42E-02	HMPL
CAS16-14PC	0.3	5.87E-07	1.16E-07	1.64E-02	3.36E-02	HMPL
CAS16-14PC	6.85	1.58E-06	2.72E-07	1.32E-02	4.34E-02	HMPL

CAS16-14PC	7.3	9.19E-07	2.10E-07	1.80E-02	3.38E-02	HMPL
CAS16-14PC	15.06	4.07E-07	7.25E-08	1.34E-02	3.51E-02	HMPL
CAS16-14PC	15.5	4.11E-07	6.23E-08	1.23E-02	3.08E-02	HMG
CAS16-14PC	16.26	6.85E-07	6.45E-08	7.12E-03	3.26E-02	TU
CAS16-14PC	16.38	1.96E-07	2.98E-08	1.12E-02	3.13E-02	MIX
CAS16-14PC	16.45	4.23E-07	6.26E-08	1.15E-02	3.61E-02	HMG
CAS16-14PC	18.08	4.76E-07	7.17E-08	1.21E-02	3.95E-02	HMG
CAS16-14PC	20.85	5.41E-07	8.18E-08	1.25E-02	2.95E-02	HMG
CAS16-14PC	21.7	4.94E-07	5.36E-08	8.50E-03	3.23E-02	TU
CAS16-14PC	22.15	1.03E-06	1.37E-07	1.10E-02	3.17E-02	HMPL
CAS16-14PC	22.4	2.08E-06	2.49E-07	9.87E-03	4.75E-02	HMPL
CAS16-36PC	1.65	6.18E-07	1.10E-07	1.55E-02	5.04E-02	HMPL
CAS16-36PC	3.5	3.63E-07	7.43E-08	1.71E-02	3.56E-02	HMPL
CAS16-36PC	6.8	4.77E-07	7.70E-08	1.36E-02	3.27E-02	HMPL
CAS16-36PC	10.2	1.18E-06	1.93E-07	1.27E-02	5.26E-02	HMPL
CAS16-36PC	10.8	8.86E-07	2.13E-07	2.01E-02	3.44E-02	HMPL
CAS16-36PC	16	8.79E-07	1.38E-07	1.21E-02	3.40E-02	HMPL
CAS16-36PC	16.5	7.62E-07	1.23E-07	1.24E-02	4.76E-02	HMPL
CAS16-36PC	20.26	9.71E-08	1.59E-08	1.40E-02	3.49E-02	HMPL
CAS16-36PC	20.53	4.08E-07	6.58E-08	1.17E-02	3.48E-02	HMPL

CAS16-36PC	21	6.10E-07	7.35E-08	1.05E-02	3.26E-02	HMPL
CAS16-36PC	21.35	1.01E-06	1.11E-07	9.46E-03	2.63E-02	HMPL
CAS16-36PC	21.41	8.01E-07	6.93E-08	7.78E-03	3.43E-02	MIX
CAS16-36PC	21.42	3.94E-07	4.94E-08	1.04E-02	3.10E-02	MIX
CAS16-36PC	21.5	1.90E-07	2.44E-08	1.01E-02	3.03E-02	HMG
CAS16-36PC	22.58	7.54E-07	1.07E-07	1.07E-02	4.03E-02	HMG
CAS16-36PC	24.09	5.40E-07	7.16E-08	1.11E-02	3.01E-02	HMG
CAS16-36PC	24.5	6.00E-07	5.68E-08	8.80E-03	3.71E-02	HMG
CAS16-36PC	24.54	2.01E-07	2.11E-08	9.08E-03	2.91E-02	MIX
CAS16-36PC	25.93	3.29E-07	1.79E-08	4.39E-03	3.48E-02	TU
CAS16-36PC	25.97	3.38E-07	4.43E-08	1.10E-02	3.26E-02	HMPL
CAS16-36PC	26.7	5.84E-07	6.97E-08	1.06E-02	3.63E-02	HMPL
CAS16-12PC	1.5	7.30E-07	1.51E-07	1.60E-02	4.45E-02	HMPL
CAS16-12PC	3	1.12E-06	2.60E-07	1.84E-02	4.55E-02	HMPL
CAS16-12PC	4.5	4.26E-07	6.42E-08	1.25E-02	3.63E-02	HMPL
CAS16-12PC	6	4.37E-07	9.49E-08	1.58E-02	3.61E-02	HMPL
CAS16-12PC	7.5	6.70E-07	1.67E-07	2.01E-02	4.50E-02	HMPL
CAS16-12PC	9	4.67E-07	7.25E-08	1.17E-02	3.38E-02	HMPL
CAS16-12PC	10.5	6.60E-07	9.62E-08	1.09E-02	3.15E-02	HMPL
CAS16-12PC	12	2.82E-07	4.99E-08	1.34E-02	3.68E-02	TU

CAS16-12PC	13.5	3.02E-07	5.55E-08	1.37E-02	3.70E-02	HMPL
CAS16-12PC	15	1.01E-06	1.66E-07	1.17E-02	3.38E-02	TU
CAS16-12PC	16.5	1.15E-06	1.99E-07	1.21E-02	3.26E-02	HMPL

Table 8 - Meter composite depth (MCD) correspondence with original coring depth in meter.

CAS16-04PC				CAS16-14PC		CAS16-36PC		CAS16-12PC	
MCD (m)	Depth (m)	MCD (m)	Depth (m)	MCD (cm)	Depth (m)	MCD (m)	Depth (m)	MCD (m)	Depth (m)
0.01	3.35	4.39	17.98	0.1	4.98	0.01	1.46	0.01	0.28
0.17	3.51	4.40	18.10	0.9	5.06	0.17	1.62	1.52	1.79
0.18	3.55	4.46	18.16	0.10	5.25	0.18	2.91	1.53	1.95
0.26	3.63	4.47	18.18	0.21	5.36	0.44	3.17	1.72	2.14
0.27	3.68	4.81	18.52	0.22	6.78	0.45	3.84	1.73	2.17
0.30	3.71	4.82	18.74	0.40	6.96	0.57	3.96	2.13	2.57
0.34	3.91	5.18	19.10	0.41	7.06	0.58	8.33	2.14	2.59
0.35	3.95			0.44	7.09	0.61	8.36	2.87	3.32
0.48	4.08			0.45	7.21	0.62	10.17	2.88	3.37
0.49	4.27			0.49	7.25	0.66	10.21	5.37	5.86
0.95	4.73			0.50	10.07	0.67	10.23	5.38	5.90
0.96	4.81			0.55	10.12	0.70	10.26	6.73	7.37
1.10	4.95			0.56	14.74	0.71	10.28	6.74	7.65
1.11	5.10			0.64	14.82	0.74	10.31	7.88	8.79
1.14	5.13			0.65	14.85	0.75	10.33	7.89	8.87
1.15	5.21			0.72	14.92	0.95	10.53	9.63	10.61
1.30	5.36			0.73	14.97	0.96	10.60	9.64	10.66

1.31	5.60
1.37	5.66
1.38	5.70
1.47	5.79
1.48	5.85
1.83	6.20
1.84	9.45
1.94	9.55
1.95	9.64
1.96	9.65
1.97	9.86
2.74	10.63
2.75	10.69
2.79	10.73
2.80	11.50
2.87	11.57
2.88	16.26
2.92	16.30
2.93	16.40
3.27	16.74

0.74	14.98	1.12	10.76	9.80	10.82
0.75	15.15	1.13	10.78	9.81	10.99
0.77	15.17	1.32	10.97	10.67	11.85
0.78	15.25	1.33	15.88	10.68	12.45
0.82	15.29	1.41	15.96	10.72	12.49
0.83	15.86	1.42	15.99	10.73	12.79
0.86	15.89	1.55	16.12	10.86	12.92
0.87	22.01	1.56	16.22	10.87	13.08
0.91	22.05	1.77	16.43	11.45	13.66
0.92	22.08	1.78	16.45	11.46	13.71
0.98	22.14	1.98	16.65	11.73	13.98
0.99	22.19	1.99	16.69	11.74	14.46
1.01	22.21	2.01	16.71	12.03	14.75
1.02	22.32	2.02	20.22	12.04	14.80
1.04	22.34	2.05	20.25	12.07	14.83
1.05	22.38	2.06	20.41	12.08	15.18
1.12	22.45	2.20	20.55	12.50	15.60
1.13	22.76	2.21	20.77	12.51	15.65
1.14	23.02	2.81	21.37	13.55	16.69
1.16	23.04	2.82	25.96	13.56	16.72

3.28	16.78
3.42	16.92
3.43	16.96
3.91	17.44
3.92	17.51

2.88	26.02	14.11	17.27
2.89	26.57	14.12	17.32
3.31	26.99	14.81	18.01
		14.82	18.51
		14.89	18.58



## RÉFÉRENCES BIBLIOGRAPHIQUES

- Adams, J., 1990. Paleoseismicity of the Cascadia Subduction Zone: Evidence from turbidites off the Oregon-Washington Margin. *Tectonics* 9, 569–583. <https://doi.org/10.1029/TC009i004p00569>
- BCSF, 2005. Séisme des Saintes (Guadeloupe) du 21 novembre 2004, note préliminaire, BCSF2005-NP3, 62 p., 101 fig., 28 tableaux, 5 annexes.
- Beck, C., 2009. “Late Quaternary lacustrine paleo-seismic archives in north-western Alps: Examples of earthquake-origin assessment of sedimentary disturbances.” *Earth-Science Reviews* 96, 327–344. <https://doi.org/10.1016/j.earscirev.2009.07.005>
- Beck, C., Reyss, J.-L., Leclerc, F., Moreno, E., Feuillet, N., Barrier, L., Beauducel, F., Boudon, G., Clément, V., Deplus, C., Gallou, N., Lebrun, J.-F., Le Friant, A., Nercessian, A., Paterne, M., Pichot, T., Vidal, C., 2012. Identification of deep subaqueous co-seismic scarps through specific coeval sedimentation in Lesser Antilles: implication for seismic hazard. *Natural Hazards and Earth System Science* 12, 1755–1767. <https://doi.org/10.5194/nhess-12-1755-2012>
- Bertil, D., S. Bazin, D. Mallarino, F. Beauducel, Localisation des principales répliques du séisme des Saintes du 21 Novembre 2004, Centre de Données Sismologiques des Antilles, 15 Avril 2005.
- Bieber, A., St-Onge, G., Feuillet, N., Carlut, J., Moreno, E., Michel, E., 2021. Regional chronostratigraphy in the eastern Lesser Antilles quaternary fore-arc and accretionary wedge sediments: Relative paleointensity, oxygen isotopes and reversals. *Quaternary Geochronology* 65, 101179. <https://doi.org/10.1016/j.quageo.2021.101179>
- Biju-Duval, B., Moore, J.C., et al., 1984. Initial Reports of the Deep Sea Drilling Project, 78A, Initial Reports of the Deep Sea Drilling Project. U.S. Government Printing Office. <https://doi.org/10.2973/dsdp.proc.78a.1984>
- Bilek, S.L., Lay, T., 2018. Subduction zone megathrust earthquakes. *Geosphere* 14, 1468–1500. <https://doi.org/10.1130/GES01608.1>
- Bouysse, P., Westercamp, D., 1990. Subduction of Atlantic aseismic ridges and Late Cenozoic evolution of the Lesser Antilles island arc. *Tectonophysics* 175, 349–355, 357–380.

Briden, J.C., Rex, D.C., Faller, A.M., Tomblin, J.F., 1979. K-Ar Geochronology and Palaeomagnetism of Volcanic Rocks in the Lesser Antilles Island Arc. Philosophical Transactions of the Royal Society A: Mathematical, Physical and Engineering Sciences 291, 485–528. <https://doi.org/10.1098/rsta.1979.0040>

Brunet, M., Le Friant, A., Boudon, G., Lafuerza, S., Talling, P., Hornbach, M., Ishizuka, O., Lebas, E., Guyard, H., IODP Expedition 340 Science Party, 2016. Composition, geometry, and emplacement dynamics of a large volcanic island landslide offshore Martinique: From volcano flank-collapse to seafloor sediment failure?: SUBMARINE LANDSLIDES OFFSHORE MARTINIQUE. Geochem. Geophys. Geosyst. 17, 699–724. <https://doi.org/10.1002/2015GC006034>

Brunhes, B., 1906. Recherches sur la direction d'aimantation des roches volcaniques. J. Phys. Theor. Appl. 5, 705–724. <https://doi.org/10.1051/jphystap:019060050070500>

Carlut, J., Quidelleur, X., 2000. Absolute paleointensities recorded during the Brunhes chron at La Guadeloupe Island. Physics of the Earth and Planetary Interiors 120, 255–269.

Caron, M., St-Onge, G., Montero-Serrano, J.-C., Rochon, A., Georgiadis, E., Giraudeau, J., Massé, G., 2019. Holocene chronostratigraphy of northeastern Baffin Bay based on radiocarbon and palaeomagnetic data. Boreas 48, 147–165. <https://doi.org/10.1111/bor.12346>

Chang, L., Hong, H., Bai, F., Wang, S., Pei, Z., Paterson, G.A., Heslop, D., Roberts, A.P., Huang, B., Tauxe, L., Muxworthy, A.R., 2020. Detrital remanent magnetization of single-crystal silicates with magnetic inclusions: constraints from deposition experiments. Geophysical Journal International 224, 2001–2015. <https://doi.org/10.1093/gji/ggaa559>

Channell, J.E.T., Hodell, D.A., Lehman, B., 1997. Relative geomagnetic paleointensity and  $\delta^{18}\text{O}$  at ODP Site 983 ŽGardar Drift, North Atlantic/ since 350 ka 16.

Channell, J.E.T., Singer, B.S., Jicha, B.R., 2020. Timing of Quaternary geomagnetic reversals and excursions in volcanic and sedimentary archives. Quaternary Science Reviews 228, 106114. <https://doi.org/10.1016/j.quascirev.2019.106114>

Channell, J.E.T., Xuan, C., Hodell, D.A., 2009. Stacking paleointensity and oxygen isotope data for the last 1.5 Myr (PISO-1500). Earth and Planetary Science Letters 283, 14–23. <https://doi.org/10.1016/j.epsl.2009.03.012>

Chapron, E., Beck, C., Pourchet, M., Deconinck, J.-F., 1999. 1822 earthquake-triggered homogenite in Lake Le Bourget (NW Alps). Terra Nova 11, 86–92. <https://doi.org/10.1046/j.1365-3121.1999.00230.x>

- Chrystèle, V., Mazabraud, Y., Lardeaux, J.-M., Corsini, M., Schneider, D., Voitus, E., Zami, F., 2016. Tectonic evolution of Les Saintes archipelago (Guadeloupe, French West Indies): relation with the Lesser Antilles arc system. *Bulletin de la Société Géologique de France* 187, 3–10.
- Cita, M.B., 2008. Deep-sea homogenites, in: Tsunamiites. Elsevier, pp. 207–224. <https://doi.org/10.1016/B978-0-12-823939-1.00013-6>
- Cornée, J.-J., Léticée, J.-L., Münch, P., Quillévéré, F., Lebrun, J.-F., Moissette, P., Braga, J.-C., Melinte-Dobrinescu, M., De Min, L., Oudet, J., Randrianasolo, A., 2012. Sedimentology, palaeoenvironments and biostratigraphy of the Pliocene-Pleistocene carbonate platform of Grande-Terre (Guadeloupe, Lesser Antilles forearc): Sedimentology, palaeoenvironments and biostratigraphy. *Sedimentology* 59, 1426–1451. <https://doi.org/10.1111/j.1365-3091.2011.01311.x>
- Damuth, J.E., 1977. Late Quaternary sedimentation in the western equatorial Atlantic. *Geological Society of America Bulletin* 88, 695–710.
- Davies, J.H., 1999. The role of hydraulic fractures and intermediate-depth earthquakes in subduction-zone magmatism. *Nature* 398, 142–145. <https://doi.org/10.1038/18202>
- DeMets, C., Jansma, P.E., Mattioli, G.S., Dixon, T.H., Farina, F., Bilham, R., Calais, E., Mann, P., 2000. GPS geodetic constraints on Caribbean-North America Plate Motion. *Geophysical Research Letters* 27, 437–440. <https://doi.org/10.1029/1999GL005436>
- Deplus, C., Le Friant, A., Boudon, G., Komorowski, J.-C., Villemant, B., Harford, C., Séguofin, J., Cheminée, J.-L., 2001. Submarine evidence for large-scale debris avalanches in the Lesser Antilles Arc. *Earth and Planetary Science Letters* 192, 145–157. [https://doi.org/10.1016/S0012-821X\(01\)00444-7](https://doi.org/10.1016/S0012-821X(01)00444-7)
- Deschamps, C.-E., St-Onge, G., Montero-Serrano, J.-C., Polyak, L., 2018. Chronostratigraphy and spatial distribution of magnetic sediments in the Chukchi and Beaufort seas since the last deglaciation. *Boreas* 47, 544–564. <https://doi.org/10.1111/bor.12296>
- Deville, E., Mascle, A., Callec, Y., Huyghe, P., Lallement, S., Lerat, O., Mathieu, X., Padron de Carillo, C., Patriat, M., Pichot, T., Loubrieux, B., Granjeon, D., 2015. Tectonics and sedimentation interactions in the east Caribbean subduction zone: An overview from the Orinoco delta and the Barbados accretionary prism. *Marine and Petroleum Geology* 64, 76–103. <https://doi.org/10.1016/j.marpetgeo.2014.12.015>

Dixon, T.H., Farina, F., DeMets, C., Jansma, P., Mann, P., Calais, E., 1998. Relative motion between the Caribbean and North American plates and related boundary zone deformation from a decade of GPS observations. *Journal of Geophysical Research: Solid Earth* 103, 15157–15182. <https://doi.org/10.1029/97JB03575>

Draper, G., Jackson, T.A., Donovan, S.K., 1994. Geologic provinces of the Caribbean Region. *Caribbean Geology: An Introduction*. Kingston, Jamaica, UWI Publishers' Association 3–12.

Feuillet, N., 2016. CASEIS cruise, RV Pourquoi pas ? <https://doi.org/10.17600/16001800>

Feuillet, N., Beauducel, F., Jacques, E., Tapponnier, P., Delouis, B., Bazin, S., Vallée, M., King, G.C.P., 2011a. The  $M_w = 6.3$ , November 21, 2004, Les Saintes earthquake (Guadeloupe): Tectonic setting, slip model and static stress changes. *Journal of Geophysical Research* 116. <https://doi.org/10.1029/2011JB008310>

Feuillet, N., Beauducel, F., Tapponnier, P., 2011b. Tectonic context of moderate to large historical earthquakes in the Lesser Antilles and mechanical coupling with volcanoes. *Journal of Geophysical Research* 116. <https://doi.org/10.1029/2011JB008443>

Feuillet, N., Manighetti, I., Tapponnier, P., 2001. Extension active perpendiculaire à la subduction dans l'arc des Petites Antilles (Guadeloupe, Antilles françaises). *Comptes Rendus de l'Académie des Sciences-Series IIA-Earth and Planetary Science* 333, 583–590.

Feuillet, N., Manighetti, I., Tapponnier, P., Jacques, E., 2002. Arc parallel extension and localization of volcanic complexes in Guadeloupe, Lesser Antilles: EXTENSIONAL ACTIVE FAULTING IN GUADELOUPE. *Journal of Geophysical Research: Solid Earth* 107, ETG 3-1-ETG 3-29. <https://doi.org/10.1029/2001JB000308>

Feuillet, N., Tapponnier, P., Manighetti, I., Villemant, B., King, G.C.P., 2004. Differential uplift and tilt of Pleistocene reef platforms and Quaternary slip rate on the Morne-Piton normal fault (Guadeloupe, French West Indies): QUATERNARY DEFORMATION IN GUADELOUPE. *Journal of Geophysical Research: Solid Earth* 109. <https://doi.org/10.1029/2003JB002496>

Germa, A., Quidelleur, X., Labanieh, S., Lahitte, P., Chauvel, C., 2010. The eruptive history of Morne Jacob volcano (Martinique Island, French West Indies): Geochronology, geomorphology and geochemistry of the earliest volcanism in the recent Lesser Antilles arc. *Journal of Volcanology and Geothermal Research* 198, 297–310. <https://doi.org/10.1016/j.jvolgeores.2010.09.013>

Giunta, G., Orioli, S., 2011. The Caribbean Plate Evolution: Trying to Resolve a Very Complicated Tectonic Puzzle, in: Sharkov, E. (Ed.), New Frontiers in Tectonic Research - General Problems, Sedimentary Basins and Island Arcs. InTech. <https://doi.org/10.5772/18723>

Goldfinger, C., 2011. Submarine Paleoseismology Based on Turbidite Records. Annu. Rev. Mar. Sci. 3, 35–66. <https://doi.org/10.1146/annurev-marine-120709-142852>

Goldfinger, C., Grijalva, K., Burgmann, R., Morey, A.E., Johnson, J.E., Nelson, C.H., Gutierrez-Pastor, J., Ericsson, A., Karabanov, E., Chaytor, J.D., Patton, J., Gracia, E., 2008. Late Holocene Rupture of the Northern San Andreas Fault and Possible Stress Linkage to the Cascadia Subduction Zone. Bulletin of the Seismological Society of America 98, 861–889. <https://doi.org/10.1785/0120060411>

Goldfinger, C., Morey, A.E., Nelson, C.H., Gutiérrez-Pastor, J., Johnson, J.E., Karabanov, E., Chaytor, J., Eriksson, A., 2007. Rupture lengths and temporal history of significant earthquakes on the offshore and north coast segments of the Northern San Andreas Fault based on turbidite stratigraphy. Earth and Planetary Science Letters 254, 9–27. <https://doi.org/10.1016/j.epsl.2006.11.017>

Goldfinger, C., Nelson, C.H., Johnson, J.E., The Shipboard Scientific Party, 2003. Holocene earthquake records from the Cascadia subduction zone and northern San Andreas fault based on precise dating of offshore turbidites. Annual Review of Earth and Planetary Sciences 31, 555–577. <https://doi.org/10.1146/annurev.earth.31.100901.141246>

Gràcia, E., Vizcaino, A., Escutia, C., Asioli, A., Rodés, Á., Pallàs, R., Garcia-Orellana, J., Lebreiro, S., Goldfinger, C., 2010. Holocene earthquake record offshore Portugal (SW Iberia): testing turbidite paleoseismology in a slow-convergence margin. Quaternary Science Reviews 29, 1156–1172. <https://doi.org/10.1016/j.quascirev.2010.01.010>

Hayes, G.P., Moore, G.L., Portner, D.E., Hearne, M., Flamme, H., Furtney, M., Smoczyk, G.M., 2018. Slab2, a comprehensive subduction zone geometry model. Science 362, 58–61. <https://doi.org/10.1126/science.aat4723>

Heezen, B.C., Ewing, W.M., 1952. Turbidity currents and submarine slumps, and the 1929 Grand Banks [Newfoundland] earthquake. American Journal of Science 250, 849–873. <https://doi.org/10.2475/ajs.250.12.849>

Hounslow, M.W., Bootes, P.A., Whyman, G., 1990. 25. Remanent magnetization of sediments undergoing deformation in the Barbados accretionary prism: ODP LEG110. <https://doi.org/10.2973/odp.proc.sr.110.155.1990>

Ikehara, K., Kanamatsu, T., Nagahashi, Y., Strasser, M., Fink, H., Usami, K., Irino, T., Wefer, G., 2016. Documenting large earthquakes similar to the 2011 Tohoku-oki earthquake from sediments deposited in the Japan Trench over the past 1500 years. *Earth and Planetary Science Letters* 445, 48–56. <https://doi.org/10.1016/j.epsl.2016.04.009>

James, K.H., 2013. Caribbean Geology: Extended and Subsided Continental Crust Sharing History with Eastern North America, the Gulf of Mexico, the Yucatán Basin and Northern South America. *GS* 40. <https://doi.org/10.12789/geocanj.2013.40.001>

James, K.H., 2005. A simple synthesis of Caribbean geology. *Caribbean Journal of Earth Science* 39, 69–82.

Johns, W.E., Lee, T.N., Beardsley, R.C., Candela, J., Limeburner, R., Castro, B., 1998. Annual Cycle and Variability of the North Brazil Current. *J. Phys. Oceanogr.* 28, 103–128. [https://doi.org/10.1175/1520-0485\(1998\)028<0103:ACAVOT>2.0.CO;2](https://doi.org/10.1175/1520-0485(1998)028<0103:ACAVOT>2.0.CO;2)

Johns, W.E., Townsend, T.L., Fratantoni, D.M., Wilson, W.D., 2002. On the Atlantic inflow to the Caribbean Sea. *Deep Sea Research Part I: Oceanographic Research Papers* 49, 211–243.

Jones, C.A., 2015. Thermal and Compositional Convection in the Outer Core, in: *Treatise on Geophysics*. Elsevier, pp. 115–159. <https://doi.org/10.1016/B978-0-444-53802-4.00141-X>

Kastens, K.A., Cita, M.B., 1981. Tsunami-induced sediment transport in the abyssal Mediterranean Sea. *Geol Soc America Bull* 92, 845. [https://doi.org/10.1130/0016-7606\(1981\)92<845:TSTITA>2.0.CO;2](https://doi.org/10.1130/0016-7606(1981)92<845:TSTITA>2.0.CO;2)

Kent, D.V., Spariosu, D.J., 1983. High resolution magnetostratigraphy of Caribbean Plio-Pleistocene deep-sea sediments. *Palaeogeography, Palaeoclimatology, Palaeoecology* 42, 47–64. [https://doi.org/10.1016/0031-0182\(83\)90038-X](https://doi.org/10.1016/0031-0182(83)90038-X)

Keppie, D.F., 2014. *The Analysis of Diffuse Triple Junction Zones in Plate Tectonics and the Pirate Model of Western Caribbean Tectonics*, SpringerBriefs in Earth Sciences. Springer New York, New York, NY. <https://doi.org/10.1007/978-1-4614-9616-8>

Keppie, F., 2013. The Rationale and Essential Elements for the New ‘Pirate’ Model of Caribbean Tectonics. *GS* 40. <https://doi.org/10.12789/geocanj.2013.40.002>

- Laurencin, M., Graindorge, D., Klingelhoefer, F., Marcaillou, B., Evain, M., 2018. Influence of increasing convergence obliquity and shallow slab geometry onto tectonic deformation and seismogenic behavior along the Northern Lesser Antilles zone. *Earth and Planetary Science Letters* 492, 59–72. <https://doi.org/10.1016/j.epsl.2018.03.048>
- Le Friant, A., Harford, C.L., Deplus, C., Boudon, G., Sparks, R.S.J., Herd, R.A., Komorowski, J.C., 2004. Geomorphological evolution of Montserrat (West Indies): importance of flank collapse and erosional processes. *Journal of the Geological Society* 161, 147–160. <https://doi.org/10.1144/0016-764903-017>
- Le Friant, A., Lock, E.J., Hart, M.B., Boudon, G., Sparks, R.S.J., Leng, M.J., Smart, C.W., Komorowski, J.C., Deplus, C., Fisher, J.K., 2008. Late Pleistocene tephrachronology of marine sediments adjacent to Montserrat, Lesser Antilles volcanic arc. *Journal of the Geological Society* 165, 279–289. <https://doi.org/10.1144/0016-76492007-019>
- Leclerc, F., Feuillet, N., Deplus, C., 2016. Interactions between active faulting, volcanism, and sedimentary processes at an island arc: Insights from Les Saintes channel, Lesser Antilles arc: FAULTING, VOLCANISM, AND TURBIDITY SYSTEMS. *Geochemistry, Geophysics, Geosystems* 17, 2781–2802. <https://doi.org/10.1002/2016GC006337>
- Limonta, M., Garzanti, E., Resentini, A., Andò, S., Boni, M., Bechstädt, T., 2015. Multicyclic sediment transfer along and across convergent plate boundaries (Barbados, Lesser Antilles). *Basin Research* 27, 696–713. <https://doi.org/10.1111/bre.12095>
- Lindsay, J.M., Trumbull, R.B., Siebel, W., 2005. Geochemistry and petrogenesis of late Pleistocene to Recent volcanism in Southern Dominica, Lesser Antilles. *Journal of Volcanology and Geothermal Research* 148, 253–294. <https://doi.org/10.1016/j.jvolgeores.2005.04.018>
- Lisé-Pronovost, A., St-Onge, G., Gogorza, C., Jouvet, G., Francus, P., Zolitschka, B., 2014. Rock-magnetic signature of precipitation and extreme runoff events in south-eastern Patagonia since 51,200 cal BP from the sediments of Laguna Potrok Aike. *Quaternary Science Reviews* 98, 110–125. <https://doi.org/10.1016/j.quascirev.2014.05.029>
- Lisiecki, L.E., Raymo, M.E., 2005. A Pliocene-Pleistocene stack of 57 globally distributed benthic  $\delta^{18}\text{O}$  records: PLIOCENE-PLEISTOCENE BENTHIC STACK. *Paleoceanography* 20, n/a-n/a. <https://doi.org/10.1029/2004PA001071>
- Lohmann, K.J., 2010. Magnetic-field perception. *Nature* 464, 1140–1142. <https://doi.org/10.1038/4641140a>

Macdonald, R., Hawkesworth, C.J., Heath, E., 2000. The Lesser Antilles volcanic chain: a study in arc magmatism. *Earth-Science Reviews* 49, 1–76.

Mascle, A., Moore, J.C., et al. (Eds.), 1988. Proceedings of the Ocean Drilling Program, 110 Initial Reports, Proceedings of the Ocean Drilling Program. Ocean Drilling Program. <https://doi.org/10.2973/odp.proc.ir.110.1988>

Morena, P., 2020. Paléosismologie et potentiel sismogène de la zone de subduction des Petites Antilles à partir de l'enregistrement sédimentaire. L'UNIVERSITE DE BRETAGNE OCCIDENTALE.

Münch, Ph., Cornee, J.-J., Lebrun, J.-F., Quillevere, F., Verati, C., Melinte-Dobrinescu, M., Demory, F., Smith, B., Jourdan, F., Lardeaux, J.-M., De Min, L., Leticee, J.-L., Randrianasolo, A., 2014. Pliocene to Pleistocene vertical movements in the forearc of the Lesser Antilles subduction: insights from chronostratigraphy of shallow-water carbonate platforms (Guadeloupe archipelago). *Journal of the Geological Society* 171, 329–341. <https://doi.org/10.1144/jgs2013-005>

Newell, R.E., Kidson J.W., Vincent G., Boer G.J., 1972. The general circulation of the tropical atmosphere. MIT Press, Cambridge in: Picard, M., Schneider, J.-L., Boudon, G., 2006. Contrasting sedimentary processes along a convergent margin: the Lesser Antilles arc system. *Geo-Marine Letters* 26, 397–410. doi:10.1007/s00367-006-0046-y.

Pacheco, J.F., Sykes, L.R., 1992. Seismic moment catalog of large shallow earthquakes, 1900 to 1989. *Bulletin of the Seismological Society of America* 82, 1306–1349.

Patton, J.R., Goldfinger, C., Morey, A.E., Romsos, C., Black, B., Djadjadihardja, Y., Udrehk, 2013. Seismoturbidite record as preserved at core sites at the Cascadia and Sumatra–Andaman subduction zones. *Natural Hazards and Earth System Science* 13, 833–867. <https://doi.org/10.5194/nhess-13-833-2013>

Picard, M., Schneider, J.-L., Boudon, G., 2006. Contrasting sedimentary processes along a convergent margin: the Lesser Antilles arc system. *Geo-Marine Letters* 26, 397–410. <https://doi.org/10.1007/s00367-006-0046-y>

Pouderoux, H., Lamarche, G., Proust, J.-N., 2012. Building an 18 000-year-long paleo-earthquake record from detailed deep-sea turbidite characterisation in Poverty Bay, New Zealand. *Natural Hazards and Earth System Sciences* 12, 2077–2101. <https://doi.org/10.5194/nhess-12-2077-2012>

Ratzov, G., Collot, J.-Y., Sosson, M., Migeon, S., 2010. Mass-transport deposits in the northern Ecuador subduction trench: Result of frontal erosion over multiple seismic cycles. *Earth and Planetary Science Letters* 296, 89–102. <https://doi.org/10.1016/j.epsl.2010.04.048>

- Reid, R.P., Carey, S.N., Ross, D.R., 1996. Late Quaternary sedimentation in the Lesser Antilles island arc. Geological Society of America Bulletin 108, 78–100. [https://doi.org/10.1130/0016-7606\(1996\)108<0078:LQSITL>2.3.CO;2](https://doi.org/10.1130/0016-7606(1996)108<0078:LQSITL>2.3.CO;2)
- Ricci, J., Carlut, J., Valet, J.-P., 2018. Paleosecular variation recorded by Quaternary lava flows from Guadeloupe Island. Scientific Reports 8. <https://doi.org/10.1038/s41598-018-28384-z>
- Roberts, A.P., Tauxe, L., Heslop, D., 2013. Magnetic paleointensity stratigraphy and high-resolution Quaternary geochronology: successes and future challenges. Quaternary Science Reviews 61, 1–16. <https://doi.org/10.1016/j.quascirev.2012.10.036>
- Samper, A., Quidelleur, X., Komorowski, J.-C., Lahitte, P., Boudon, G., 2009. Effusive history of the Grande Découverte Volcanic Complex, southern Basse-Terre (Guadeloupe, French West Indies) from new K–Ar Cassignol–Gillot ages. Journal of Volcanology and Geothermal Research 187, 117–130. <https://doi.org/10.1016/j.jvolgeores.2009.08.016>
- Samper, A., Quidelleur, X., Lahitte, P., Mollex, D., 2007. Timing of effusive volcanism and collapse events within an oceanic arc island: Basse-Terre, Guadeloupe archipelago (Lesser Antilles Arc). Earth and Planetary Science Letters 258, 175–191. <https://doi.org/10.1016/j.epsl.2007.03.030>
- Schlupp, A., C. Sira, M. Cara, S. Bazin, C. Michel, J. Régnier, C. Beauval, N. Feuillet, J.-B. De Chabalier, A.-V. Barras, S. Auclair, M.-P. Bouin, C. Duclos, M. Granet (2008) - Séisme de Martinique du 29 novembre 2007, rapport du BCSF : synthèse sismologique et étude macrosismique, BCSF2008-R1, 132 p., 266 figures, 3 tableaux, 5 annexes.
- Seibert, C., 2019. Transferts Sédimentaires et Grands Séismes dans l’Arc des Petites Antilles : Apport de la Paléosismologie en mer. UNIVERSITE PARIS DIDEROT.
- Seibert, C., Feuillet, N., Ratzov, G., Beck, C., Cattaneo, A., 2020. Seafloor morphology and sediments transfers in the mixed carbonated-siliciclastic environment of the Lesser Antilles forearc along Barbuda and St. Lucia. Marine Geology 106242. <https://doi.org/10.1016/j.margeo.2020.106242>
- Sigurdsson, H., Leckie, R.M., Acton G.D., et al., 1997. 1. Introduction: Geologic studies of the Caribbean Sea, in: Caribbean Volcanism, Cretaceous/Tertiary Impact, and Ocean-Climate History Synthesis of Leg 165. - DTU Orbit (25/04/14) Party, Shipboard Scientific and Ida Lind. “Caribbean Volcanism, Cretaceous/Tertiary Impact, and Ocean-Climate History Synthesis of Leg 165.”. Proc. ODP Init. Repts.1997, 165. 377-400.

Sigurdsson, H., Carey, S.N., 1981. Marine Tephrochronology and Quaternary Explosive Volcanism in the Lesser Antilles Arc, in: Self, S., Sparks, R.S.J. (Eds.), *Tephra Studies*. Springer Netherlands, Dordrecht, pp. 255–280. [https://doi.org/10.1007/978-94-009-8537-7\\_16](https://doi.org/10.1007/978-94-009-8537-7_16)

Simon, Q., Suganuma, Y., Okada, M., Haneda, Y., 2019. High-resolution  $^{10}\text{Be}$  and paleomagnetic recording of the last polarity reversal in the Chiba composite section: Age and dynamics of the Matuyama–Brunhes transition. *Earth and Planetary Science Letters* 519, 92–100. <https://doi.org/10.1016/j.epsl.2019.05.004>

Singer, B.S., 2014. A Quaternary geomagnetic instability time scale. *Quaternary Geochronology* 21, 29–52. <https://doi.org/10.1016/j.quageo.2013.10.003>

Spassov, S., Valet, J.-P., 2012. Detrital magnetizations from redeposition experiments of different natural sediments. *Earth and Planetary Science Letters* 351–352, 147–157. <https://doi.org/10.1016/j.epsl.2012.07.016>

Stanley, D.J., Maldonado, A., 1981. Depositional models for fine-grained sediment in the western Hellenic Trench, Eastern Mediterranean. *Sedimentology* 28, 273–290. <https://doi.org/10.1111/j.1365-3091.1981.tb01680.x>

Stoner, J.S., St-Onge, G., 2007. Chapter Three Magnetic Stratigraphy in Paleoceanography: Reversals, Excursions, Paleointensity, and Secular Variation, in: Developments in Marine Geology. Elsevier, pp. 99–138. [https://doi.org/10.1016/S1572-5480\(07\)01008-1](https://doi.org/10.1016/S1572-5480(07)01008-1)

St-Onge, G., Chapron, E., Mulsow, S., Salas, M., Viel, M., Debret, M., Foucher, A., Mulder, T., Winiarski, T., Desmet, M., Costa, P.J.M., Ghaleb, B., Jaouen, A., Locat, J., 2012. Comparison of earthquake-triggered turbidites from the Saguenay (Eastern Canada) and Reloncavi (Chilean margin) Fjords: Implications for paleoseismicity and sedimentology. *Sedimentary Geology* 243–244, 89–107. <https://doi.org/10.1016/j.sedgeo.2011.11.003>

St-Onge, G., Mulder, T., Piper, D.J.W., Hillaire-Marcel, C., Stoner, J.S., 2004. Earthquake and flood-induced turbidites in the Saguenay Fjord (Québec): a Holocene paleoseismicity record. *Quaternary Science Reviews* 23, 283–294. <https://doi.org/10.1016/j.quascirev.2003.03.001>

Symithe, S., Calais, E., de Chabalier, J.B., Robertson, R., Higgins, M., 2015. Current block motions and strain accumulation on active faults in the Caribbean: CURRENT CARIBBEAN KINEMATICS. *Journal of Geophysical Research: Solid Earth* 120, 3748–3774. <https://doi.org/10.1002/2014JB011779>

Tanty, C., Carlut, J., Valet, J.-P., Germa, A., 2015. Palaeosecular variation recorded by 9 ka to 2.5-Ma-old lavas from Martinique Island: new evidence for the La Palma aborted reversal 617 ka ago. *Geophysical Journal International* 200, 915–932. <https://doi.org/10.1093/gji/ggu423>

Tanty, C., Valet, J.-P., Carlut, J., Bassinot, F., Zaragosi, S., 2016. Acquisition of detrital magnetization in four turbidites: MAGNETIC STUDY OF TURBIDITES. *Geochemistry, Geophysics, Geosystems* 17, 3207–3223. <https://doi.org/10.1002/2016GC006378>

Tatsumi, Y., 2005. The subduction factory: how it operates in the evolving Earth. *GSA today* 15, 4.

Tatsumi, Y., Eggins, S.M., 1995. Subduction Zone Magmatism. Blackwell, Cambridge, 211 pp. in : Macdonald, R., Hawkesworth, C.J., Heath, E., 2000. The Lesser Antilles volcanic chain: a study in arc magmatism. *Earth-Science Reviews* 49, 1–76.

Tauxe, L., 1993. Sedimentary records of relative paleointensity of the geomagnetic field: Theory and practice. *Reviews of Geophysics* 31, 319. <https://doi.org/10.1029/93RG01771>

Tauxe, L., Banerjee, S.K., Butler, R.F. and van der Voo R, Essentials of Paleomagnetism, 5th Web Edition, 2018.

Tauxe, L., Kent, D.V., 1984. Properties of a detrital remanence carried by haematite from study of modern river deposits and laboratory redeposition experiments. *Geophys J Int* 76, 543–561. <https://doi.org/10.1111/j.1365-246X.1984.tb01909.x>

Tauxe, L., Steindorf, J.L., Harris, A., 2006. Depositional remanent magnetization: Toward an improved theoretical and experimental foundation. *Earth and Planetary Science Letters* 244, 515–529. <https://doi.org/10.1016/j.epsl.2006.02.003>

Valet, J.-P., Tanty, C., Carlut, J., 2017. Detrital magnetization of laboratory-redeposited sediments. *Geophysical Journal International* 210, 34–41. <https://doi.org/10.1093/gji/ggx139>

Van Daele, M., Meyer, I., Moernaut, J., De Decker, S., Verschuren, D., De Batist, M., 2017. A revised classification and terminology for stacked and amalgamated turbidites in environments dominated by (hemi)pelagic sedimentation. *Sedimentary Geology* 357, 72–82. <https://doi.org/10.1016/j.sedgeo.2017.06.007>

Westbrook, G.K., Mascle, A., Biju-Duval, B., 1984. Geophysics and the structure of the Lesser Antilles Forearc. *Initial Reports Deep Sea Drilling Program, LXXVIIIA* 23–38.

Wilson, D.S., 1984. Paleomagnetic results from Deep Sea Drilling Project Leg 78A. Init. Repts DSDP 78, 583–591.

Wright, A., 1984. Sediment accumulation rates of the Lesser Antilles intraoceanic island arc, Deep Sea Drilling Project leg 78A. Init. Repts DSDP 78, 583–591.

Xuan, C., Channell, J.E.T., Hodell, D.A., 2016. Quaternary magnetic and oxygen isotope stratigraphy in diatom-rich sediments of the southern Gardar Drift (IODP Site U1304, North Atlantic). *Quaternary Science Reviews* 142, 74–89. <https://doi.org/10.1016/j.quascirev.2016.04.010>

Zhang, Y., Chiessi, C.M., Mulitza, S., Sawakuchi, A.O., Häggi, C., Zabel, M., Portilho-Ramos, R.C., Schefuß, E., Crivellari, S., Wefer, G., 2017. Different precipitation patterns across tropical South America during Heinrich and Dansgaard-Oeschger stadials. *Quaternary Science Reviews* 177, 1–9. <https://doi.org/10.1016/j.quascirev.2017.10.012>

Ziegler, L.B., Constable, C.G., Johnson, C.L., Tauxe, L., 2011. PADM2M: a penalized maximum likelihood model of the 0–2 Ma palaeomagnetic axial dipole moment: PADM2M revised. *Geophysical Journal International* 184, 1069–1089. <https://doi.org/10.1111/j.1365-246X.2010.04905.x>